
Study of ν and $\bar{\nu}$ Oscillations in the Three-flavour PMNS Paradigm at the T2K Experiment:

Determination of the CP-Violating Phase and
the search for $\bar{\nu}_\mu \rightarrow \bar{\nu}_e$ Oscillations



Thesis submitted in accordance with the requirements of the University of Liverpool
for the degree of Doctor in Philosophy by Francis Bench

June 2021

Abstract

T2K (Tokai to Kamioka) is an accelerator-based long-baseline neutrino oscillation experiment that aims to study the parameters which govern these oscillations. An almost pure ν_μ or $\bar{\nu}_\mu$ beam with flux sharply peaked at a neutrino energy of 0.6 GeV is produced at the J-PARC facility in Japan before passing through a suite of near detectors then travelling 295 km through the Earth's crust to the 50 ktonne water Cherenkov far detector, Super-Kamiokande. The near detectors, located 280 m from the beam production target, measure the unoscillated flavour composition of the beam and constrain the flux and neutrino-nucleus interaction models. Together, the near and far detectors measure the change in flavour composition, therefore allowing the oscillation parameters to be determined.

This thesis presents a simultaneous analysis of observations from five Super-Kamiokande event samples, selected to measure the disappearance of ν_μ and the appearance of ν_e . Working in the three active neutrino flavour paradigm and using the PMNS parameterisation, constraints are obtained on the oscillation parameters δ_{CP} , $\sin^2 \theta_{23}$, Δm_{32}^2 , and $\sin^2 \theta_{13}$ in both mass orderings. Additionally, the $\bar{\nu}_\mu \rightarrow \bar{\nu}_e$ oscillation channel was specifically analysed in order to determine whether such events could be fully distinguished from the expected backgrounds and it was found that the background-only hypothesis was disfavoured at a significance of 2.4σ . For all fits to the oscillation parameters, the best-fit was found to be in the normal mass ordering and the corresponding best-fit points and $\pm 1\sigma$ ranges are as follows, where the global best-fit measurement on $\sin^2 2\theta_{13}$ from reactor antineutrino experiments was used as a constraint except when producing the T2K constraint on $\sin^2 \theta_{13}$.

$$\begin{aligned}\delta_{CP} &= -2.01^{+0.93}_{-0.76} \\ \sin^2 \theta_{23} &= 0.552^{+0.024}_{-0.048} \\ \Delta m_{32}^2 &= 2.49 \pm 0.05 \times 10^{-3} \text{ eV}^2 \text{c}^{-4} \\ \sin^2 \theta_{13} &= 2.54^{+0.49}_{-0.38} \times 10^{-2}\end{aligned}\tag{1}$$

For δ_{CP} , the best-fit point is close to the maximally CP-violating value of $-\frac{\pi}{2}$, and CP-conservation is excluded at close to the 90% confidence level. The observed constraint on δ_{CP} is stronger than expected from sensitivity studies, but was found to be compatible with the three-flavour oscillation model. The T2K constraints on Δm_{32}^2 and $\sin^2 \theta_{13}$ are competitive with recent measurements from other experiments, and are world-leading for $\sin^2 \theta_{23}$ and δ_{CP} .

Acknowledgements

I would like to thank my supervisors, Costas Andreopoulos and Neil McCauley for the detailed feedback and support which made the last few years possible and for giving me the opportunity to work on an exciting project.

Secondly, I am much indebted to my colleagues in the VALOR fitter group who have guided me through the long process of learning the physics, statistical tools, and software development required to run the analyses presented in this thesis. Without the mentorship, expertise, and friendship of Costas Andreopoulos, Chris Barry, Andy Chappell, Tom Dealtry, Steve Dennis, Rhiannon Jones, Marco Roda, Davide Sgalaberna, and Raj Shah, I could not have done this. In addition, it has been a pleasure to work with and mentor my good friends Maria Antonova and Jaiden Parlone, whose company I have greatly enjoyed while exploring Tokyo, eating ramen and maguro katsudon, and laughing at over-the-top films.

My fellow collaborators on the T2K experiment have provided a welcoming and productive work environment and without whom I would have no data to analyse! The conveners of the oscillation analysis and NIWG groups in particular, Christophe Bronner, Patrick Dunne, Asher Kaboth, Luke Pickering, Benjamin Quilain, Mark Scott, and Clarence Wret have always patiently provided feedback, explanations, and guidance which supported the development of the work presented in this thesis. To my fellow analysers in the MaCh3 and p-theta fitter groups, Edward Atkin, Lukas Berns, Taichiro Koga, Artur Sztuc, and Kevin Wood, thank you for discussing many ideas and providing invaluable cross-checks of my analyses.

The analyses presented in this thesis would not have been possible without the use of high-performance computing facilities. I have made extensive use of Compute Canada, thanks to the sponsorship of Hirohisa Tanaka and Blair Jamieson, and of Liverpool University High Energy Physics Computing, made possible principally by John Bland.

I would like to thank Jane Scanlon for her many hours spent proofreading this thesis and for reining in my tendency to place commas anywhere and everywhere!

I am grateful for the time spent and many cups of coffee consumed with my fellow students in Liverpool during the first three years of my PhD. Also, I would like to thank my close friends, family, and the Liverpool University Singers for filling my evenings and weekends with the joy and laughter which has kept me sane during the pandemic.

Finally, my deepest gratitude is for my parents, whose love and support has made this both possible and worthwhile.

Declaration

This thesis has been composed by myself and has not been submitted for any other qualification. The works presented in this thesis, including the production of simulated data and the analysis of both simulated and observed data, are official results of the T2K experiment and were carried out by me, with the exception of the following cases, which acted as inputs or cross-checks to my original work:

- The following works are produced and validated by my fellow T2K collaborators, are summarised from T2K documentation, and make use of fits to external data as indicated within their respective sections, as appropriate:
 - The T2K flux prediction and the modelling of the associated uncertainties, detailed in Section 4.1.
 - The neutrino-nucleus interaction models and their associated uncertainties, detailed in Section 4.2. The effects of varying the corresponding systematic parameters are specified by a number of response functions. These are produced by the XsecResponse software package [1], actively developed by myself and my fellow T2K collaborators. During the course of my studies, I undertook an upgrade to XsecResponse, enabling the production of response functions for the nucleon removal energy uncertainty. Additionally, for all systematic parameters, I implemented corrections to the outgoing charged lepton momentum due to the Coulomb potential of the nucleus.
 - The near detector event selections, constraint on the flux and cross-section uncertainties, and the resulting covariance matrix, detailed in Section 4.3.
 - The far detector event selections, nominal simulated data, observed data, constraint on the detector uncertainties, and the resulting covariance matrix, detailed in Sections 4.4 and 4.5.
 - While the analysis of Chapter 5 represents my original work, some of the studies used to validate the results and compare them to previous analyses, in particular those of Sections 5.1.3, 5.5 and 5.6.5, were produced by my fellow T2K collaborators.
- The comparison of T2K oscillation parameter constraints to those from other experiments and to global fits, detailed in Sections 2.3 and 5.7, are produced by the NuFIT and PDG collaborations.

As the above works are not original, they are not described in the same level of detail as my original works, but are included to aid in understanding and to give context to the original works.

The analyses of Chapters 5 and 6 represent the majority of my original work presented in this thesis and was performed as part of the VALOR neutrino oscillation analysis fitter group [2], developed over the past eleven years by a number of analysers, including myself. During my studies, I personally led and developed a year long major overhaul of both the VALOR software development kit (SDK) and the VALOR T2K oscillation analysis built off it. Prior to the overhaul, all analysis choices (such as binning, event samples, and systematic parameters) and their implementation were hard-coded into the analysis, as were a number of T2K-specific assumptions. As a result, making any extensions to the analysis (such as adding new samples or analysis methods) was unreasonably difficult. Due to the upgrades I undertook, the analysis choices are now flexibly defined in configuration files, allowing the addition of new T2K samples, and the SDK is experiment-agnostic, enabling the capability to simultaneously fit data from multiple experiments. In addition, an extensive re-write and optimisation of the code for applying systematic parameters; applying tuning from external flux measurements; generating, storing, and reading simulated data; calculating the marginal likelihood; calculating Feldman-Cousins critical values; and almost all analysis programs and scripts resulted in a 37% increase in efficiency while improving the quality and flexibility of the code and ease of maintenance. All upgrades were extensively validated against the old version of the code, with all analysis results successfully reproduced. Finally, I worked to implement into VALOR the analysis improvements for the T2K Runs 1-10 analysis compared to the T2K Runs 1-9 analysis, including an update of the neutrino-nucleus interaction model, as described in Section 5.2.5.

After implementing all of the above improvements, I personally ran and managed both the VALOR T2K Runs 1-9 $\bar{\nu}_e$ appearance analysis and the Runs 1-10 oscillation analysis, producing, validating, and interpreting the following results: expected kinematic distributions and their comparisons to the observed data (for both analyses), expected and observed p -values to exclude each considered $\bar{\nu}_e$ appearance hypothesis, oscillation parameter sensitivity studies, observed constraints on the oscillation parameters (using both the constant $\Delta\chi^2$ and Feldman-Cousins methods), evaluations of the validity and robustness of the results against alternative interaction models (for both analyses), and comparisons of the expected and observed constraints (for both analyses).

Over the course of my studies, I have directly contributed to a number of T2K publications, having written much of the oscillation analysis methodology, results, and discussion sections in Refs. [3, 4], along with contributions to [5].

Chapter 2 describes a historical and phenomenological background to the physics of neutrino oscillations. It is a summary of the research of both my predecessors and contemporaries, and is produced from a review of a wide range of literature. Chapter 3 de-

scribes the T2K experiment, its detectors, and the accelerator and beam which provide the studied neutrinos, and is derived from both internal and publicly available published T2K documentation. Chapter 4 describes the inputs to my original analyses, as discussed above. Finally, Chapter 7 is a brief summary of the findings of my original works, along with a description of the future prospects of CP-violation measurements, constructed from a combination of T2K documentation (both internal and public) and publications from the NOvA, T2HK, and DUNE collaborations.

Contents

Abstract	i
Acknowledgements	iii
Declaration	v
1 Introduction	1
2 An Overview of Neutrino Physics	3
2.1 A Brief History of Neutrino Physics	3
2.1.1 Prediction	3
2.1.2 Discoveries	4
2.1.3 Neutrino Oscillations	6
2.1.3.1 The Solar Neutrino Problem	6
2.1.3.2 The Atmospheric Neutrino Anomaly	6
2.1.3.3 Discovery of Neutrino Oscillations	8
2.2 Phenomenology of Neutrino Oscillations	12
2.2.1 Neutrino Oscillations in Vacuum	12
2.2.2 Mass Ordering	14
2.2.3 PMNS Parameterisation	14
2.2.3.1 Two-flavour Approximation	15
2.2.4 Neutrino Oscillations in Matter	15
2.2.4.1 Approximate Oscillation Probabilities at T2K	16
2.2.5 CP Violation	20
2.2.5.1 Chirality, Charge Conjugation and Parity in Neutrino Oscillations	20
2.2.5.2 Matter/Antimatter Asymmetry	21
2.2.5.3 Sakharov Conditions	21
2.2.5.4 Magnitude of CP-violating Effects	22
2.3 Historical and Recent Oscillation Parameter Measurements	23
2.3.1 θ_{12} and Δm_{21}^2	23
2.3.2 θ_{23} , $ \Delta m_{32}^2 $ and the Mass Ordering	24
2.3.2.1 Constraints from Accelerator-based Experiments	24
2.3.2.2 Constraints from Atmospheric Neutrino Experiments . .	26

2.3.2.3	Constraints from Reactor Antineutrino Experiments	27
2.3.3	θ_{13} and δ_{CP}	28
3	The T2K Experiment	31
3.1	Neutrino Beam	31
3.1.1	Off-axis Beam	35
3.2	Near Detectors	37
3.2.1	INGRID	37
3.2.2	ND280	39
3.2.2.1	Fine-Grained Detectors	39
3.2.2.2	Time Projection Chambers	41
3.2.2.3	π^0 Detector	41
3.2.2.4	Electromagnetic Calorimeters	42
3.2.2.5	Side Muon Range Detectors	42
3.3	The Far Detector - Super-Kamiokande	44
4	Inputs to the Oscillation Analysis	47
4.1	Flux Prediction	47
4.1.1	Tuning the Predicted Flux to External Hadron Multiplicity Measurements	48
4.1.2	Uncertainties in the Flux Prediction	49
4.2	Neutrino Interaction Modelling	52
4.2.1	Nuclear Model	53
4.2.2	Charged Current Quasi-Elastic (CCQE) Interactions	55
4.2.3	Multi-nucleon (2p2h) Interactions	57
4.2.4	Single Pion Production	58
4.2.5	Deep Inelastic Scattering (DIS) and Multiple Pion (MPi) Production	61
4.2.6	Final State Interactions (FSI), Secondary Interactions (SI) and Photo-nuclear (PN) Interactions	62
4.2.7	Treatment of the Nucleon Removal Energy	63
4.2.7.1	Effect on Reconstructed Neutrino Kinematics	64
4.2.7.2	Sources and Treatment of Uncertainty	65
4.2.7.3	Implementation into the Oscillation Analysis	65
4.2.8	Additional Sources of Uncertainty in the Cross-Section Model	67
4.3	Near Detector Constraint on the Flux and Cross-Section Models	69
4.3.1	Near Detector Samples	70
4.3.2	Near Detector Fit Methodology	72
4.3.3	Results of the Near Detector Fit	73
4.4	Super-K Event Samples	77
4.4.1	Common Selection Criteria	77
4.4.2	$\bar{\nu}_\mu$ CCQE-like Selection Criteria	78

4.4.3	$\bar{\nu}_e$ CCQE-like Selection Criteria	83
4.4.4	$\bar{\nu}_e$ CC1 π^+ -like Selection Criteria	89
4.5	Super-K Detector and Cross-Section Uncertainties	89
4.5.1	Super-K Detector Effects	91
4.5.2	Secondary Interaction and Photo-nuclear Effect Uncertainties . .	96
4.5.3	Combined Super-K Detector, SI, and PN Uncertainties	96
4.6	Summary	96
5	Three-Flavour Joint $\nu/\bar{\nu}$ Oscillation Analysis	99
5.1	Analysis Strategy	99
5.1.1	Evaluation of a Hypothesis' Likelihood	100
5.1.1.1	Construction of Expected Kinematic Distributions . .	100
5.1.1.2	Construction of the Likelihood	101
5.1.2	Construction of Confidence Regions	102
5.1.3	Validation of the Analysis	105
5.2	Summary of Analysis Inputs and Implementation Choices	106
5.2.1	Beam Exposure	106
5.2.2	Reaction Modes	106
5.2.3	Kinematic Binning	108
5.2.4	Treatment of Systematic and Oscillation Parameters	109
5.2.5	Updates Since the Previous Analysis	112
5.3	Predicted Kinematic Distributions and Event Rates	115
5.3.1	Effect of Systematic Uncertainties on the Predicted Kinematic Distributions	119
5.4	Predicted Sensitivity to the Oscillation Parameters	121
5.5	Robustness of the Analysis to Alternate Cross-Section Models	126
5.6	Results	127
5.6.1	Comparison of Predicted and Observed Kinematic Distributions	128
5.6.2	Observed Constraints on the Oscillation Parameters	128
5.6.3	Feldman-Cousins Confidence Intervals for δ_{CP}	134
5.6.4	Comparison of Predicted and Observed Constraints	137
5.6.5	Comparison to the Previous T2K Results	141
5.7	Putting the Results into Context - the Current Status of Neutrino Oscillation Parameter Measurements	142
5.7.1	θ_{23} , $ \Delta m_{3j}^2 $ and the Mass Ordering	143
5.7.2	θ_{13} and δ_{CP}	144
5.8	Summary	146
6	Search for $\bar{\nu}_\mu \rightarrow \bar{\nu}_e$ Oscillations	147
6.1	Aims and the Tested Hypotheses	147
6.2	Hypothesis Test Methodology	148
6.2.1	Construction of the Marginal Likelihood	148

6.2.2	Construction of the Hypothesis Test	149
6.2.3	Validation of the Analysis	151
6.3	Summary of Analysis Inputs and Implementation Choices	151
6.3.1	Beam Exposure	151
6.3.2	Reaction Modes	151
6.3.3	Kinematic Binning	151
6.3.4	Treatment of Systematic and Oscillation Parameters	152
6.4	Predicted Kinematic Distributions and Event Rates	153
6.5	Expected and Observed Results	156
6.5.1	Comparison to the NOvA Experiment	158
6.6	Summary	158
7	Conclusions and Outlook	161
7.1	Summary of the T2K Oscillation Parameter Constraints	161
7.2	Summary of the Search for $\bar{\nu}_\mu \rightarrow \bar{\nu}_e$ Oscillations	162
7.3	The Future of T2K and CP-violation Measurements	162
A	Flux, Interaction Model, and Detector Systematic Parameters used in the T2K Run 1-10 Analysis	167
B	Predicted Event Rates for the T2K Run 1-10 Analysis	175
Bibliography		179
Abbreviations		195
List of Figures		197
List of Tables		203

Chapter 1

Introduction

Since the discovery of neutrino oscillations, several important questions regarding their nature remain open: What are the parameters that determine their oscillations? Can neutrinos offer sufficient charge-parity symmetry violation to explain the survival of matter over antimatter in the early universe? What are the masses of the neutrinos and how are these masses generated?

Definitive answers to these questions would be of great importance in aiding our understanding of the early universe, its evolution and why we exist. The immensity of these problems will require decades of research to solve and cannot be tackled by any single thesis or experiment, but in this work, a degree of progress towards these goals will be demonstrated through the analysis of data taken by the Tokai to Kamioka (T2K) experiment (see Chapters 3 and 4) using the VALOR neutrino fitting software.

Constraints on several neutrino oscillation parameters have been produced, and although T2K cannot directly measure the neutrino masses, their mass-squared differences have been constrained and are reported in Chapter 5. In addition, a search for the $\bar{\nu}_\mu \rightarrow \bar{\nu}_e$ oscillation, which has not yet been directly observed, was undertaken in Chapter 6.

Chapter 2

An Overview of Neutrino Physics

2.1 A Brief History of Neutrino Physics

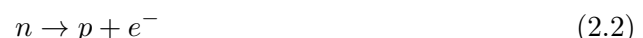
In this chapter, the experimental evidence for neutrinos and their oscillations will be outlined, then a description of the theory thought to govern the behaviour of three-flavour neutrino oscillations will follow, before finally giving a brief overview of the current state of neutrino oscillation measurements.

2.1.1 Prediction

In the early 20th century, the beta decay process was thought to be completely described by a process in which the nucleus, N , decays to a daughter nucleus, N' , where the atomic number, Z , increases by one while the atomic mass, A , remains constant and an electron, e^- is emitted:



While they had not been discovered at the time, with the benefit of hindsight, we can express this decay in terms of neutrons, n , and protons, p , as:



In 1914, James Chadwick discovered that the energy spectrum of electrons emitted during the beta decay of radium was continuous [6] (subsequently confirmed in 1927 [7], see Fig. 2.1), not discrete as was expected from applying energy conservation to Eq. (2.2). This is in contrast to the spectra of alpha and gamma decays, which gave discrete energy spectra. In addition, as the neutron, proton and electron are all spin- $\frac{1}{2}$ particles, producing two spin- $\frac{1}{2}$ particles from the decay of one would violate angular momentum conservation. By 1933, Wolfgang Pauli had proposed a solution: instead of an energy and momentum conservation violating process, what Chadwick had observed was a two-body decay with energy being carried away by a neutral, spin- $\frac{1}{2}$ and light particle, which came to be known as the neutrino [8].

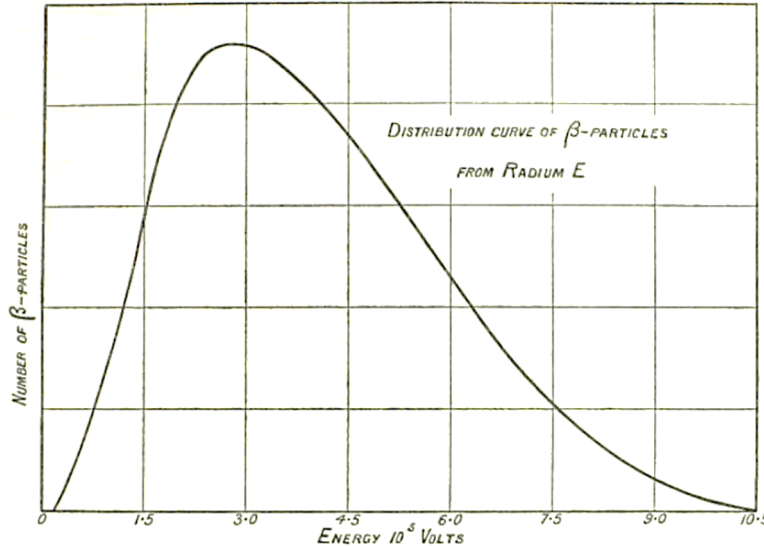


Figure 2.1: Beta decay spectrum of ^{210}Bi (referred to in the figure as Radium E), demonstrating the continuous nature of the decay. Reproduced from Ref. [7].

2.1.2 Discoveries

The existence of the neutrino was experimentally confirmed by Reines and Cowan at the Savannah River nuclear power plant in 1956 [9]. As a by-product of nuclear fission reactions, an unshieldable flux of electron anti-neutrinos, $\bar{\nu}_e$, is produced. These were detected using a layered detector of water- CdCl_2 solution (acting as the target mass) and scintillation counters. The detector was placed underground and encased in a lead shield to reduce contamination from both cosmic and reactor-induced backgrounds. After interacting via the inverse beta decay reaction (see Eq. (2.3)), observation of the delayed coincidence between signals from positrons, e^+ , and the capture of neutrons on Cd provided a clear neutrino signal. This signal was found to be dependent on the reactor power, consistent with the predicted cross-section, and more than 20 times greater than the observed reactor-induced backgrounds.

$$\bar{\nu}_e + p \rightarrow e^+ + n \quad (2.3)$$

So far, neutrinos had been observed to produce electrons in interactions with matter, but the question of whether they could produce the other known charged lepton, the muon, remained open until the discovery of the muon neutrino, ν_μ , in 1962 by Lederman, Schwartz and Steinberger at Brookhaven National Laboratory [10]. By firing 15 MeV protons onto a Be target to produce pions, which subsequently decayed into neutrinos, a neutrino beam was created. This beam was incident on an iron shield, behind which lay a 10-ton spark chamber for the detection of charged particles. 34 single muon-like events were observed and found to be consistent with being produced by beam neutrinos, while only 6 electron-like events were observed. The large difference in muon and electron production rates indicated that they could not be produced by only one flavour of neutrino, therefore proving the existence of the muon neutrino.

After the discovery of the τ lepton in 1975 [11], a corresponding neutrino, the ν_τ , was also expected. This was discovered in 2001 by the DONUT collaboration at FERMILAB [12]. An 800 GeV proton beam impacted into a tungsten beam dump to produce D_s mesons, which subsequently decayed into τ and $\bar{\nu}_\tau$. The former would then decay into ν_τ , forming a neutrino beam directed towards a shielded layered steel and emulsion target. ν_τ charged current (CC) interactions within the emulsion were characterised by < 5 mm τ tracks ending in a kink indicative of the decay of the τ into another, invisible, ν_τ and a visible daughter particle. Four ν_τ interactions were observed, one of which is shown in Fig. 2.2, with an estimated background of 0.34 events.

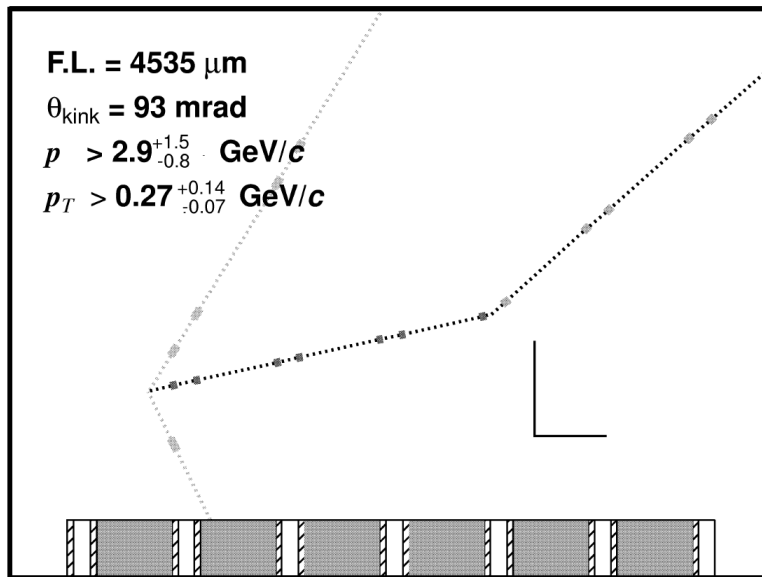


Figure 2.2: One of four ν_τ events observed by the DONUT experiment, clearly displaying the kink resulting from the decay of a τ into an invisible ν_τ and a visible daughter particle. “The neutrinos are incident from the left. The scale is given by the perpendicular lines with the vertical line representing 0.1mm and the horizontal 1.0 mm. The target material is shown by the bar at the bottom of each part of the figure representing steel (shaded), emulsion (cross-hatched) and plastic (no shading).”. Adapted from Ref. [12]

The observation of three active light neutrino flavours is in direct agreement with results from LEP, which measured 2.984 ± 0.008 active neutrino flavours from measuring the Z boson decay branching fractions to invisible particles compared to visible Standard Model particles [13]. This measurement constrains only the number of *active* (i.e. couples to the electroweak force), *light* neutrinos, so does not account for sterile neutrinos, whose existence is the subject of many current searches and anomalous results [14–16]; however, further discussion of sterile neutrinos is beyond the scope of this thesis.

2.1.3 Neutrino Oscillations

Having now established the existence of three distinct neutrino flavour states, the phenomenon underpinning the majority of this thesis can be discussed. This is the neutrino oscillation, whereby the flavour composition of neutrinos can spontaneously change from one flavour to another.

2.1.3.1 The Solar Neutrino Problem

With neutrinos known to be produced during nuclear fission and fusion reactions, they were seen as an opportunity to further study the fusion reactions taking place within the Sun, as predicted by the Standard Solar Model (SSM). The Homestake experiment [17], located ~ 1500 m underground in the Homestake Gold Mine in South Dakota, measured the solar neutrino flux from 1970 until 1994. Detection of neutrinos occurred via the inverse beta decay reaction on ^{37}Cl , according to Eq. (2.4), within a 615 tonne tank of C_2Cl_4 . Starting off with the radioactively stable ^{37}Cl [18], a neutrino interaction would produce the radioactive ^{37}Ar , which could be extracted by bubbling helium through the tank, allowing the ^{37}Ar decays to be counted. The resulting solar neutrino flux was measured to be approximately a third of the value predicted by the solar neutrino model.



Homestake was not alone in obtaining measurements that were seemingly at odds with the solar neutrino model, with Kamiokande also observing deficits [19, 20]. Subsequently, two experiments utilising gallium-based detectors, SAGE [21] and GALLEX [22] observed smaller deficiencies. These experiments overcame one of the limiting factors of Homestake, the relatively high energy threshold of chlorine compared to gallium, which, as indicated by Fig. 2.3, forbade Homestake from measuring the dominant contribution to the solar neutrino flux, the proton-proton (pp) chain reactions. By measuring lower energy neutrinos and observing lower deficiencies, they demonstrated that the effect is energy dependent. This discrepancy between the predicted and observed fluxes came to be known as the solar neutrino problem.

2.1.3.2 The Atmospheric Neutrino Anomaly

Another anomaly was found by measuring the flux of neutrinos originating from the Earth's atmosphere. Such neutrinos are produced when cosmic rays interact with nuclei in the upper atmosphere to produce hadronic showers which decay into muons and neutrinos [24]. The Kamiokande, Super-Kamiokande, IMB-3 and Soudan-2 experiments, amongst others, measured the double ratio of μ -like and e -like fluxes, given by Eq. (2.5), by which flux and cross section uncertainties cancel. The higher precision measurements [25–28] found this to be smaller than one, as shown in Fig. 2.4, indicating that there was a disappearance of ν_μ and/or an appearance of ν_e compared to

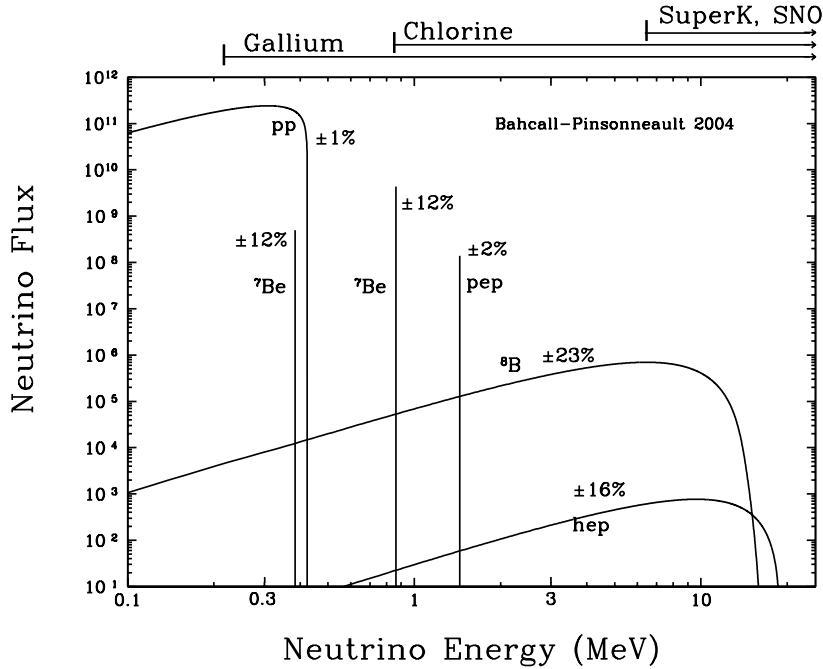


Figure 2.3: Solar neutrino flux spectra broken down by source. Reproduced from [23].

the predictions. Together, these anomalous measurements came to be known as the atmospheric neutrino anomaly.

$$R = \frac{(\mu/e)_{data}}{(\mu/e)_{MC}} \quad (2.5)$$

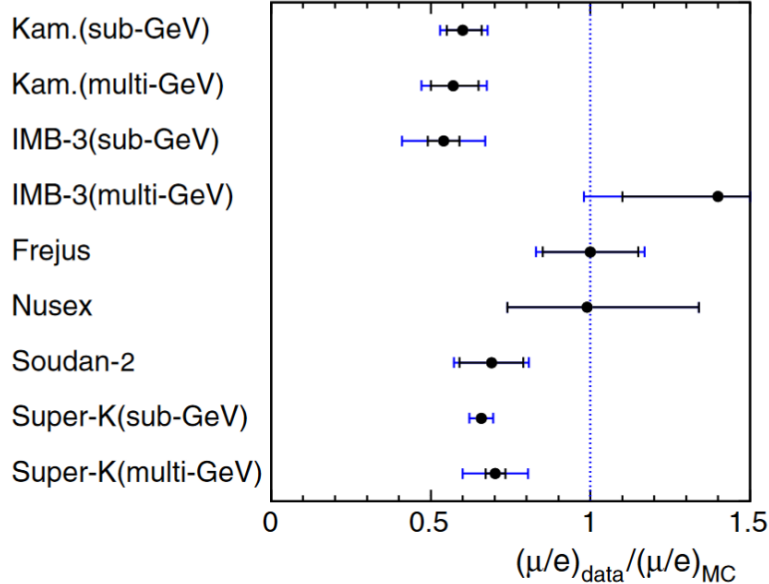


Figure 2.4: Double ratio of atmospheric neutrino fluxes, as measured by several experiments. Reproduced from Ref. [29].

2.1.3.3 Discovery of Neutrino Oscillations

The solution to these problems was not found until the early 2000's, when the combination of three measurements demonstrated the existence of neutrino oscillations beyond any reasonable doubt. The solar neutrino problem was solved in 2002 by the SNO experiment [30], which utilised an underground 400 tonne heavy water Cherenkov detector to detect ${}^8\text{B}$ solar neutrinos by the following charged current (CC), neutral current (NC) and elastic scattering (ES) reactions, where d is a deuteron and $\alpha = e, \mu, \tau$.

$$\nu_e + d \rightarrow p + p + e^- \quad (\text{CC}) \quad (2.6)$$

$$\nu_\alpha + d \rightarrow p + n + \nu_\alpha \quad (\text{NC}) \quad (2.7)$$

$$\nu_\alpha + e^- \rightarrow \nu_\alpha + e^- \quad (\text{ES}) \quad (2.8)$$

As Fig. 2.3 shows, the endpoint of the ${}^8\text{B}$ solar neutrino flux spectrum is far below the threshold for μ or τ production, so by the CC reaction in Eq. (2.6), SNO was only able to detect the ν_e flux. By contrast, the NC reaction, Eq. (2.7), is flavour-blind, so is sensitive to the total neutrino flux. Additionally, the ES reaction is again sensitive to all flavours, but has reduced sensitivity to ν_μ and ν_τ . By combining measurements of these reactions, SNO observed a ν_e flux of approximately a third of the SSM predicted value, a $\nu_\mu + \nu_\tau$ flux differing by 5.5σ from zero, and finally a NC flux consistent with the SSM. The combined measurement for the solar neutrino flux and its contributions are displayed in Fig. 2.5. Given this final result, it was clear that about a third of the ν_e 's originating in the Sun had undergone flavour transformations into ν_μ 's and ν_τ 's.

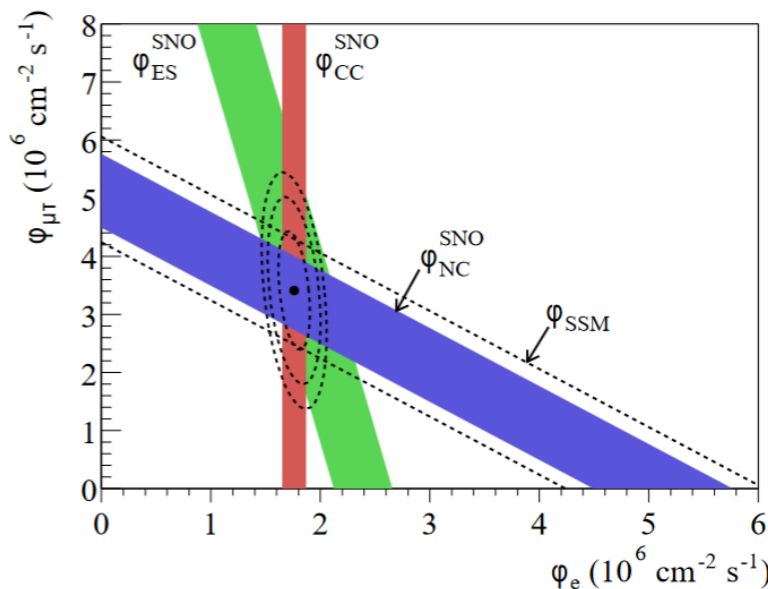


Figure 2.5: Observed total ${}^8\text{B}$ solar flux (ellipse) and $\pm 1\sigma$ errors on the contributions (coloured bands), shown with a band (dashed) representing the SSM predicted total flux. Reproduced from Ref. [30].

The atmospheric neutrino anomaly was solved by the Super-Kamiokande (Super-K) experiment [24] (an experimental overview of which will be given in Section 3.3) in

1998. A dependence on the zenith angle (and therefore the distance travelled by the neutrino) of the observed ratio in Eq. (2.5) and event rate was observed, as shown in Figs. 2.6 and 2.7.

While SNO and Super-K provided compelling evidence for neutrino oscillations, they did not exclude all viable alternative models. This exclusion came from the KamLAND experiment, which observed the disappearance of $\bar{\nu}_e$ produced by nuclear reactors, illustrated in Fig. 2.8. The results were consistent with global fits to solar neutrino data and inconsistent with alternative models, which had predicted negligible disappearance [31].

Together, the SNO, Super-K, and KamLAND experiments clearly demonstrated that neutrinos are capable of undergoing flavour oscillations and that such a process is dependent on the distance travelled by the neutrino. The mechanism by which these oscillations are thought to occur will be discussed in the next section.

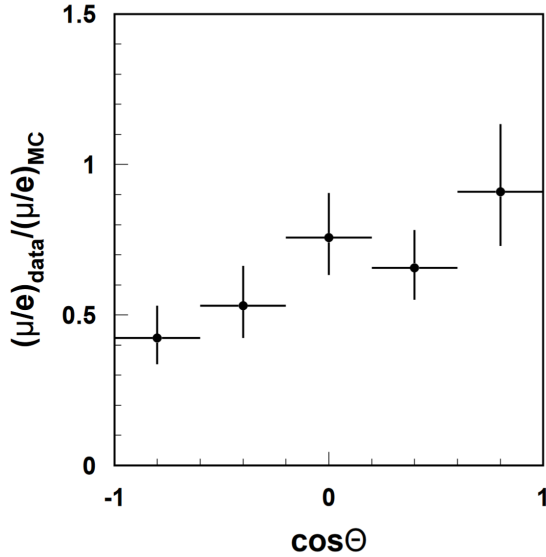
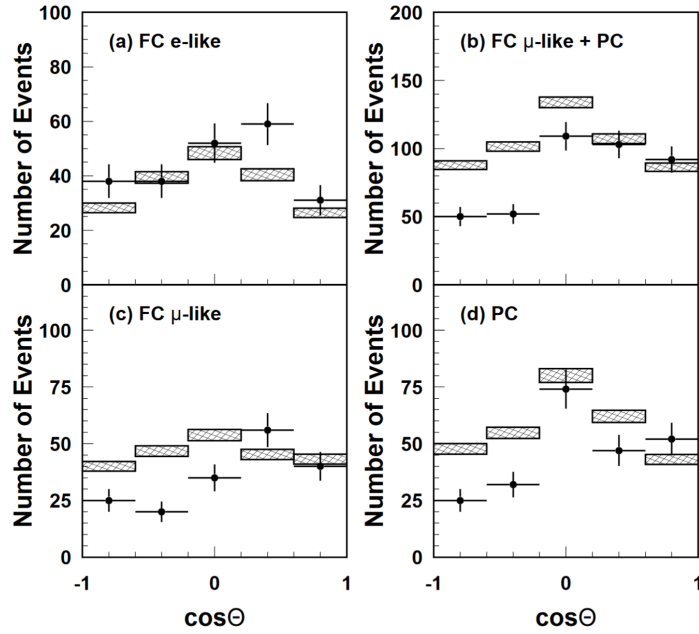
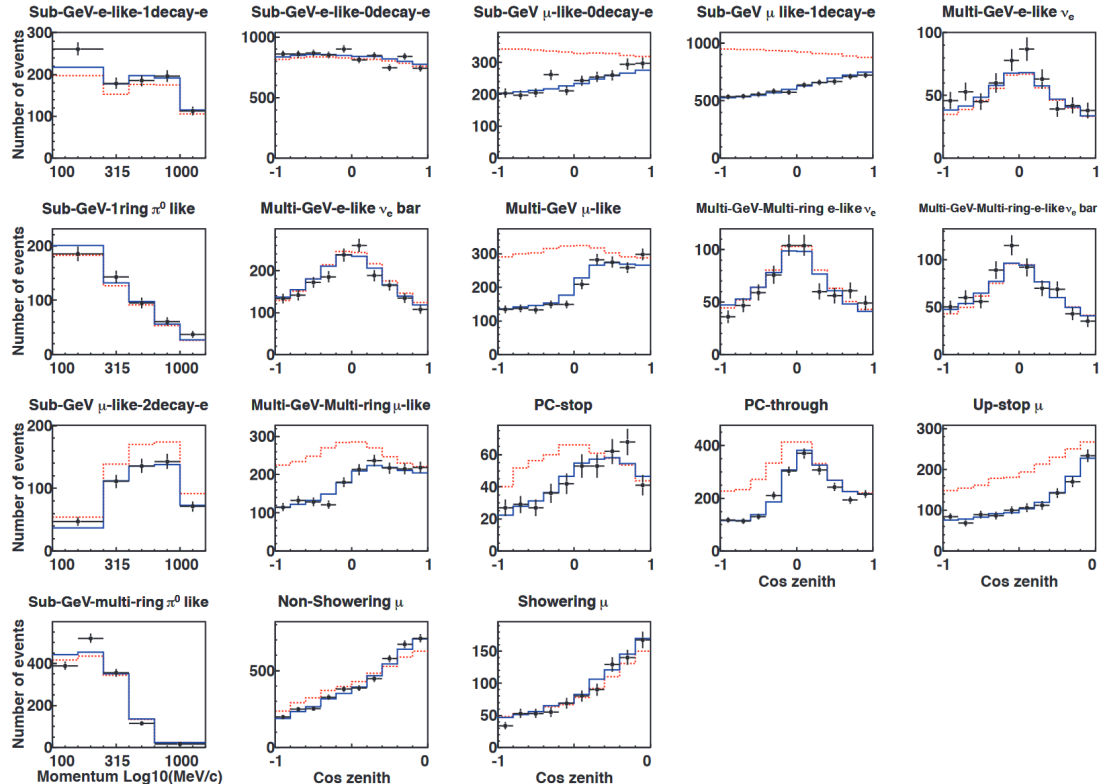


Figure 2.6: Dependence of the atmospheric flux double ratio on the zenith angle. Reproduced Ref. from [32].



(a) Initial observation from 1998. Shown with observed (points) and predicted (shaded) neutrino event rate. The prediction is generated under the assumption of no neutrino oscillations. Shown divided by μ -like and e -like event samples, as well as Fully Contained (FC) and Partially Contained (PC) event selections. Reproduced from Ref. [32].



(b) Updated observations from 2015. Shown with observed (points) and predicted (red and blue lines) neutrino event rate. The predictions are generated under the assumption of no neutrino oscillations (red) and with best-fit oscillation parameters (blue). Reproduced from Ref. [33].

Figure 2.7: Dependence of the observed and predicted neutrino event rate on the zenith angle, Θ , in the Super-K Experiment. Shown both for the initial observation in 1998, and for an updated analysis in 2015, demonstrating the persistence of their findings with additional data and event samples and at a broad range of neutrino energies.

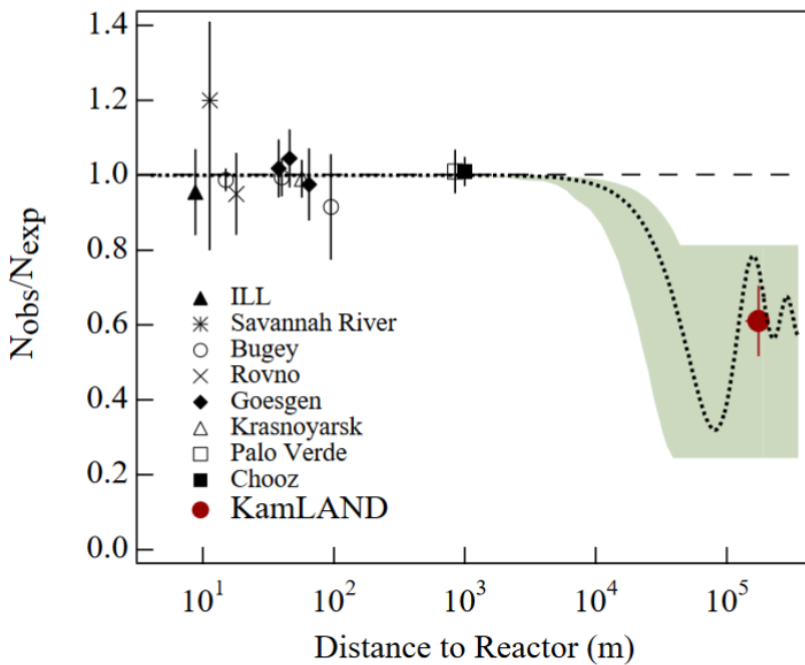


Figure 2.8: Ratio of the observed and predicted $\bar{\nu}_e$ fluxes in the KamLAND experiment, amongst other reactor experiments. The KamLAND data point is shown as a flux-weighted average over the distances to contributing reactors, with the dot width indicating the range of distances. The dotted line shows the best fit (of the time) neutrino oscillation prediction from a global fit to solar neutrino data, and the shaded region shows the corresponding 95% uncertainty. The dashed line shows the prediction for the case of no neutrino oscillations. The alternative models seeing to explain prior neutrino oscillation data correspond to a negligible reduction in the expected flux compared to the observation. Reproduced Ref. from [31].

2.2 Phenomenology of Neutrino Oscillations

2.2.1 Neutrino Oscillations in Vacuum

Neutrino oscillations arise from the (weakly interacting) neutrino flavour eigenstates ($\alpha = e, \mu, \tau$) being comprised of a linear superposition of the neutrino mass eigenstates ($k = 1, 2, 3$) of mass m_k , as shown in Eq. (2.9), where t is time and U is a unitary mixing matrix known as the Pontecorvo-Maki-Nakagawa-Sakata (PMNS) matrix, shown in Eq. (2.10).

$$|\nu_\alpha\rangle = \sum_k U_{\alpha k} |\nu_k\rangle \quad (2.9)$$

$$U = \begin{pmatrix} U_{e1} & U_{\mu 1} & U_{\tau 1} \\ U_{e2} & U_{\mu 2} & U_{\tau 2} \\ U_{e3} & U_{\mu 3} & U_{\tau 3} \end{pmatrix} \quad (2.10)$$

By multiplying both sides of Eq. (2.9) by U^* , the mass states can be expressed as a superposition of the flavour states:

$$|\nu_k\rangle = \sum_\alpha U_{\alpha k}^* |\nu_\alpha\rangle \quad (2.11)$$

Using the time-dependent Schrödinger equation, the time evolution of the mass states are obtained:

$$i \frac{d}{dt} \begin{pmatrix} \nu_1 \\ \nu_2 \\ \nu_3 \end{pmatrix} = \hat{H}_{\text{vac}} \begin{pmatrix} \nu_1 \\ \nu_2 \\ \nu_3 \end{pmatrix} \quad (2.12)$$

Where \hat{H}_{vac} is the vacuum Hamiltonian, expressed as follows, with E being the energy of the neutrino (as it is created at a definite energy). The effects of modifying the Hamiltonian to account for neutrinos propagating through matter will be considered in Section 2.2.4.

$$\hat{H}_{\text{vac}} = \frac{1}{2E} \begin{pmatrix} m_1^2 & 0 & 0 \\ 0 & m_2^2 & 0 \\ 0 & 0 & m_3^2 \end{pmatrix} \quad (2.13)$$

With the vacuum Hamiltonian from Eq. (2.13), the solution to Eq. (2.12) is given by Eq. (2.14), where it is shown that the mass states evolve as plane waves with each mass state having momentum p_k :

$$|\nu_k(t)\rangle = e^{-i(E_k t - \vec{p}_k \cdot \vec{x})} |\nu_k\rangle \quad (2.14)$$

Therefore a neutrino that is created as flavour α at $t = 0$ will evolve as a changing superposition of the mass states:

$$|\nu_\alpha(t)\rangle = \sum_k U_{\alpha k}^* e^{-i(E_k t - \vec{p}_k \cdot \vec{x})} |\nu_k\rangle \quad (2.15)$$

Then by using Eq. (2.11), the flavour state α can be expressed as a superposition of the all flavour states, β :

$$|\nu_\alpha(t)\rangle = \sum_\beta \left(\sum_k U_{\alpha k}^* e^{-i(E_k t - \vec{p}_k \cdot \vec{x})} U_{\beta k} \right) |\nu_\beta\rangle \quad (2.16)$$

Now the probability for a neutrino of flavour α to oscillate to a flavour β can be calculated, where $j = 1, 2, 3$:

$$P(\nu_\alpha \rightarrow \nu_\beta) = |\langle \nu_\beta | \nu_\alpha \rangle|^2 = \sum_{k,j} U_{\alpha k}^* U_{\beta k} U_{\alpha j} U_{\beta j}^* e^{-i((E_k - E_j)t - (\vec{p}_k - \vec{p}_j) \cdot \vec{x})} \quad (2.17)$$

The following simplifying approximations are now made: The \vec{p}_k and \vec{x} vectors are perfectly aligned such that their scalar product is $p_k L$, where L is baseline at which the measurement is made; The ultra-relativistic limit applies so that (in natural units) the approximations $t = L$ and $E_k - p_k \approx \frac{m_k^2}{2E}$ can be used. Applying all of these approximation to Eq. (2.17) gives the oscillation probability as a function of the baseline and initial neutrino energy:

$$P(\nu_\alpha \rightarrow \nu_\beta) = \sum_{k,j} U_{\alpha k}^* U_{\beta k} U_{\alpha j} U_{\beta j}^* e^{-i \frac{\Delta m_{kj}^2 L}{2E}} \quad (2.18)$$

Where, for brevity, the following definition of the mass-squared splittings has been used:

$$\Delta m_{kj}^2 = m_k^2 - m_j^2 \quad (2.19)$$

Using the unitarity of the PMNS matrix, the oscillation probability given by Eq. (2.18) can be written as given by Eq. (2.20), where $\delta_{\alpha\beta}$ is the Kronecker delta. So far, only the oscillation of neutrinos has been considered, but by assuming Charge-Parity-Time reversal symmetry (CPT) holds, then $P(\bar{\nu}_\alpha \rightarrow \bar{\nu}_\beta) = P(\nu_\beta \rightarrow \nu_\alpha)$, so to obtain $P(\bar{\nu}_\alpha \rightarrow \bar{\nu}_\beta)$ from $P(\nu_\alpha \rightarrow \nu_\beta)$, U must be replaced with U^* . The effect is to change the sign of the third term in Eq. (2.20) from + for neutrinos to - for antineutrinos [34]. The survival probability is obtained by setting $\alpha = \beta$ and the appearance probability is obtained by setting $\alpha \neq \beta$.

$$P(\bar{\nu}_\alpha \rightarrow \bar{\nu}_\beta) = \delta_{\alpha\beta} - 4 \sum_{k>j} \Re \left[U_{\alpha k}^* U_{\beta k} U_{\alpha j} U_{\beta j}^* \right] \sin^2 \left(\frac{\Delta m_{kj}^2 L}{4E} \right) \\ (-) 2 \sum_{k>j} \Im \left[U_{\alpha k}^* U_{\beta k} U_{\alpha j} U_{\beta j}^* \right] \sin \left(\frac{\Delta m_{kj}^2 L}{2E} \right) \quad (2.20)$$

As Eq. (2.20) shows, oscillations will only occur for non-zero Δm_{kj}^2 . This means that as neutrino oscillations have been observed, the mass eigenstates cannot all have zero mass, i.e massive neutrinos must exist. This is in direct disagreement with the Standard Model, which, in its original formalism, only allows massless neutrinos.

2.2.2 Mass Ordering

As the oscillation probability is dependent on the *difference* in the square of the neutrino masses rather than the masses themselves, any experiment measuring neutrino oscillations will not be able to provide a direct measurement of the neutrino masses. While attempts at directly measuring neutrino masses are ongoing, so far only upper limits have been determined, while precise measurements of Δm_{21}^2 and $|\Delta m_{23}^2|$ have been made, with the sign of the latter currently unknown [35] (see Section 2.3). This results in there being two possible orderings for the neutrino masses: The normal ordering (NO), with $m_1^2 < m_2^2 < m_3^2$, and the inverted ordering (IO), with $m_3^2 < m_1^2 < m_2^2$, as shown in Fig. 2.9. At times it is convenient to refer to the NO Δm_{32}^2 and the IO Δm_{31}^2 at once, so for brevity, these will often be referred to as Δm_{3j}^2 . Often in literature the terminology ‘mass hierarchy’ (MH) is used instead of ‘mass ordering’ (MO). As the mass states are not necessarily hierarchic [35], in this thesis the term ‘mass ordering’ will be preferred, but they can be taken as synonymous.

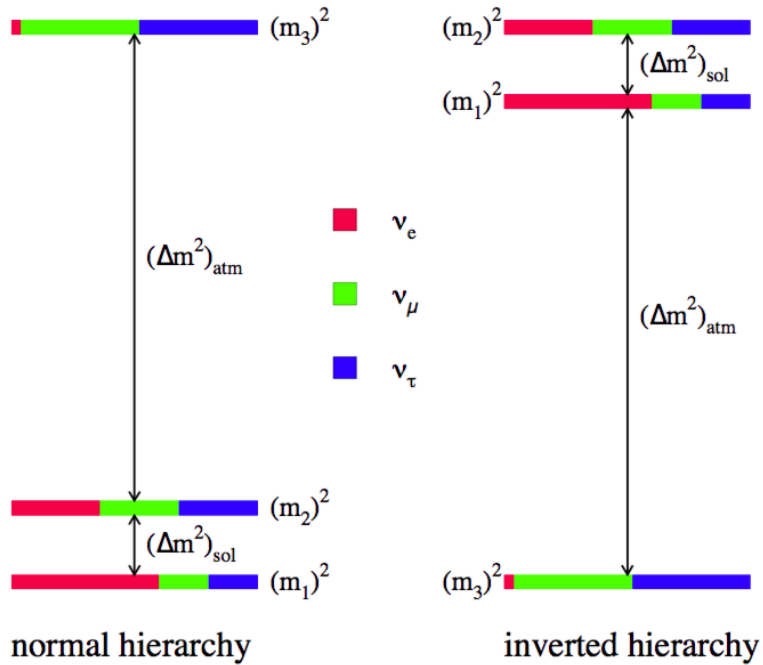


Figure 2.9: Illustration of the normal and inverted neutrino mass orderings (or hierarchies) with flavour state fractions shown according to a specific choice of oscillation parameters. Note that $(\Delta m^2)_{\text{sol}} = \Delta m_{21}^2$ and $(\Delta m^2)_{\text{atm}} = \Delta m_{32}^2$ (NO) and Δm_{13}^2 (IO). Reproduced from Ref. [36].

2.2.3 PMNS Parameterisation

A convenient parametrisation of the PMNS matrix, and one which will be used throughout this thesis, is written in Eq. (2.21) as the product of three simpler matrices using three mixing angles, θ_{12} , θ_{23} and θ_{13} and a Charge-Parity (CP) symmetry violating (CP-violating) complex phase, δ_{CP} . The contractions $s_{ij} = \sin \theta_{ij}$ and $c_{ij} = \cos \theta_{ij}$ are used for brevity. An explanation of CP-symmetry and justification for why this phase

may violate it will be given in Section 2.2.5.

$$U = \begin{pmatrix} U_{e1} & U_{\mu 1} & U_{\tau 1} \\ U_{e2} & U_{\mu 2} & U_{\tau 2} \\ U_{e3} & U_{\mu 3} & U_{\tau 3} \end{pmatrix} = \begin{pmatrix} 1 & 0 & 0 \\ 0 & c_{23} & s_{23} \\ 0 & -s_{23} & c_{23} \end{pmatrix} \begin{pmatrix} c_{13} & 0 & s_{13} e^{-i\delta_{CP}} \\ 0 & 1 & 0 \\ -s_{13} e^{-i\delta_{CP}} & 0 & c_{13} \end{pmatrix} \begin{pmatrix} c_{12} & s_{12} & 0 \\ -s_{12} & c_{12} & 0 \\ 0 & 0 & 1 \end{pmatrix} \quad (2.21)$$

2.2.3.1 Two-flavour Approximation

To gain some intuition on neutrino oscillations, it is useful to re-write the oscillation probability in vacuum under the approximation of only two light, active neutrino flavours. This reduces number of parameters such that instead of having three mixing angles and two mass-squared splittings, there are now one of each, θ and Δm^2 . The corresponding oscillation probability is as follows, where the + sign applies only when $\alpha \neq \beta$ and all quantities are expressed in natural units:

$$P(\nu_\alpha \rightarrow \nu_\beta) = P(\bar{\nu}_\alpha \rightarrow \bar{\nu}_\beta) = \delta_{\alpha\beta} \stackrel{-}{(+)} \sin^2(2\theta) \sin^2\left(\frac{\Delta m^2 L}{4E}\right) \quad (2.22)$$

2.2.4 Neutrino Oscillations in Matter

Up to this point, only neutrinos travelling through a vacuum have been considered; however, much of this thesis uses data from the T2K experiment (see Chapter 3), which uses neutrinos that are produced on and propagate through the Earth before being detected, so it is important to account for the effects of neutrinos interacting with the matter they travel through. As the neutrinos of interest are those which survive the journey to the detector, only coherent scattering interactions with matter need to be considered.

NC neutrino-matter scattering, via the exchange of a Z boson with a proton, neutron or electron, is independent of neutrino flavour, therefore this process does not affect the oscillation probability [37, 38]. CC interactions, however, do provide a flavour-dependent effect: As the Earth's matter overwhelmingly contains electrons instead of muons or taus, only $\bar{\nu}_e$ can undergo CC scattering in the Earth's crust, and this takes place via the reaction in Eq. (2.23). This process provides potential energy, V , shown in Eq. (2.24), where the - sign is for antineutrinos, G_F is the Fermi coupling constant and N_e is the electron number density in the Earth's crust (approximately $1.6 \times 10^{30} \text{ e}^- \text{m}^{-3}$ for T2K [39]).



$$V = \stackrel{+}{(-)} \sqrt{2} G_F N_e \quad (2.24)$$

To show how the oscillation probabilities are affected by this potential, it is convenient to first rewrite the evolution of the mass states *in vacuum* (given by Eq. (2.12)) as the evolution of the flavour states, using Eqs. (2.9) and (2.11):

$$i \frac{d}{dt} \begin{pmatrix} \nu_e \\ \nu_\mu \\ \nu_\tau \end{pmatrix} = U \hat{H}_{\text{vac}} U^\dagger \begin{pmatrix} \nu_e \\ \nu_\mu \\ \nu_\tau \end{pmatrix} = \hat{H}_{\text{vac}}^F \begin{pmatrix} \nu_e \\ \nu_\mu \\ \nu_\tau \end{pmatrix} \quad (2.25)$$

where the following effective vacuum flavour state Hamiltonian, \hat{H}_{vac}^F , has been used. In the right-hand side of Eq. (2.26), \hat{H}_{vac} has been reparameterised in terms of Δm_{21}^2 and Δm_{31}^2 instead of the m_1^2 , m_2^2 and m_3^2 used previously in Eq. (2.13).

$$\hat{H}_{\text{vac}}^F = U \hat{H}_{\text{vac}} U^\dagger = \frac{1}{2E} U \begin{pmatrix} 0 & 0 & 0 \\ 0 & \Delta m_{21}^2 & 0 \\ 0 & 0 & \Delta m_{31}^2 \end{pmatrix} U^\dagger \quad (2.26)$$

Working in this convenient reparametrisation, the effects of the matter potential of Eq. (2.24) can be introduced by modifying the effective vacuum Hamiltonian in Eq. (2.25) as follows:

$$\hat{H}_{\text{vac}}^F \rightarrow \hat{H}_{\text{matter}}^F = U \hat{H}_{\text{vac}} U^\dagger + \begin{pmatrix} V & 0 & 0 \\ 0 & 0 & 0 \\ 0 & 0 & 0 \end{pmatrix} \quad (2.27)$$

2.2.4.1 Approximate Oscillation Probabilities at T2K

Using the effective Hamiltonian in matter of Eq. (2.27), approximate oscillation probabilities for the T2K experiment can be derived. Taking advantage of the fact that $|\Delta m_{21}^2| \ll |\Delta m_{31}^2|$ (see Section 2.3) and $VE \ll |\Delta m_{31}^2|$ (at energies relevant to T2K, i.e. $\lesssim 10$ GeV), $\hat{H}_{\text{matter}}^F$ can be split into two terms, $\hat{H}_{\text{matter}}^F = \hat{H}_0 + \hat{H}_1$ (see Eqs. (2.28) and (2.29)), allowing the oscillation amplitude to be expanded perturbatively in \hat{H}_1 [40].

$$\hat{H}_0 = \frac{1}{2E} U \begin{pmatrix} 0 & 0 & 0 \\ 0 & 0 & 0 \\ 0 & 0 & \Delta m_{31}^2 \end{pmatrix} U^\dagger \quad (2.28)$$

$$\hat{H}_1 = \frac{1}{2E} U \begin{pmatrix} 0 & 0 & 0 \\ 0 & \Delta m_{21}^2 & 0 \\ 0 & 0 & 0 \end{pmatrix} U^\dagger + \begin{pmatrix} V & 0 & 0 \\ 0 & 0 & 0 \\ 0 & 0 & 0 \end{pmatrix} \quad (2.29)$$

Expanding up to the first order in VE and Δm_{21}^2 gives the following appearance

probability [3, 40–42]:

$$\begin{aligned}
 P\left(\vec{\nu}_\mu \rightarrow \vec{\nu}_e; \text{NO; matter}\right) \simeq & \\
 4|\mathcal{T}_3^{\mu e}|^2 \frac{\sin^2([1-\xi]\Delta_{31})}{[1-\xi]^2} + 4|\mathcal{T}_2^{\mu e}|^2 \frac{\sin^2(\xi\Delta_{21})}{\xi^2} \\
 + 8|\mathcal{T}_2^{\mu e}||\mathcal{T}_3^{\mu e}| \frac{\sin([1-\xi]\Delta_{31})}{1-\xi} \frac{\sin(\xi\Delta_{21})}{\xi} \cos\Delta_{32} \cos\delta_{CP} \\
 {}^{(+)}_{-} 8|\mathcal{T}_2^{\mu e}||\mathcal{T}_3^{\mu e}| \frac{\sin([1-\xi]\Delta_{31})}{1-\xi} \frac{\sin(\xi\Delta_{21})}{\xi} \sin\Delta_{32} \sin\delta_{CP}
 \end{aligned} \tag{2.30}$$

At the T2K baseline and energy at the flux peak (approx. 295 km and 0.6 GeV, respectively), the matter effect changes the $P(\vec{\nu}_\mu \rightarrow \vec{\nu}_\mu)$ oscillation probability by $\sim 0.1\%$, so is neglected here [42]. Expanding Eq. (2.20) gives the following survival probability [41]:

$$\begin{aligned}
 P\left(\vec{\nu}_\mu \rightarrow \vec{\nu}_\mu; \text{matter}\right) \simeq P\left(\vec{\nu}_\mu \rightarrow \vec{\nu}_\mu; \text{vacuum}\right) \simeq & \\
 1 - 4\mathcal{T}_1^{\mu\mu}\mathcal{T}_3^{\mu\mu} \sin^2\Delta_{31} \\
 - 4\mathcal{T}_2^{\mu\mu}\mathcal{T}_3^{\mu\mu} \sin^2\Delta_{32} \\
 - 4\mathcal{T}_1^{\mu\mu}\mathcal{T}_2^{\mu\mu} \sin^2\Delta_{21} \\
 \xrightarrow{|\Delta_{21}| \ll |\Delta_{32}|} 1 - 4\mathcal{T}_3^{\mu\mu}(1 - \mathcal{T}_3^{\mu\mu}) \sin^2\left(\Delta_{32} + \frac{\Delta_{21}\mathcal{T}_1^{\mu\mu}}{1 - \mathcal{T}_3^{\mu\mu}}\right)
 \end{aligned} \tag{2.31}$$

Where in Eqs. (2.30) and (2.31) the following contractions have been used, for brevity:

$$\Delta_{ij} = \frac{\Delta m_{ij}^2 L}{4E} \tag{2.32}$$

$$\xi = \frac{2VE}{\Delta m_{31}^2} \tag{2.33}$$

$$\mathcal{T}_i^{\alpha\beta} = U_{\alpha i}U_{\beta i}^* \tag{2.34}$$

i.e.

$$\begin{aligned}
 \mathcal{T}_2^{\mu e} &= U_{\mu 2}U_{e 2}^* = c_{12}c_{23}c_{13}s_{12} - s_{12}^2s_{23}s_{13}c_{13}e^{i\delta_{CP}} \simeq c_{12}c_{23}c_{13}s_{12} \\
 \mathcal{T}_3^{\mu e} &= U_{\mu 3}U_{e 3}^* = c_{13}s_{13}s_{23}e^{i\delta_{CP}} \\
 \mathcal{T}_1^{\mu\mu} &= U_{\mu 1}U_{\mu 1}^* = c_{23}^2s_{12}^2 + c_{12}^2s_{13}^2s_{23}^2 + 2c_{12}c_{23}s_{12}s_{13}s_{23} \cos\delta_{CP} \\
 \mathcal{T}_2^{\mu\mu} &= U_{\mu 2}U_{\mu 2}^* = c_{12}^2c_{23}^2 + s_{12}^2s_{13}^2s_{23}^2 - 2c_{12}c_{23}s_{12}s_{13}s_{23} \cos\delta_{CP} \\
 \mathcal{T}_3^{\mu\mu} &= U_{\mu 3}U_{\mu 3}^* = s_{23}^2c_{13}^2
 \end{aligned} \tag{2.35}$$

It is important to note that, for antineutrinos, the sign of ξ changes from $+$ to $-$. Similarly, as $\Delta m_{32}^2 \gg \Delta m_{21}^2$ in both mass orderings, the overall effect of switching between NO and IO is to change the signs of Δ_{31} , Δ_{32} and ξ , also changes from $+$ to $-$. Also, while these approximate oscillation probabilities are useful for gaining an

understanding of neutrino oscillations, they are not used in the analyses reported in this thesis. Instead, the full oscillation probabilities are calculated numerically, as will be shown in Section 5.1.1. These full oscillation probabilities with the matter effect are displayed as a function of L/E in Fig. 2.10a.

Given the baseline (295 km) and peak energy (0.6 GeV) of T2K, along with the recent global best fit measurements of the oscillation parameters (see Section 2.3), several remarks can be made about the above approximate oscillation probabilities:

- Consider the survival probability of Eq. (2.31). As $|m_{21}^2| \ll |\Delta m_{32}^2|$ (and therefore also $|m_{21}^2| \ll |\Delta m_{31}^2|$) and $\theta_{13} \sim 8.5^\circ$ [35], two related effects occur: First, as the survival probability has the amplitude $4\mathcal{T}_3^{\mu\mu}(1 - \mathcal{T}_3^{\mu\mu})$, it can be shown to have a minimum at approximately $\sin^2 \theta_{23} = 1/(2 \cos^2 \theta_{13}) \sim 0.51$, representing maximal mixing between $\tilde{\nu}_\mu$ and $\tilde{\nu}_e$. Second, the dominant term has dependence on $\sin^2 2\theta_{23}$, which leads to a two-fold degeneracy in $\sin^2 \theta_{23}$, where values of $\sin^2 \theta_{23}$ greater (less) than maximal mixing are referred to as being in the ‘upper (lower) octant’ (so called due to the resulting eight-fold degeneracy in θ_{23}).
- Evaluating the size of each term of the appearance probability in Eq. (2.30) separately, it is found that: the first term (referred to as the ‘atmospheric’ term) dominates and is dependent on $\sin^2 \theta_{13}$, $\sin^2 \theta_{23}$ and Δm_{31}^2 . The second term (referred to as the ‘solar’ term) is found to be comparatively small at T2K compared to the other terms. The third and fourth terms (referred to as ‘interference’ terms), are sub-dominant in that their combined amplitude is $\sim 20\%$ of that of the atmospheric term [3]; however, they are of importance as they allow for measurements of δ_{CP} and the appearance probability for neutrinos to be different from that of antineutrinos if $\sin \delta_{CP} \neq 0$. The consequences of this will be further discussed in Section 2.2.5.
- Neglecting the relatively small difference of Δ_{21} , only the signs of Δ_{31} and Δ_{32} change when switching between NO and IO, leaving their absolute values approximately unchanged. This means that only a single change occurs in the approximated oscillation probabilities when the assumed MO changes: the sign of the $\cos \delta_{CP}$ interference term in Eq. (2.30) (due to the asymmetry of $\sin \Delta_{31}$). As this term is sub-dominant at T2K, the sign of Δ_{32} and therefore the MO will also have a sub-dominant (but non-negligible) effect.
- Similarly to the above point, the sign of the $\cos \delta_{CP}$ interference term also changes when δ_{CP} is exchanged for $\pi - \delta_{CP}$. None of the other terms change sign in this way, so together with the sign change from switching between NO and IO, these result in the appearance probability being degenerate at NO δ_{CP} and IO $\pi - \delta_{CP}$. However, this degeneracy is easily removed by performing fits to fixed true NO and IO separately.
- To highlight the effects at T2K of propagation through matter, the appearance

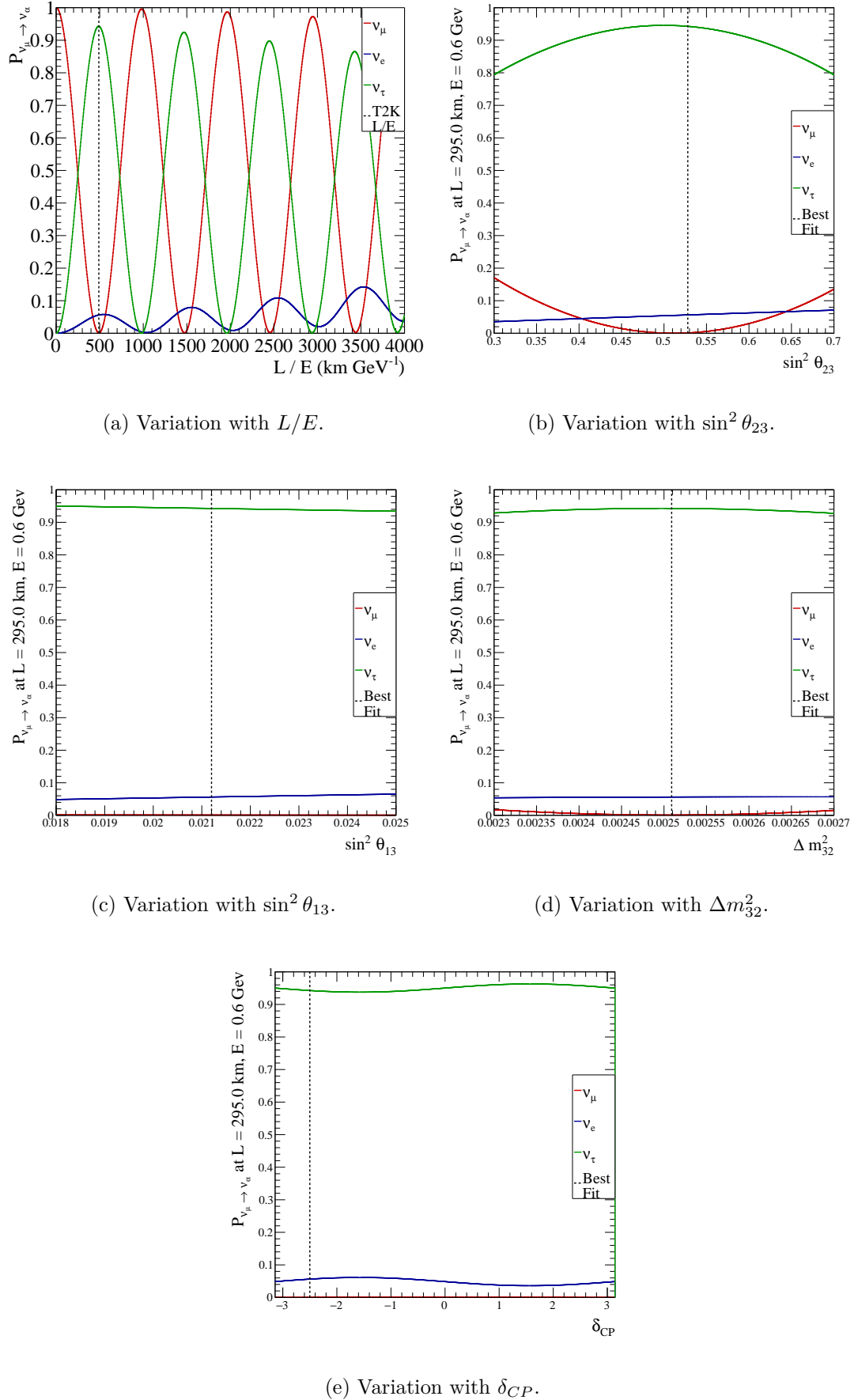


Figure 2.10: Variation of oscillation probabilities at T2K with the oscillation parameters and L/E , generated assuming the global best-fit oscillation parameter values from Section 2.3.

probability *in vacuum* can be written as Eq. (2.36) [3] (by expanding Eq. (2.20)). By comparing to the same probability in matter, Eq. (2.30), and considering that the atmospheric term is dominant, it is clear that the main effect of propagating through matter rather than vacuum is a $\sim 10\%$ enhancement of the atmospheric term at the energy of the T2K flux peak (corresponding to $\xi \sim 0.05$) [3].

- As previously discussed, the atmospheric term dominates the $\vec{\nu}_\mu \rightarrow \vec{\nu}_e$ oscillation probability. As this term has $\sin^2(\Delta_{31})$ dependence in vacuum, the first maximum of this probability clearly occurs at a ratio of baseline and energy given by Eq. (2.37), where the factor of 1.27 comes from the conversion between natural units and km/GeV. Using the global best fit value of Δm_{32}^2 (see Section 2.3), this ratio becomes ~ 490 km GeV $^{-1}$. The baseline and peak energy of the T2K experiment have been designed to be close to this first oscillation maximum.

$$\begin{aligned} P(\vec{\nu}_\mu \rightarrow \vec{\nu}_e; \text{NO; vacuum}) \simeq & \\ & 4|\mathcal{T}_3^{\mu e}|^2 \sin^2 \Delta_{31} + 4|\mathcal{T}_2^{\mu e}|^2 \sin^2 \Delta_{21} \\ & + 8|\mathcal{T}_2^{\mu e}||\mathcal{T}_3^{\mu e}| \sin \Delta_{31} \sin \Delta_{21} \cos \Delta_{32} \cos \delta_{CP} \\ & {}^{(+)} - 8|\mathcal{T}_2^{\mu e}||\mathcal{T}_3^{\mu e}| \sin \Delta_{31} \sin \Delta_{21} \sin \Delta_{32} \sin \delta_{CP} \end{aligned} \quad (2.36)$$

$$\frac{L(\text{km})}{E(\text{GeV})} = \frac{\pi}{2} \frac{1}{1.27 \Delta m_{32}^2 (\text{eV}^2 \text{c}^{-4})} \sim 490 \text{ (km GeV}^{-1}\text{)} \quad (2.37)$$

By considering the oscillation parameters contributing to the dominant terms of the appearance and survival probabilities discussed above, it is clear that the T2K experiment is most suited to measuring $\sin^2 \theta_{23}$, $\sin^2 \theta_{13}$, Δm_{32}^2 and δ_{CP} , but is relatively insensitive to $\sin^2 \theta_{12}$ and Δm_{21}^2 . As a result, the oscillation parameter constraints obtained in this thesis will be on the former group of parameters, rather than the latter.

2.2.5 CP Violation

The possible conservation or violation of Charge-Parity (CP) symmetry is of great interest, and could provide a missing piece of the puzzle to resolving the observed matter-antimatter asymmetry in the universe. Before considering this in detail, further explanation of chirality, charge conjugation and parity is required.

2.2.5.1 Chirality, Charge Conjugation and Parity in Neutrino Oscillations

Two analogous properties of a particle can be defined, which will be useful in the following discussion of CP-symmetry: helicity and chirality. First, a particle's helicity is the scalar product of its spin, \vec{s} and three-momentum, \vec{p} , vectors, $\vec{s} \cdot \vec{p} / |\vec{p}|$. For fermions, the helicity takes values $-\frac{1}{2}$ and $+\frac{1}{2}$, which are referred to as being “left-handed” and “right-handed”, respectively. However, as neutrinos have been demonstrated to undergo oscillations and therefore are massive, a Lorentz boost may reverse the sign of the three-momentum and therefore the helicity [43]. So instead, an analogous, relativistically

invariant quantity is used, chirality. Similarly to helicity, a particle has either left-handed or right-handed chirality. Furthermore, the Standard Model requires that only left-handed particles and right-handed antiparticles may undergo weak interactions [43]. Experimentally, this is supported by the non-observation of right-handed neutrinos or left-handed antineutrinos [44].

The charge conjugation operator, \hat{C} , when applied to a neutrino, converts it to an antineutrino and vice versa. i.e. $\hat{C}|\nu\rangle = |\bar{\nu}\rangle$ and $\hat{C}|\bar{\nu}\rangle = |\nu\rangle$. The parity operator, \hat{P} , when applied to a left (right)-handed (anti)neutrino, reverses the sign of the particle's spacial components, thus reversing its chirality. As \hat{C} does not change the chirality of the neutrino and \hat{P} does not change it to an antineutrino, and as right (left)-handed (anti)neutrinos do not exist, neutrino oscillations do not exhibit either charge conjugation or parity symmetry. However, the application of *both* \hat{C} and \hat{P} , i.e. CP conjugation, potentially results in a symmetry of neutrino oscillations: the $\nu_\mu \rightarrow \nu_e$ and $\bar{\nu}_\mu \rightarrow \bar{\nu}_e$ oscillation probabilities (see Eq. (2.30)) are only equal if $\sin \delta_{CP} = 0$ (as the terms involving the other oscillation parameters have been determined to be non-zero, see Section 2.3).

2.2.5.2 Matter/Antimatter Asymmetry

During the early universe, at temperatures $\gtrsim 20$ MeV, the reversible baryon(b)-antibaryon annihilation reaction



was in thermal equilibrium [45]. As the universe expanded, the temperature and baryon number density (n_b) reduced, losing thermal equilibrium and effectively stopping the reverse process and slowing the rate of the forward process considerably, almost fixing the number of baryons and antibaryons. From this, the ratio of baryons to photons today is implied to be to be $n_b/n_\gamma \sim 10^{-19}$, which is at odds with the the observed lack of gamma rays from baryon-antibaryon annihilation in astrophysical measurements, giving a ratio of $n_b/n_\gamma \sim 6 \times 10^{-10}$. This difference is thought to be caused by an asymmetry in the number densities of baryons and antibaryons in the early universe [45–48]:

$$\frac{n_b - n_{\bar{b}}}{n_\gamma} \sim 6 \times 10^{-10} \quad (2.39)$$

Without such an asymmetry, matter would likely not have survived to the present day. Other possible explanations for the survival of matter, such as the universe being dominated by a ‘patchwork’ of matter and antimatter-dominated regions, or the universe containing a diffuse antimatter, are currently disfavoured by observations [48].

2.2.5.3 Sakharov Conditions

How such an asymmetry is generated is currently unknown; however, for this asymmetry to exist, it is necessary for the universe to satisfy three conditions [49], named after the

physicist Andrei Sakharov:

1. **Baryon number violation** - If the total baryon number of the universe was initially zero, in order to generate the observed asymmetry, baryon number violating processes are required [50]. There are many proposed sources of baryon number violation, both in the Standard Model (sphaleron processes) and beyond (e.g. proton decay) [45, 48]; however, no such processes have been experimentally observed to date and further discussions on such topics are beyond the scope of this thesis.
2. **Both C and CP symmetry violation** - Without C and CP violation, interactions involving baryons and antibaryons would occur at the same rate, so no asymmetry would form from a universe with a total baryon number of zero. The Standard Model already violates both of these symmetries in the electroweak sector [51], but it is presently unclear as to whether the magnitude of these effects are enough to generate the observed asymmetry.
3. **Interactions occurring out of thermal equilibrium** - Under thermal equilibrium, the forward and backwards reactions of Eq. (2.38) would proceed at the same rate, preventing an asymmetry from forming. The expansion of the early universe satisfies this condition [45].

2.2.5.4 Magnitude of CP-violating Effects

From Eq. (2.30), it is clear that for $\sin \delta_{CP} \neq 0$, the $\nu_\mu \rightarrow \nu_e$ oscillation probability is different from that of antineutrinos, and this difference changes depending on the size of $\sin \delta_{CP}$; therefore, CP-violation is not a binary effect, it must also have a magnitude. This magnitude is typically characterised by the Jarlskog invariant [52], J , which can be expressed for neutrinos in the standard PMNS parametrisation as in Eq. (2.40) and has a maximum value of $1/6\sqrt{3}$ (both in the quark and neutrino sectors) [43]. As δ_{CP} has not yet been definitively measured, J_ν is currently unknown, so neutrinos are a potential source of CP-violating effects, rather than a known source.

$$J_\nu = c_{12}s_{12}c_{23}s_{23}c_{13}^2s_{13} \sin \delta_{CP} \quad (2.40)$$

How much CP-violation does there have to be in order to explain the observed baryon asymmetry? This depends on the mechanism by which the asymmetry is generated. For example, under the assumption of the leptogenesis and type I seesaw mechanisms, the observed baryon asymmetry can be obtained by values of δ_{CP} indicated by Fig. 2.11 and has a strong dependence on some parameters of the mechanism, which, in this example are the Majorana phases [53].

CP-violation has been observed in the quark sector from the decay of K_2^0 mesons [54]. However, the Jarlskog invariant for quarks is $J_q = (3.00^{+0.15}_{-0.09}) \times 10^{-5}$ [55]. This is much smaller than the maximal value, and cannot explain the observed baryon asymmetry [43].

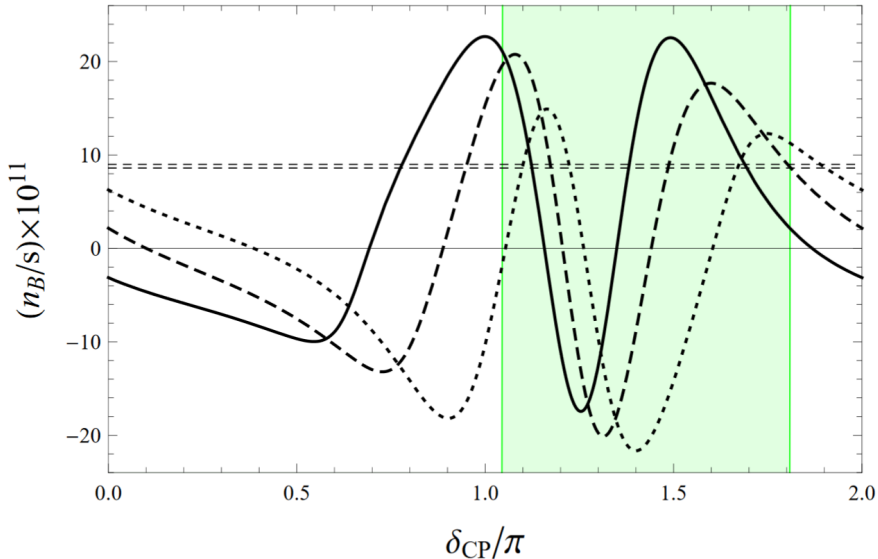


Figure 2.11: The baryon asymmetry (expressed as the baryon density divided by the entropy density) as a function of δ_{CP} for various assumed values of the Majorana phases (solid, dashed and dotted curves), under the assumption of the leptogenesis and type I seesaw mechanisms. The dashed horizontal lines show the range of the observed baryon asymmetry. The shaded region denotes the allowed region for δ_{CP} at the 90% confidence level using T2K data collected up to 2017. Reproduced from Ref. [53].

2.3 Historical and Recent Oscillation Parameter Measurements

In this section, a brief overview will be given of the progress in measuring the neutrino oscillation parameters of the standard PMNS formalism, both during and since the events of the history section (Section 2.1); however, up-to-date measurements of the parameters T2K are best suited to measure, namely $\sin^2 \theta_{23}$, Δm_{32}^2 and δ_{CP} (see Section 2.2.4.1), will not be discussed here, as the T2K data analysed in this thesis provides a strong contribution to the latest global fits to these parameters [55, 56]. Instead, a historical perspective will be taken on these measurements, where appropriate using T2K data collected up to 2016 only (i.e. using results published prior to the analyses presented in this thesis). A more complete discussion of the current global fits will follow in Section 5.7, putting the results of this thesis in context. For the parameters where T2K data does not contribute to the global fits, namely θ_{12} and Δm_{21}^2 , current measurements will be discussed in this section.

2.3.1 θ_{12} and Δm_{21}^2

The dominant contributions to measurements of θ_{12} and Δm_{21}^2 come from solar neutrino experiments and from long baseline reactor antineutrino experiments [55, 56]. Historically, chlorine and gallium-based experiments such as Homestake, SAGE and GALLEX measured the solar neutrino flux and characterised the solar neutrino problem (see Section 2.1.3.1). These measurements were joined by those from water Cher-

enkov experiments such as Kamiokande, and more recently Super-K and SNO, and also the liquid scintillator-based Borexino experiment. The chlorine, gallium, and liquid scintillator-based experiments had/have energy thresholds of $\sim 0.2 - 0.8$ MeV, in contrast to $3.5 - 6.5$ MeV for the water Cherenkov experiments. Together, these gave measurements of neutrinos from the ${}^7\text{Be}$, ${}^8\text{B}$ and the more abundant pp reactions across a range of energies [55] (see Fig. 2.3) and provided stringent tests of solar models, which to date remain one of the larger sources of uncertainty in the determination of θ_{12} and Δm_{21}^2 [56]. Unlike the solar neutrino experiments, the KamLAND experiment is a long baseline reactor antineutrino experiment and utilises a 1 kt liquid scintillator detector to measure $\bar{\nu}_e$ events from several nuclear reactors at an average baseline of ~ 180 km.

Until recently, there was a long-standing $\sim 2\sigma$ tension between the Δm_{21}^2 results of KamLAND and the combined fits to the solar neutrino experiments caused by differences in the low-energy region of the observed spectra, and a stronger day-night asymmetry observed by Super-K than expected from solar models; however, recent updates to the Super-K data has reduced these differences and resolved the tension [56, 57].

Fig. 2.12 shows the constraints on θ_{12} and Δm_{21}^2 from KamLAND data compared to those from a combination of solar experiments from both 2018 (indicating the previous tension) and 2020 (tension resolved). It is clear that the solar experiments drive the constraint on θ_{12} , while KamLAND drives the constraint on Δm_{21}^2 . From the combination of both solar and KamLAND data, the 2020 best fit values and 1σ errors for these parameters are [56]:

$$\begin{aligned}\sin^2 \theta_{12} &= 0.304^{+0.012}_{-0.012} \\ \Delta m_{21}^2 &= (7.42^{+0.21}_{-0.20}) \times 10^{-5} \text{ eV}^2 \text{c}^{-4}\end{aligned}\tag{2.41}$$

2.3.2 θ_{23} , $|\Delta m_{32}^2|$ and the Mass Ordering

The dominant contributions to measurements of θ_{23} and $|\Delta m_{32}^2|$ come from accelerator-based long baseline (LBL) experiments (for both parameters) and medium baseline reactor experiments (for $|\Delta m_{32}^2|$), with atmospheric experiments also providing sub-dominant constraints on both parameters. Constraints on the mass ordering are provided most strongly by accelerator-based LBL and atmospheric experiments, with reactor experiments contributing less strongly [57].

2.3.2.1 Constraints from Accelerator-based Experiments

Accelerator-based LBL experiments impact high-energy protons into a target to produce pions and kaons which subsequently decay into (predominantly) $\bar{\nu}_\mu$ in the GeV range. The disappearance of which, and in some cases the appearance of $\bar{\nu}_e$ and/or $\bar{\nu}_\tau$, are observed to measure the oscillation parameters. Such experiments often use a near detector located close to the beam production site (to measure the unoscillated

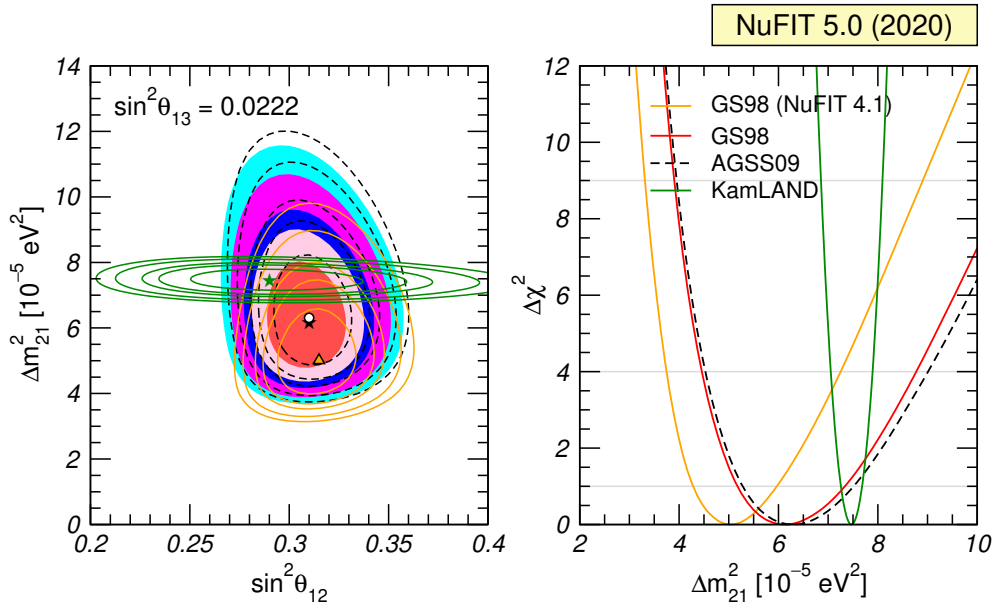


Figure 2.12: Left: 1σ , 90%, 2σ , 99% and 3σ confidence regions for Δm_{21}^2 vs. θ_{12} with the GS98 (solid coloured contours with the best fit at the black star for 2020 data, and orange contours with the best fit at the orange triangle for 2018 data) and AGSS09 (dashed contours with the best fit at the white circle) solar models, and for KamLAND (green contours, with the best fit at the green star). Right: $\Delta\chi^2$ as a function of Δm_{21}^2 , marginalised over θ_{12} . Reproduced from Ref. [56].

flux and constrain the neutrino-nucleus interaction model) together with a far detector, to measure the oscillated flux [35].

The first accelerator-based LBL experiment was K2K, which operated from 1994–2004 and used water Cherenkov based near and far detectors with a broad neutrino energy spectrum with $L/E \sim 190$ km GeV $^{-1}$ at the flux peak. K2K confirmed the phenomenon of ν_μ disappearance [58], as previously indicated by atmospheric neutrino observations from Super-K, amongst others (see Section 2.1.3.2). Subsequently, the MINOS experiment and its upgrade, MINOS+, operated during 2005–2013 and used magnetised tracking calorimeter detectors for both near and far detectors. MINOS and MINOS+ used $L/E \sim 250$ km GeV $^{-1}$ and 110 km GeV $^{-1}$, respectively. MINOS measured ν_μ disappearance (along with insignificant ν_e appearance) to produce constraints on the oscillation parameters [59] which, as Fig. 2.13 shows, remain competitive with the current generation of experiments, but had little sensitivity to the mass ordering. With a wide-spectrum beam and a lower L/E than MINOS, MINOS+ confirmed the energy dependence of ν_μ disappearance [35].

The current generation of accelerator-based LBL experiments are T2K and NOvA. Unlike in previous generations, these experiments situate most of their detectors off the central axis of the neutrino beam in order to obtain a neutrino energy spectrum sharply-peaked close to the first oscillation maximum, with $L/E \sim 490$ km GeV $^{-1}$ and 410 km GeV $^{-1}$ for T2K and NOvA, respectively. T2K began operation in 2010 and uses a suite of near detectors of differing technologies, along with the water Cherenkov

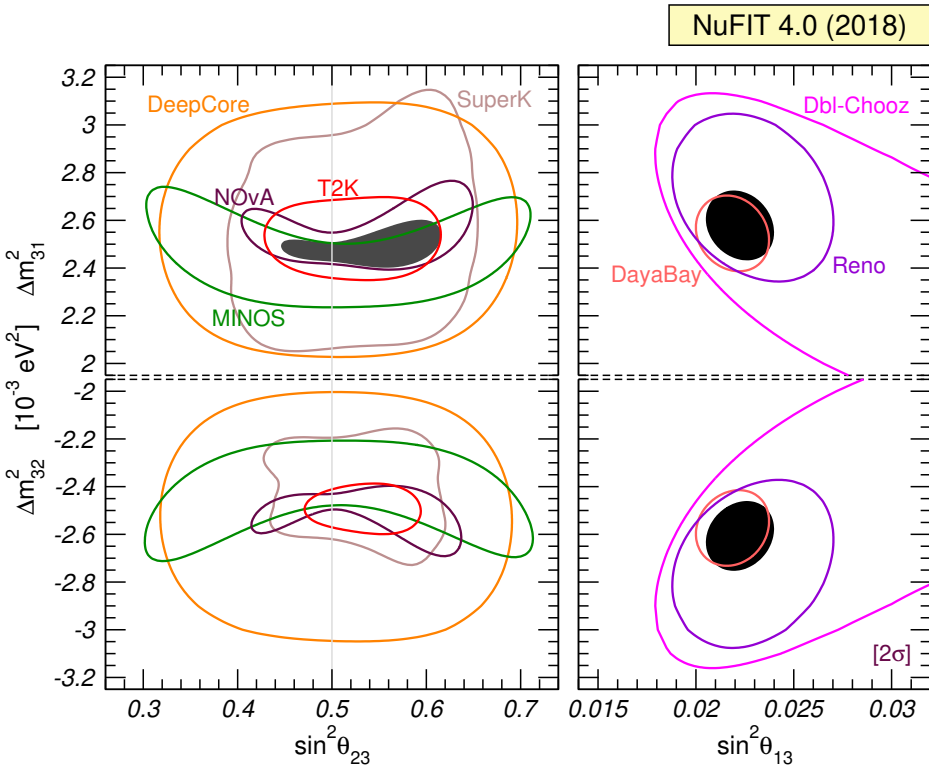


Figure 2.13: 2σ confidence regions for Δm_{3j}^2 vs. $\sin^2 \theta_{23}$ (left) and Δm_{3j}^2 vs. $\sin^2 \theta_{13}$ (right). Upper panels correspond to the normal mass ordering (i.e. $j = 1$, $\Delta m_{31}^2 = \Delta m_{32}^2 + \Delta m_{21}^2 > 0$), while lower panels correspond to the inverted mass ordering (i.e. $j = 2$, $\Delta m_{32}^2 = \Delta m_{31}^2 - \Delta m_{21}^2 < 0$). Confidence regions are shown for various atmospheric, reactor and accelerator-based LBL experiments (coloured hollow regions), as well as a combined fit (black solid regions). The regions are defined with respect to the best fit across both mass orderings so the IO confidence regions are smaller than those of the NO, in which the best-fit point is found. Adapted from Ref. [57].

detector, Super-K, as the far detector. A more complete description of T2K and its detectors will be given in Chapter 3. By contrast, NOvA employs functionally identical near and far detectors, using liquid scintillator based tracking calorimeters. Although both experiments simultaneously fit to both $\bar{\nu}_\mu$ disappearance and $\bar{\nu}_e$ appearance, it is the disappearance channel that provides the greatest constraint on θ_{23} and $|\Delta m_{32}^2|$. As Fig. 2.13 shows, T2K and NOvA provide some of the strongest constraints on these parameters to date and both favour the upper octant of θ_{23} while still being compatible with maximal mixing [35, 57]. Both T2K and NOvA weakly disfavour the inverted mass ordering, T2K with $\Delta\chi^2_{\text{IO-NO}} \equiv \chi^2_{\text{IO best fit}} - \chi^2_{\text{NO best fit}} \sim 4$, and NOvA with $\Delta\chi^2_{\text{IO-NO}} \sim 2$ [57].

2.3.2.2 Constraints from Atmospheric Neutrino Experiments

Similarly to accelerator-based experiments, atmospheric neutrino experiments detect neutrinos produced from the decays of pions and kaons; however, instead of resulting from the interactions between accelerated protons and a target, they are produced by cosmic ray interactions in the upper atmosphere. Such neutrinos have a much wider

range of energies (covering GeV, TeV and rarely even PeV [60]) and baselines (being produced anywhere from the atmosphere above the detector, i.e. ~ 10 km, to the other side of the Earth, i.e. $\sim 1.3 \times 10^4$ km).

After the initial observations of atmospheric neutrinos in 1965 by the Kolar Gold Mines [61] and East Rand Proprietary Mines experiments [62], they were studied as backgrounds to nucleon decay experiments such as Kamiokande [63] (which operated during 1987–1995). From such observations followed the atmospheric neutrino anomaly, the solution to which was found in 1998 by Super-K [24], as discussed in Section 2.1.3.2. More recently (2010 onwards), the IceCube experiment, using an ice Cherenkov detector instrumented with PMTs, has taken measurements of cosmic neutrinos, but also contains a sub-detector, DeepCore, with more densely packed PMTs in order to detect atmospheric neutrinos [35]. While the observations discussed here are primarily of ν_μ disappearance, ν_τ appearance has also been observed, both by IceCube DeepCore [64] and by the accelerator-based LBL OPERA experiment [35, 65]. While the atmospheric experiments do not constrain θ_{23} and $|\Delta m_{32}^2|$ as strongly as the previously discussed accelerator-based LBL experiments, as Fig. 2.13 shows, the results from IceCube DeepCore and Super-K are in good agreement with the results from accelerator-based LBL experiments, and provide a useful cross-check of the 3-flavour oscillation model at a range of energies and baselines [57]. Additionally, Super-K is sensitive to the mass ordering and shows a preference for NO with $\Delta\chi^2_{\text{IO-NO}} = 4.3$ [57].

2.3.2.3 Constraints from Reactor Antineutrino Experiments

Reactor antineutrino experiments take advantage of the intense $\bar{\nu}_e$ flux emitted by nuclear fission reactors. Similarly to accelerator-based LBL experiments, these experiments typically use both near detectors (to reduce systematic uncertainties by measuring the $\bar{\nu}_e$ flux) and far detectors (to measure the oscillated flux). Such experiments measure the disappearance of $\bar{\nu}_e$ only (due to the energy threshold of μ and τ production [35]) and, at medium baselines, are sensitive to both $|\Delta m_{32}^2|$ and θ_{13} [35].

In the late 1990s, the CHOOZ and Palo Verde experiments, each using a single liquid scintillator based detector, measured reactor $\bar{\nu}_e$ flux in order to investigate the possibility of neutrino oscillations in the $\Delta m^2 \gtrsim 10^{-3}$ eV 2 c $^{-4}$ region, as indicated by the atmospheric neutrino anomaly (see Section 2.1.3.2) [35]. Although neither experiment found evidence for neutrino oscillations, limits were set on both $|\Delta m_{32}^2|$ and $\sin^2 2\theta_{13}$ [66, 67].

Regarding the current generation of reactor antineutrino experiments, a number of such experiments have been in operation since the mid to late 2000s, namely Double Chooz, Reno and Daya Bay. In contrast to the earlier experiments, these operate using a combination of functionally identical near and far liquid scintillator detectors, in order to reduce uncertainties from the $\bar{\nu}_e$ flux [35]. As Fig. 2.13 shows, these experiments are sensitive to both $|\Delta m_{32}^2|$ and θ_{13} , with the strongest constraint offered by the Daya Bay experiment, whose measurement of $|\Delta m_{32}^2|$ is both compatible with and

approximately as constraining as the accelerator-based LBL experiments. However, the reactor experiments have little sensitivity to the mass ordering or to θ_{23} [57].

From the combination of data from accelerator, atmospheric and reactor experiments, the 2018 best fit values and 1σ errors for the parameters discussed in this section are as follows, and the best fit point is found to be in the normal mass ordering [57]:

$$\begin{aligned}\sin^2 \theta_{23} &= 0.528^{+0.015}_{-0.019} \\ \Delta m_{32}^2 &= (2.525^{+0.033}_{-0.031}) \times 10^{-3} \text{ eV}^2 \text{c}^{-4} \\ \Delta\chi^2_{\text{IO-NO}} &= 9.3\end{aligned}\quad (2.42)$$

2.3.3 θ_{13} and δ_{CP}

The dominant contribution to measurements of θ_{13} comes from reactor experiments (see Section 2.3.2.3) and, as shown by Fig. 2.13, this is mainly driven by the Daya Bay experiment. Accelerator-based LBL experiments can also have some sensitivity to θ_{13} , but the resulting constraints are not competitive with those of the reactor experiments, so the global best fit values are typically calculated using reactor data only [57].

Establishing θ_{13} to be non-zero was crucial in determining whether CP violation could possibly occur in neutrino oscillations. As can be seen from Eqs. (2.30) and (2.35), the CP-violating term of $P(\vec{\nu}_\mu \rightarrow \vec{\nu}_e)$ is only non-zero if θ_{12} , θ_{23} and θ_{13} are also all non-zero. In 2011, the T2K experiment reported the first indications of non-zero θ_{13} , at a significance of 2.5σ [68]. Subsequently, in 2012, the Daya Bay experiment reported the discovery of non-zero θ_{13} at greater than 5σ significance [69], opening up the possibility of measuring δ_{CP} .

In order to obtain a non-negligible sensitivity to δ_{CP} , it is essential to make measurements of the appearance of one flavour of neutrino from an initial flux of a different type (as shown by e.g. the comparison of $P(\vec{\nu}_\mu \rightarrow \vec{\nu}_e)$ and $P(\vec{\nu}_\mu \rightarrow \vec{\nu}_\mu)$ in Eqs. (2.30) and (2.31)) and important to perform such measurements for both neutrinos and anti-neutrinos (due to the interference term of e.g. Eq. (2.30)). For these reasons, currently only accelerator-based LBL experiments are sensitive to δ_{CP} , namely T2K and NOvA. As Fig. 2.14 shows, the global fit is mainly driven by T2K, which observed a stronger than expected constraint due to an excess (deficit) in the (anti)neutrino event rate compared to expectation, driving $\sin \delta_{CP}$ towards -1 . For NOvA in the normal mass ordering, the neutrino and antineutrino datasets show very weak preferences for different values of $\sin \delta_{CP}$, while their combination disfavours $\sin \delta_{CP} \simeq -1$ at the $\Delta\chi^2 \simeq 3.5$ level, in mild tension with the T2K results [57].

From the combination of data from accelerator-based LBL experiments, the 2018 best fit values and errors for the parameters discussed in this section are as follows [57]. Additionally, a best fit value and error for $\sin^2 \theta_{13}$ is reported from a fit to reactor experiments only [35]. At the 3σ confidence level, neither CP conservation ($\sin \delta_{CP} = 0$) nor maximal CP violation ($\sin \delta_{CP} = \pm 1$) can be excluded. Here, the value of δ_{CP} has

been converted from the convention used by the global fit (interval of $[0, 360]^\circ$) to the convention used by T2K (interval of $[-\pi, +\pi]$ radians).

$$\begin{aligned} \sin^2 \theta_{13} \text{ reactor + accelerator LBL} &= (2.240^{+0.065}_{-0.066}) \times 10^{-2} \\ \sin^2 \theta_{13} \text{ reactor-only} &= (2.12 \pm 0.08) \times 10^{-2} \\ \delta_{CP} \text{ best fit point } \pm 1\sigma &= -2.50^{+0.70}_{-0.49} \\ \delta_{CP} \text{ } 3\sigma \text{ range} &= [-\pi, 0.56] \cup [2.09, \pi] \end{aligned} \quad (2.43)$$

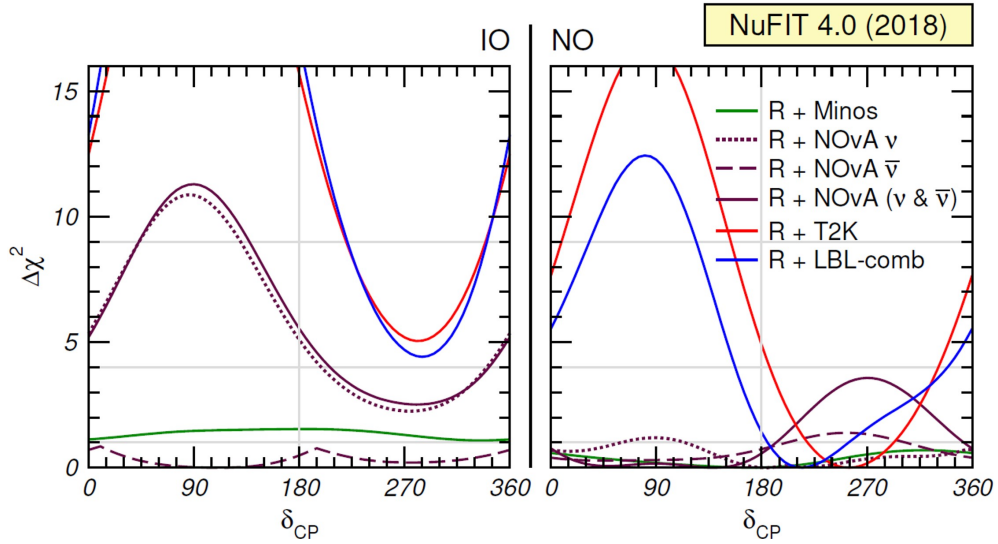


Figure 2.14: $\Delta\chi^2$ as a function of δ_{CP} for various accelerator-based LBL experiments as well as their combination. Left (right) panels are for IO (NO), and $\Delta\chi^2$ is defined with respect to the minimum across both mass orderings. The $\Delta\chi^2$ functions are produced using the full information from both accelerator and reactor experiments on θ_{13} , θ_{23} and Δm_{3j}^2 . Δm_{21}^2 and $\sin^2 \theta_{12}$ are fixed to the global best fit values. Reproduced from Ref. [57].

Chapter 3

The T2K Experiment

T2K (Tokai to Kamioka) [70] is an accelerator-based long baseline neutrino experiment that utilises a high purity ν_μ or $\bar{\nu}_\mu$ beam to study neutrino oscillations. T2K was proposed in the early 2000s to search for $\nu_\mu \rightarrow \nu_e$ oscillations (and therefore measure the mixing angle θ_{13}) and to make precision measurements of ν_μ disappearance (and therefore measure θ_{23} and Δm_{32}^2) [71, 72].

Shortly after the start of data taking in 2010, T2K reported the first indication of non-zero θ_{13} at a significance of 2.5σ [73], which was subsequently confirmed at the 7.3σ level in 2014 [74]. In addition, T2K has continued to provide the worlds most precise measurements of θ_{23} for a number of years [3, 42, 75]. With the initial goals met and the establishment of non-zero θ_{13} , T2K aims to improve upon the measurements of θ_{23} and Δm_{32}^2 , as well as searching for $\bar{\nu}_\mu$ to $\bar{\nu}_e$ oscillations and seeking the first hints of CP-violation in the lepton sector.

Such oscillation parameter measurements are made possible by the use of a ν_μ or $\bar{\nu}_\mu$ beam produced at J-PARC (Japan Proton Accelerator Research Complex) in Tokai, Japan. As shown by Fig. 3.1, the beam first passes through a collection of near detectors before travelling 295 km through the Earth's crust to the far detector, Super-K. The detectors are located 2.5° off the central axis of the beam, causing the neutrino flux to be sharply peaked at 0.6 GeV. In this chapter, each of these components of the experiment will be described in detail.

While the focus of this thesis is neutrino oscillations, T2K also has a broad program of measurements beyond oscillations, including cross-section measurements [76, 77], and searches for sterile neutrinos [78] and CPT-symmetry violation [79].

3.1 Neutrino Beam

In order to measure $\bar{\nu}_\mu \rightarrow \bar{\nu}_e$ oscillations, a beam of $\bar{\nu}_\mu$ must first be produced. This is done using a combination of three accelerators, an overview of which is shown in Fig. 3.2. A beam of H^- ions is accelerated up to 400 MeV by a linear accelerator (LINAC) and formed into bunches, before being converted to H^+ (i.e. protons) by charge-exchange with a stripping foil [80]. These protons are injected into the rapid cycling synchrotron (RCS), containing two bunches per cycle, and are accelerated up

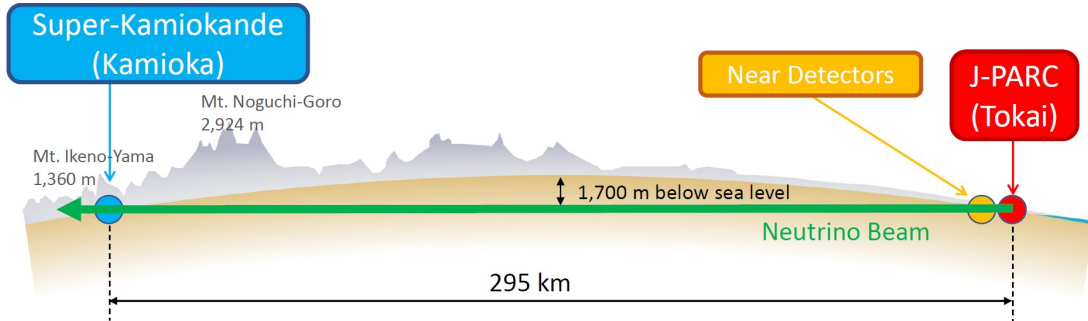


Figure 3.1: A diagram of the path taken by the T2K neutrino beam from its creation in the J-PARC facility, through the near detectors, and towards the far detector, Super-Kamiokande.

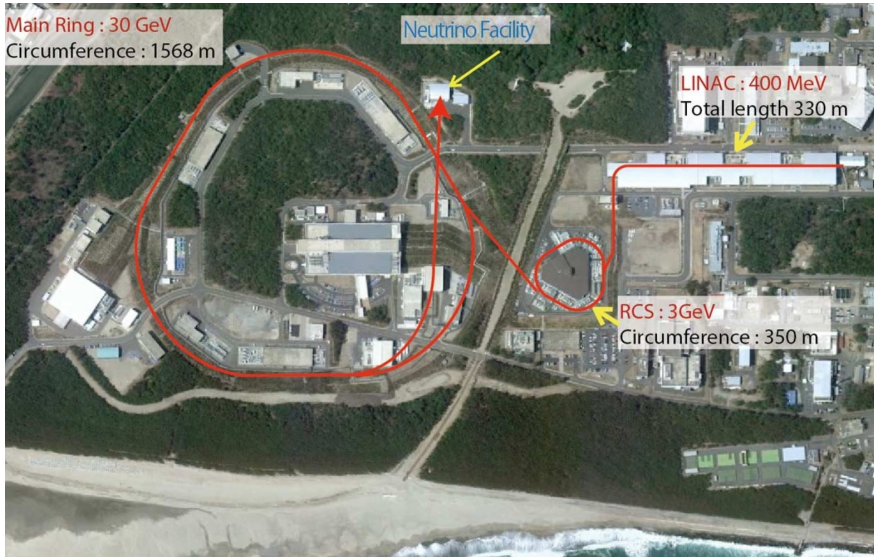


Figure 3.2: Accelerator layout at J-PARC. Adapted from Ref. [82]

to 3 GeV [80, 81]. Then, over multiple RCS cycles, proton bunches are injected into the main ring (MR) synchrotron, which holds up to 8 bunches and accelerates them to 30 GeV with a maximum beam power of 523 kW. With the use of kicker magnets, a fast extraction system then extracts the 8 bunch beam spill in a single cycle into a two-section neutrino beamline, shown in Fig. 3.3. The proton beam spill has a width of $\sim 5 \mu\text{s}$ [70], which opens the trigger window at both near and far neutrino detectors and is vital for discriminating beam neutrinos from the various backgrounds such as cosmic rays.

In the primary beamline, a collection of normal conducting and superconducting magnets is used to steer the proton beam towards Kamioka, focus it, and to select the off-axis angle. Also within this beamline are systems which monitor the beam's position, angle, intensity, profile and losses [83]. The secondary beamline contains a 1.9 interaction length graphite target, into which the proton beam strikes, with 85% of the protons interacting to produce mainly pions and kaons. Before striking the target, the proton beam intensity is measured by current transformers, which allows the number of

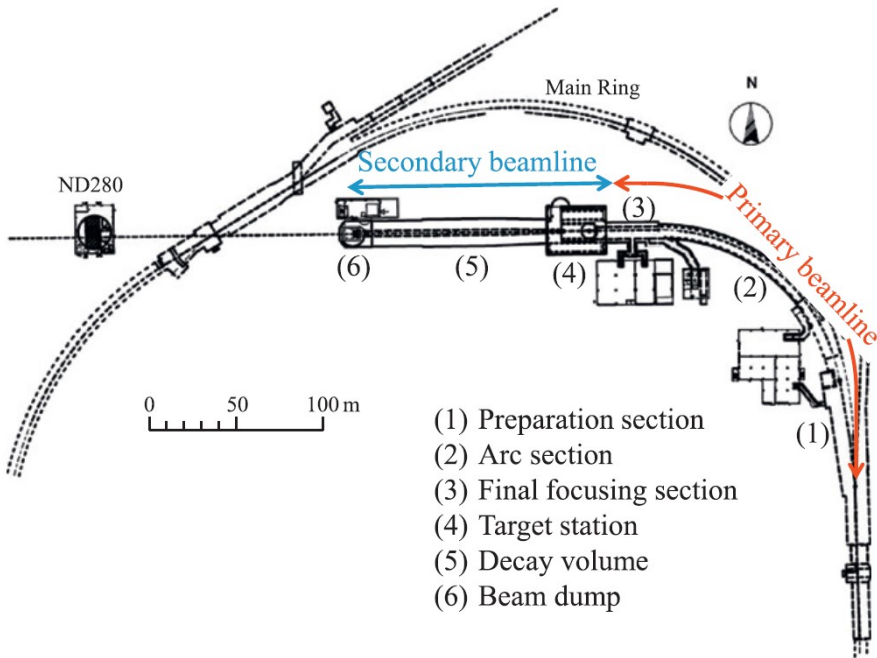


Figure 3.3: Diagram of the neutrino beamlines at J-PARC.

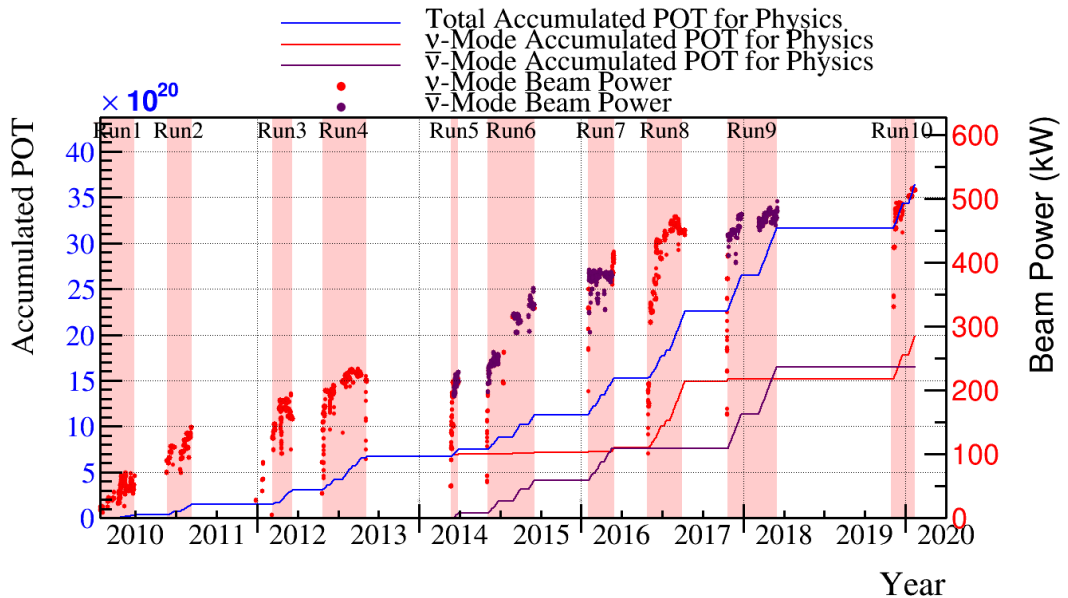


Figure 3.4: Accumulation of POT over time, divided into run periods. The power of the J-PARC proton beam is also shown.

delivered protons on target (POT) to be calculated, which is one of the main measures of the collected dataset size.

The number of POT accumulated over time since the start T2K operations is shown in Fig. 3.4. As the figure indicates, T2K received beam during ten separate run periods between 2010 and 2020. While the main analysis of this thesis (see Chapter 5) uses the full dataset across T2K Runs 1-10, the $\bar{\nu}_e$ appearance analysis of Chapter 6 was finalised before the collection of the Run 10 data.

The pions and kaons then travel through the decay volume and are focussed by a

series of magnetic horns before decaying to produce neutrinos, primarily through the decays shown in Eq. (3.1) (with branching fractions [55] for the decay of the parent particle shown in brackets), and similarly for antineutrinos. Depending on the direction of the current in the magnetic horns, either positively or negatively charged particles can be selected, resulting in a beam predominantly composed of ν_μ or $\bar{\nu}_\mu$, which are referred to as being ‘ ν -mode’ and ‘ $\bar{\nu}$ -mode’ beams, respectively. This selection cannot completely remove all wrong-sign particles, leading to a small contamination of $\bar{\nu}$ (ν) in the ν -mode ($\bar{\nu}$ -mode) beam. Additionally, there is a secondary source of contamination: while the decays in Eq. (3.1) produce mainly ν_μ , there is a small contribution from ν_e . Despite these contaminations, both ν -mode and $\bar{\nu}$ -mode beams are of a high purity, as shown in Fig. 3.5.

$$\begin{aligned}
 \pi^+ &\rightarrow \mu^+ + \nu_\mu & (99.99\%) \\
 \pi^+ &\rightarrow \mu^+ + \nu_\mu + \gamma & (0.02\%) \\
 \pi^+ &\rightarrow e^+ + \nu_e & (0.01\%) \\
 K^+ &\rightarrow \mu^+ + \nu_\mu & (63.56\%) \\
 K^+ &\rightarrow \pi^0 + e^+ + \nu_e & (5.07\%) \\
 K^+ &\rightarrow \pi^0 + \mu^+ + \nu_\mu & (3.35\%) \\
 K_L^0 &\rightarrow \pi^- + e^+ + \nu_e & (40.55\%) \\
 K_L^0 &\rightarrow \pi^- + \mu^+ + \nu_\mu & (27.04\%) \\
 \mu^+ &\rightarrow e^+ + \nu_e + \bar{\nu}_\mu & (\simeq 100\%)
 \end{aligned} \tag{3.1}$$

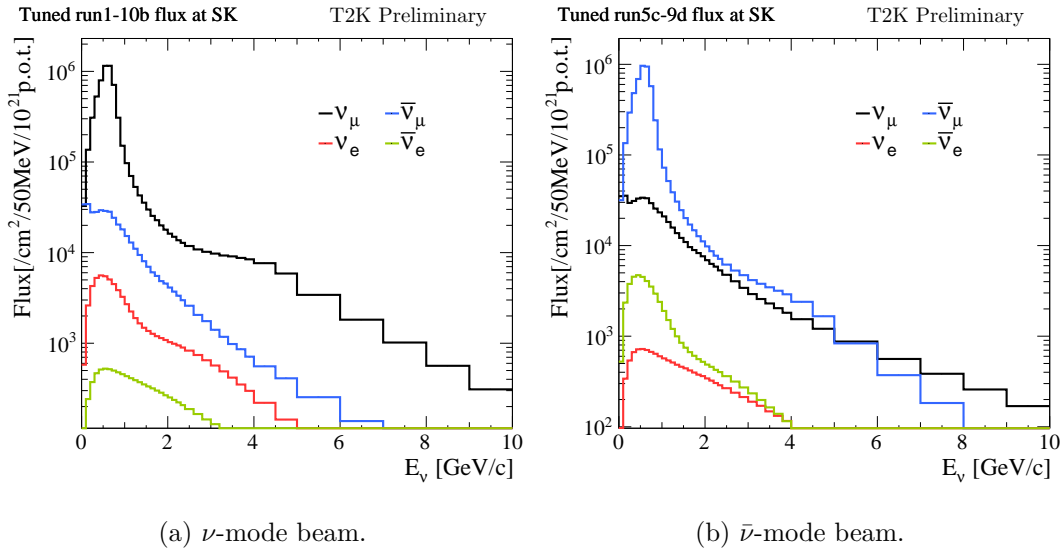


Figure 3.5: The predicted unsoscillated neutrino fluxes at Super-K, broken down by neutrino flavour. This corresponds to the full collected dataset (T2K Runs 1-10) analysed in this thesis. Reproduced from Ref. [84].

Downstream of the decay volume lies a beam dump, which absorbs almost all of the remaining hadrons and $\lesssim 5$ GeV muons [83] while having negligible effect on the neutrino beam. The surviving muons are detected by the muon monitor, MUMON,

which uses an ionisation chamber and silicon PIN photodiode to infer the direction and intensity of the neutrino beam with a precision of 0.25 mrad and 2.9%, respectively [85].

3.1.1 Off-axis Beam

As the neutrino oscillation probability depends on the neutrino energy, and the process of reconstructing this energy from the observable information in Super-K is imperfect (as will be shown in Section 4.5), a more clear oscillation signal would be observed from a sharply-peaked neutrino flux. In order to achieve this at T2K, the neutrino beam is tuned by taking advantage of the angular dependence of the decays listed in Eq. (3.1). In particular, the central axis of the neutrino beam is pointed slightly away from Super-K, with the angle between them referred to as the ‘off-axis angle’, θ_{OA} .

Taking the example of the most prominent decay contributing to the T2K neutrino beam, $\pi^+ \rightarrow \mu^+ + \nu_\mu$, the neutrino energy, E_ν , can be related to θ_{OA} , as well as the muon mass, pion mass, energy and momentum, m_μ , m_π , E_π , and p_π , respectively, as given by Eq. (3.2) [86]. As a result, increasing θ_{OA} from 0° decreases the second term of the denominator and therefore results in a wide range of pion energies contributing to a relatively small range in neutrino energies, as demonstrated by Fig. 3.6.

The effect of varying the off-axis angle on the neutrino flux at Super-K can be seen in Fig. 3.7, along with a comparison to the ν_μ survival and ν_e appearance probabilities. The off-axis angle chosen for T2K is 2.5° , which ensures that the flux is sharply peaked at 0.6 GeV, corresponding to the maximum ν_e appearance probability. This ensures that T2K will observe a clear $\nu_\mu \rightarrow \nu_e$ oscillation signal, which is vital to progressing the T2K goals of constraining both θ_{13} and δ_{CP} .

$$E_\nu = \frac{m_\pi^2 - m_\mu^2}{2(E_\pi - p_\pi \cos \theta_{\text{OA}})} \quad (3.2)$$

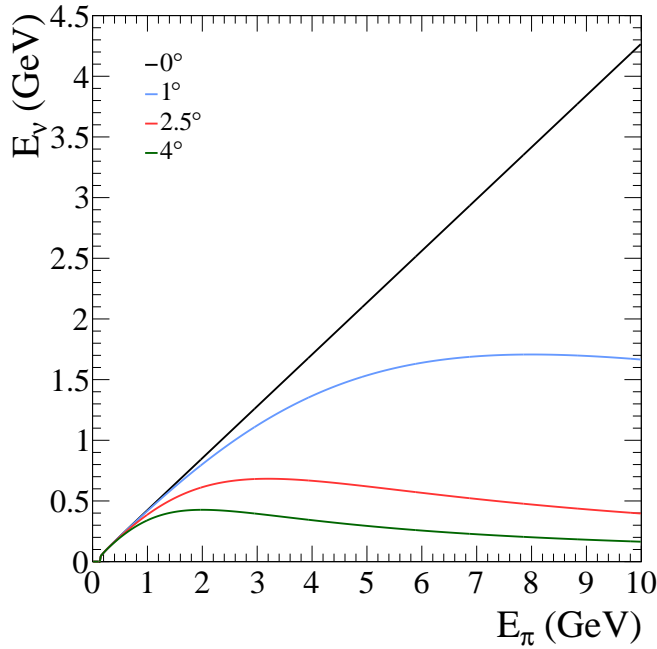


Figure 3.6: Variation of neutrino energy with pion energy and off-axis angle, calculated according to Eq. (3.2).

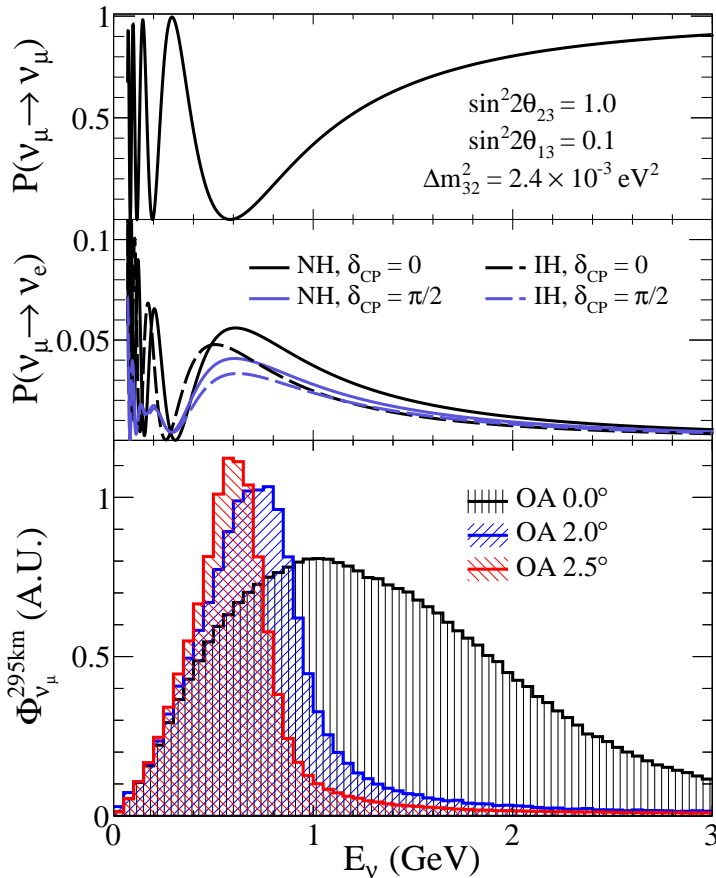


Figure 3.7: The effect of the off-axis angle (OA) on the predicted unoscillated flux at Super-K. Also shown are the ν_μ survival and ν_e appearance probabilities for an assumed set of oscillation parameters.

3.2 Near Detectors

The T2K experiment makes use of a number of detectors, located at varying distances from the target station. These are divided into two groups: ‘near detectors’, located at negligible L/E values to measure the unoscillated neutrino beam; and ‘far detectors’, located at larger L/E in order to measure the oscillated neutrino flux. This section will focus on the T2K near detector complex, located 280 m from the target station. While it contains many detectors, data from only two are (indirectly) used in the analyses presented in this thesis: the on-axis detector, INGRID (Interactive Neutrino Grid), and the off-axis detector, ND280 (Near Detector at 280 m), both displayed in relation to each other and to the neutrino beam in Fig. 3.8. Together, these detectors measure the unoscillated neutrino flux and flavour composition, the beam direction, and neutrino-nucleus cross-sections. Such measurements are used to predict the neutrino flux and therefore the event rates at the far detector.

3.2.1 INGRID

INGRID [86, 87], pictured in Fig. 3.9, is an on-axis neutrino detector, designed to monitor the neutrino beam by detecting muon tracks produced from ν_μ CC interactions. The statistics collected at INGRID are sufficient for daily measurements of the observed beam profile, and from such data the centre of the beam is measured to a precision of 0.4 mrad per day [70], exceeding the required precision of 1 mrad [87]. Additionally, the measured neutrino event rates agree with the MC predictions to within 2% [42]. The observed event rates and beam direction as measured over the entire history of T2K is shown in Fig. 3.10 for both INGRID and MUMON, which are generally in agreement to within 0.3 mrad.

INGRID is composed of 14 identical modules arranged in a cross shape (with an additional two diagonally-located modules not used in the analysis, which measure the

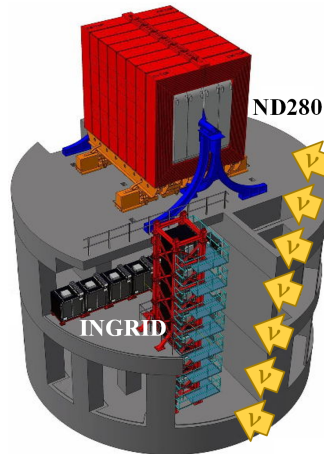


Figure 3.8: The near detector complex containing the two main detectors, ND280 (off-axis) and INGRID (on-axis). The direction of the neutrino beam is indicated by the yellow arrows.

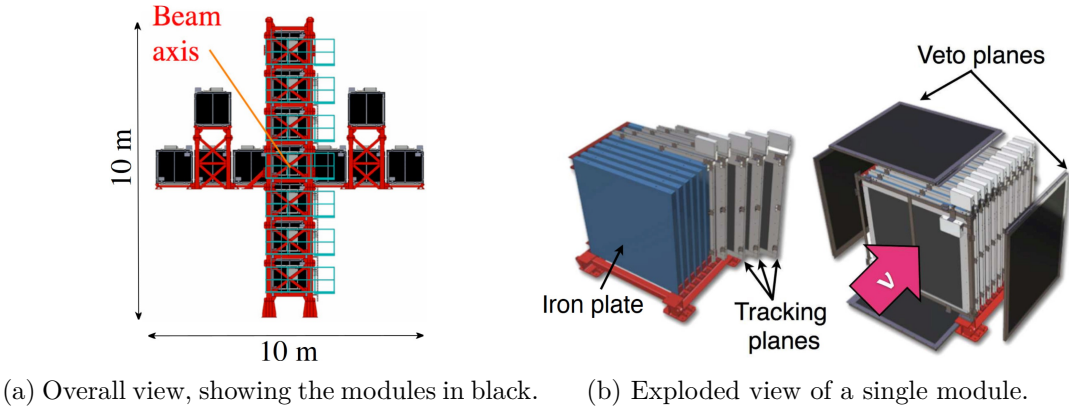


Figure 3.9: The INGRID on-axis detector. Reproduced from Ref. [86].

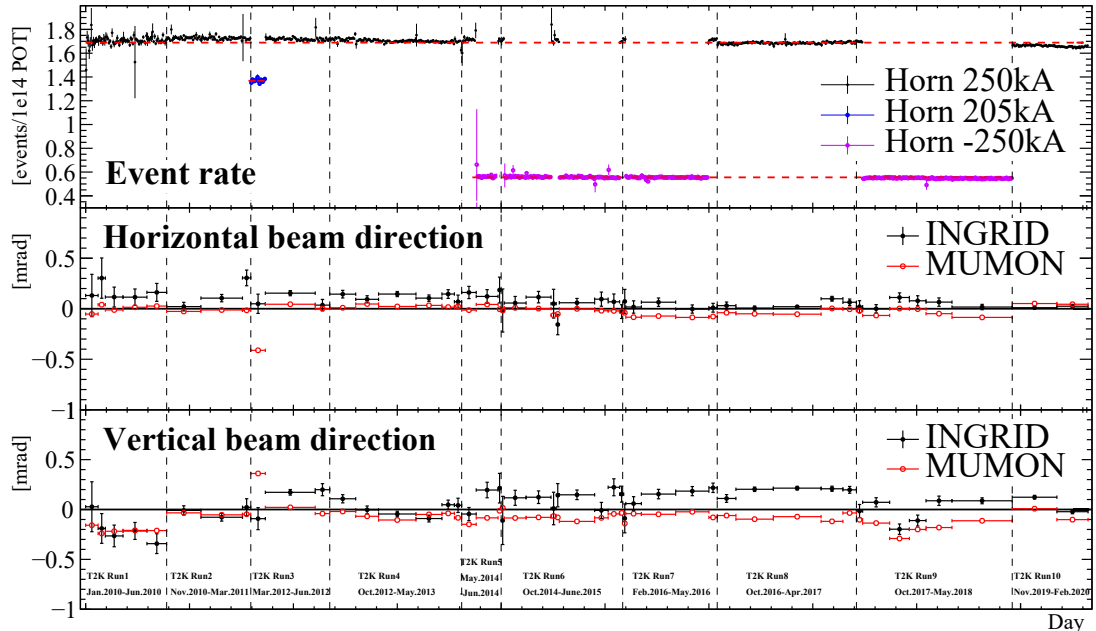


Figure 3.10: Observed properties of the J-PARC neutrino beam over the history of the T2K experiment. The upper panel shows the event rates as observed by INGRID in both neutrino and antineutrino beam modes, labelled with positive and negative magnetic horn currents, respectively. The central and lower panels show the horizontal and vertical beam directions observed by both INGRID and MUMON and expressed as the angular offset from the designed beam centre. The vertical dashed lines separate the individual run periods.

axial symmetry of the beam) where the beam is designed to pass through the centre. Each module is a tracking detector consisting of alternating iron interaction mass layers and horizontally and vertically aligned layers of $10\text{ mm} \times 50\text{ mm}$ scintillator bars, arranged to allow three-dimensional track reconstruction. Each module is surrounded by a scintillating veto layer to detect charged particles originating from outside the module [87].

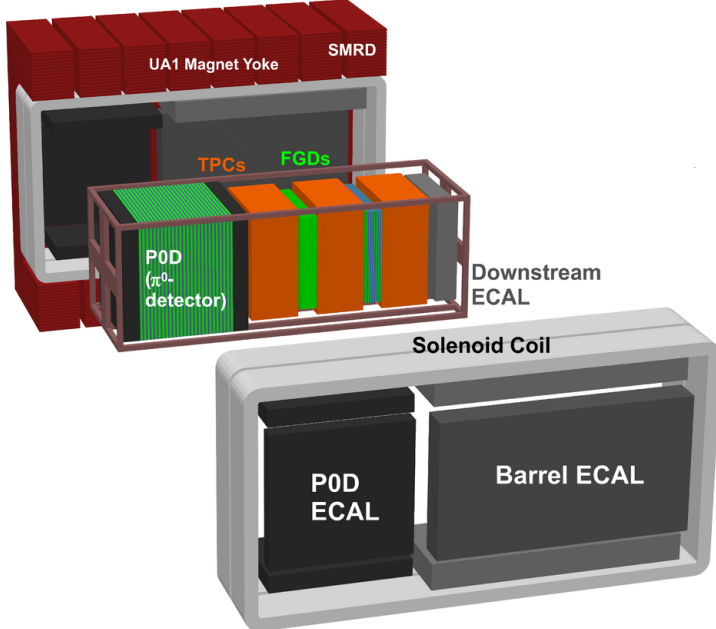


Figure 3.11: Exploded view of the ND280 off-axis detector and its sub-detectors. The central tracker region consists of the P0D, TPCs, and FGDs, and is surrounded by the ECALs and the magnet. The SMRD is inserted in the air gaps in the magnet yoke. The neutrino beam travels from the left to the right sides of the figure.

3.2.2 ND280

The primary near detector, ND280 is a magnetised detector located at an off-axis angle of 2.5° . It has a variety of goals, such as measuring the flux, energy spectra and flavour content of the neutrino beam, measuring the cross-sections of various neutrino-nucleus interaction types, and measuring the backgrounds to the $\bar{\nu}_\mu \rightarrow \bar{\nu}_e$ search at Super-K (in particular, the dominant background, NC1 π^0).

In order to satisfy these goals, ND280 is composed of a number of heterogeneous sub-detectors, all of which are pictured in Fig. 3.11. At the core of ND280 is a tracker region consisting of a π^0 detector (P0D) and three time projection chambers (TPCs) separated with two fine-grained detectors (FGDs). Surrounding the tracker region are a number of electromagnetic calorimeters (ECALs), which are in turn surrounded by a 0.2 T magnet, allowing the charge and momentum of charged particles to be measured. The internal dimensions of the magnet are $7.0 \text{ m} \times 3.6 \text{ m} \times 3.5 \text{ m}$ [88] and within the air gaps in the magnet yoke lies the side muon range detector (SMRD). The following sections give a brief overview of each of these sub-detectors, their purposes, and performance.

3.2.2.1 Fine-Grained Detectors

The primary target mass (of 2.2 tonnes) for neutrino interactions is provided by the FGDs, detailed in Ref. [89]. The two FGDs are composed of different materials: FGD1 consists of hydrocarbon scintillator bars, a frequently-used target in external neutrino

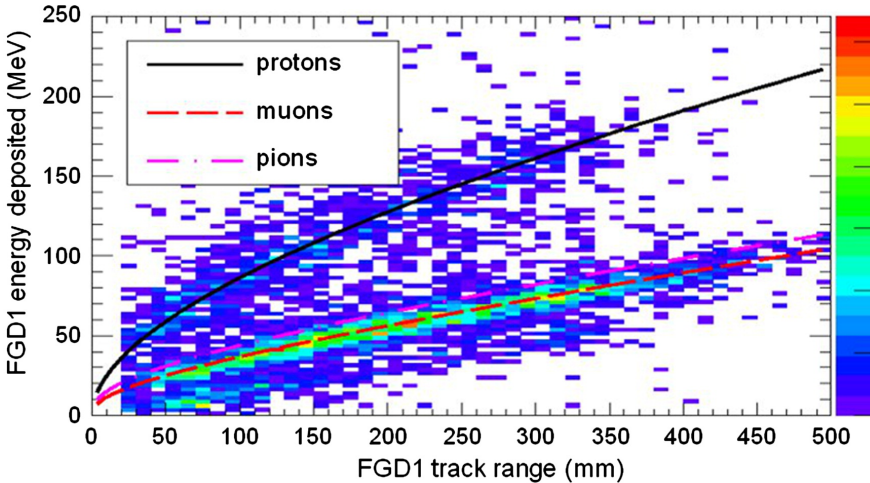


Figure 3.12: The total energy deposited by charged particle tracks in FGD1 as a function of track range. The coloured histogram displays the observed neutrino beam data, while the curves display the MC expectation for protons, muons and pions. Reproduced from Ref. [89].

interaction data, while FGD2 consists of alternating scintillator and water layers. By comparing the neutrino event rates across both FGDs, the neutrino cross-section in water can be measured, which is key to reducing systematic uncertainties in the interaction model when predicting event rates in the water-based Super-K detector.

The FGD scintillator bars have a square cross-section with 9.61 mm sides and a length of 1864.3 mm. They are arranged in alternating horizontal and vertical layers perpendicular to the beam direction to allow for three-dimensional reconstruction. A total of 5760 bars are used in FGD1, while FGD2 uses 2688 bars (due to the presence of water layers). Each bar is coated in reflective TiO₂ for optical isolation and to ensure efficient detection of scintillation light. The light is read out of each bar by a wavelength-shifting fibre going through a hole in the centre, with one end of the fibre attached to a multi-pixel photon counter, which detects and digitizes the light signal [70].

The FGDs also allow for high-resolution determination of the track vertex while being thin enough that charged leptons pass into the TPCs, and all tracks detected in the TPCs are required to match a vertex detected in a FGD. Additionally, measuring the total deposited energy of tracks in the FGD allows protons to be discriminated from muons and pions, as shown in Fig. 3.12. As neutrino charged current quasi-elastic (CCQE) interactions produce a proton, while resonance pion production (a significant background to CCQE) does not, the ability of the FGDs to separate the kinematics of events producing protons and pions aids in better separating the CCQE-like and CC1 π -like samples at Super-K (see Section 4.4). Observed neutrino interactions in both FGDs are used to constrain [90] the interaction model systematic uncertainties in the analyses presented in this thesis, as will be detailed in Section 4.3.

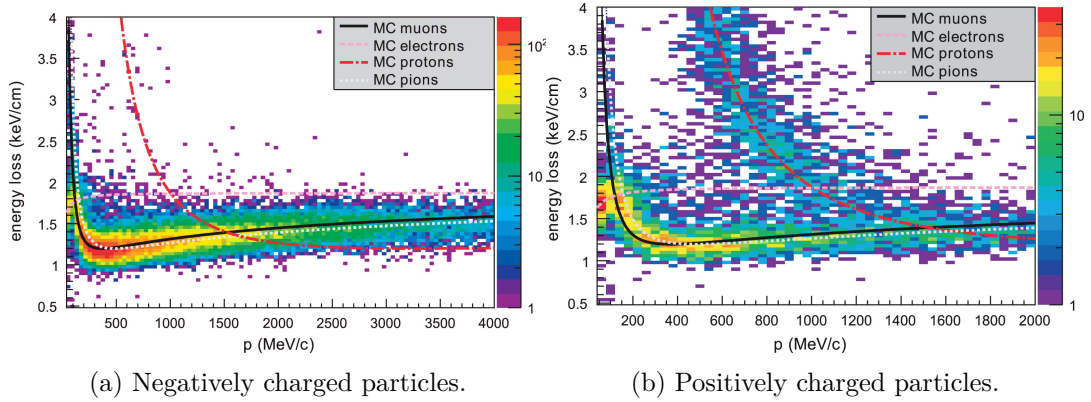


Figure 3.13: Distribution of the energy loss in the TPCs as a function of momentum for both negatively and positively charged particles produced in neutrino interactions, compared to the expected curves for muons, electrons, protons and pions. Reproduced from Ref. [91].

3.2.2.2 Time Projection Chambers

Charged particle momentum, charge, identification, and tracking information are provided by the three TPCs, detailed in Ref. [91]. Each TPC has dimensions $2.3\text{ m} \times 2.4\text{ m} \times 1.0\text{ m}$ and uses a drift volume containing an argon-based gas mixture in an electric field parallel to the 0.2 T magnetic field direction and perpendicular to the neutrino beam direction. Charged particles passing through this drift volume are deflected while ionising the gas and the ionisation electrons are subsequently detected by micromegas [92] and used to infer the trajectory, momentum, and charge of the parent particle, all of which is used to select the near detector samples.

The TPCs achieve a energy resolution of $7.8 \pm 0.2\%$ for $400 - 500\text{ MeV}/c$ minimum ionizing particles, exceeding the requirement of 10% needed to accurately distinguish muons and electrons in order to reduce the effects of ν_e contamination in the neutrino beam. The expected and observed energy losses as a function of momentum for particles in the TPCs are displayed in Fig. 3.13 and show an excellent ability to distinguish between muons and electrons, corresponding to only a 0.2% probability of misidentifying a muon as an electron for tracks below $1\text{ GeV}/c$ [91].

3.2.2.3 π^0 Detector

The P0D, detailed in Ref. [93], is designed to measure the cross-section of NC1 π^0 interactions, which are background process particularly important for the $\bar{\nu}_\mu \rightarrow \bar{\nu}_e$ search at Super-K. The P0D consists of alternating layers of interaction mass and scintillator and is arranged as a central region, optionally filled with water, sandwiched between two ECALs. By comparing the interaction rates with and without water, the NC1 π^0 interaction cross-section in water (i.e. at Super-K) can be measured. Data collected by the P0D is not directly used in the near detector fit (see Section 4.3), but is instead used to produce NC1 π^0 cross-section measurements.

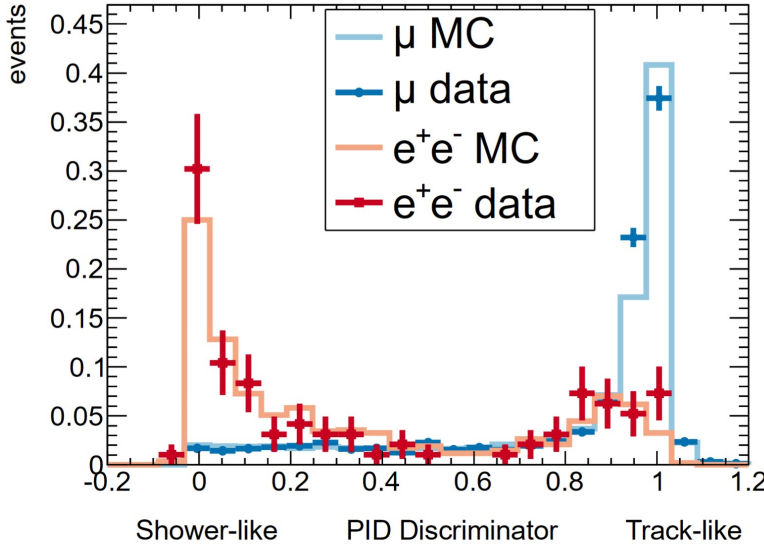


Figure 3.14: The particle identification (PID) statistic for the barrel ECAL, showing the ability to distinguish between track-like and shower-like particle events in both MC and data. Reproduced from Ref. [94].

3.2.2.4 Electromagnetic Calorimeters

Energy measurements of particles escaping the FGDs, TPCs and P0D are provided by the ECALs, detailed in Ref. [94]. This information is important for the purpose of particle identification, particularly for the detection of photons resulting from π^0 events.

All of the ECALs consist of alternating layers of scintillator bars and lead absorber sheets, but differ slightly in construction and purpose. All ECAL scintillator bars have a 40 mm \times 10 mm cross-section, and as with the FGD bars described above, are coated with reflective TiO₂ and light readout is provided by wavelength-shifting fibres connected to multi-pixel photon counters.

The Barrel and Downstream ECALs, surrounding the FGDs and TPCs, are required to reconstruct electromagnetic showers, complementing the TPCs and consisting of 10 - 11 radiation lengths of absorber material in order to contain at least half of the energy resulting from π^0 decays. The ECALs show an excellent ability to separate track-like particles (e.g. muons) from shower-like particles (e.g. electrons), as shown in Fig. 3.14, and an energy resolution of up to $\sim 7.5\%$, as shown by Fig. 3.15. By contrast, the P0D ECAL contains fewer scintillator/absorber layers, corresponding to 4.9 interaction lengths, and is primarily used to tag escaping energy and distinguish muons from photons. The particle identification information provided by the ECALs is used in the selection of the near detector samples.

3.2.2.5 Side Muon Range Detectors

At T2K energies, muons behave as minimum ionising particles and therefore typically escape the tracker and ECAL regions at large angles, leaving relatively few TPC

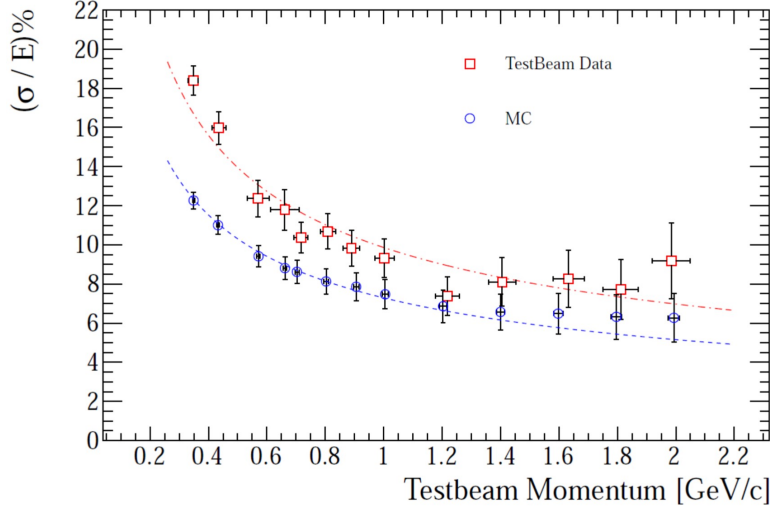


Figure 3.15: Predicted and observed energy resolution, σ/E , of the Downstream ECal for electromagnetic showers. The dashed lines show a fit to a stochastic resolution model.

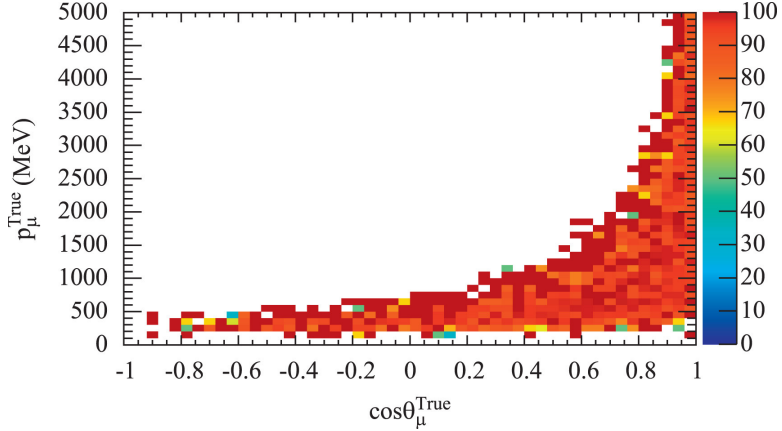


Figure 3.16: Track finding efficiency (%) of SMRD-only reconstruction for events with at least two muon hits in the detector as a function of true muon momentum, p_μ^{True} , and cosine of the angle with respect to the beam direction, $\cos\theta_\mu^{\text{True}}$. Reproduced from Ref. [95].

hits [95]. Therefore, from the TPC alone, accurate reconstruction of muon momentum would be difficult. To aid in this, the SMRD, detailed in Ref. [95], is designed to measure muon momentum. The SMRD is a plastic scintillating detector that lies in the gaps of the iron plates that constitute the magnet yoke and surrounds the tracker and ECAL regions. The thickness of the iron interleaved with the SMRD is sufficient to stop the majority of high-angle muons, and by measuring the range of muon tracks, the momentum can be inferred. The track finding efficiency of the SMRD remains high across a wide range of parameter space, as shown in Fig. 3.16. A secondary purpose of the SMRD is to detect muons from cosmic ray interactions and to therefore act as a cosmic trigger.

3.3 The Far Detector - Super-Kamiokande

The Super-Kamiokande (Super-K) detector, detailed in Ref. [96], is a water Cherenkov detector, which was originally commissioned in 1996 to study neutrinos originating from the atmosphere [24], the Sun [97, 98], and other astrophysical sources, as well as constraining proton decay [99, 100]. In addition to these goals, Super-K operates as the far detector for accelerator-based long baseline experiments, starting with K2K in 1999-2004 [101] and continuing with T2K since 2010.

Super-K is located 295 km from the neutrino beam production target and lies beneath 1 km of rock in the Kamioka mine to reduce the rate of cosmic muon interactions to 2 Hz, five orders of magnitude lower than the surface rate [102]. As shown in Fig. 3.17, Super-K is a 41 m × 39 m cylindrical stainless steel tank filled with 50 kton of high-purity water and instrumented with 13,000 photomultiplier tubes (PMTs). The detector is separated into two optically isolated, concentric cylindrical sub-detectors: An inner detector (ID) surrounded by a 2 m thick outer detector (OD). The OD is instrumented with outward-facing PMTs in order to veto charged particle background events entering from outside of the detector volume. The ID is instrumented with inward-facing PMTs covering ∼ 40% of the ID surface area and is designed to detect charged particles originating from within the ID, such as those produced by neutrino interactions.

Event reconstruction in Super-K is provided by the detection (by the PMTs) of Cherenkov light [103] emitted by charged particles travelling through the water faster than the phase velocity of light in water. This light is emitted as a ring around the particle’s direction of motion, with a half-opening angle, θ , of [43]

$$\cos \theta = \frac{1}{n\beta} \quad (3.3)$$

where $n \sim 1.33$ is the refractive index of water [55] and β is the particle’s speed as a fraction of the speed of light in vacuum. At T2K energies, electrons or muons produced from neutrino CC interactions will typically be above the Cherenkov threshold (i.e. $\beta > 1/n$ [43]), but taus, hadrons and nucleons are typically not, so are not directly visible. By detecting the ring-shaped pattern on the walls of the Super-K detector along with PMT hit timing information, the interaction vertex, momentum, and particle identification can be inferred. In water and at T2K energies, electrons interact much more frequently than muons, resulting in greater scattering and in electromagnetic showers. Consequently, the Cherenkov rings produced by electrons are less sharply-defined than those from muons or pions (examples of which are shown in Fig. 3.18) and this is used to discriminate between these particles, achieving a < 1% mis-identification rate for CCQE events across the T2K energy range [3]. Additionally, the reconstruction algorithm searches for delayed electron-like Cherenkov rings consistent with the Michel decay of either the primary muon or muons produced from pion decay. Super-K achieves a momentum, p , and angle resolution for true CCQE single-muon events of

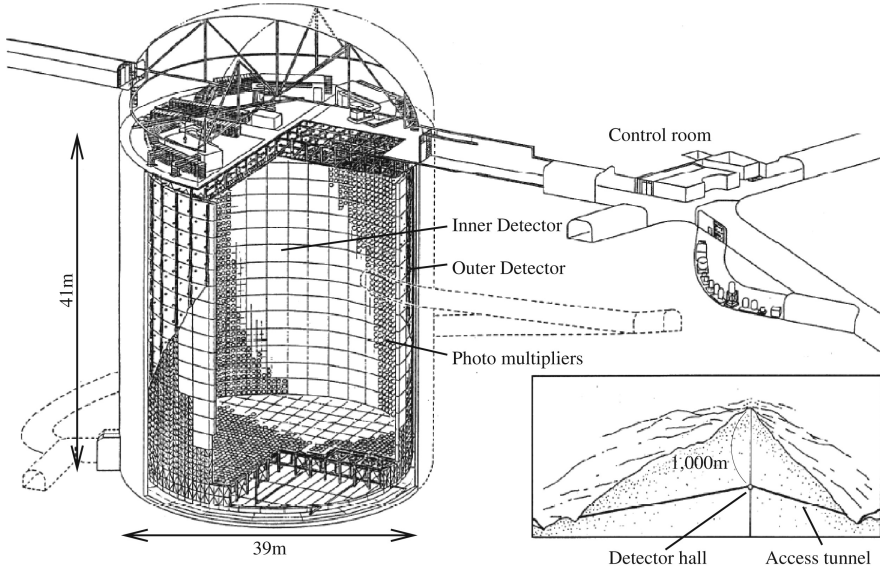


Figure 3.17: Cutaway view of the Super-Kamiokande detector. Reproduced from Ref. [70].

$(1.7 + 0.7/\sqrt{p(\text{GeV}/c)})\%$ and 1.8° , respectively, and $(0.6 + 2.6/\sqrt{p(\text{GeV}/c)})\%$ and 3.0° for true CCQE single-electron events [104].

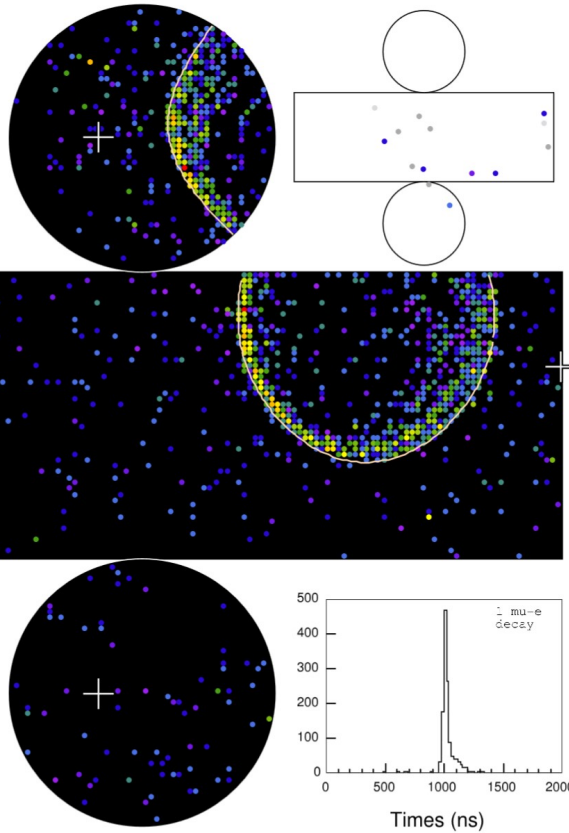
The water circulating inside the Super-K tank has recently been doped with a 0.02% concentration of $\text{Gd}_2(\text{SO}_4)_3$ in order to allow the detection of neutrons, previously invisible in water Cherenkov detectors, by radiative neutron capture on Gd. This will allow for neutrino and antineutrino events to be distinguished by detecting the neutron in the reaction $\bar{\nu}_l + p \rightarrow l^+ + n$. The effects will be to reduce backgrounds in the proton decay and $\bar{\nu}_\mu \rightarrow \bar{\nu}_e$ searches (although neutron capture data is not currently used in the oscillation analysis [105]) and to increase sensitivity to the detection of supernova relic neutrinos [106]. The current 0.02% concentration of $\text{Gd}_2(\text{SO}_4)_3$ is sufficient to give a $\sim 50\%$ neutron capture efficiency, but the concentration will soon be increased to 0.2%, giving an efficiency of $\sim 90\%$ [107].

Super-Kamiokande IV

T2K Beam Run 330024 Spill 797537
 Run 66776 Sub 770 Event 17898746
 10-05-11:12:14:27
 T2K beam dt = 1899.2 ns
 Inner: 1332 hits, 3282 pe
 Outer: 6 hits, 3 pe
 Trigger: 0x80000007
 D_{wall} : 1136.5 cm
 μ -like, $p = 537.6$ MeV/c

Charge (pe)

- >26.7
- 23.3-26.7
- 20.2-23.3
- 17.3-20.2
- 14.7-17.3
- 12.2-14.7
- 10.0-12.2
- 8.0-10.0
- 6.2- 8.0
- 4.7- 6.2
- 3.3- 4.7
- 2.2- 3.3
- 1.3- 2.2
- 0.7- 1.3
- 0.2- 0.7
- < 0.2



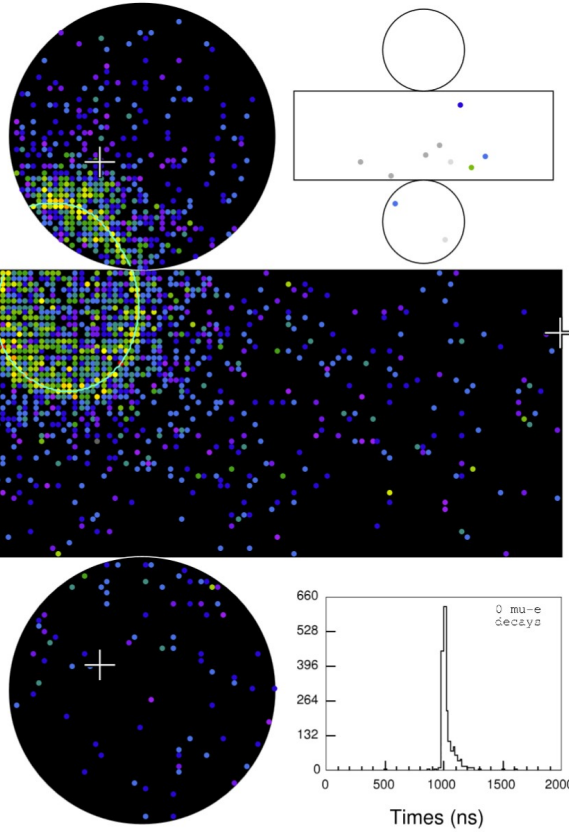
(a) Muon-like event.

Super-Kamiokande IV

T2K Beam Run 440058 Spill 1830074
 Run 70557 Sub 936 Event 228624972
 12-10-23:06:26:24
 T2K beam dt = 1354.0 ns
 Inner: 1846 hits, 4789 pe
 Outer: 4 hits, 9 pe
 Trigger: 0x80000007
 D_{wall} : 788.8 cm
 e -Like, $p = 466.0$ MeV/c

Charge (pe)

- >26.7
- 23.3-26.7
- 20.2-23.3
- 17.3-20.2
- 14.7-17.3
- 12.2-14.7
- 10.0-12.2
- 8.0-10.0
- 6.2- 8.0
- 4.7- 6.2
- 3.3- 4.7
- 2.2- 3.3
- 1.3- 2.2
- 0.7- 1.3
- 0.2- 0.7
- < 0.2



(b) Electron-like event.

Figure 3.18: Examples of single-lepton events at Super-K and their resulting Cherenkov rings. Triggered PMTs are displayed as coloured dots, with the colour indicating the signal strength. Reproduced from Ref. [108].

Chapter 4

Inputs to the Oscillation Analysis

The original analyses presented in this thesis are concerned with performing tests of the three-flavour oscillation model discussed in Section 2.2 and constraining the parameters that govern its behaviour. These analyses depend on a number of inputs, which enter into the analysis as illustrated by Fig. 4.1 and are listed as follows: The simulation of the J-PARC proton beam, its interaction with the target and the resulting neutrino flux are detailed in Section 4.1 followed by a description of the neutrino interaction cross-section model in Section 4.2. Observed data at ND280 are used to tune the flux and cross-section model parameters along with their uncertainties and correlations between them, as discussed in Section 4.3, which are propagated to the far detector fit. The criteria used to select event samples at Super-K are detailed in Section 4.4 and the simulation of detector effects in Super-K is described in Section 4.5.

The original analyses presented in this thesis use data collected and analysed at different times, with the $\bar{\nu}_e$ appearance analysis of Chapter 6 using T2K Run 1-9 data (see Section 3.1) and the analysis of Chapter 5 concerned with constraining the three-flavour neutrino oscillation parameters using the full T2K Run 1-10 data. After the T2K Run 9 analyses had been finalised, along with the collection of the T2K Run 10 data, the cross-section and flux models were updated and the near detector fit methodology was improved. As the analysis of Chapter 5 is considered to be the main result of this thesis, the current chapter will focus primarily upon the models and methodology used for said analysis, with the differences between the T2K Run 1-9 and Run 1-10 inputs discussed in Section 5.2.5.

4.1 Flux Prediction

In order to predict the unoscillated neutrino fluxes at the near and far detectors, the following simulation chain is used [84]: The propagation of the proton beam and its interactions with the graphite beam target (along with those of any daughter hadrons) is modelled by FLUKA v2011.2x.6 [109]. Kinematic information is passed from FLUKA to a bespoke GEANT3-based [110] MC simulation, JNUBEAM v13av7 [111], which simulates the propagation of particles exiting the target, travelling through the magnetic field produced by the horns, any subsequent further interactions and decays, the

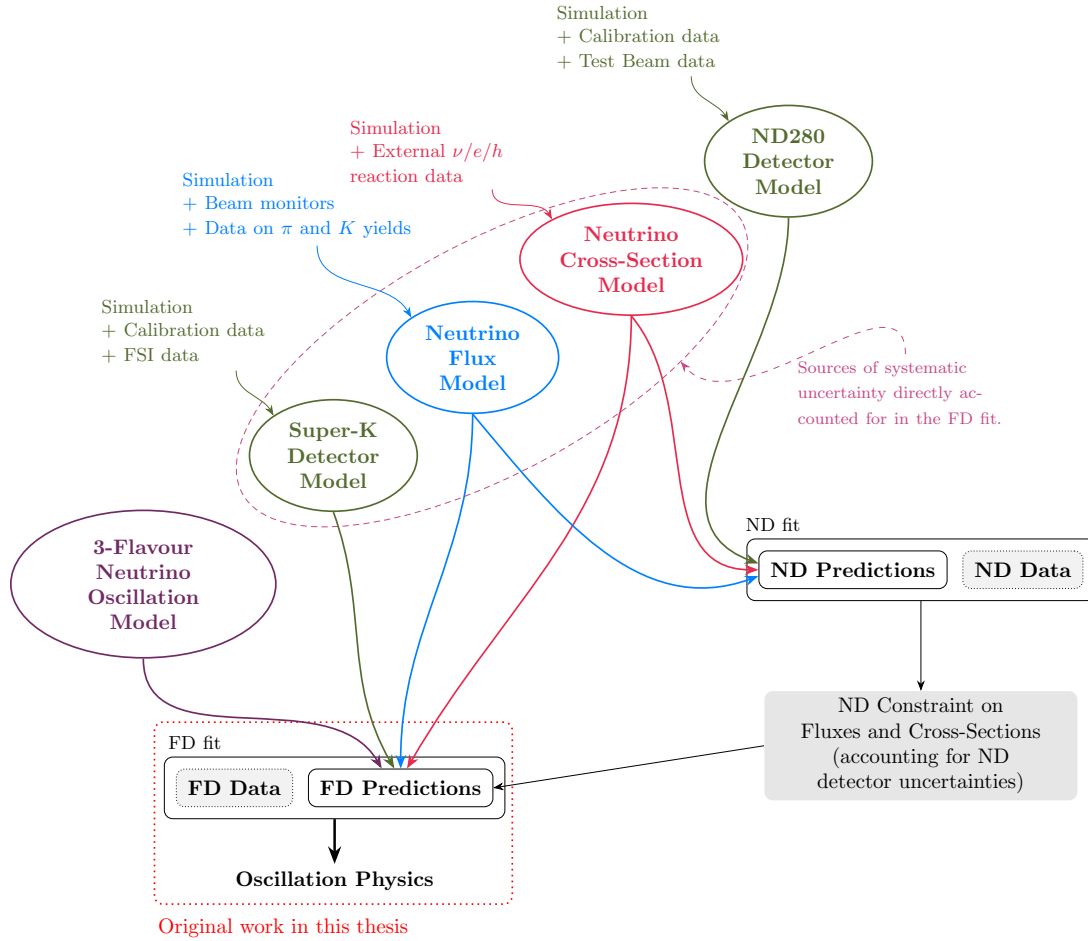


Figure 4.1: High-level overview of the oscillation analysis, showing the flux, cross-section, detector, and oscillation model inputs to the near and far detector fits and how the fits relate to each other. Flux and cross-section systematic uncertainties are constrained by the ND and correlated between the ND & FD. All systematic uncertainties are marginalised in the FD fit.

production of neutrinos, and their propagation to the near and far detectors to predict their energy spectrum. Any interactions that occur outside of the target are modelled by GCALOR 1.05/04 [112]. Finally, data from the NA61/SHINE experiment [113] are used to tune the hadron multiplicities of these simulations.

4.1.1 Tuning the Predicted Flux to External Hadron Multiplicity Measurements

As discussed in Section 3.1, the neutrinos that form the beam result mainly from the decay of hadrons produced in proton-graphite interactions. The production of these hadrons must be accurately modelled in order to accurately determine the composition of the beam and the neutrino flux spectra. The NA61/SHINE experiment [113–115] uses a 31 GeV/c proton beam incident on a graphite target to measure the result-

ing hadron multiplicities, which are used to tune the unoscillated flux predictions at T2K. Data was collected across two periods, one using a thin (0.04 interaction lengths) graphite target [115] and the other using a replica of the T2K target (1.9 interaction lengths) [114].

The NA61/SHINE detector uses a wide acceptance spectrometer consisting of a number of TPCs, some located within 1.1-1.5 T magnetic fields and with 5×10^{-3} $(\text{GeV}/c)^{-1}$ momentum resolution. The combination of TPC energy loss and time-of-flight mass measurements allow for charged particles to be identified and sorted into samples according to sign and hadron species. The data is binned in hadron momentum, angle, and for the replica target measurements, the position on the target along the beam direction from which the track emerged. A total of 0.5×10^6 (2.8×10^6) events were reconstructed for the thin (replica) target data collection periods [113–115].

NA61/SHINE measures both the interactions of primary hadrons within the target as well as subsequent re-interactions within the target (the latter for the replica target only), accounting for $\sim 90\%$ of the T2K neutrino flux at the peak energy [84]. This is further demonstrated by Fig. 4.2, which shows the phase space measured by the NA61/SHINE experiment covering almost all of the predicted phase space of hadrons produced in proton-graphite interactions that yield a neutrino at Super-K.

The predicted flux spectra are tuned by applying one of two different weights to each interaction. First, the ratio of observed (i.e. NA61/SHINE) to simulated (i.e. FLUKA) differential multiplicities is directly applied as a weight to each interaction. Due to the limited statistics of the replica target dataset, only pion multiplicities can be constrained in this way. Second, for all other particles and for out-of-target events, a weight is applied based on the probability for propagating hadrons to undergo additional interactions with various target nuclei, producing secondary hadrons. This second weight is applied using the ratio of the observed (by a variety of experiments, including NA61/SHINE thin and replica target data) and predicted cross-sections for each interaction, multiplied by the probability of the hadron escaping the target without undergoing further interactions [84].

The effect of these weights on the predicted unoscillated neutrino flux spectra at Super-K are shown in Fig. 4.3, and the general effect is to enhance (suppress) neutrino (antineutrino) event rates at most energies. The tuned Super-K predicted unoscillated fluxes are shown in Fig. 3.5. These effects, and corresponding flux spectra are also considered for ND280, but for brevity they are not shown here.

4.1.2 Uncertainties in the Flux Prediction

There are a number of systematic uncertainties in the nominal flux prediction, all of which are indirectly accounted for in the oscillation analysis and are detailed in Ref. [111], unless otherwise indicated. These uncertainties and their relative sizes are shown in Fig. 4.4 along with the combined uncertainty, and are briefly summarised as follows:

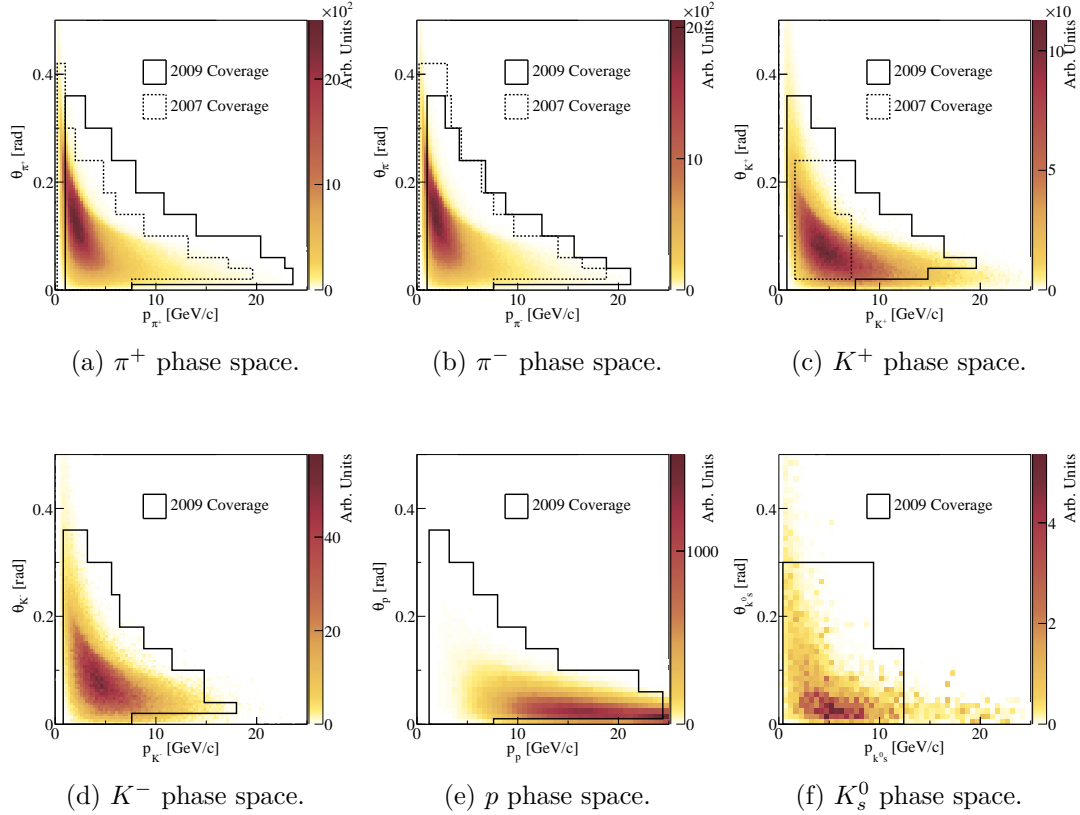


Figure 4.2: The predicted (coloured histograms) phase space of hadrons which decay to produce neutrinos, with the regions of phase space covered by NA61/SHINE (outlines). p denotes the momentum of the hadron, while θ denotes the angle of the outgoing hadron track with respect to the incident proton direction. The regions labelled as ‘2007 Coverage’ and ‘2009 Coverage’ correspond to the thin and replica target data, respectively. The phase spaces for positively charged hadrons correspond to measurements of the ν -mode beam, while those for negatively charged or neutral hadrons correspond to measurements of the $\bar{\nu}$ -mode beam. Reproduced from Ref. [116].

- **Hadron Interactions** - A variety of sources contribute to this uncertainty. First are the experimental uncertainties resulting from the hadron multiplicity measurements. Second are the uncertainties from extrapolating the multiplicity measurements to regions of phase space outside of those covered by NA61/SHINE, and to different target materials. Third are the uncertainties in the production cross-sections of primary pions and kaons, as well as from secondary nucleons produced inside the target.
- **Proton beam profile & off-axis angle** - A major source of uncertainty in the flux prediction arises from uncertainties in the proton beam centre vertical position and angle, changes to which effectively alter the off-axis angle of the neutrino beam and therefore can have a significant effect on the predicted flux spectrum at the far detector. The uncertainty on the off-axis angle is also directly measured by INGRID.
- **Horn current & field** - Uncertainties in the current of the magnetic focussing

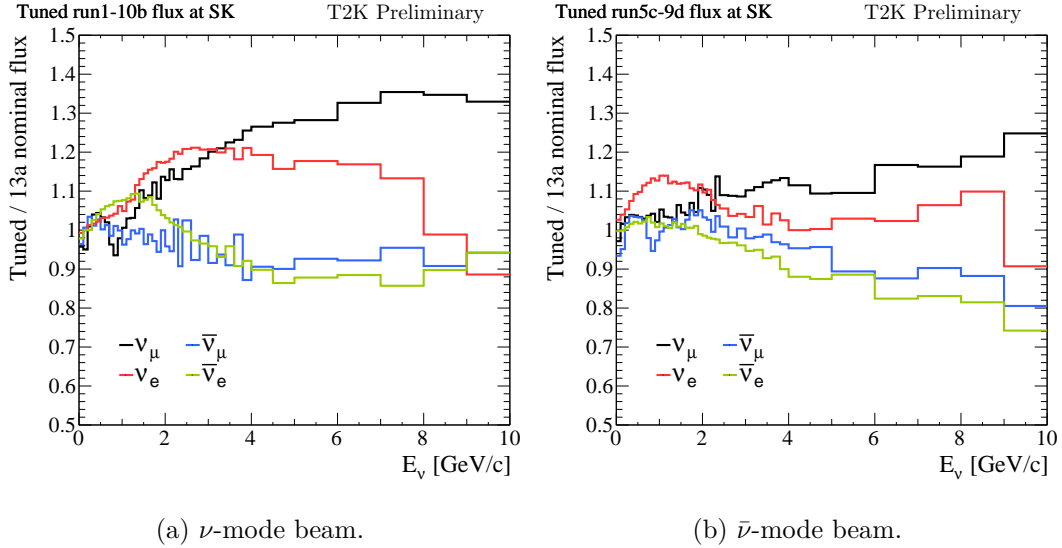


Figure 4.3: Ratio of the tuned to nominal unoscillated predicted neutrino fluxes at Super-K, broken down by neutrino flavour and shown for both beam modes. Reproduced from Ref. [84].

horns come from a variety of sources, such as the calibration of the coils and the electronics, along with the stability of the monitoring system. An additional uncertainty from an observed time-dependent anomaly in the on-axis magnetic field is also accounted for.

- **Horn & target alignment** - Uncertainties in the relative positional and rotational alignment of the target and each magnetic horn are accounted for.
- **Material modelling** - There are a number of materials that are not directly modelled in the JNUBEAM simulated geometry, such as the water coolant in the magnetic horns and the striplines carrying the current to the horns. As such, these materials do not affect the nominal flux prediction, so their effects are incorporated as an additional uncertainty [116].
- **Number of protons** - An uncertainty on the total number of protons incident on the target, affecting the overall normalisation of the flux, is introduced based on corresponding uncertainties in the calibration and analysis method of the current transformers that measure the proton beam current [116].

As Fig. 4.4 shows, the dominant contribution to the flux uncertainties across most neutrino energies is from the hadron interactions described above, except for ~ 1 GeV $\bar{\nu}_\mu$ where the proton beam profile and off-axis angle uncertainties are dominant. The overall uncertainty in the right-sign neutrino flux is at the $\sim 5\%$ level.

The above flux uncertainties are combined into an overall uncertainty in each of the true neutrino energy bins and for each beam mode and neutrino flavour, as listed in Tables A.1 and A.2. Each uncertainty is then implemented into the oscillation analysis

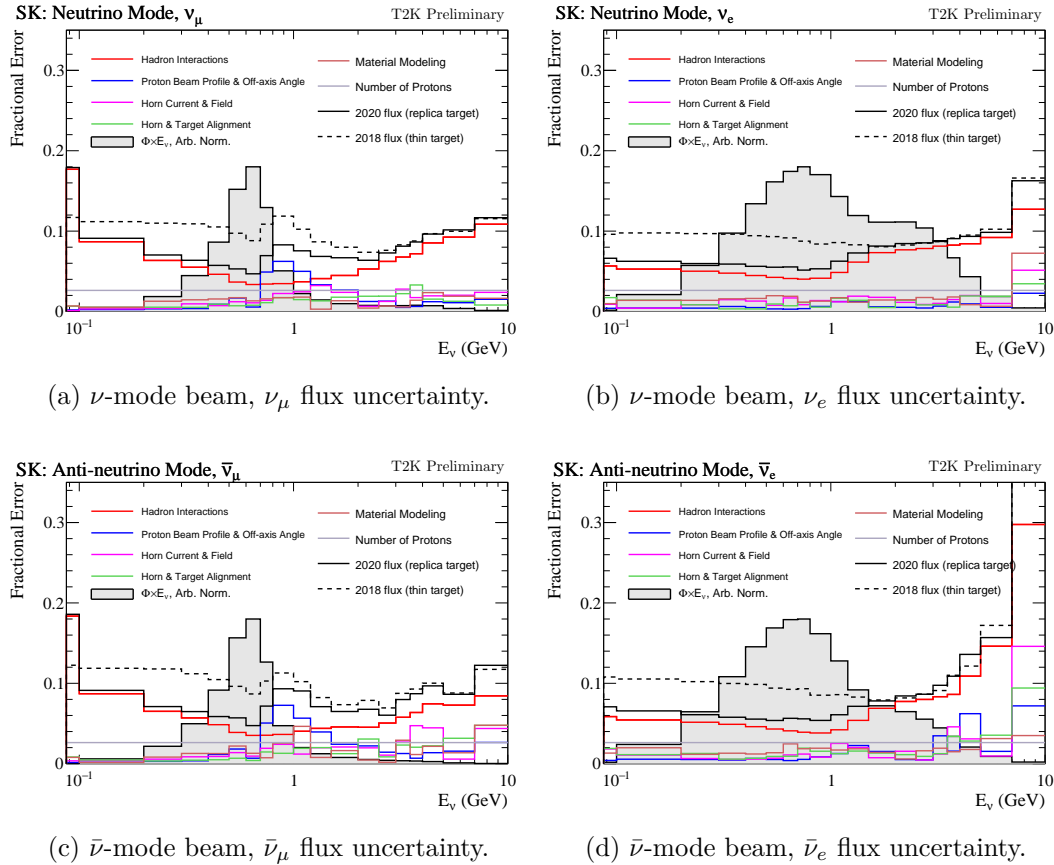


Figure 4.4: The total fractional uncertainty (black solid line), and contributing uncertainties (coloured solid lines) on the unoscillated flux predictions (shaded area), broken down by beam mode and neutrino flavour. Reproduced from Ref. [84].

as a normalisation parameter, with a nominal value and fractional error determined by the near detector fit of Section 4.3.

4.2 Neutrino Interaction Modelling

As neutrinos carry no electric charge, they must be detected indirectly through the products of neutrino interactions with matter inside the detector. Therefore the accurate modelling of these interactions is crucial in predicting the rates and kinematic distributions of neutrino events in both the near and far detectors. This modelling, for all detectors and interaction processes, is achieved using the NEUT Monte Carlo generator [117, 118] v5.4.0. As the cross-sections of Fig. 4.5 show, the predominant interaction processes occurring near the energy of the T2K flux peak are quasi-elastic-like (QE-like), with baryon resonances (RES) and deep inelastic scattering (DIS) processes increasingly contributing at higher energies. This section, summarised from [119, 120], will describe the nominal interaction model used at T2K (also referred to as the ‘cross-section model’), including how the initial state of the nucleus and each interaction process are modelled and how the associated uncertainties are incorporated into the oscillation analysis. These uncertainties are summarised in Tables A.3 and A.4 of Ap-

pendix A and their correlations are displayed in Fig. A.2.

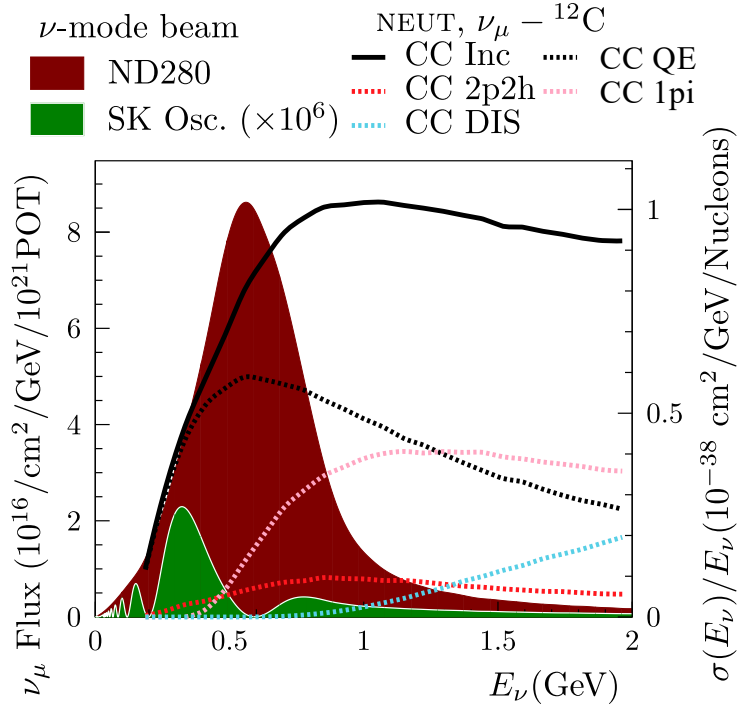


Figure 4.5: The predicted neutrino CC cross-sections per nucleon as a function of neutrino energy overlaid with the predicted fluxes at ND280 FDG1 and at Super-K (with oscillations applied according to the best-fit values of Ref. [121]). Predictions are generated by the NEUT MC generator and are shown both for the total, CC Inc, and broken down by interaction type. Adapted from Ref. [3].

4.2.1 Nuclear Model

In order to predict neutrino-nucleus interaction cross-sections, the initial state of the struck nucleus must be known, in particular the distributions of nucleon kinematics, the distributions of energy needed to remove them from the nucleus, and modifications to the outgoing particle kinematics from the nuclear potential. This initial state is simulated using two different models: The Benhar spectral function [122] for QE interactions and the relativistic Fermi gas (RFG) for all other interactions. The spectral function is a more sophisticated and realistic model of the nuclear ground state (being favoured over RFG in electron scattering data [123] and exclusive neutrino cross-section measurements [124–126]), but is derived under the assumption of two-body interactions and tuned to electron-scattering data, so is not necessarily valid for non-QE interactions.

The Benhar spectral function [122] characterises the initial state of the nucleus using a two-dimensional distribution of momentum and removal energy for the constituent nucleons while accounting for correlations between them and for the occupancy of each nuclear shell. An example of a spectral function, shown for ^{16}O , is displayed in Fig. 4.6. The single-nucleon contribution is extracted (with corrections applied for detector effects, FSI and radiative effects) from measurements of missing energy and

momentum observed in $(e, e' p)$ scattering on ^{12}C [127] and ^{16}O [128]. The contribution from correlated pairs of nucleons results from theoretical calculations in infinite nuclear matter (as finite nuclear size effects are small) [122], makes up approximately 20% of the strength of the spectral function, and is relevant only at large momentum and removal energy.

The RFG model characterises the initial nuclear state as a constant density sphere where the nucleon momenta follow a quadratic distribution up to a maximum, the Fermi momentum, determined by the number of nucleons and valid for infinite nuclear matter. Unlike the spectral function, for RFG the nucleon removal energy has a single value for each nucleon momentum, as shown in Fig. 4.6 [120].

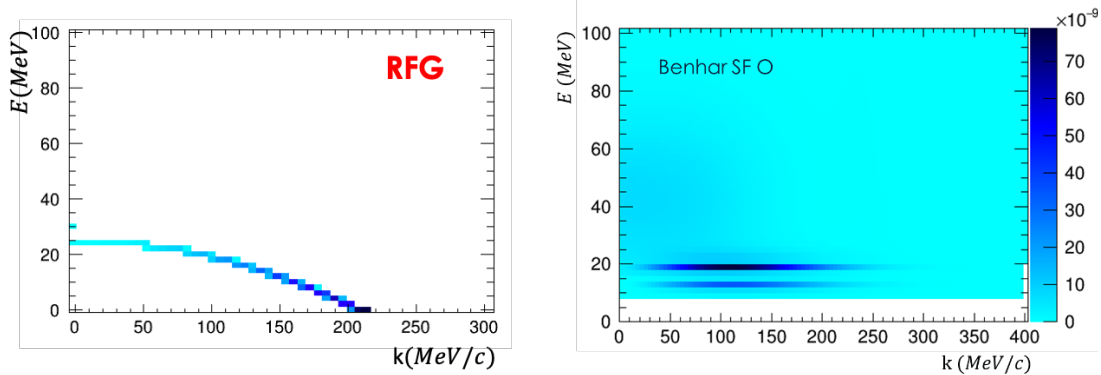


Figure 4.6: The relativistic Fermi gas model (left) and the Benhar spectral function (right) describing the nuclear ground state for ^{16}O as a function of initial nucleon momentum, k , and removal energy, E , as implemented in the NEUT MC generator. For the spectral function, the $1p_{1/2}$ and $1p_{3/2}$ nuclear shells are visible as sharply defined lines at approximately 12 and 18 MeV, respectively, while the $1s_{1/2}$ nuclear shell is significantly broader, spanning a wide range of removal energies. Reproduced from Ref. [119].

Both the spectral function and RFG models are based on the ‘plane wave impulse approximation’, where the incoming neutrino interacts with a single non-relativistic nucleon (or pair on nucleons in the case of 2p2h interactions) such that the neutrino-nucleus interaction cross-section factorises into the incoherent sum over all neutrino-nucleon interaction cross-sections.

Once the initial state of the nucleus has been simulated, the following effects are accounted for:

- The primary neutrino-nucleon interaction is simulated. The dominant types of interaction: CCQE, 2p2h, resonance and non-resonance pion production, and DIS are detailed in Sections 4.2.2 to 4.2.5.
- For CCQE interactions, the nucleon removal energy is subtracted from the available energy of final state. The effect of the removal energy and the treatment of its uncertainties is detailed in Section 4.2.7.
- Particles produced in the neutrino-nucleus interaction may themselves interact

with the nuclear remnant, potentially altering the set of observable particles and, if not properly accounted for, causing a bias in the reconstructed neutrino energy. The modelling of such interactions and their associated uncertainties are detailed in Section 4.2.6.

- The momentum of the outgoing negatively (positively) charged lepton is decreased (increased) due to the electrostatic Coulomb potential of the nuclear remnant. Electron and positron scattering measurements of the QE peak [129] gives the size of this effect and shows that, at the level of precision required by T2K, the momentum shift is effectively independent of the un-shifted lepton kinematics. Therefore this effect is implemented as a constant momentum shift of -4.3 (+3.3) MeV for negatively (positively) charged leptons.

The following sections describe these effects in detail.

4.2.2 Charged Current Quasi-Elastic (CCQE) Interactions

CCQE interactions are dominant around the T2K flux peak, as shown by Fig. 4.5, and give the majority of T2K’s sensitivity to the oscillation parameters. Such interactions involve a neutrino (antineutrino) of flavour l interacting with a neutron (proton) to produce a proton (neutron) and a negatively (positively) charged lepton of flavour l , as shown by Fig. 4.7.

The single-nucleon CCQE interaction cross-section is calculated using the Llewellyn Smith model [130] and depends on the neutrino energy, nucleon and lepton mass, and the four-momentum transfer to the nucleus, Q^2 . This Q^2 dependence is described by a number of form factors, one of which, F_A introduces a large uncertainty in the total cross-section [131], while the others are either well constrained by electron scattering experiments or have a comparatively small effect, with their uncertainties included within the overall ν_μ/ν_e cross-section uncertainty discussed in Section 4.2.8. The weak axial form factor, F_A , is modelled by a dipole of the form given by Eq. (4.1), where $F_A(0)$ is well-determined from beta decay experiments and the axial mass, M_A^{QE} , is constrained by neutrino scattering experiments [132] and its uncertainty is incorporated into the oscillation analyses. However, no uncertainty is assigned to M_A^{QE} for interactions on hydrogen nuclei (i.e. free protons), as no nuclear effects are expected and the measured uncertainties are negligible [120].

$$F_A(Q^2) = \frac{F_A(0)}{\left(1 + Q^2 / [M_A^{QE}]^2\right)^2} \quad (4.1)$$

For neutrino CCQE interactions, the energy of the interacting neutrino can be reconstructed by measuring the energy, E_l , momentum, p_l , and angle, θ_l , of the primary outgoing lepton using Eq. (4.2), assuming that the struck nucleon is initially at rest and where m_p , m_n , and m_l are the proton, neutron and lepton masses, respectively, and E_b is the nucleon removal energy. For antineutrino CCQE events, the same equation can

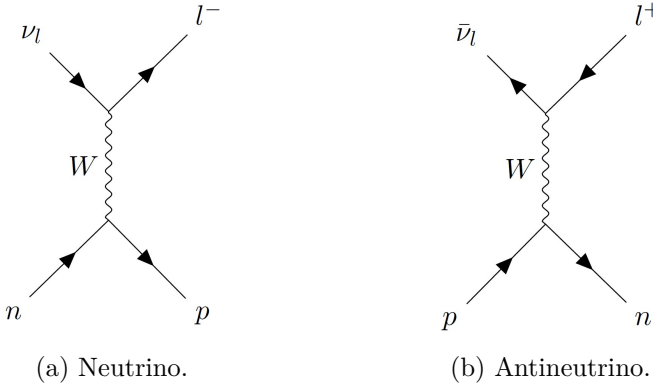


Figure 4.7: Feynman diagrams for CCQE interactions. Reproduced from Ref. [133].

be used with the neutron and proton masses exchanged, though the difference between the neutrino and antineutrino reconstructed energies is negligible at T2K.

$$E_{\text{rec}} = \frac{m_p^2 - (m_n - E_b)^2 - m_l^2 + 2(m_n - E_b)E_l}{2(m_n - E_b - E_l + p_l \cos \theta_l)} \quad (4.2)$$

While the spectral function model is generally successful when used in predicting neutrino interaction cross-sections, observations [134, 135] have shown that it fails to accurately predict the cross-section at low Q^2 , as illustrated by Fig. 4.8. As the spectral function model uses the impulse approximation, which is expected to break down at momentum transfers $\lesssim 400$ MeV/c, such failures are not unexpected [119, 136]. To account for these problems and to allow the spectral function prediction to be modified at low Q^2 , five ad hoc shape uncertainties have been implemented in the oscillation analysis, where each scales the CCQE cross-sections in a range of 0.05 GeV 2 for $Q^2 \in [0, 2.5]$ GeV 2 . These parameters are fit to a number of ND280 and MINERvA CC0 π datasets and result in a greatly improved goodness-of-fit between the data and spectral function predictions [119].

The dipole form of F_A assumed in NEUT has typically been used historically but is not necessarily well motivated [137–140] and causes an under-estimation of uncertainties in the $Q^2 \gtrsim 1$ GeV 2 region, where neutrino scattering data used to constrain the form factors is sparse. Alternative form factor parameterisations, such as three-component [120] or z-expansion [139] form factors, have been fit to neutrino scattering data and are being considered for future analyses. Until then, and in order to account for this shortcoming of the dipole form factor, additional freedom is given to the model with the inclusion of an additional three ad hoc shape uncertainties, each implemented into the oscillation analysis to scale the CCQE cross-sections in the following regions of Q^2 : [0.25, 0.5] GeV 2 , [0.5, 1.0] GeV 2 , and > 1.0 GeV 2 . The uncertainties are listed in Tables A.3 and A.4, along with a summary of all other interaction model related uncertainties.

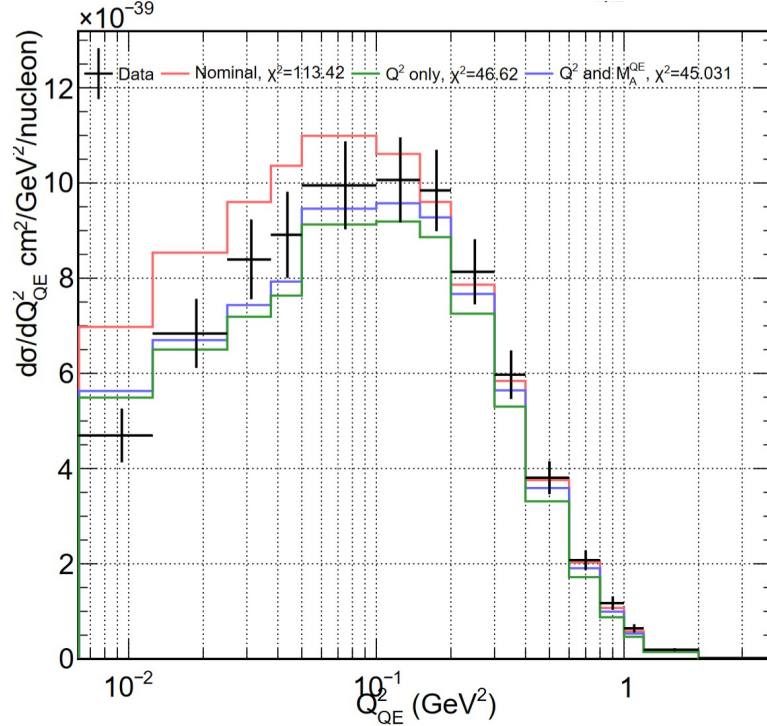


Figure 4.8: A comparison of three different spectral function model predictions to observations from the MINERvA experiment [134] as a function of four-momentum transfer, Q^2 . The red histogram corresponds to the nominal prediction, with M_A^{QE} fixed to 1.03 GeV and no Q^2 -dependent scaling applied. The green histogram corresponds to predictions after applying the Q^2 -dependent scaling parameters (fit to ND280 and MINERvA CC0 π datasets) and the blue histogram also includes the effect of fitting M_A^{QE} . Reproduced from Ref. [119].

4.2.3 Multi-nucleon (2p2h) Interactions

The two particle two hole (2p2h) process involves the interaction of the neutrino with two nucleons, possibly ejecting both nucleons. There are three contributing types of 2p2h interaction: Meson exchange currents (MEC), nucleon-nucleon correlations (NN), and interference between MEC and NN. These are all simulated in NEUT using the Nieves 2p2h model [141]. The NN (MEC) contribution occupies much of the same region of phase space as QE (RES) interactions, as shown by Fig. 4.9, as well as partially filling in the gap (in cross-section vs. true energy transfer) between QE and RES.

As the final state of 2p2h interactions (before FSI is considered) differs from CCQE interactions only by the number of nucleons in the final state and there is much overlap in their phase spaces, they are effectively indistinguishable from CCQE events in Super-K, so are often referred to as being ‘CCQE-like’. However, 2p2h events do not produce QE kinematics, so the formula used to reconstruct the neutrino energy, Eq. (4.2), may produce biased results for such events.

The 2p2h process is poorly constrained, with a number of valid models available (e.g. Nieves [141], Martini [142], and SuSAv2 [143, 144]) predicting 2p2h to contribute

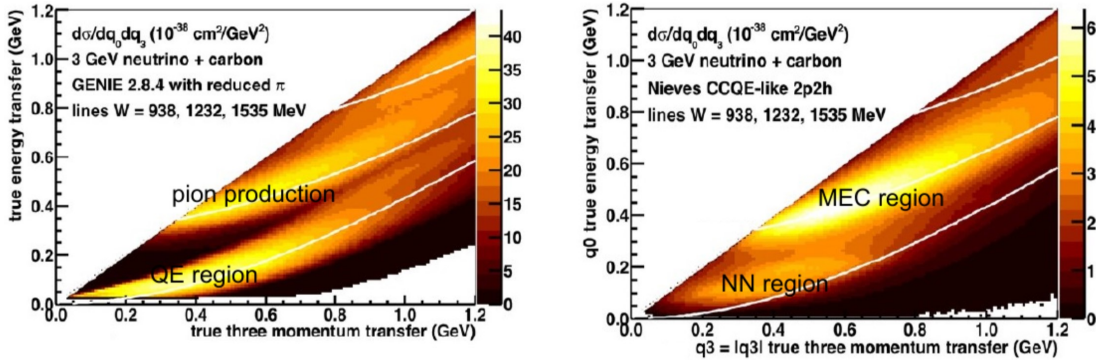


Figure 4.9: Cross-sections for 3 GeV neutrinos incident on ^{12}C . The left panel shows the total cross-section, with the QE and pion production dominated regions indicated. The right panel shows the 2p2h contribution to the total cross-section, with the NN and MEC dominated regions indicated. Note the different colour-axis scales between the two panels. Reproduced from Ref. [120].

between 10-20% of the total CCQE-like cross-section. The uncertain nature of this process necessitates a number of uncertainties to be implemented into the oscillation analysis:

- Two uncorrelated normalisation uncertainties for the total ν and $\bar{\nu}$ 2p2h cross-sections.
- A normalisation uncertainty for controlling the relative 2p2h cross-sections for ^{12}C and ^{16}O (100% correlated between ν and $\bar{\nu}$ interactions).
- An uncertainty in the shape of the 2p2h cross-section for ^{16}O , which accounts for the freedom within the Nieves model to change the (poorly constrained) relative contributions of MEC and NN interactions to the total 2p2h cross-section.
- Four uncorrelated, energy-dependent shape uncertainties covering the difference between the cross-section predictions of the Nieves, Martini, and SuSAv2 models. Two of the uncertainties are applied to ν interactions and the other two are applied to $\bar{\nu}$ interactions and are split to cover energies either side of 600 MeV. The near detectors have little sensitivity to difference between these models and therefore to these parameters, so they are not fit at the near detectors and are passed to the far detector fits with no constraint.

4.2.4 Single Pion Production

Interactions that produce a single pion in the final state aren't just a major background to samples selecting CCQE events, but they also constitute an important T2K signal sample (see Section 4.4). Pion production primarily occurs via resonance production of a $\Delta(1232)$ baryon, which subsequently decays to a pion and a nucleon, but can also be produced by other resonances, coherent interactions with the whole nucleus, or by multi-pion processes which, due to pion FSI, only appear to produce a single pion in the final state. Examples of these interactions are shown in Fig. 4.10.

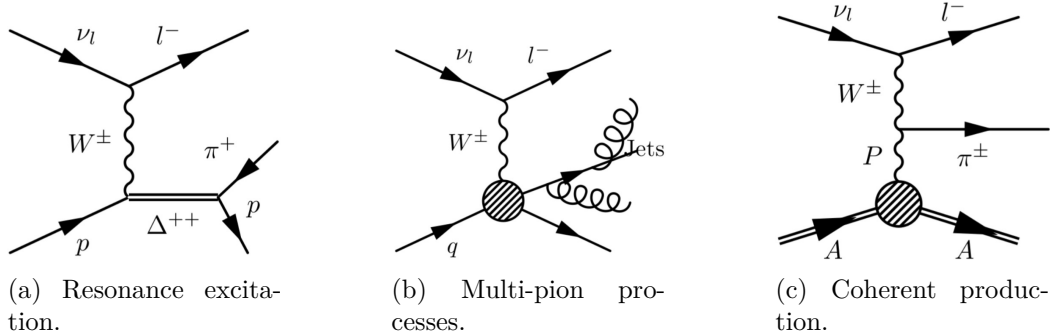


Figure 4.10: Feynman diagram examples for various processes that result in a single-pion being detected in the final state. Reproduced from Ref. [120].

In NEUT, single pion production is simulated according to the Rein-Sehgal model [145], which considers a number of resonances (and interference between them) up to a hadronic invariant mass of $W = 2$ GeV, above which pion-producing events are considered to be deep inelastic scattering events. Non-resonance contributions also exists and will be discussed below. The Rein-Sehgal model neglects the effects of lepton mass but corrections to account for it are added according to Refs. [146–148]. Additionally, the Rein-Sehgal form factors are modified according to fits to $\Delta(1232)$ electroproduction data [149, 150].

As will be discussed in Section 4.4, there exists an event sample at Super-K that selects for ν_e events associated with single π^+ production. The previously discussed formula for reconstructed energy, Eq. (4.2), applies only to CCQE events, so for the single pion sample Eq. (4.3) is used instead [151], where m_Δ is the mass associated with the Δ resonance. Notably, the nucleon removal energy is not considered in this equation (as will be discussed in Section 4.2.7) due to nuclear effects in pion production being poorly known, especially regarding the propagation of the Δ within the nuclear remnant [152].

$$E_{\text{rec}} = \frac{m_p E_l - \frac{1}{2}(m_\Delta^2 - m_l^2 - m_p^2)}{m_l - E_l + p_l \cos \theta_l} \quad (4.3)$$

Similarly to CCQE interactions, the Q^2 dependence of the cross-section for resonance pion production events is described by a number of form factors. Most of these are either well-constrained by electron scattering data or have negligible contributions, but as for CCQE, there remains an axial form factor term that is assumed to have a dipole form characterised by an uncertain axial mass, M_A^{RES} . However, unlike in the CCQE dipole form factor, the value of the form factor at $Q^2 = 0$, C_5^A , is not well constrained, so the uncertainties on M_A^{RES} and C_5^A are incorporated into the oscillation analysis.

A small background non-resonance contribution (where pions are produced without an intermediate resonance state) is also modelled for the dominant isospin-1/2 ($I_{1/2}$) interaction [153, 154], again according to the recommendations of Rein and Sehgal [145]. An uncertainty is incorporated into the oscillation analysis that allows the strength of this background to be scaled as a function of energy. Together with M_A^{RES} and C_5^A ,

these parameters are tuned to ANL, BNL [155], and MiniBooNE [156] neutrino-mode datasets [119]. Due to the lack of antineutrino-mode datasets to tune this background and a tendency for events with charged pions with momentum $\lesssim 200$ MeV/c to be misidentified as QE-like, a conservative 100% additional uncertainty is applied to these events to account for such effects. For future iterations of the analysis, an alternative pion production model [157] that accounts for interference between resonance and non-resonance amplitudes is under consideration.

In coherent pion production interactions, a neutrino scatters off a nucleus to produce a pion, transferring only a small amount of energy to the nucleus so as to not excite it. The NEUT simulation models such interactions using the Rein-Sehgal coherent model [158], but results from the MINERvA experiment show (see Fig. 4.11) that this model over-estimates both the neutrino and antineutrino coherent cross-sections [159]. The more recent Berger-Sehgal model [160] is in better agreement with the MINERvA data. Until this model can be properly implemented into NEUT, the predictions are re-weighted on an ad hoc basis using comparisons to the MINERvA data and conservatively, uncorrelated normalisation uncertainties are assigned to the CC and NC coherent cross-sections [119].

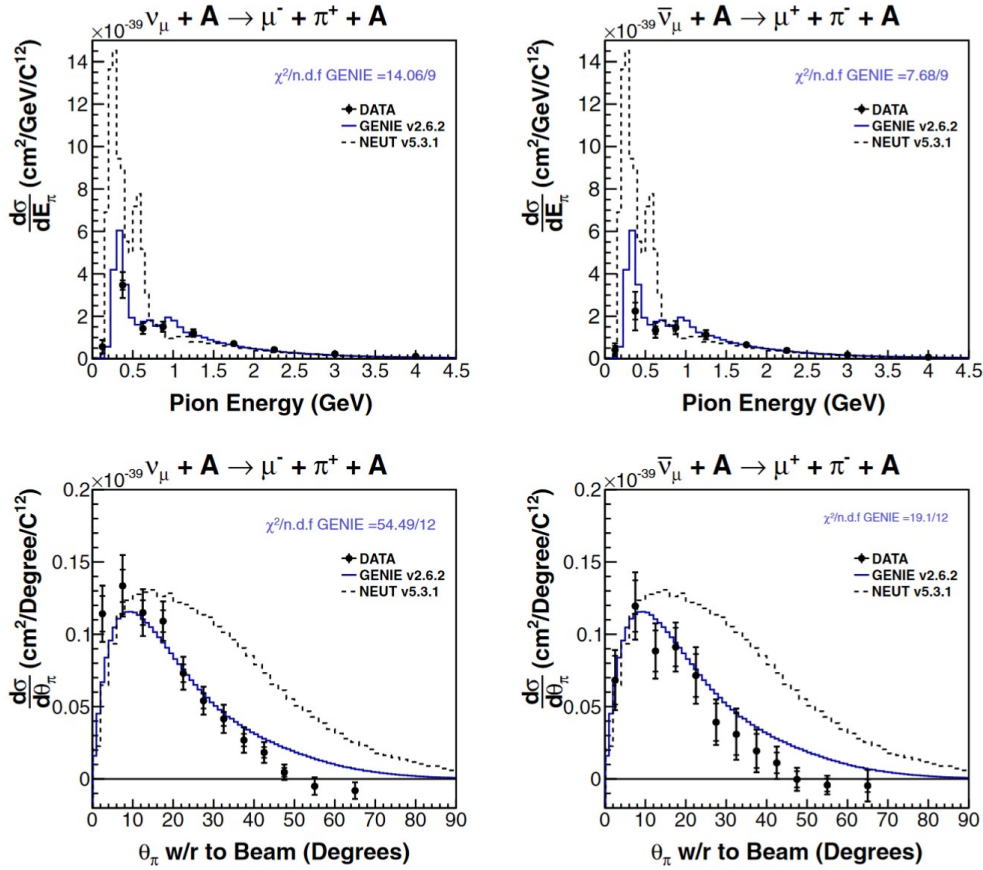


Figure 4.11: Coherent pion production differential cross-sections observed by the MINERvA experiment and compared to predictions from the NEUT and GENIE MC generators. Reproduced from Ref. [159].

Finally, NEUT includes contributions from diffractive pion production according

to the model of Rein [161]. This process is analogous to coherent pion production but, instead of interacting with a nucleus composed of many nucleons, the interaction takes place with a single nucleon, i.e. with hydrogen nuclei. The cross-section for the process is almost negligible, contributing << 0.1% of the total CC cross-section at 1 GeV [119]. However, this process is poorly constrained so is assigned a 100% normalisation uncertainty, which is folded into the collective ‘CC misc’ uncertainties discussed further in Section 4.2.8.

4.2.5 Deep Inelastic Scattering (DIS) and Multiple Pion (MPi) Production

At higher neutrino energies, a neutrino interacting with a nucleon may transfer enough energy to break apart the nucleon, producing a number of hadrons. This process is known as deep inelastic scattering and becomes dominant for neutrino energies around 5 GeV. As the T2K flux and oscillation probabilities at these energies are relatively low, these events do not correspond to being either direct signal or backgrounds in the Super-K selections and are therefore not considered in the same level as detail as the QE-like and single pion processes. Nevertheless, accurate characterisation of DIS effects on the final state kinematics is important for constraining flux and pion FSI uncertainties, which do have significant effects in the oscillation analyses.

In NEUT, the DIS interaction cross-sections are calculated according to the GRV98 parton distribution functions (PDFs) [162], which describe the probability to find a quark of a given type as a function of the nucleon momentum carried by the struck quark. A known problem with such PDFs is that the perturbative QCD techniques used to model them breaks down at low Q^2 [119], so corrections from Bodek and Yang [163] are applied to allow the PDFs to be used at the Q^2 values typically encountered at T2K. Depending on the hadronic invariant mass, W , associated with the interaction, one of two models are selected as follows:

- For $1.3 < W < 2$ GeV, a custom multi-pion model is used. First, the hadron and lepton kinematics are randomly sampled according to differential cross sections derived from the above PDFs. Then the pion multiplicity is randomised according to a multiplicity model tuned to neutrino scattering data [164]. To avoid double-counting with single pion events, only events producing at least two pions are permitted. A shape uncertainty is incorporated into the oscillation analysis to cover differences in the pion multiplicities between two valid multiplicity models: the NEUT default and the AGKY [165] models.
- For $W > 2$ GeV, DIS events are simulated using an external MC generator, PYTHIA v5.72 [166], which simulates the fragmentation of quarks and the resulting production of particles using a Lund string model.

For both multi-pion and DIS events, the difference between predictions generated with and without Bodek-Yang corrections applied are incorporated into the oscillation

analyses as conservative shape uncertainties, and separate neutrino and antineutrino normalisation uncertainties are assigned to the total multi-pion plus DIS cross-section based on differences between the NEUT prediction and the PDG world-average measurements [35].

4.2.6 Final State Interactions (FSI), Secondary Interactions (SI) and Photo-nuclear (PN) Interactions

Particles produced in the neutrino-nucleus interaction may themselves interact with the nuclear remnant, potentially altering the set of observable particles, and if not properly accounted for, causing a bias in the reconstructed neutrino energy. Such interactions are referred to as ‘final state interactions’ (FSI). Similarly, once particles have exited the nuclear remnant, they can undergo ‘secondary interactions’ (SI) in the detector material before detection. The treatment for hadrons and leptons differs as follows.

Hadron FSI and SI, are implemented directly in NEUT using a ‘cascade’ model where they are treated as classical particles undergoing a series of independent scattering interactions (each preserving energy and momentum) as they move though the nuclear remnant (starting from a randomly-determined position extracted from the Woods-Saxon potential distribution [167]) or the detector. The mean free path of such scattering events takes into account the effects of the nuclear medium or detector materials and is tuned to measurements of free particle-nucleon scattering. A significant source of uncertainty in the oscillation analysis comes from pion FSI, as, if a pion is produced but not detected due to FSI, then the reconstructed neutrino energy will be biased. As pions move through the nuclear remnant, the dominant interactions they undergo are elastic/inelastic pion scattering, pion absorption, and charge exchange, all illustrated in Fig. 4.12. In addition to potentially causing a reconstructed energy bias, charge exchange processes affect the rate of π^0 production, which is an important background in ν_e appearance searches. The cross-sections of each of these processes are constrained primarily by results from the DUET experiment [168], amongst others listed in Ref. [169], and associated shape uncertainties are implemented into the oscillation analysis to account for scaling the probability of each process occurring.

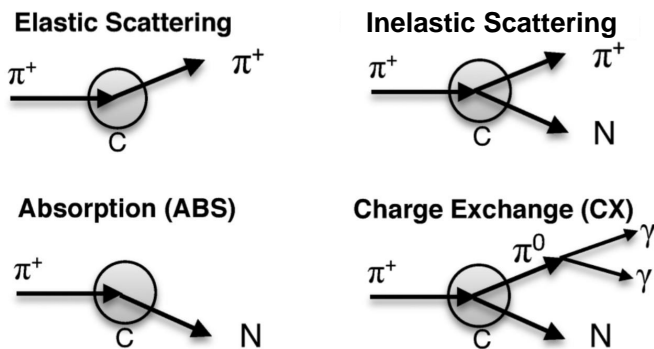


Figure 4.12: Illustration of the dominant types of π^+ FSI and SI with the nucleus, C. ‘N’ represents any number of nucleons leaving the nucleus. Adapted from Ref. [168].

Lepton FSI is not currently included in the NEUT MC, but its impact was studied using correction factors derived from an alternate neutrino event generator, NuWro [170], which modifies the prediction of the spectral function formalism according to the method of Ref. [123]. When detector smearing and acceptance effects are considered together with those of lepton FSI, the effects of lepton FSI are largely washed-out, resulting in an overall negligible effect [119]. Therefore in the NEUT MC, lepton FSI is not currently simulated and there is no detriment to the analysis.

For π^0 particles, there are additional considerations: The lifetime of these particles outside the nucleus is negligible so do not undergo secondary interactions [171]. Also, photons resulting from the decay $\pi^0 \rightarrow \gamma\gamma$ can be absorbed in the detector before they can be detected, a process known as the photo-nuclear (PN) effect. This reduces the efficiency of π^0 rejection when selecting the Super-K event samples, stopping all photons with energy < 150 MeV from being detected. Uncertainties in both SI and PN effects are neither fit at the near detector (due to a lack of sensitivity) nor handled directly in the oscillation analysis, but are accounted for, along with detector effects, when building the Super-K covariance matrix described in Section 4.5.

4.2.7 Treatment of the Nucleon Removal Energy

The treatment of the nucleon removal energy (also named the ‘binding energy’, E_b) is one of the major updates to the analysis of Chapter 5 compared to previous analyses. It is an important uncertainty and incorporating it into the oscillation analysis formed a significant part of the original work for the main analysis presented in this thesis, so in this section it will be described in detail.

In the previous iteration of the T2K analyses, the initial nuclear state was modelled for CCQE interactions by a relativistic Fermi gas, which as previously discussed, is a simpler and less realistic model than the spectral function. Under such a model, the nucleon removal energy has a fixed value for a given nucleon momentum and only a single uncertainty was assigned to the removal energy on all target nuclei and nucleons. Of all the uncertainties considered in the previous analysis, the removal energy gave the greatest contribution to the overall uncertainty in the Super-K predicted event rates [3]. The more realistic spectral function model gives a distribution of removal energies depending on the nuclear shell structure which necessitates a more sophisticated treatment of the removal energy and its uncertainties. This updated treatment results in the contribution of the removal energies to the overall uncertainty in the Super-K predicted event rates being reduced by a factor of 4 to 36, depending on the sample.

In addition to the improvements stated above, there is the potential for further improvements to the treatment of the nucleon removal energy in future analyses. For example, it is expected that interactions with different Q^2 could have different probabilities for sampling different nuclear shells and therefore that the removal energies should have Q^2 dependence [172, 173]. Such a treatment would not be permitted in the current spectral function and impulse approximation formalism as this breaks the as-

sumed factorisation between the nuclear structure and the neutrino-nucleon interaction as the initial nuclear state would no longer be characterised just in terms of nucleon momentum and removal energy distributions.

4.2.7.1 Effect on Reconstructed Neutrino Kinematics

While the nucleon removal energy only directly affects the hadron(s) produced in the interaction, there is an indirect effect on the kinematics of the outgoing lepton(s) and therefore on the observables at Super-K: The removal energy reduces the amount of available energy in the final state, so the interactions that are kinematically allowed to occur, on average, correspond to those with lower momentum in the outgoing lepton(s). For this reason, increasing (reducing) the removal energy compared to the nominal simulated values shifts the average lepton momentum to lower (higher) values. As the lepton momentum observed by Super-K is used to reconstruct the neutrino energy (see Eq. (4.2)), of which accurate knowledge is key to determining the neutrino oscillation parameters (see Section 2.2.4.1), an incorrect characterisation of the removal energy could lead to a bias in the measured oscillation parameter constraints. Studies previously performed by T2K have shown that measurements of Δm_{3j}^2 and $\sin^2 \theta_{23}$ are particularly sensitive to uncertainties in the removal energy [174]. The effect on the distribution of reconstructed neutrino energies after shifting the removal energies by 10 MeV from their nominal values is shown in Fig. 4.13 for a 600 MeV mono-energetic neutrino beam.

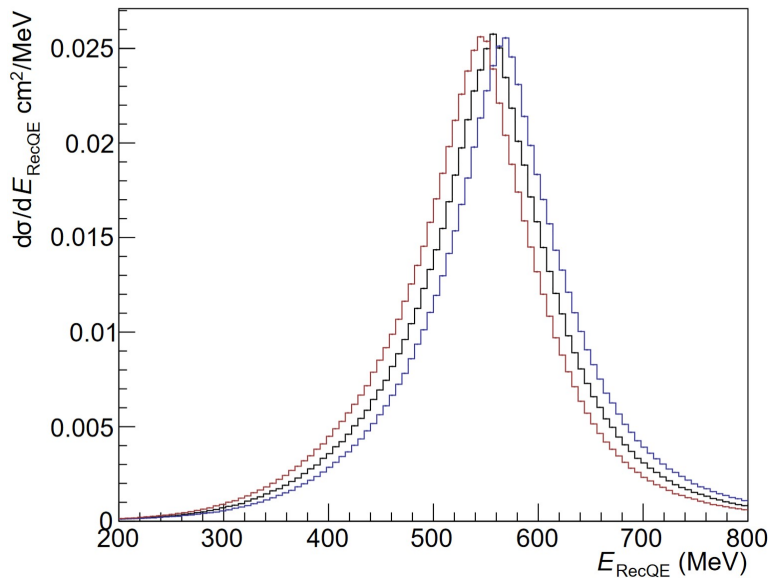


Figure 4.13: The differential cross-section for QE interactions as a function of reconstructed neutrino energy, as predicted by the NEUT MC generator for ν_μ with a true energy of 600 MeV. Predictions are shown for the nominal values of the nucleon removal energy (black), as well as for the values shifted by -10 MeV (blue) and +10 MeV (red). Reproduced from Ref. [119].

4.2.7.2 Sources and Treatment of Uncertainty

As the spectral function is different for different nuclei and for protons and neutrons, four correlated uncertainties are required to cover neutrino and antineutrino interactions on both C and O. As ND280 contains both C and O targets, all four parameters are constrained during the near detector fit (see Section 4.3), whereas Super-K contains no C target so only the uncertainties for O are directly considered in the oscillation analyses presented in this thesis. There are three components to these uncertainties which are combined to give the four overall uncertainties and correlations between them. The first two of which determine the correlations, while the third determines the size of the pre ND fit uncertainties. The three components are as follows [119]:

- As the spectral function is constrained by electron scattering experiments, which cover only interactions on initial state protons, they only constrain the removal energy for antineutrino CCQE interactions. The spectral function of initial state neutrons cannot be directly constrained in the same way, due to the difficulty of reliably detecting neutrons, but calculations [172, 175] indicate that the removal energy differs between protons and neutrons by 1-4 MeV depending on the nuclear shell and target. To account for this, a 2 MeV 100% anti-correlated uncertainty is assigned to the difference between the neutrino and antineutrino removal energies (leading to a total 4 MeV relative difference between the neutrino and antineutrino removal energies themselves).
- The different nuclear structure of C and O result in different spectral functions and therefore different distributions of the nucleon removal energy. As supported by measurements [172], a 1.5 MeV 100% anti-correlated uncertainty is assigned to the difference between the C and O removal energies (leading to a total 3 MeV relative difference between the C and O removal energies themselves).
- Measurements of the peak removal energy for various nuclear shells of both C and O have resolutions varying between 2 and 6 MeV [127, 128, 172], so the total uncertainties on the removal energies are conservatively required to be 6 MeV and are 100% correlated between all four removal energy uncertainties.

At present, uncertainties in the removal energies are only considered for CCQE interactions, as the effects of such shifts in the removal energy will have the greatest effect on CCQE events (due to being the lowest-energy common interaction at T2K) and the majority of T2K’s sensitivity to the oscillation parameters comes from these events. Work is ongoing within T2K to implement corresponding uncertainties for resonance pion production events.

4.2.7.3 Implementation into the Oscillation Analysis

Note: This section contains a mixture of original and non-original work. In particular, the implementation of the nucleon removal energy uncertainties into the oscillation

analysis from Item 4 of the below list onwards is original work.

As previously discussed, any change in the removal energies has the effect of shifting the average momentum of the primary outgoing lepton and therefore altering the reconstructed neutrino energy. The momentum of charged leptons is observable at Super-K (as opposed to hadron kinematics, which are not), so uncertainties in the removal energies are implemented into the oscillation analysis by simulating changes to the kinematic distributions of neutrino events due to alterations in the reconstructed neutrino energy for each event, as follows:

1. A number of pre-determined values corresponding to shifts in the nominal nucleon removal energies, ΔE_b , are selected, covering at least the $\pm 3\sigma$ postfit uncertainty range: $\Delta E_b \in [-10, -7.5, -5, -2.5, 0, 2.5, 5, 7.5, 10, 12.5, 15]$ MeV.
2. The simulated NEUT MC CCQE events are used to form a three-dimensional distribution of neutrino energy, lepton momentum, and lepton angle. One such distribution exists for each relevant neutrino flavour ($\nu_\mu, \bar{\nu}_\mu, \nu_e, \bar{\nu}_e$) and each considered value of ΔE_b .
3. The above distributions are profiled and subtracted from each other to obtain the average shift in lepton momentum as a function of neutrino energy and lepton angle due to a given value of ΔE_b .
4. For each simulated true CCQE event in each Super-K event sample (see Section 4.4) from the NEUT MC:
 - (a) The true neutrino energy and lepton angle associated with the event are used, as above, to obtain the average expected lepton momentum shift, Δp_l , corresponding to each considered value of ΔE_b .
 - (b) The lepton energy is recalculated using $E_l = \sqrt{(p_l + \Delta p_l)^2 + m_l^2}$ and the reconstructed neutrino energy is recalculated using Eq. (4.2) or Eq. (4.3) (with $p_l \rightarrow p_l + \Delta p_l$) for events reconstructed as belonging to the CCQE-like or CC1 π -like samples, respectively.
 - (c) The event enters into two binned kinematic distributions (which are functions of true and reconstructed neutrino energy and lepton angle, see Section 5.2.3) for each ΔE_b value: one recording the original kinematics ($N_{\text{events}}(b, \Delta E_b = 0)$) and the other recording the kinematics after shifting the nucleon removal energy ($N_{\text{events}}(b, \Delta E_b)$), where b denotes a kinematic bin.
5. Using the information stored in these kinematic distributions, it can be seen how, on average, events in each Super-K event sample migrate between kinematic bins as ΔE_b is varied for either neutrinos or antineutrinos. This use of averages is essential, as the oscillation analyses are binned and therefore do not have access to event-by-event information (see Section 5.1), so the above distributions must be

pre-computed for use in the oscillation analyses. Specifically, this is implemented as follows:

- (a) Weights for each kinematic bin and value of ΔE_b are calculated according to Eq. (4.4). The kinematic binning has been chosen to ensure that there are no bins containing 0 events so that events cannot be lost when applying these weights.
- (b) A series of cubic polynomials are defined in order to smoothly interpolate the weights between the above pre-determined values of ΔE_b in the range $[-10, 15]$ MeV.
- (c) The value of each ΔE_b and their corresponding uncertainties are directly incorporated into the analysis as systematic parameters. These are listed as $f_{Shape_{\Delta E_b O\nu}}^{\text{ND}}$ and $f_{Shape_{\Delta E_b O\bar{\nu}}}^{\text{ND}}$ in Table A.4 along with their best-fit values and pre/post ND fit uncertainties.
- (d) As will be described in Section 5.1, during the oscillation analyses a large number of predicted kinematic distributions are produced at randomly drawn values of ΔE_b (amongst other parameters). The number of events in every bin of each predicted kinematic distribution is multiplied by the above weight, $w(b, \Delta E_b)$. In this way, the predictions are modified according to the average effect of changing the nucleon removal energy.

$$w(b, \Delta E_b) = \frac{N_{\text{events}}(b, \Delta E_b)}{N_{\text{events}}(b, \Delta E_b = 0)} \quad (4.4)$$

Using the above method, the effect of variations in the nucleon removal energy can be accounted for when building predicted kinematic distributions in the oscillation analyses, as shown by Fig. 4.14. Therefore any potential biases in the oscillation parameter constraints that would have occurred with an insufficient characterisation of the removal energy are mitigated. Additionally, the amount by which the uncertainties in the removal energy contribute to uncertainties in the predicted Super-K event rates is greatly reduced. The implementation of the removal energy uncertainties has been extensively validated by ensuring consistent behaviour across all three T2K oscillation analysis fitters (see Section 5.1.3).

4.2.8 Additional Sources of Uncertainty in the Cross-Section Model

There are a number of additional uncertainties accounted for in the cross-section model which either do not fit into any of the above categories or are applicable to multiple categories together. These will be briefly discussed in this section.

The CCQE and CC1 π form factors have been tuned using bubble chamber neutrino scattering data (see Sections 4.2.2 and 4.2.4), but such data are sparse in the relevant energy range for antineutrinos [176], so it is possible that there could be differences

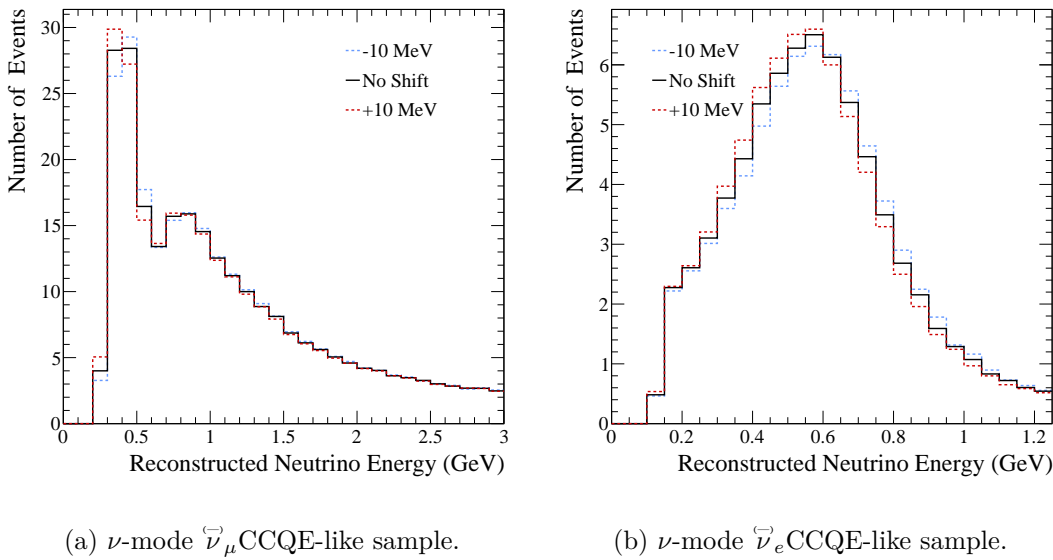


Figure 4.14: Changes to the predicted reconstructed neutrino energy distribution in different Super-K event samples (see Section 4.4) when the nucleon removal energies for neutrino events on ^{16}O are varied by 10 MeV from nominal. Predictions are generated according to the method of Section 5.1.1.1 using events from the NEUT MC generator across the full range of energies considered by T2K (as opposed to Fig. 4.13, which uses mono-energetic neutrinos) and with neutrino oscillations applied using realistic estimates of the oscillation and systematic parameters (specifically those labelled ‘Asimov A’ in Table 5.8 for the oscillation parameters and the pre ND fit systematic parameter values from Tables A.1 to A.6).

between the neutrino and antineutrino form factors. This is supported by measurements from the MINERvA experiment of $\text{CC}1\pi$ production, where predictions cannot be accommodated by both neutrino and antineutrino datasets [177]. Another source of neutrino-antineutrino differences is from the Coulomb correction to the outgoing lepton momentum (see Section 4.2.1) as this effect is of different magnitude and sign for neutrino and antineutrino events. Therefore to cover uncertainties in the relative neutrino and antineutrino cross sections resulting from both the form factors and the Coulomb correction, two 100% anti-correlated normalisation uncertainties are added to the oscillation analysis, one to scale the overall neutrino CC cross section and the other to scale that for antineutrinos.

There are a number of factors contributing to uncertainties in the relative ν_μ - ν_e and $\bar{\nu}_\mu$ - $\bar{\nu}_e$ cross-sections. First, radiative corrections to the tree-level CCQE process are considered. A full computation of such corrections are not yet available but have been calculated for the outgoing lepton leg of CCQE interactions in Ref. [178]. These corrections are not currently accounted for in NEUT and are of the order $\alpha_{EM} \ln(Q^2/m_t^2)$ (where α_{EM} is the fine structure constant) so are stronger for ν_e interactions than ν_μ . Additionally, uncertainties in the form factors combined with the alteration of kinematics due to the mass of the outgoing lepton leads to further uncertainty in the cross-sections [178]. Collectively, these effects are accounted for by two 50% anti-correlated normalisation uncertainties, one to scale the relative ν_μ to ν_e CC cross sections and the

other for antineutrinos. These parameters are not constrained in the near detector fit due to a lack of sensitivity.

The NC1 γ process represents a small, yet irreducible background to the search for ν_e and $\bar{\nu}_e$ in Super-K. As shown by the study of Ref. [179], the NEUT predicted cross-section for this process is approximately half of that calculated using the Alvarez-Ruso model [180]. In the absence of adequate external or ND280 data to constrain this process, the difference between these valid models is accounted for in the oscillation analysis by a 100% normalisation uncertainty [181].

A number of comparatively rare miscellaneous CC and NC processes are known to occur and while they are tracked in NEUT, they do not contribute in any significant way to either signal or direct background samples. Such processes include CC/NC1K, CC/NC1 η , CC1 γ and CC diffractive pion production. Uncertainties in these processes are poorly understood, so two conservative 100% normalisation uncertainties are assigned: one for the CC processes and the other for NC processes, where the latter is not constrained in the near detector fit due to a lack of sensitivity.

4.3 Near Detector Constraint on the Flux and Cross-Section Models

The flux and cross-section models rely on a number of uncertain parameters, as discussed in Sections 4.1 and 4.2. When these models are used to make predictions of the kinematic distributions at Super-K, these parameters can significantly alter the predictions and thus affect the oscillation parameter constraints inferred from them, therefore their accurate and precise determination is essential to the oscillation analyses. Although constraints from external sources have been discussed previously, the nominal values and uncertainties of these parameters can be further constrained, and their correlations assessed, through the use of data collected at the T2K near detector, ND280. In this section, summarised from Ref. [90], the ND280 event selections and fit methodology will be detailed. The result of the fit is recorded as a vector of flux and cross-section parameter best-fit values along with a covariance matrix holding their uncertainties and correlations, which are passed to the oscillation analysis. The ND280 detector parameters are accounted for in the near detector fit, but as they are not relevant to the far detector fit, their best-fit values and covariance matrix entries are not passed to the oscillation analysis.

Two independent near detector fitters are separately used to constrain the flux and cross-section parameters. One scans the parameter space using a gradient descent minimiser and frequentist statistics, while the other uses a Markov chain MC and Bayesian statistics. Both fitters act as cross-checks to each other and ensure that the resulting constraints are not overly sensitive to the choice between valid statistical methods. Validations were performed using fits to simulated data generated at assumed true parameter values and the results from both groups were found to be in excellent agreement, with less than 0.01% differences in the predicted event rates, responses to

parameter variations, and parameter sensitivities [90]. For the analyses presented in this thesis, results from the fitter using frequentist statistics are used.

4.3.1 Near Detector Samples

In order to fit the flux and cross-section parameters described above, the data collected at ND280 must first be sorted into appropriate samples. As discussed in Section 3.2, ND280 is a magnetised detector and can therefore distinguish positively and negatively charged leptons, allowing neutrinos and antineutrinos to be selected separately, but being located a short distance (280m) from the beam production target it measures the unoscillated $\bar{\nu}_\mu$ flux only. Each sample is binned in muon momentum across the full range relevant at T2K, $p_\mu \in [0, 30]$ GeV, and in the opening angle of the muon with respect to the nominal beam direction across the full angular range, $\cos \theta_\mu \in [-1, 1]$. The samples are selected for CC events only, based on pion multiplicity, but differing between beam modes as follows:

- ν -mode samples: ν_μ CC 0π , ν_μ CC $1\pi^+$, and ν_μ CC other
- $\bar{\nu}$ -mode samples: $\bar{\nu}_\mu$ CC 0π , $\bar{\nu}_\mu$ CC $1\pi^-$, $\bar{\nu}_\mu$ CC other, ν_μ CC 0π , ν_μ CC $1\pi^+$, and ν_μ CC other

The criteria for selecting events and categorising them into the above samples follows three broad steps, where the primary and any secondary particles are identified before the final categorisation into one of the samples described above. These steps are detailed as follows [182]:

1. First, a CC-inclusive sample is selected by identifying the primary μ^- or μ^+ and ensuring events are of sufficient quality:
 - (a) **Event quality** - As described in Section 3.1, the beam is produced in a series of ~ 5 μ s spills, each containing eight bunches. Events at ND280 are only selected if they occur within a bunch time window. Any events which occur in different bunches within the same spill are treated independently to avoid event pile-up.
 - (b) **Total multiplicity** - Events are only selected where at least one track can be reconstructed crossing a TPC.
 - (c) **Fiducial volume and track quality** - It is required that the track vertex is located within the fiducial volume of an FGD and that at least one track can be reconstructed within the FGD. Additionally, short tracks tend to be poorly reconstructed in the TPCs, so at least 18 TPC hit clusters are required.
 - (d) **Upstream background veto** - Tracks which originate in one sub-detector and undergo a large scatter after travelling to an FGD can be reconstructed as two tracks. In order to exclude such a possibility, any event where the

second highest momentum track starts at least 150 mm upstream of the primary track is rejected. Additionally, any event with the primary track vertex in FGD2 and a secondary track vertex in FGD1 is rejected.

- (e) **Broken tracks** - The reconstruction procedure may break a track into two components: one fully contained FGD-only track and a second track starting in the last layers of the FGD before passing into a TPC. In this case, the second track would be considered a muon candidate, while the first would not. If such an event is detected, it is important to ensure that the muon candidate track (i.e. the second track described above) travels far enough through the FGD, so it is rejected if the starting position is further away than 425 mm from the upstream edge of the FGD.
 - (f) **Muon identification** - The type of particle corresponding to primary track is identified by comparing the track curvature and measured energy deposition over distance in the TPC to simulations generated with true muons, electrons and protons. For the ν -mode selections, only negatively charged muons are accepted, while for the $\bar{\nu}$ -mode selections, both positively and negatively charged muons are accepted.
2. Next, secondary particles are identified by applying the following selection criteria to all tracks other than those corresponding to the muon candidate. Two possible selection ‘paths’ are available:
- The standard case, for particles created in a FGD having sufficient momentum and small enough angle to enter a TPC, is as follows:
 - (a) **Vertex position and timing** - Secondary track vertices are required to be in the same time bunch and located within the same FGD fiducial volume as the muon candidate.
 - (b) **Fiducial volume and track quality** - Same as Item 1c above.
 - (c) **Particle identification** - The measured energy deposition over distance is compared to simulations to determine whether the track corresponds to a pion, positron or proton in the case where the particle is positively charged, or a pion or electron if negatively charged. Neutral pions are indirectly identified by the presence of an electron and positron from their decay.
 - In the other case, for particles created in a FGD with insufficient momentum or too large an angle to enter a TPC, information recorded solely from an FGD can be used to identify charged pions:
 - (a) **Vertex position and timing** - Secondary vertices are required to be in the same time bunch and located within the same FGD fiducial volume as the muon candidate. If a track is reconstructed, it is required to be fully contained in the FGD.

- (b) **Particle identification** - The measured energy deposition over distance is compared to simulations to determine whether a track corresponds to a positively or negatively charged pion. If no FGD track is reconstructed, then pions can be identified by detecting the electron/-positron resulting from the Michel decay of the pion. Such electrons are identified by searching for an electron-like signal delayed $2.19 \mu\text{s}$ after the bunch time window, due to the decay time of the muon.
3. Finally, with both primary muon and any secondary particles identified, the event can be assigned to a sample:
 - (a) If no charged pions, electrons, or positrons are identified, then the event is assigned to the CC 0π sample corresponding to the relevant beam mode and muon charge.
 - (b) If only a single charged pion is reconstructed (either directly or via Michel decay), then the event is assigned to the CC 1π sample corresponding to the relevant beam mode and muon charge.
 - (c) If neither of the above criteria have been met, then the event is assigned to the CC other sample corresponding to the relevant beam mode and muon charge.

4.3.2 Near Detector Fit Methodology

The near detector fit minimises the binned negative log-likelihood, λ , of Eq. (4.5) [90, 183], simultaneously accounting for observations from all samples along with the effects of limited MC statistics and the prior constraints on the flux, \vec{f} , cross-section, \vec{x} , and ND280 detector, \vec{d} , systematic parameters.

$$\begin{aligned}
 -2 \ln \lambda = & 2 \sum_s^{\text{samples}} \sum_r^{\text{bins}} \left[N_{r,s}^{\text{obs}} \cdot \ln \left(\frac{N_{r,s}^{\text{obs}}}{N_{r,s}^{\text{exp}}} \right) + N_{r,s}^{\text{exp}} - N_{r,s}^{\text{obs}} \right] \\
 & + 2 \sum_s^{\text{samples}} \sum_r^{\text{bins}} \frac{(\beta_{r,s} - 1)^2}{2\sigma_{\beta_{r,s}}^2} \\
 & + \sum_{i,j}^{\text{flux pars.}} \Delta f_i \left(V_f^{-1} \right)_{i,j} \Delta f_j \\
 & + \sum_{i,j}^{\text{xsec pars.}} \Delta x_i \left(V_x^{-1} \right)_{i,j} \Delta x_j \\
 & + \sum_{i,j}^{\text{det. pars.}} \Delta d_i \left(V_d^{-1} \right)_{i,j} \Delta d_j
 \end{aligned} \tag{4.5}$$

The first term of Eq. (4.5) is from the usual Poisson likelihood, giving the likelihood of the data being a statistical fluctuation of the prediction, where s denotes an ND280 event sample, r denotes a bin in reconstructed $(p_\mu, \cos \theta_\mu)$ space, $N_{r,s}^{\text{obs}}$ is the number

of observed events in a particular bin and sample, and $N_{r,s}^{\text{exp}} \equiv N_{r,s}^{\text{exp}}(\vec{f}, \vec{x}, \vec{d})$ is the expected number of events in the same bin.

The second term of Eq. (4.5) is to account for the effects of limited MC statistics used to populate the expected $(p_\mu, \cos \theta_\mu)$ distributions. Following the method of Barlow and Beeston [184], this term gives the log-likelihood of the generated prediction being a statistical fluctuation of an infinite statistics simulation. This is done by introducing a scaling parameter for each bin, $\beta_{r,s}$, which would multiply the number of expected events generated at finite MC statistics to obtain that which would be generated using infinite MC statistics. As the MC statistics is 10-20 times the observed POT [90], the $\beta_{r,s}$ follow a Gaussian distribution [185] and the value of each can be solved analytically according to Eq. (4.6), where $\sigma_{\beta_{r,s}}$ is the relative statistical uncertainty of the prediction in a given bin [90].

$$\beta_{r,s}^2 + (N_{r,s}^{\text{exp}} \sigma_{\beta_{r,s}}^2 - 1)\beta_{r,s} - N_{r,s}^{\text{obs}} \sigma_{\beta_{r,s}}^2 = 0 \quad (4.6)$$

The remaining terms of Eq. (4.5) apply a penalty to the log-likelihood based on variations of the flux, Δf , cross-section, Δx , and detector, Δd , parameters away from their nominal values according to their prior constraints represented by the covariance matrices V_f , V_x , and V_d .

There exists a single normalisation parameter in each $(p_\mu, \cos \theta_\mu)$ bin to account for a number of ND280 detector uncertainties resulting from particle tracking and identification efficiencies in addition to those in charge and momentum measurements [186]. Such uncertainties can migrate events between bins or scale the predicted event rate. The detector uncertainties are randomly varied 2×10^3 times according to their prior covariances to give a distribution of the predicted event rate in each bin, the mean and covariance of which are assigned to the normalisation parameters in \vec{d} and V_d [90].

4.3.3 Results of the Near Detector Fit

Using data from T2K runs 2-9, the near detector fit obtains the following results [90]. The postfit flux and cross-section covariance matrix is shown in Fig. 4.15 and for readability, the flux and cross-section components are shown separately in Figs. A.1 and A.2. The best-fit values of these parameters along with pre/post-fit uncertainties are listed in Tables A.1 to A.4. In addition, the pre-fit and post-fit parameter values and their uncertainties are shown in Figs. 4.16 and 4.17. Good agreement is seen between the postfit simulated $(p_\mu, \cos \theta_\mu)$ distributions and the observed data at ND280, examples of which are shown in Fig. 4.18 projected to p_μ .

In order to fully assess the compatibility of the data with the postfit model, an ensemble of predictions are generated at randomly drawn flux, cross-section, and detector parameter values and are used to form a distribution of the resulting $-2 \ln \lambda$ values, which is compared to the value from the data fit. The fraction of predictions with greater $-2 \ln \lambda$ values than that of the data (i.e. less likely than the data) gives

the p -value, which is found to be 0.74, demonstrating excellent compatibility between the data and postfit model.

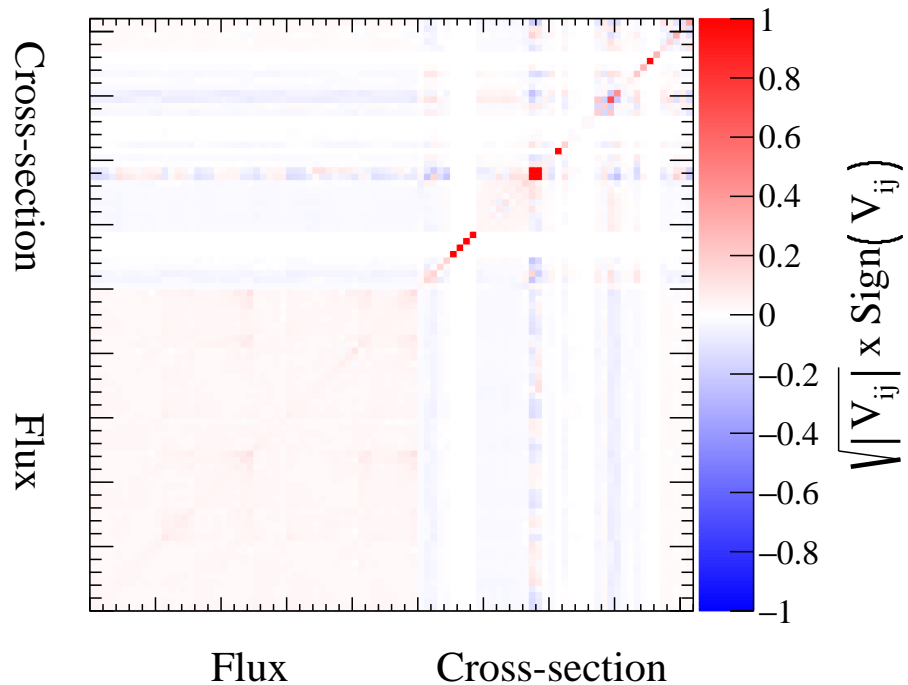


Figure 4.15: The flux and cross-section covariance matrix resulting from the near detector fit. The flux and cross-section parts are shown independently and in more detail in Figs. A.1 and A.2.

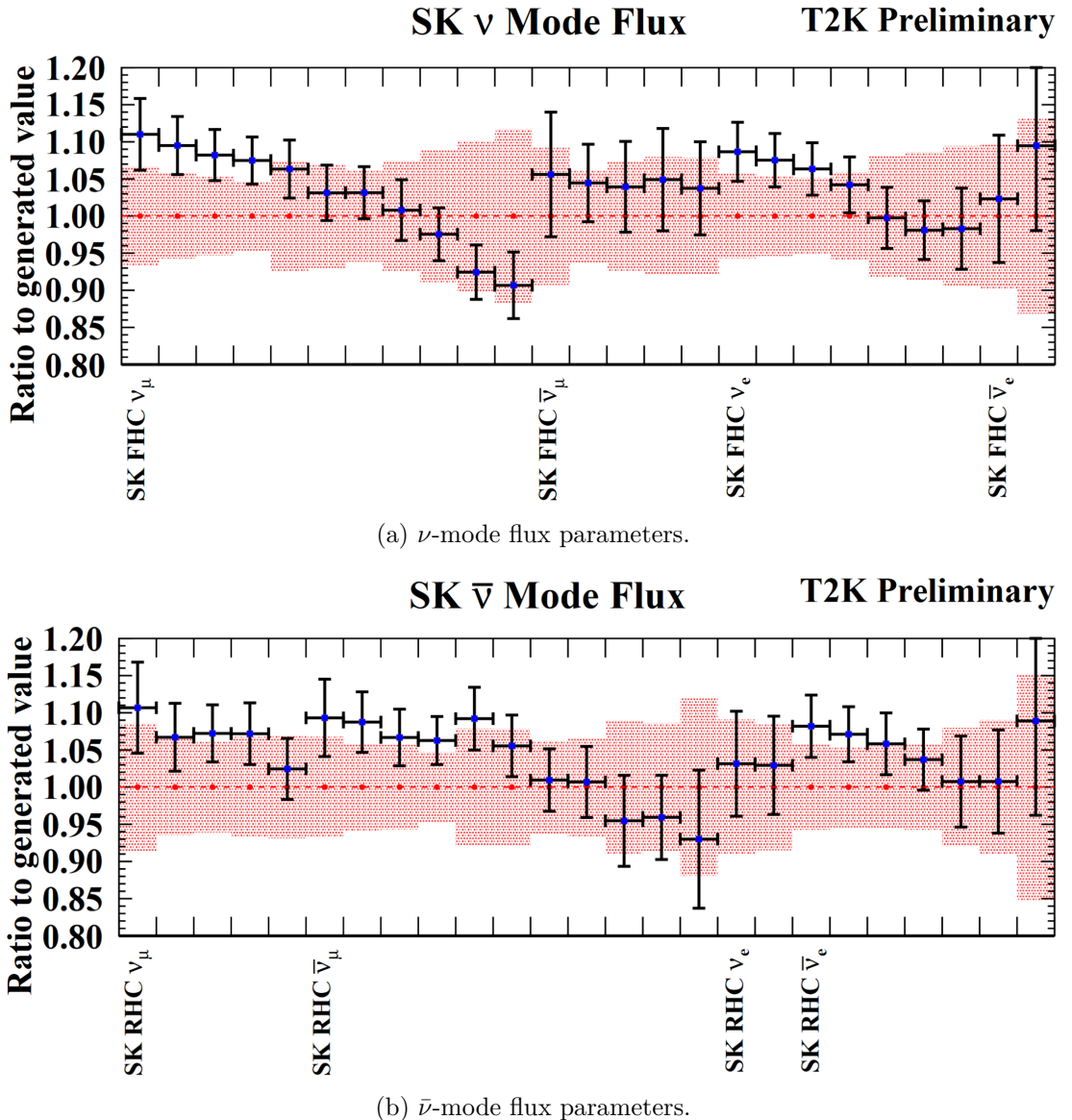


Figure 4.16: Flux parameter values before and after the near detector fit. Values are shown as a fraction of the parameter values used to generate the NEUT MC simulation. The pre-fit parameter values and uncertainties are shown as red points and shaded regions, respectively. The post-fit parameter values and uncertainties are shown as blue points and black error bars, respectively. Each bin corresponds to a single parameter, arranged in the same order as in Tables A.1 and A.2. Reproduced from Ref. [90].

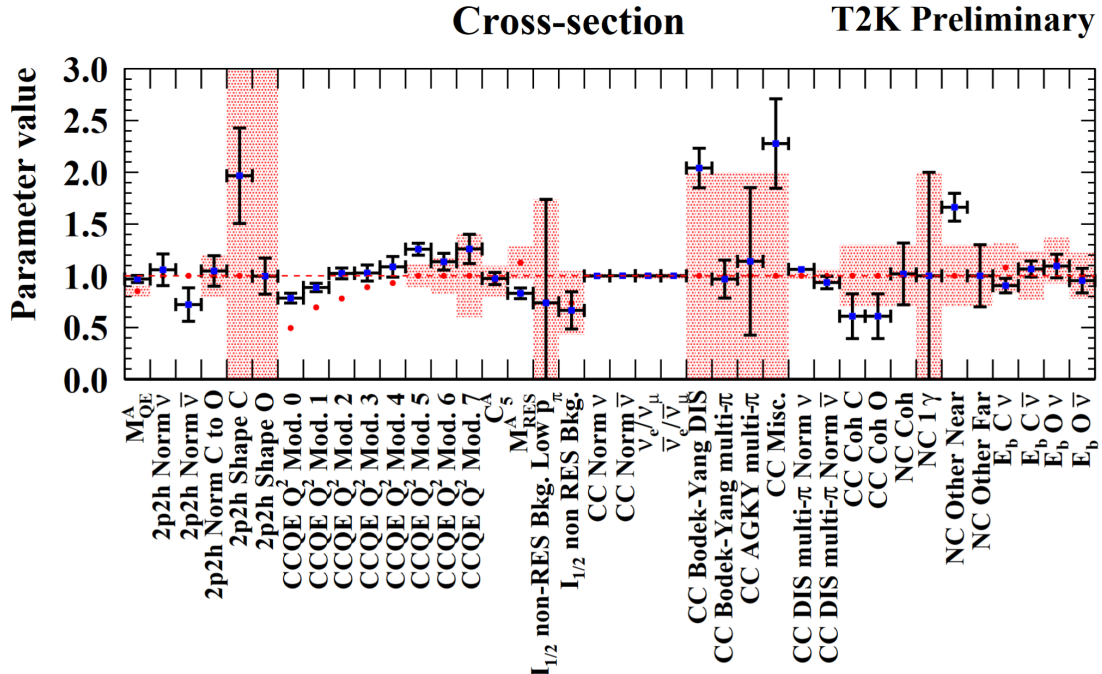


Figure 4.17: Interaction model parameter values before and after the near detector fit. Values are shown as a fraction of the parameter values used to generate the NEUT MC simulation. The pre-fit parameter values and uncertainties are shown as red points and shaded regions, respectively. The post-fit parameter values and uncertainties are shown as blue points and black error bars, respectively. Reproduced from Ref. [90].

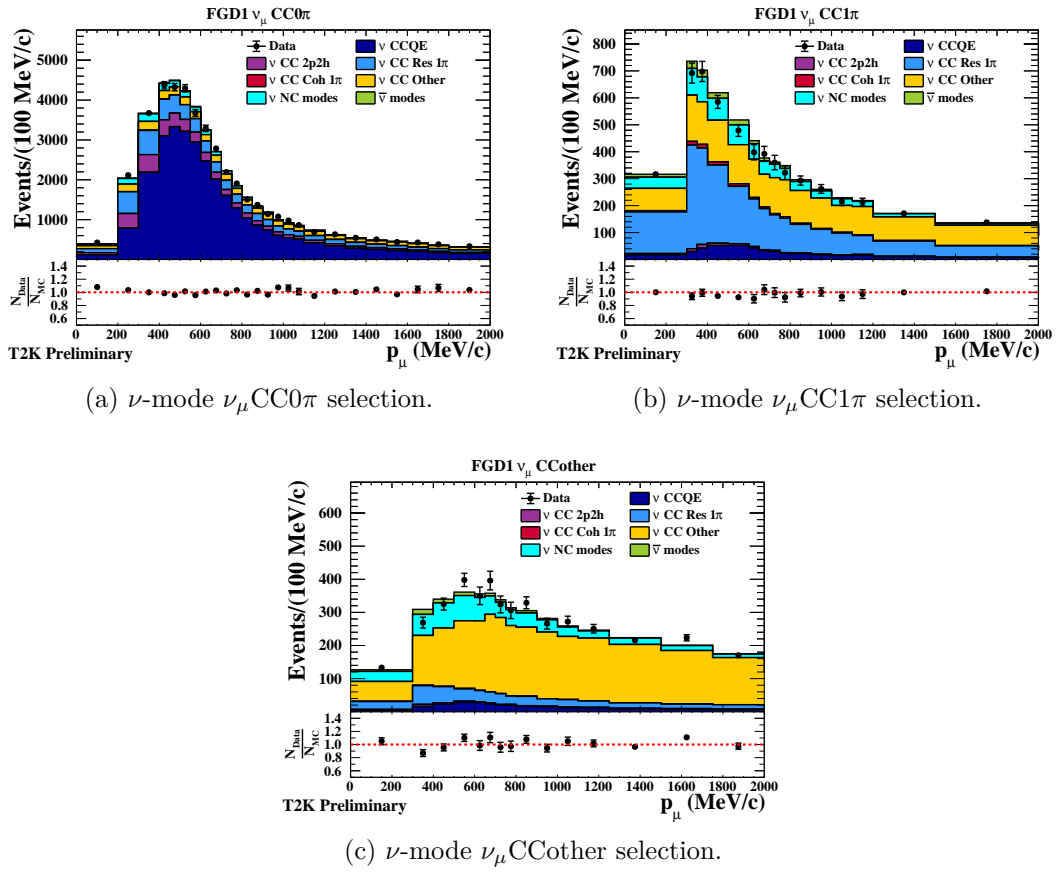


Figure 4.18: p_μ projections of observed (dots) and postfit MC distributions (coloured histogram stack) at FGD1 in ND280. Reproduced from Ref. [90].

4.4 Super-K Event Samples

A number of samples containing simulated or observed events at Super-K are analysed in order to constrain the neutrino oscillation parameters. All of these samples are intended to measure events originating from the neutrino beam, rather than from solar or atmospheric sources, and as such are optimised to select high-purity ν_μ and ν_e CCQE-like and CC1 π -like events (where ν_τ samples are neglected as the energy threshold for τ production is ~ 3.5 GeV so their effects are negligible at T2K energies [187]). Although work is in progress to implement other CC1 π -like samples into the T2K analyses, at present only a single CC1 π -like sample is included. As the Super-K detector is not magnetised, neutrinos and antineutrinos cannot be distinguished directly, so whether a sample is neutrino-like or antineutrino-like is determined by the beam mode. Therefore the samples used in the analyses presented in this thesis are as follows:

- ν -mode samples: ν_μ CCQE-like, ν_e CCQE-like, and ν_e CC1 π^+ -like.
- $\bar{\nu}$ -mode samples: $\bar{\nu}_\mu$ CCQE-like and $\bar{\nu}_e$ CCQE-like.

The following sections will outline the selection criteria used to build these samples, starting with those common to all samples in Section 4.4.1, before detailing the ν_μ CCQE-like, ν_e CCQE-like, and ν_e CC1 π^+ -like selection criteria in Sections 4.4.2 to 4.4.4. The sample-specific selection criteria are chosen separately for each sample to maximise sensitivity to θ_{23} and δ_{CP} in fits to atmospheric neutrino data [3] (the same fits discussed in Section 4.5.1). The selection criteria optimisation process is detailed in Ref. [188].

4.4.1 Common Selection Criteria

There are a number of selection criteria which are common to all considered samples:

1. **Good beam spill** - In order to consider analysing events originating from a particular beam spill, a number of beamline status parameters such as the beam direction and horn currents must be acceptable. Also, the PMTs are constantly registering hits due to background ‘dark noise’, so a minimum number of PMT hits are required to accept a beam spill. In addition, two sets of GPS data are used to ensure timing information is accurately coordinated between the Tokai and Kamioka sites, therefore spills coincident with failures in both GPS systems or with inconsistencies in their timings are rejected [108].
2. **Data quality** - Subruns (i.e. approximately minute-long data collection periods) are accepted or rejected based on the Super-K detector status, such data acquisition system failures, or external reasons such as blasting in the Kamioka mine. Additionally, data is not collected during brief special data blocks, to allow e.g. counters to be sent a reset signal [108].
3. **Timing** - Any events with activity up to $100 \mu\text{s}$ before the beam spill are rejected in order to prevent contamination from electrons resulting from the decay

of cosmic muons. Additionally, any events occurring over $2 \mu\text{s}$ before the leading edge of the beam spill, or over $10 \mu\text{s}$ afterwards are also rejected to avoid contamination [108].

4. **Containment** - In order to accurately measure event properties, they are required to be both fully contained by the inner detector and within its fiducial volume. Fully contained events are selected by ensuring minimal activity in the outer detector. The criteria for whether an event is within the fiducial volume differs depending on the sample and is tuned to simultaneously maximise sensitivity to θ_{23} and δ_{CP} while minimising systematic uncertainties. In all cases, the fiducial volume selection criteria depends on both the distance between the event vertex to its closest point on the detector wall (referred to as ‘*wall*’) and on the distance from the event vertex to the detector wall along the track direction (referred to as ‘*towall*’), ensuring that a sufficient number of PMTs are illuminated [3].
5. **Energy** - Any events with a reconstructed neutrino energy $> 30 \text{ GeV}$ are rejected, as they could not have been produced by neutrinos resulting from a 30 GeV proton beam.

4.4.2 $\bar{\nu}_\mu$ CCQE-like Selection Criteria

The criteria used to accept $\bar{\nu}_\mu$ CCQE-like events (in both ν and $\bar{\nu}$ modes) are outlined in the following list [105, 188], with the effects of notable selection criteria shown in Figs. 4.19 to 4.22 and the final reconstructed neutrino energy distribution of the selected events shown in Fig. 4.23. The number of simulated and observed candidate events passing each selection stage along with selection efficiencies and purities are shown in Tables 4.1 and 4.2.

1. Full containment within the Super-K inner detector and reconstructed inside the fiducial volume with $wall > 50 \text{ cm}$ and $towall > 250 \text{ cm}$.
2. A single Cherenkov ring is reconstructed. This removes events in the beam spill window with more than one charged particle above the Cherenkov threshold such as pions or other charged leptons. The proton produced in neutrino CCQE interactions almost never reaches the Cherenkov threshold, so this does not remove CCQE events. In addition, this does not remove events containing electrons produced from the Michel decay of muons, as, due to the muon lifetime, these are typically produced after the beam spill window.
3. The Cherenkov ring is identified as $\bar{\nu}_\mu$ -like over $\bar{\nu}_e$ -like, requiring $\ln(L_e/L_\mu) < 0.2p_e$, where L is the likelihood of the particle hypotheses denoted by the subscript, and p_e is the reconstructed electron momentum in the case of the $\bar{\nu}_e$ -like hypothesis. Although this comparison (and others like it in this chapter) compares quantities with different units, it is justified as working on a purely empirical basis, as seen in Fig. 4.21.

4. Reconstructed muon momentum, $p_\mu > 200$ MeV/c to reject charged pions and misidentified electrons from the decay of unobserved muons and pions [42].
5. Either zero or one electron(s) resulting from the Michel decay of muons are reconstructed. Such a decay electron indicates either the presence of a muon or a pion (through $\pi^\pm \rightarrow \mu^\pm$ decay), even if the parent particle was below the Cherenkov threshold.
6. The Cherenkov ring is identified as ν_μ -like over π^+ -like, requiring $\ln(L_{\pi^+}/L_\mu) < 0.15p_\mu$

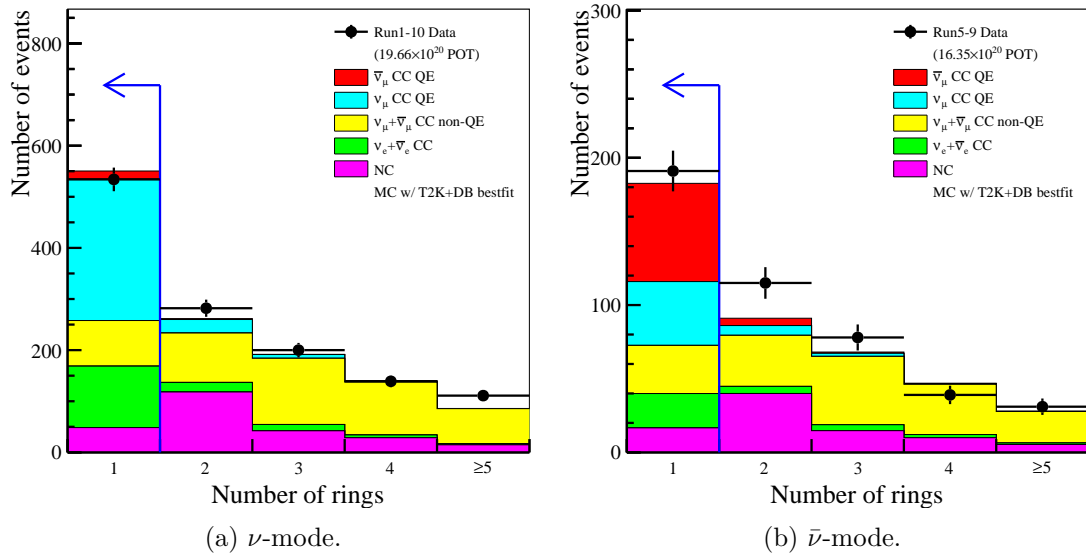


Figure 4.19: Distribution of the simulated (coloured histograms) and observed (black points) number of reconstructed Cherenkov rings in the $\bar{\nu}_\mu$ CCQE-like sample. The region of accepted events is indicated by the blue arrow. Reproduced from Ref. [105].

Selection Stage	$\nu_e + \bar{\nu}_e$	$\nu + \bar{\nu}$	$\nu_\mu + \bar{\nu}_\mu$	ν_μ	$\bar{\nu}_\mu$	MC total	Data
	CC	NC	CC non-QE	CCQE	CCQE		
Containment	159.2	252.2	487.2	312.5	18.2	1229.4	1266
No. of Cherenkov rings	120.2	48.5	89.2	276.5	16.0	550.4	534
μ vs. e discrimination	0.1	18.3	84.4	270.3	15.9	389.1	367
Momentum threshold	0.1	18.1	84.4	270.0	15.9	388.5	366
No. of Michel electrons	0.1	17.6	58.0	266.4	15.8	357.9	329
μ vs. π^+ discrimination	0.1	8.9	56.7	263.1	15.6	344.4	318
Efficiency (%)	0.1	3.5	11.6	84.2	85.5	28.0	-
Purity (%)	0.0	2.6	16.5	76.4	4.5	-	-

Table 4.1: The expected and observed number of ν -mode $\bar{\nu}_\mu$ CCQE-like candidate events passing each Super-K selection stage. Predictions are generated using the full T2K Runs 1-10 beam exposure, with normal mass ordering and oscillation parameters set close to previous T2K best fit values: $\Delta m_{21}^2 = 7.53 \times 10^{-5}$ eV $^2/c^4$, $\Delta m_{32}^2 = 2.54 \times 10^{-3}$ eV $^2/c^4$, $\sin^2 \theta_{12} = 0.304$, $\sin^2 \theta_{13} = 0.0219$, $\sin^2 \theta_{23} = 0.550$, and $\delta_{CP} = -1.728$. Adapted from Ref. [105].

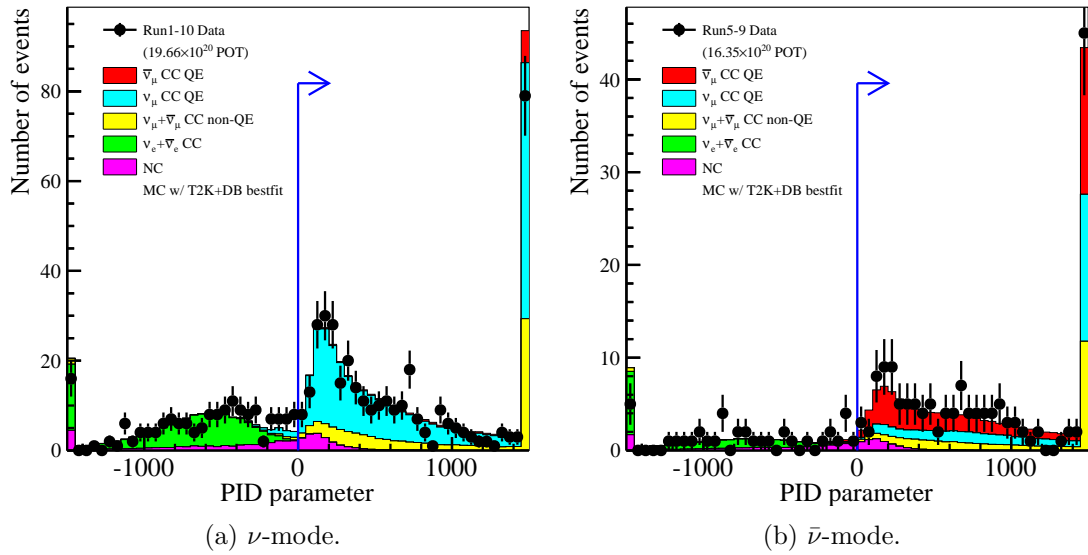


Figure 4.20: $\bar{\nu}_\mu/\bar{\nu}_e$ discrimination PID parameter distributions in the $\bar{\nu}_\mu$ CCQE-like sample. Both simulated (coloured histograms) and observed (black points) distributions are shown. This parameter is defined as the distance from the cut described in Item 3 of the above list. The region of accepted events is indicated by the blue arrow. Reproduced from Ref. [105].

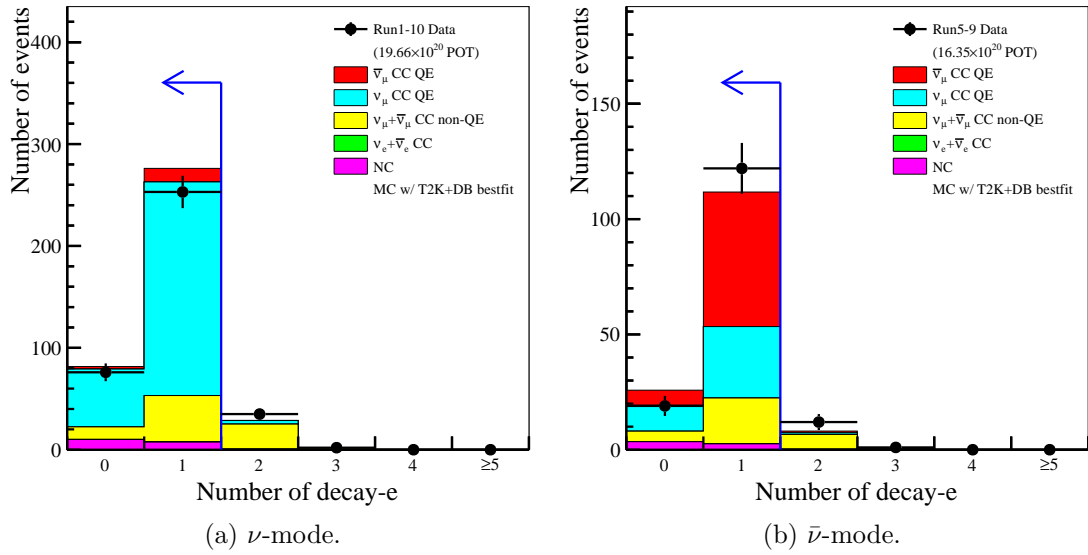


Figure 4.21: Distribution of the simulated (coloured histograms) and observed (black points) number of reconstructed decay electrons in the $\bar{\nu}_\mu$ CCQE-like sample. The region of accepted events is indicated by the blue arrow. Reproduced from Ref. [105].

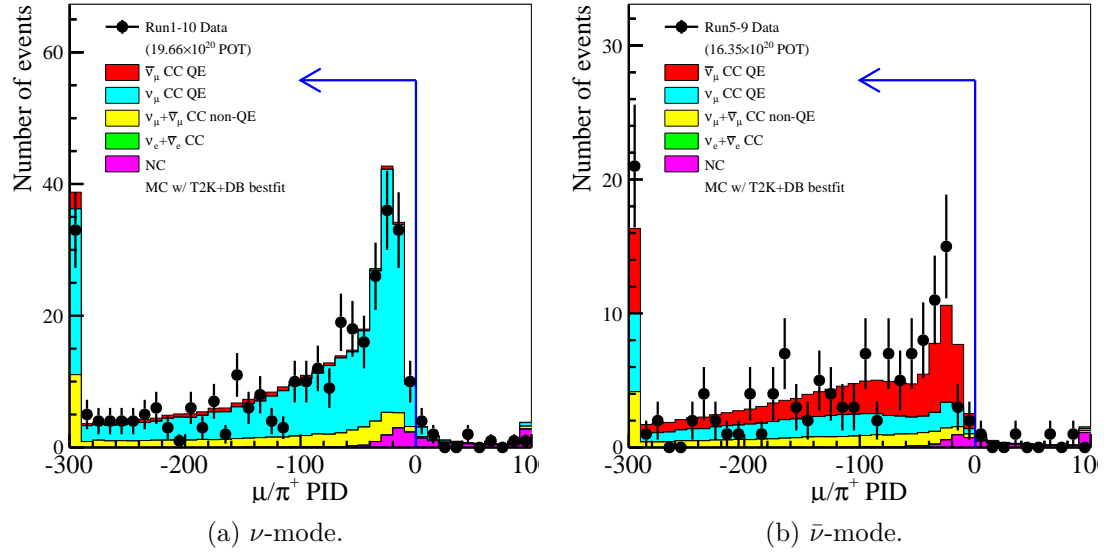


Figure 4.22: $\bar{\nu}_\mu/\pi^+$ discrimination PID parameter distributions in the $\bar{\nu}_\mu$ CCQE-like sample. Both simulated (coloured histograms) and observed (black points) distributions are shown. This parameter is defined as the distance from the cut described in Item 6 of the above list. The region of accepted events is indicated by the blue arrow. Reproduced from Ref. [105].

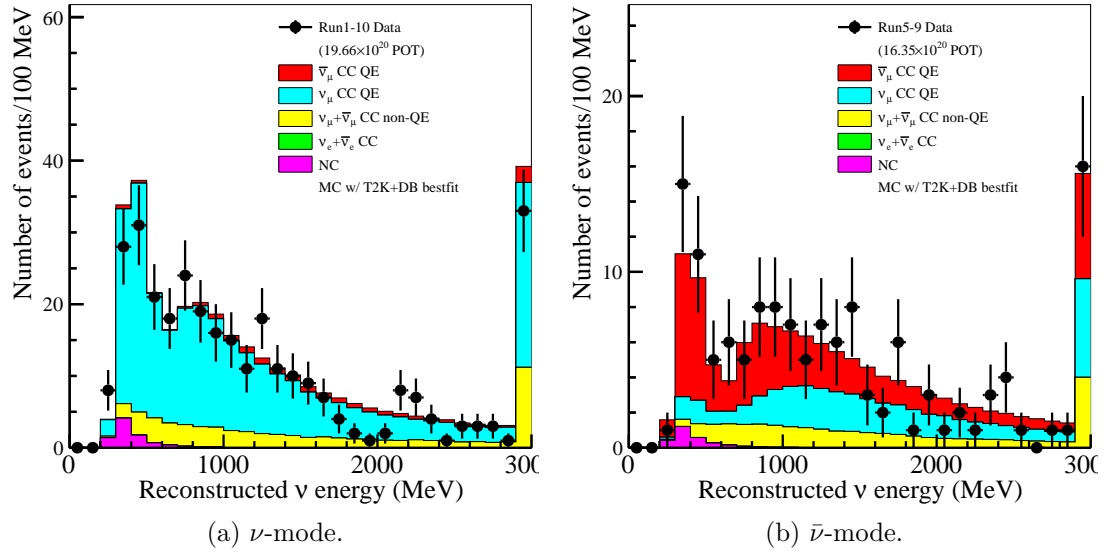


Figure 4.23: Distribution of the simulated (coloured histograms) and observed (black points) reconstructed neutrino energy in the $\bar{\nu}_\mu$ CCQE-like sample, shown after all selection criteria have been applied. Reproduced from Ref. [105].

Selection Stage	$\nu_e + \bar{\nu}_e$		$\nu + \bar{\nu}$		$\nu_\mu + \bar{\nu}_\mu$		MC total	Data
	CC	NC	CC	non-QE	ν_μ	$\bar{\nu}_\mu$		
Containment	35.3	86.6		169.3	52.7	72.7	416.6	454
No. of Cherenkov rings	23.3	16.6		32.7	43.3	66.7	182.6	191
μ vs. e discrimination	0.0	6.3		31.4	42.9	65.8	146.3	154
Momentum threshold	0.0	6.2		31.4	42.9	65.7	146.2	154
No. of Michel electrons	0.0	6.0		24.4	42.2	64.9	137.6	141
μ vs. π^+ discrimination	0.0	2.8		24.0	41.7	64.3	132.8	137
Efficiency (%)	0.0	3.3		14.2	79.1	88.4	31.9	-
Purity (%)	0.0	2.1		18.1	31.4	48.4	-	-

Table 4.2: The expected and observed number of $\bar{\nu}$ -mode $\bar{\nu}_\mu$ CCQE-like candidate events passing each Super-K selection stage. Predictions are generated using the full T2K Runs 1-10 beam exposure, with normal mass ordering and oscillation parameters set close to previous T2K best fit values: $\Delta m_{21}^2 = 7.53 \times 10^{-5} \text{ eV}^2/\text{c}^4$, $\Delta m_{32}^2 = 2.54 \times 10^{-3} \text{ eV}^2/\text{c}^4$, $\sin^2 \theta_{12} = 0.304$, $\sin^2 \theta_{13} = 0.0219$, $\sin^2 \theta_{23} = 0.550$, and $\delta_{CP} = -1.728$. Adapted from Ref. [105].

4.4.3 ν_e CCQE-like Selection Criteria

The criteria used to accept ν_e CCQE-like events (in both ν and $\bar{\nu}$ modes) are outlined in the following list [105, 188], with the effects of notable selection criteria shown in Figs. 4.24 to 4.29 and the final reconstructed neutrino energy distribution of the selected events shown in Fig. 4.30. The number of simulated and observed candidate events passing each selection stage along with selection efficiencies and purities are shown in Tables 4.3 and 4.4.

1. Full containment within the Super-K inner detector and reconstructed inside the fiducial volume with $wall > 80$ cm and $towall > 170$ cm.
2. A single Cherenkov ring is reconstructed. This removes events in the beam spill window with more than one charged particle above the Cherenkov threshold such as pions or other charged leptons. The proton produced in neutrino CCQE interactions almost never reaches the Cherenkov threshold, so this does not remove CCQE events. In addition, this does not remove events containing electrons produced from the Michel decay of muons, as, due to the muon lifetime, these are typically produced after the beam spill window.
3. The Cherenkov ring is identified as ν_e -like over ν_μ -like, requiring $\ln(L_e/L_\mu) > 0.2p_e$, where L is the likelihood of the particle hypotheses denoted by the subscript, and p_e is the reconstructed electron momentum in the case of the ν_e -like hypothesis.
4. Visible energy > 100 MeV to reject contamination from below-threshold muon decays [3].
5. No electrons resulting from the Michel decay of muons are reconstructed. Such a decay electron indicates either the presence of a muon or a pion (through $\pi^\pm \rightarrow \mu^\pm$ decay), even if the parent particle was below the Cherenkov threshold.
6. Reconstructed neutrino energy < 1250 MeV, as the expected number of oscillated ν_e events is negligible at greater energies and the background beam ν_e and NC contributions dominate, as shown in Fig. 4.28.
7. The Cherenkov ring is identified as ν_e -like over π^0 -like, requiring $\ln(L_{\pi^0}/L_e) < 175 - 0.875m_{\pi^0}$, where m_{π^0} is the reconstructed π^0 mass in units of MeV/c².

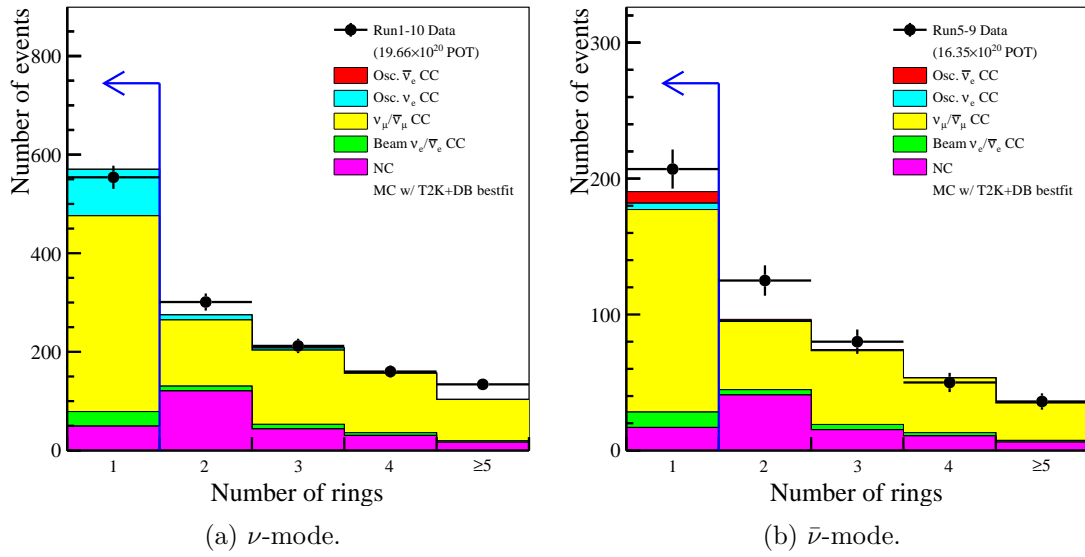


Figure 4.24: Distribution of the simulated (coloured histograms) and observed (black points) number of reconstructed Cherenkov rings in the $\bar{\nu}_e$ CCQE-like sample. The region of accepted events is indicated by the blue arrow. Reproduced from Ref. [105].

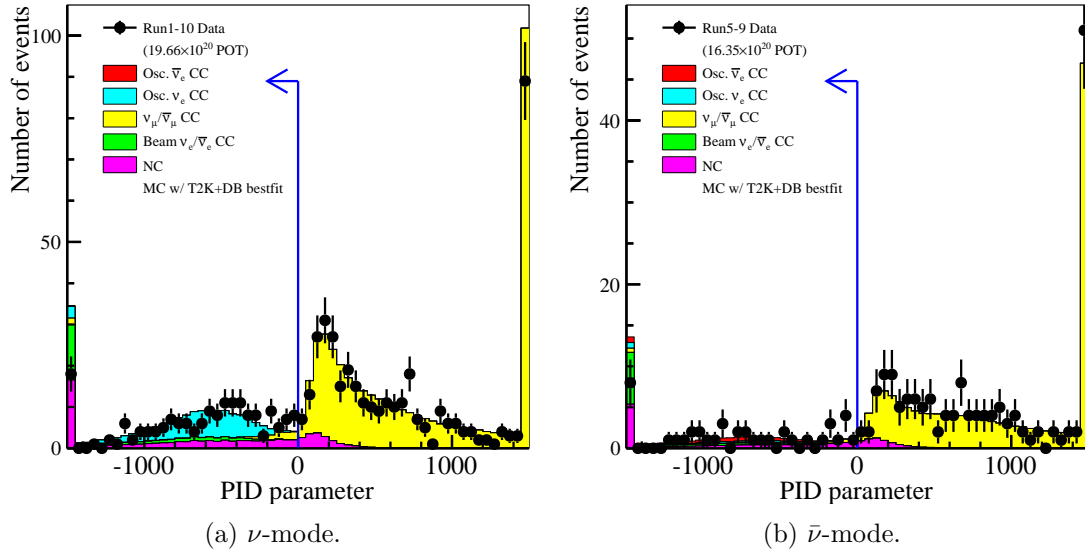


Figure 4.25: $\bar{\nu}_e/\bar{\nu}_\mu$ discrimination PID parameter distributions in the $\bar{\nu}_e$ CCQE-like sample. Both simulated (coloured histograms) and observed (black points) distributions are shown. This parameter is defined as the distance from the cut described in Item 3 of the above list. The region of accepted events is indicated by the blue arrow. Reproduced from Ref. [105].

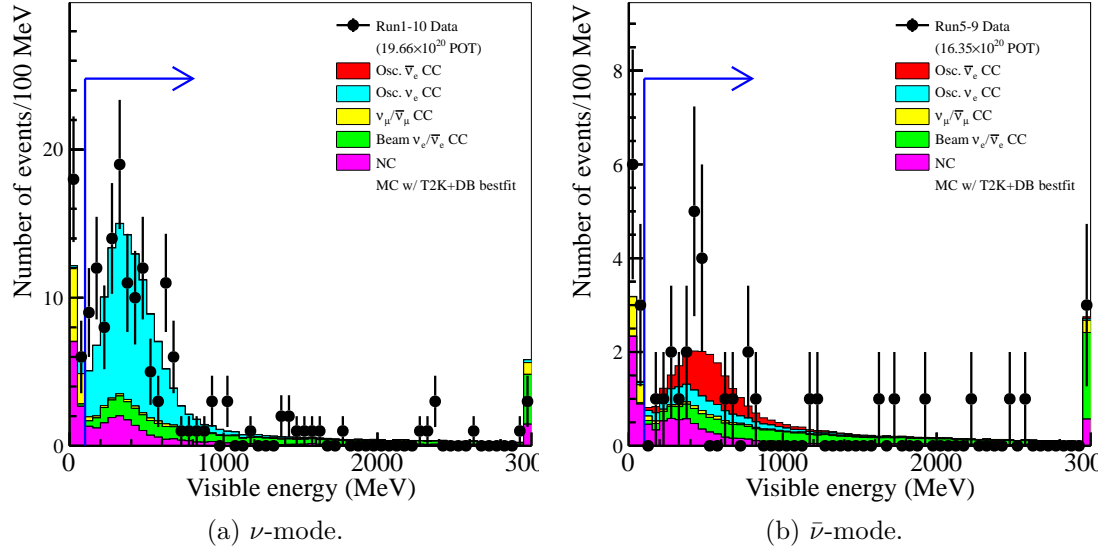


Figure 4.26: Distribution of the simulated (coloured histograms) and observed (black points) visible energy in the $\bar{\nu}_e$ CCQE-like sample. The region of accepted events is indicated by the blue arrow. Reproduced from Ref. [105].

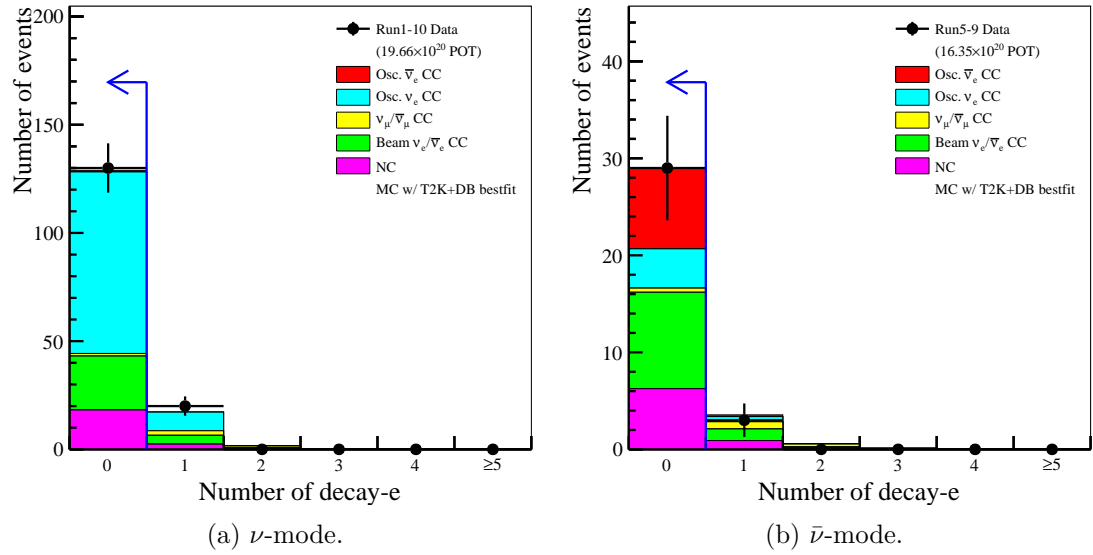


Figure 4.27: Distribution of the simulated (coloured histograms) and observed (black points) number of reconstructed decay electrons in the $\bar{\nu}_e$ CCQE-like sample. The region of accepted events is indicated by the blue arrow. Reproduced from Ref. [105].

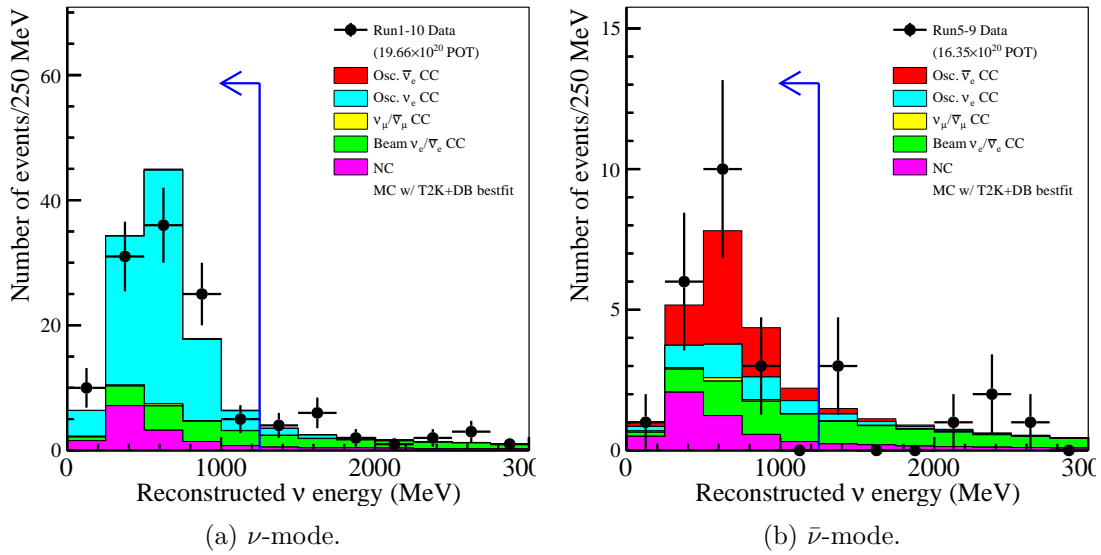


Figure 4.28: Distribution of the simulated (coloured histograms) and observed (black points) reconstructed neutrino energy in the $\bar{\nu}_e$ CCQE-like sample. The region of accepted events is indicated by the blue arrow. Reproduced from Ref. [105].

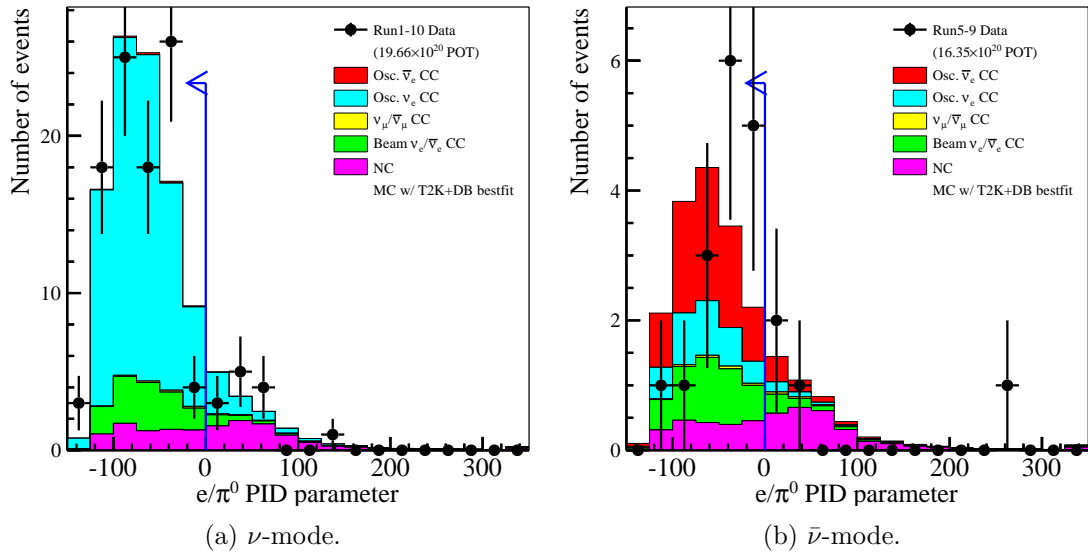


Figure 4.29: $\bar{\nu}_e/\pi^0$ discrimination PID parameter distributions in the $\bar{\nu}_e$ CCQE-like sample. Both simulated (coloured histograms) and observed (black points) distributions are shown. This parameter is defined as the distance from the cut described in Item 7 of the above list. The region of accepted events is indicated by the blue arrow. Reproduced from Ref. [105].

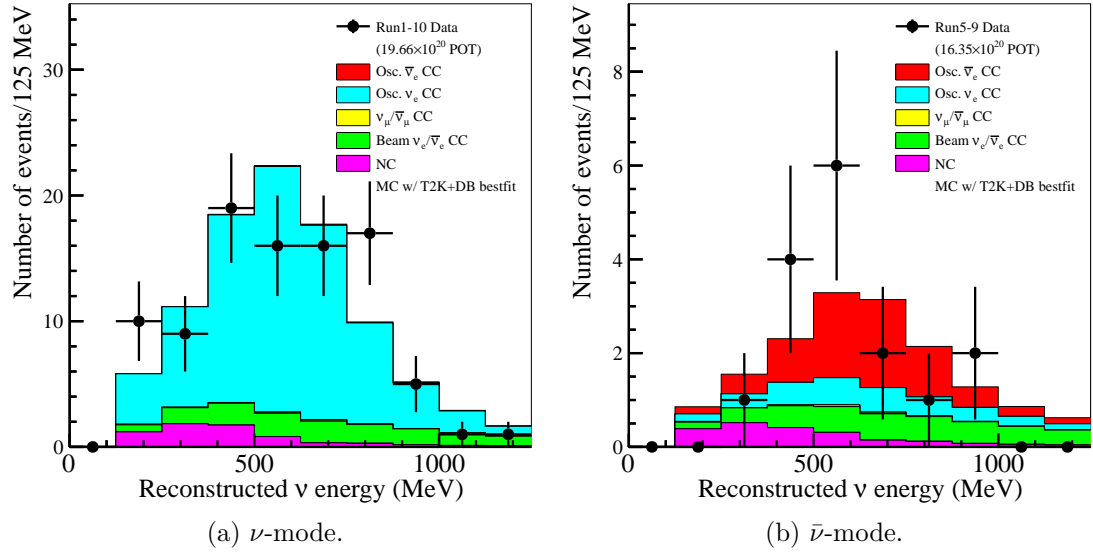


Figure 4.30: Distribution of the simulated (coloured histograms) and observed (black points) reconstructed neutrino energy in the $\bar{\nu}_e$ CCQE-like sample, shown after all selection criteria have been applied. Reproduced from Ref. [105].

Selection Stage	$\nu_\mu + \bar{\nu}_\mu$ CC	$\nu_e + \bar{\nu}_e$ CC	$\nu + \bar{\nu}$ NC	$\nu_\mu \rightarrow \nu_e$ CC	$\bar{\nu}_\mu \rightarrow \bar{\nu}_e$ CC	MC total	Data
Containment	886.4	56.7	260.5	109.8	1.0	1314.3	1361
No. of Cherenkov rings	397.2	29.5	49.2	94.0	0.8	570.7	554
e vs. μ discrimination	11.4	29.5	30.9	93.9	0.8	166.4	174
Visible energy threshold	4.3	29.3	21.2	92.7	0.8	148.3	150
No. of Michel electrons	1.2	24.9	18.2	83.9	0.7	128.9	130
E_{rec} threshold	0.8	13.1	14.1	81.2	0.5	109.8	107
e vs. π^0 discrimination	0.4	11.7	6.6	76.2	0.5	95.3	94
Efficiency (%)	0.0	20.6	2.5	69.4	47.0	7.3	-
Purity (%)	0.4	12.2	6.9	79.9	0.5	-	-

Table 4.3: The expected and observed number of ν -mode $\bar{\nu}_e$ CCQE-like candidate events passing each Super-K selection stage. Predictions are generated using the full T2K Runs 1-10 beam exposure, with normal mass ordering and oscillation parameters set close to previous T2K best fit values: $\Delta m_{21}^2 = 7.53 \times 10^{-5} \text{ eV}^2/\text{c}^4$, $\Delta m_{32}^2 = 2.54 \times 10^{-3} \text{ eV}^2/\text{c}^4$, $\sin^2 \theta_{12} = 0.304$, $\sin^2 \theta_{13} = 0.0219$, $\sin^2 \theta_{23} = 0.550$, and $\delta_{CP} = -1.728$. Adapted from Ref. [105].

Selection Stage	$\nu_\mu + \bar{\nu}_\mu$	$\nu_e + \bar{\nu}_e$	$\nu + \bar{\nu}$	$\nu_\mu \rightarrow \nu_e$	$\bar{\nu}_\mu \rightarrow \bar{\nu}_e$	MC total	Data
	CC	CC	NC	CC	CC		
Containment	321.1	22.7	89.7	6.2	9.7	449.5	498
No. of Cherenkov rings	149.1	11.3	16.9	4.7	8.5	190.4	207
e vs. μ discrimination	2.8	11.3	10.6	4.7	8.5	37.8	41
Visible energy threshold	1.5	11.2	7.4	4.6	8.5	33.6	32
No. of Michel electrons	0.4	9.9	6.3	4.1	8.3	29.0	29
E_{rec} threshold	0.3	4.3	4.7	3.4	7.8	20.5	20
e vs. π^0 discrimination	0.1	3.7	2.1	3.1	7.0	16.1	16
Efficiency (%)	0.0	16.4	2.3	1.4	49.4	72.3	-
Purity (%)	0.9	23.2	12.9	19.2	43.9	-	-

Table 4.4: The expected and observed number of $\bar{\nu}$ -mode $\bar{\nu}_e$ CCQE-like candidate events passing each Super-K selection stage. Predictions are generated using the full T2K Runs 1-10 beam exposure, with normal mass ordering and oscillation parameters set close to previous T2K best fit values: $\Delta m_{21}^2 = 7.53 \times 10^{-5} \text{ eV}^2/\text{c}^4$, $\Delta m_{32}^2 = 2.54 \times 10^{-3} \text{ eV}^2/\text{c}^4$, $\sin^2 \theta_{12} = 0.304$, $\sin^2 \theta_{13} = 0.0219$, $\sin^2 \theta_{23} = 0.550$, and $\delta_{CP} = -1.728$. Adapted from Ref. [105].

4.4.4 $\bar{\nu}_e CC1\pi^+$ -like Selection Criteria

The criteria used to accept ν -mode $\bar{\nu}_e CC1\pi^+$ -like events are the same as for the $\bar{\nu}_e CCQE$ -like samples in Section 4.4.3, with the following listed modifications. The effects of notable selection criteria shown in Figs. 4.31 to 4.33 and the final reconstructed neutrino energy distribution of the selected events shown in Fig. 4.34. The number of simulated and observed candidate events passing each selection stage along with selection efficiencies and purities are shown in Table 4.5.

1. Full containment within the Super-K inner detector and reconstructed inside the fiducial volume with $wall > 50$ cm and $towall > 270$ cm. These selection criteria are different from those for the $\bar{\nu}_e CCQE$ -like sample, as they are optimised separately for each sample to maximise sensitivity to θ_{23} and δ_{CP} in fits to atmospheric neutrino data [3] (the same fits discussed in Section 4.5.1).
2. One electron resulting from the Michel decay of muons is reconstructed. Such a decay electron indicates either the presence of a muon or a pion (through $\pi^\pm \rightarrow \mu^\pm$ decay), even if the parent particle was below the Cherenkov threshold.

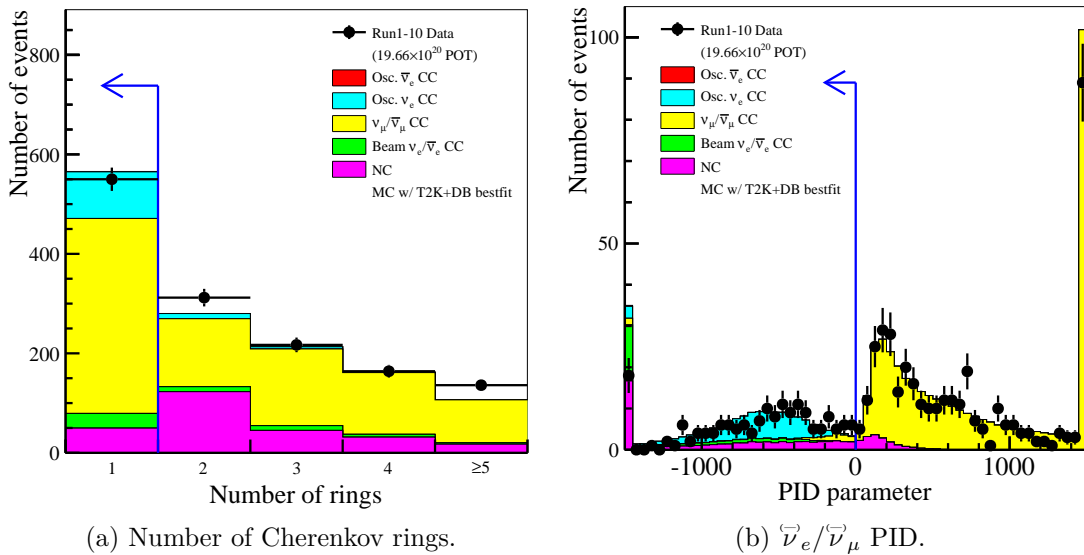


Figure 4.31: Distributions of the simulated (coloured histograms) and observed (black points) number of reconstructed Cherenkov rings and $\bar{\nu}_e/\bar{\nu}_\mu$ discrimination PID parameter (defined as the distance from the cut described in Item 3 of Section 4.4.3) in the ν -mode $\bar{\nu}_e CC1\pi^+$ -like sample. The regions of accepted events are indicated by the blue arrows. Reproduced from Ref. [105].

4.5 Super-K Detector and Cross-Section Uncertainties

There exists a number of remaining uncertainties relevant to the oscillation analyses which are not applicable to and/or cannot be constrained by the near detector fit. These are uncertainties in the Super-K detector effects and in secondary interaction (SI) and photo-nuclear (PN) effects. Whereas the latter two effects have already been

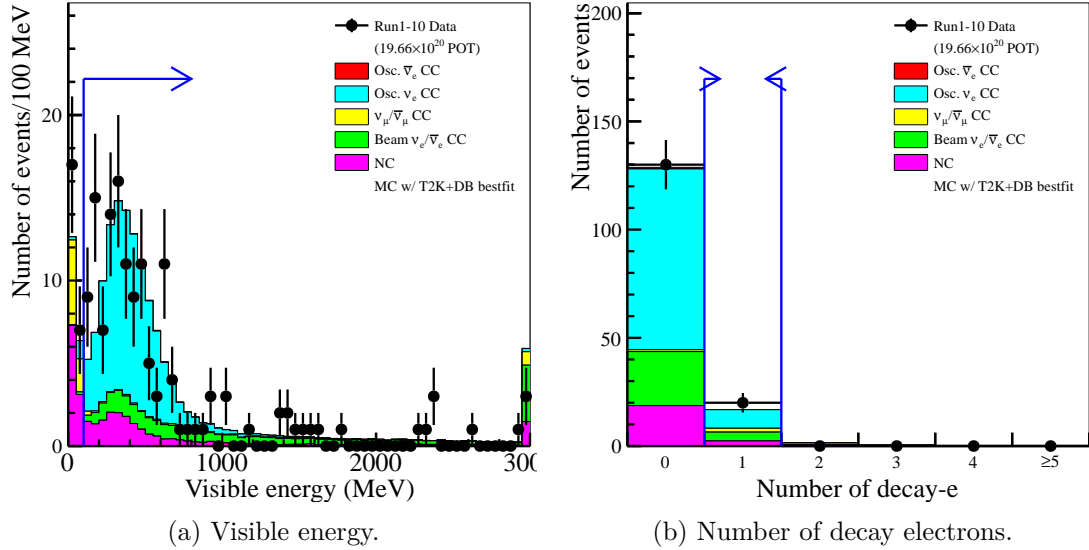


Figure 4.32: Distributions of the simulated (coloured histograms) and observed (black points) visible energy and the number of reconstructed decay electrons in the ν -mode $\bar{\nu}_eCC1\pi^+$ -like sample. The regions of accepted events are indicated by the blue arrows. Reproduced from Ref. [105].

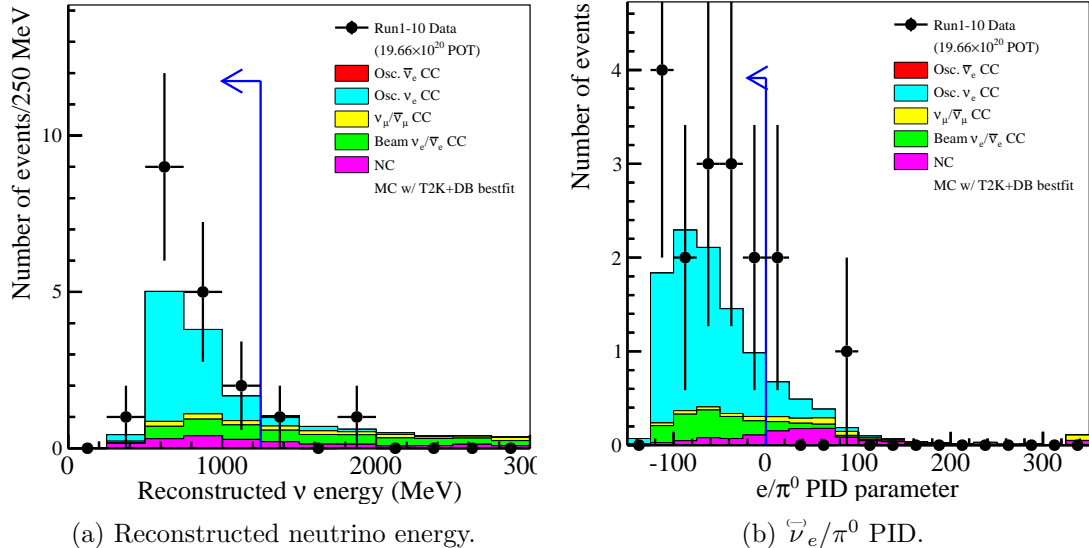


Figure 4.33: Distributions of the simulated (coloured histograms) and observed (black points) reconstructed neutrino energy and $\bar{\nu}_e/\pi^0$ discrimination PID parameter (defined as the distance from the cut described in Item 7 of Section 4.4.3) in the ν -mode $\bar{\nu}_eCC1\pi^+$ -like sample. The regions of accepted events are indicated by the blue arrows. Reproduced from Ref. [105].

described in Section 4.2.6, the Super-K detector effects will be detailed in Section 4.5.1. For each above group of uncertainties, a covariance matrix is constructed to describe the uncertainties and their correlations, then they are summed in quadrature to produce a single Super-K covariance matrix which is passed to the oscillation analyses. The NEUT MC generator is used to simulate neutrino interactions in Super-K, then the propagation of particles within Super-K and the modelling of detector effects are simulated using a

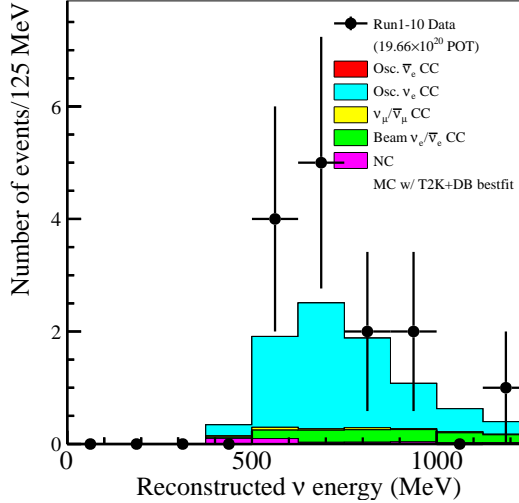


Figure 4.34: Distribution of the simulated (coloured histograms) and observed (black points) reconstructed neutrino energy in the ν -mode $\bar{\nu}_e \text{CC}1\pi^+$ -like sample, shown after all selection criteria have been applied. Reproduced from Ref. [105].

Selection Stage	$\nu_\mu + \bar{\nu}_\mu$ CC	$\nu_e + \bar{\nu}_e$ CC	$\nu + \bar{\nu}$ NC	$\nu_\mu \rightarrow \nu_e$ CC	$\bar{\nu}_\mu \rightarrow \bar{\nu}_e$ CC	MC total	Data
Containment	893.2	57.6	266.5	109.8	1.0	1328.1	1379
No. of Cherenkov rings	392.0	29.6	49.6	93.7	0.8	565.7	550
e vs. μ discrimination	10.7	29.5	32.0	93.6	0.8	166.6	169
Visible energy threshold	3.6	29.4	21.6	92.3	0.8	147.6	145
No. of Michel electrons	1.8	4.1	2.4	8.6	0.0	16.8	20
E_{rec} threshold	0.5	1.4	1.1	7.8	0.0	10.9	17
e vs. π^0 discrimination	0.2	1.2	0.3	7.1	0.0	8.8	14
Efficiency (%)	0.0	2.0	0.1	6.4	0.9	0.7	-
Purity (%)	2.0	13.1	3.8	80.9	0.1	-	-

Table 4.5: The expected and observed number of ν -mode $\bar{\nu}_e \text{CC}1\pi^+$ -like candidate events passing each Super-K selection stage. Predictions are generated using the full T2K Runs 1-10 beam exposure, with normal mass ordering and oscillation parameters set close to previous T2K best fit values: $\Delta m_{21}^2 = 7.53 \times 10^{-5} \text{ eV}^2/\text{c}^4$, $\Delta m_{32}^2 = 2.54 \times 10^{-3} \text{ eV}^2/\text{c}^4$, $\sin^2 \theta_{12} = 0.304$, $\sin^2 \theta_{13} = 0.0219$, $\sin^2 \theta_{23} = 0.550$, and $\delta_{CP} = -1.728$. Adapted from Ref. [105].

bespoke software package, SKDETSIM v13p90.

4.5.1 Super-K Detector Effects

In order to build the Super-K event samples, a number of selection criteria are applied to candidate events, as detailed in Section 4.4. Detector efficiency effects mean that the variables used to make these selections are uncertain, leading to corresponding uncertainties in the event rates for each sample. Due to the complexities of the Super-K MC production, it is not computationally feasible to implement the underlying detector uncertainties directly into the oscillation analyses. Instead, the combined effects of all detector uncertainties on the predicted Super-K event rates are accounted for and a

normalisation uncertainty is applied to each of the following sample, reaction mode, and kinematic bin combinations [105]:

- $\vec{\nu}_\mu$ CCQE-like sample (in both ν and $\bar{\nu}$ modes):
 - True $\vec{\nu}_\mu$ CCQE-like events: $E_{\text{rec}} \in [0.0, 0.4], [0.4, 1.1], [1.1, 30]$ GeV bins.
 - True $\vec{\nu}_\mu$ CC non-QE-like events for all E_{rec} .
 - True $\vec{\nu}_e$ CC events for all E_{rec} .
 - True NC events for all E_{rec} .
- $\vec{\nu}_e$ CCQE-like sample (in both ν and $\bar{\nu}$ modes), with the same $E_{\text{rec}} \in [0.0, 0.35], [0.35, 0.8], [0.8, 1.25]$ GeV bins for all reaction modes:
 - True oscillated $\vec{\nu}_e$ CCQE-like events.
 - True unoscillated $\vec{\nu}_e$ CC events.
 - True $\vec{\nu}_\mu$ CC events.
 - True NC events.
- ν -mode $\vec{\nu}_e$ CC1 π^+ -like sample, with the same $E_{\text{rec}} \in [0.3, 0.8], [0.8, 1.25]$ GeV bins for all reaction modes:
 - True oscillated $\vec{\nu}_e$ CCQE-like events.
 - True unoscillated $\vec{\nu}_e$ CC events.
 - True $\vec{\nu}_\mu$ CC events.
 - True NC events.

In the above list, where the E_{rec} ranges were divided, the ranges were chosen to have one bin covering the region around the maximum oscillation probability and with a bin either side of this range (with the exception of the ν -mode $\vec{\nu}_e$ CC1 π^+ -like sample, where there are no events below the region of maximum oscillation probability).

The detector uncertainties can be split into a number of contributions, as listed in Table 4.6, where the uncertainty on each contribution has been estimated using data from the listed control samples [3, 105].

An explanation of each control sample and their uncertainty estimation methods is as follows:

- **Cosmic μ uncertainty estimates** - First, a control sample is constructed from cosmic ray muons that stop within the inner detector. Then, in order to make the MC in the T2K μ -like samples directly comparable to this control sample, a multivariate reweighting procedure is applied to the MC, minimising data/MC differences in the reconstructed muon momentum, direction, vertex position (with the associated *towall*), and stopping position (with the associated *wall*). Finally, the relevant systematic uncertainties are estimated using the difference in efficiencies between the MC control sample data [189].

Contribution	Uncertainty (%)	Sample used for estimation
Vertex location and track direction	0.3-0.4	
Michel electron tagging efficiency	1.0	Cosmic μ
Fake Michel electron tagging rate	0.2	
Misidentifying μ as e	30	
NC π^0 rejection efficiency	26	Hybrid π^0
Reconstructed neutrino energy scale	2.13	Cosmic μ and atmospheric π^0
e/μ , e/π^0 & μ/π^+ PID selections and Cherenkov ring counting	(discussed in text)	Atmospheric neutrinos

Table 4.6: Contributions to the Super-K detector uncertainties along with the control samples used to estimate them. Adapted from Refs. [3, 105].

- **Hybrid π^0 estimate of the NC π^0 rejection efficiency** - First, a set of ‘hybrid’ π^0 control samples are constructed by overlaying either a primary e -like Cherenkov ring (from the simulated or observed atmospheric neutrino samples) or a Michel e -like Cherenkov ring (from the simulated or observed cosmic muon sample) onto a simulated photon event with kinematics following the decay of simulated NC π^0 events. Then, the difference in π^0 rejection efficiencies between the hybrid samples constructed with only MC and mixed MC and data is taken to be the systematic uncertainty. This uncertainty is not used as a single value, but is binned in lepton momentum and angle and the value listed in Table 4.6 corresponds to the overall uncertainty [189].
- **Cosmic μ and atmospheric π^0 estimate of the E_{rec} scale uncertainty** - The E_{rec} scale uncertainty accounts for effects which would alter the reconstructed neutrino energy. There are two components to this uncertainty, which are summed in quadrature to obtain the overall uncertainty:
 - The attenuation length of light in Super-K has undergone variations over the years of operation, affecting the observed PMT charge, and from this, the number of detected photons and therefore the reconstructed lepton momentum and neutrino energy. Using through-going cosmic muon data, the attenuation length is estimated to be stable within 90 ± 5 m, which translates to an effective uncertainty on the E_{rec} scale of 0.48% [190].
 - The uncertainty in the absolute energy scale is estimated from four control samples ranging in momentum from 30 MeV/c to 10 GeV/c. Three of which are from cosmic muon events which stop in the inner detector (Michel electrons from cosmic muon decay, and sub- and multi-GeV cosmic muons) and one from π^0 events produced by atmospheric neutrinos. For each control sample, simulated and observed distributions of E_{rec} are formed and the

peak positions are compared. The sub-GeV cosmic muon sample gives the largest data/MC fractional difference, 2.08%, and this difference is used as the uncertainty on the absolute E_{rec} scale [190].

Summing these two components in quadrature results in an overall E_{rec} scale uncertainty of 2.13%. This uncertainty is both applicable across the entire energy range considered in the T2K oscillation analyses and is uncorrelated with any other detector, SI, or PN uncertainty. As a result, this uncertainty is not incorporated into the overall binned uncertainties described above (as the other uncertainties constrained at Super-K are), but is directly implemented into the oscillation analyses as an independent normalisation uncertainty.

- **Atmospheric neutrino estimate of the PID and ring-counting uncertainties** - The PID and ring-counting uncertainties are estimated using a Markov chain Monte Carlo (MCMC) fit to atmospheric neutrino data. The following paragraphs, summarised from Ref. [3], give an overview of the event samples constructed from the atmospheric neutrino data and simulation, the parameters used in the fit, and how the relevant uncertainties are extracted.

Eighteen simulated and observed atmospheric neutrino samples at Super-K are constructed, covering events with zero, one, and more than one Michel electrons, each in six detector regions. Each of these samples are further divided into six true event topologies based on the number and type of visible particles: e , μ , p or π^+ , e with other visible particles, and μ with other visible particles.

For each of the above topologies, three PID variables are defined for the purposes of separating e/μ , e/π^0 , and μ/π^+ , along with a variable to distinguish events with single or multiple primary Cherenkov rings (referred to as the ‘single/multiple particle discriminator’). Two systematic parameters are assigned to each of these PID and ring-counting variables: a scale and a shift parameter. Uncertainties in the flux and cross-section models are also accounted for in this fit, but to avoid causing biases in the oscillation analyses, greatly simplified versions of these models are used, such that the fit has little sensitivity to the oscillation parameter values.

The MCMC is used to randomly sample the Poisson likelihood (of the observed atmospheric neutrino data given the simulation) across the space of the parameters described above, producing posterior predictive distributions of the above scale and shift parameters with all flux, cross-section, and oscillation parameters marginalised. Examples of these distributions are shown in Fig. 4.35, comparing the prefit and postfit MC to the atmospheric neutrino data. Then, according to these distributions, the scale and shift parameters are randomised and applied to the simulation used to select events to populate the T2K event samples. Finally, by comparing the resulting simulated and observed distributions of selected events

in each of the bins discussed above, a fractional uncertainty can be extracted for each bin, encompassing variations in all PID and ring-counting parameters.

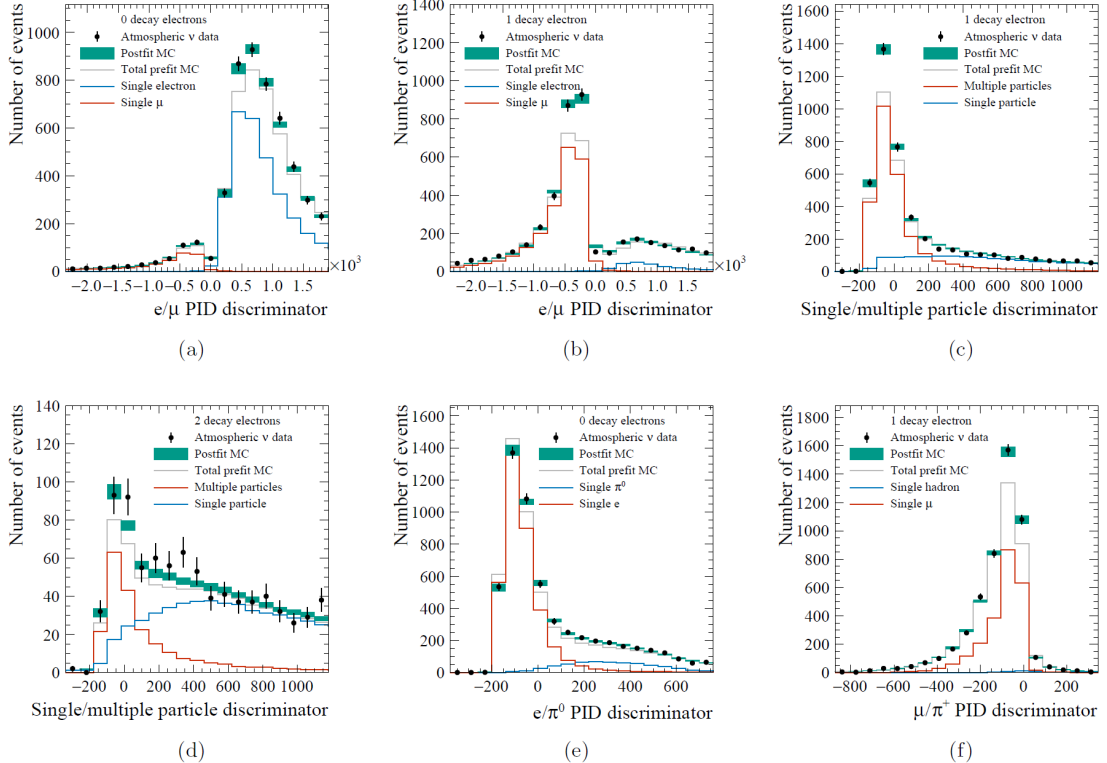


Figure 4.35: Posterior predictive distributions of the Super-K atmospheric MCMC fit to determine detector systematic uncertainties, shown for a number of discrimination parameters used in the Super-K event selections and shown split by the number of decay electrons (resulting from the Michel decay of muons). The total prefit MC predictions (grey lines) are shown along with the two components being discriminated (red and blue lines). The 68.27% credible intervals of the posterior predictive distributions resulting from the fit (green regions) are generally in excellent agreement with the observed atmospheric neutrino data (black points). Reproduced from Ref. [3].

The above contributions to the Super-K detector errors are combined into a single covariance matrix as follows [3]: The nominal MC is first weighted by the post ND fit flux and cross-section systematic parameter values (using the full flux and cross-section models described in Sections 4.1 and 4.2 instead of the simplified model used for the atmospheric neutrino fit above) and neutrino oscillation probabilities are applied (with $\sin^2 \theta_{12}$, Δm_{21}^2 and $\sin^2 \theta_{13}$ taken from the global best-fit of Ref. [35] and $\sin^2 \theta_{23}$, $|\Delta m_{3j}^2|$ and δ_{CP} set to the most probable values from Ref. [191]). Then, the above detector uncertainties are randomly sampled 10^6 times and in each case are used to weight an MC prediction and produce event rate distributions in each of the kinematic bins discussed earlier in this section. From these distributions, a covariance matrix is constructed with each row/column of the matrix corresponding to a single kinematic bin. Finally, the reconstructed energy scale uncertainty is appended to this matrix, uncorrelated with the other entries, as discussed above.

4.5.2 Secondary Interaction and Photo-nuclear Effect Uncertainties

As discussed in Section 4.2.6, pion secondary interactions (SI) and the photo-nuclear (PN) effect can change the observed final state topologies in Super-K, potentially causing a bias in the reconstructed neutrino energy. Due to a lack of sensitivity, these effects are not constrained during the near detector fit, but can be better characterised at Super-K.

The effect of pion SI in the Super-K detector are simulated using a cascade model, accounting for normalisation uncertainties in the probabilities of each pion-nucleus interaction type (see Fig. 4.12). PN interactions are simulated in the Super-K MC by allowing for photons (resulting from the $\pi^0 \rightarrow \gamma\gamma$ decay) to be absorbed with no subsequent emission above the Cherenkov threshold (with a 100% normalisation uncertainty assumed for the PN cross-section) [104]. Then, by randomly varying the pion SI and PN interaction probabilities according to their uncertainties, the resulting kinematic distributions are used to build a covariance matrix in the same way (and with the same kinematic binning) as for the above detector uncertainties.

4.5.3 Combined Super-K Detector, SI, and PN Uncertainties

Once the detector and SI+PN covariance matrices have been constructed, they are summed in quadrature to produce a single covariance matrix encompassing all of their uncertainties. This matrix is shown in Fig. 4.36 and is passed to the oscillation analyses where each row/column of this matrix is treated as corresponding to a normalisation uncertainty acting on the indicated kinematic bin(s).

4.6 Summary

In this chapter, the flux and interaction models used to predict Super-K neutrino events for the oscillation analyses, their associated uncertainties, and the simulation chain used to generate them have been detailed and are summarised as follows.

First, in Section 4.1, the flux spectra at the near and far detectors are predicted using FLUKA and JNUBEAM simulations. A number of Super-K flux normalisation uncertainties are defined (with the largest contribution to these uncertainties coming from hadron interactions) and are reduced following a fit to observed hadron multiplicities from the NA61/SHINE experiment [113–115].

Next, in Section 4.2, is a description of the interaction models used in the NEUT MC simulation of neutrino-nucleus interactions in the near and far detectors. The initial nuclear state is modelled by the Benhar spectral function [122] for CCQE interactions, and by the more simplistic relativistic Fermi gas model for all other interactions [120]. 2p2h interactions are modelled according to Nieves et al. [192]; pion production is modelled according to the Rein-Sehgal [145] model, with a NEUT Cascade model describing pion SI and FSI; DIS interactions are modelled using the GRV98 [162] parton distribution functions, with modifications to the low- Q^2 region according to Bodek and

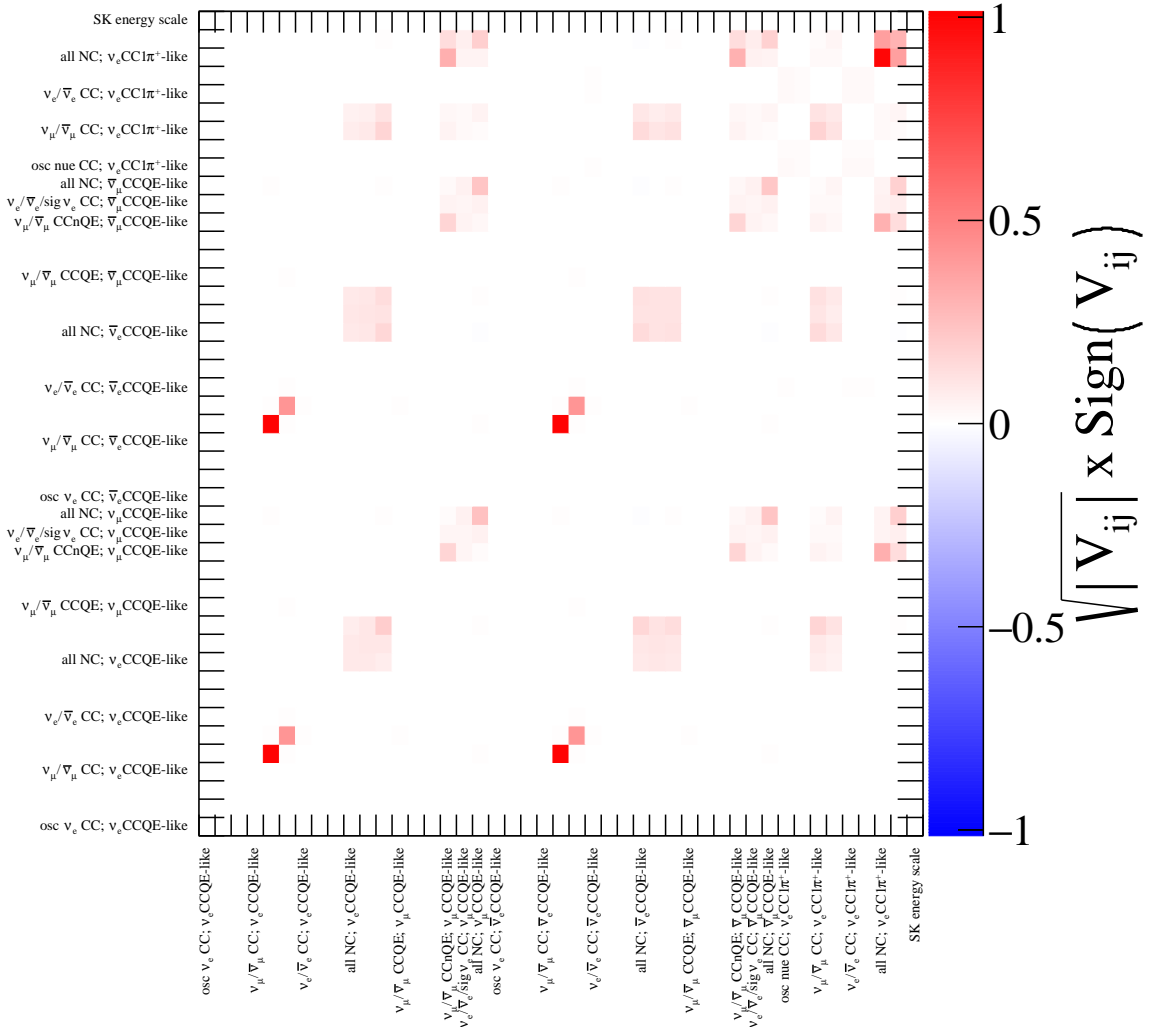


Figure 4.36: The Super-K detector + SI + PN covariance matrix.

Yang [163]. All of which have been tuned to external data [119, 120]. A number of uncertainties are associated with each of these models, either resulting from model parameters without sufficient constraints, from discrepancies between observed data and the model prediction(s), or from differing predictions across a number of valid, competing interaction models.

In Section 4.3, the selection criteria for the CC 0π , CC1 π , and CC other near detector event samples are detailed. Simulated predictions are fit to the observed near detector data, simultaneously accounting for all samples, the effect of limited MC statistics, and all flux, interaction, and ND280 detector uncertainties. The fit produces constraints on the flux and interaction model systematic parameters. These are then passed to the oscillation analyses as a vector of best-fit parameter values and as a covariance matrix containing the parameter uncertainties and correlations [90].

In Section 4.4, the selection criteria for the $\bar{\nu}_\mu$ CCQE-like, $\bar{\nu}_e$ CCQE-like, and

$\bar{\nu}_e$ CC1 π^+ -like Super-K event samples are detailed. Then, in Section 4.5, constraints are discussed on uncertainties in secondary interactions, the photo-nuclear effect, vertex location, track direction, particle identification, Cherenkov ring counting, and neutrino energy reconstruction. The effects of these uncertainties are simplified by combining them into a number of overall normalisation uncertainties, each spanning a range of reconstructed neutrino energy and interaction types. These are then passed to the oscillation analyses as a vector of best-fit parameter values and as a covariance matrix containing the parameter uncertainties and correlations [105].

Chapter 5

Three-Flavour Joint $\nu/\bar{\nu}$ Oscillation Analysis

In this chapter, data from the T2K experiment will be used to produce constraints on the following three-flavour neutrino oscillation parameters in the PMNS parametrisation (see Section 2.2.3): θ_{23} , θ_{13} , Δm_{3j}^2 , and δ_{CP} . The dataset used in this analysis corresponds to T2K Run 1-10, i.e. using the full dataset collected over the entire history of T2K to date (see Section 3.1).

First, Section 5.1 describes the analysis strategy used to evaluate the likelihood of an oscillation hypothesis and the construction of confidence regions. Then, the inputs used to constrain systematic and oscillation parameter uncertainties used in the T2K Run 1-10 analysis will be summarised in Section 5.2, followed by a discussion of the predicted kinematic distributions, event rates, and oscillation parameter constraints in Sections 5.3 and 5.4. The effects on these constraints of using alternative interaction models will be considered in Section 5.5. Finally, the observed constraints will be shown in Section 5.6 and compared to constraints obtained by other neutrino oscillation experiments in Section 5.7.

5.1 Analysis Strategy

All analyses presented in this thesis have been performed using the VALOR neutrino fitting software [2], capable of inferring parameter values and testing a variety of physics hypotheses by simultaneously fitting data from different topological samples obtained under a variety of running conditions (e.g. flux configurations) by different detectors and using a choice of statistical methods. VALOR is well validated and has been used to produce published results on the T2K experiment for a number of years [3, 5, 74, 75, 104, 121, 193–198]. In this thesis, such fits have been made using data from the T2K experiment, under the assumption of the three-flavour neutrino oscillation model, as detailed in Section 2.2.

Constraints on the oscillation parameters of interest will be inferred by producing frequentist confidence intervals from marginal log-likelihood ratios produced by simultaneously analysing the rate and shape of kinematic distributions from the five Super-K

event samples (see Section 4.4) while accounting for systematic uncertainties in the flux, interaction and detector models (as described in Chapter 4). The systematic uncertainties are characterized using systematic parameters, which act to weight the nominal MC prediction while accounting for their relative uncertainties and prior constraints. This section will describe how the marginal likelihood of a given physics hypothesis is evaluated and how the confidence intervals are constructed.

5.1.1 Evaluation of a Hypothesis' Likelihood

In order to evaluate the likelihood of a given set of oscillation parameter values, binned expected kinematic distributions must be produced for those values and compared to the observed distributions. This subsection will first discuss how the expected distributions are formed before showing how the likelihood and marginal likelihoods are calculated.

5.1.1.1 Construction of Expected Kinematic Distributions

The predicted and observed kinematic distributions are binned, with the choice of bin edges dependent on the needs of each analysis; all analyses presented in this thesis use the same choice of kinematic variables: reconstructed neutrino energy, E_{rec} , for the μ -like samples, and both E_{rec} and reconstructed lepton angle, θ , for the e -like samples. Additionally, each sample is broken down into a number of true reaction modes (a combination of neutrino-nucleus interaction type and initial and final neutrino flavour), the choice of which is dependent on the interaction models used by each analysis.

The predicted number of events in the r^{th} reconstructed bin, i.e. a two-dimensional (E_{rec}, θ) bin, of the kinematic distributions for the s^{th} Super-K sample are generated according to Eq. (5.1), where an explanation of each contributing term is as follows:

$$N^{\text{exp}}(\vec{o}, \vec{f}, s, r) = \sum_m \sum_t \sum_{r'} P(\vec{o}, m, t) \cdot T(f_{E;r}^{SK}, r, r') \cdot S(\vec{f}, m, t, r') \cdot N^{MC}(s, m, r', t) \quad (5.1)$$

- $N^{MC}(s, m, r', t)$ is the nominal predicted number of Super-K events in the true neutrino energy bin, t , and reconstructed bin, r' , for events in the s^{th} sample and with true reaction mode, m . This is taken directly from the official Super-K MC, generated using the NEUT and SKDETSIM MC simulations (see Sections 4.2 and 4.4, respectively), with the flux tuning applied (see Section 4.1), without oscillation probabilities applied, with systematic parameters applied at their nominal pre-ND fit values, and normalised to the collected exposure in each event sample. The binned MC events for a particular sample and true reaction mode are referred to as an ‘MC template’.
- $S(\vec{f}, m, t, r')$ is an overall, multiplicative, systematic error factor depending on a vector of systematic parameters, \vec{f} , each of which may give a different contribution

to S for each reaction mode, m , true energy bin, t , and reconstructed bin, $r\ell$. The choice of systematic parameters is dependent on the uncertainties present in the flux, interaction, and detector models used to produce the nominal MC.

- $T(f_{E;r}^{SK}, r, r\ell)$ is a transfer function (in practice it is implemented algorithmically) describing the migration of events between the reconstructed bins r and $r\ell$ due to uncertainty in the Super-K reconstructed energy scale. This is expressed in terms of the systematic parameter $f_{E;r}^{SK}$ (see Table A.6), which scales the reconstructed energy of Super-K MC events by the value of this parameter.
- $P(\vec{o}, m, t)$ is the three-flavour oscillation probability with matter effects, evaluated with expected oscillation parameters, \vec{o} , and at the centre of the true energy bin t containing Super-K MC events corresponding to mode m . This is not applied to events corresponding to NC interactions, as these interactions do not depend on the relative proportions of each neutrino flavour. The oscillation probability is calculated using the numerical method described in section 3.1 of Ref. [199] to find the eigenvalues of the effective matter Hamiltonian of Eq. (2.27) with a constant matter density of 2.6 g/cm³ [39] within the Earth’s crust.

The product of these quantities are summed over all bins corresponding to MC truth information to obtain $N_r^{\exp}(\vec{o}, \vec{f}, s, r)$, which are the expected kinematic distributions. These are explicitly a function of reconstructed quantities only and are therefore directly comparable to the observed kinematic distributions.

5.1.1.2 Construction of the Likelihood

In each sample, a Poisson log-likelihood ratio of the expected kinematic distribution given the data, D, (i.e. the observed kinematic distribution) is calculated as follows:

$$-2 \ln \lambda_s(D | \vec{o}, \vec{f}) = 2 \sum_r \left[N_r^{\text{obs}} \cdot \ln \left(\frac{N_r^{\text{obs}}}{N_r^{\exp}} \right) + N_r^{\exp} - N_r^{\text{obs}} \right] \quad (5.2)$$

where λ_s is the likelihood ratio in a given sample, $N_r^{\exp} \equiv N_r^{\exp}(\vec{o}, \vec{f}, s, r)$ of Eq. (5.1) is the expected number of events in a kinematic bin, and $N_r^{\text{obs}} \equiv N_r^{\text{obs}}(s, r)$ is the observed number of data events in the same kinematic bin. Here, ‘data’ can refer to either real data collected by the T2K experiment, or pseudo-data containing an integer number of events generated from an assumed set of true oscillation and systematic parameter values.

In the analyses concerned with constraining the three-flavour PMNS oscillation parameters, the total log-likelihood is calculated according to Eq. (5.3), while for the $\bar{\nu}_e$ appearance analysis, the contribution of each sample to the total likelihood differs, as will be described in Section 6.2.

$$\lambda(D | \vec{o}, \vec{f}) = \prod_s \lambda_s(D | \vec{o}, \vec{f}) \quad (5.3)$$

The total likelihood of Eq. (5.3) is dependent on both the systematic and oscillation parameters, but it is desirable for the resulting confidence regions to be a function of the oscillation parameters only. Additionally, producing a confidence region as a function of *all* oscillation parameters would be computationally intractable, so instead, multiple confidence regions are produced, each corresponding to at most two oscillation parameters, plus the mass ordering. These are denoted as the ‘parameters of interest’, \vec{o}_I , while all other $N_f = \mathcal{O}(100)$ oscillation and systematic parameters are treated as ‘nuisance parameters’, \vec{f}' , and are eliminated by converting the total likelihood into the marginal likelihood, λ_{marg} . This is calculated as in Eq. (5.4) by integrating the product of the total likelihood and the (analysis-specific) nuisance parameter prior probability density functions (PDFs), π , over the corresponding parameter space, F' .

$$\lambda_{\text{marg}}(\mathbf{D} \mid \vec{o}_I) = \int_{F'} \lambda(\mathbf{D} \mid \vec{o}, \vec{f}') \cdot \pi(\vec{f}') d^{N_f} \vec{f}' = \frac{1}{n} \sum_{i=1}^n \lambda(\mathbf{D} \mid \vec{o}_I, \vec{f}'_i) \quad (5.4)$$

In practice, this integration is performed numerically by randomly drawing n sets of nuisance parameters, as in the right-hand side of Eq. (5.4), with correlations between systematic parameters accounted for using Cholesky decomposition [200] of their respective covariance matrices (see Sections 4.3 and 4.5). Many (typically $\geq 10^4$) randomly drawn sets of \vec{f}' are required to adequately sample F' , with n being chosen for each analysis based on the number of nuisance parameters and how tightly constraining each prior PDF is. The space F' is regarded as being adequately sampled if the resulting confidence regions do not significantly change when different sets of n independent random samples are instead used. Additionally, any \vec{f}' that either results in a negative number of events or sets any parameters outside of their physical ranges is re-thrown.

5.1.2 Construction of Confidence Regions

The previous subsection described the construction of the marginal likelihood for a fixed set of values for the parameter(s) of interest, \vec{o}_I ; however, the objective is to construct confidence regions on the allowed values of these parameters. So, the marginal likelihood of Eq. (5.4) is evaluated at a number of evenly spaced ‘grid points’ in the space of \vec{o}_I , chosen to balance the resolution of the resulting best fit points and confidence intervals against computational feasibility. Then, the ratio to the maximum marginal likelihood across all grid points, $\lambda_{\text{marg}}^{\max}$, is taken, and the coordinates of this grid point are taken to be the best fit point, $\vec{o}_{I,\text{bf}}$. The n randomly drawn sets of nuisance parameters used in calculating the marginal likelihood are the same across all grid points, so that only the parameters of interest change between grid points.

As described by Wilks’ theorem [201], in the large sample limit, the negative log-likelihood ratio asymptotically tends towards a χ^2 distribution, and for brevity will hereafter be denoted $\Delta\chi^2$, defined in Eq. (5.5). This quantity is the test statistic used to construct confidence regions by finding all grid points for which Eq. (5.6) is satisfied,

where $\Delta\chi^2_{\text{crit}}$ denotes the critical value at the $X\%$ confidence level.

$$\Delta\chi^2 \equiv \Delta\chi^2(D \mid \vec{o}_I) = -2 \ln \left[\frac{\lambda_{\text{marg}}(D \mid \vec{o}_I)}{\lambda_{\text{marg}}^{\max}(D \mid \vec{o}_{I,\text{bf}})} \right] \quad (5.5)$$

$$\Delta\chi^2 < \Delta\chi^2_{\text{crit}}(\vec{o}_I, X) \quad (5.6)$$

Two different methods are used to evaluate the critical values. Typically, the critical values do not depend on the parameter(s) of interest and are pre-computed as the critical values of the χ^2 distribution [200]. This is known as the constant $\Delta\chi^2$ method, and in this thesis, will be used to produce confidence regions for all oscillation parameters except for 1D δ_{CP} . The constant $\Delta\chi^2$ method is applicable only when Wilks' theorem holds, and otherwise may give incorrect coverage. This is the case for δ_{CP} , where its cyclic nature and the presence of physical boundaries (in the event rates) at $\delta_{CP} = \pm\frac{\pi}{2}$ results in incorrect coverage, as has been observed in previous T2K analyses [3, 198]. This is also the case, albeit to a lesser extent, for $\sin^2\theta_{23}$, where the boundary corresponding to maximal ν_μ disappearance has been shown to adversely affect the coverage [202]. To account for this, a second method is used where the critical values at each grid point are determined numerically, and is referred to as the ‘Feldman-Cousins’ (FC) method, described in Ref. [203]. This method is computationally intensive to a nearly prohibitive extent, so is used only for the main result of this thesis, the 1D δ_{CP} confidence regions, and with a coarser grid of points than that used for the calculation of the marginal likelihood.

The procedure for calculating Feldman-Cousins critical values as a function of δ_{CP} and mass ordering is as follows. A number of grid points are defined in the range $\delta_{CP} = [-\pi, +\pi]$ and in each mass ordering. At all points, critical values are calculated as follows and collated to form $\Delta\chi^2_{\text{crit}}(\vec{o}_I, X)$:

1. In order to provide the correct coverage, many (typically $> 10^4$) ensembles of expected kinematic distributions are generated at each grid point, each produced assuming the δ_{CP} and mass ordering of the grid point and accounting for both statistical and nuisance parameter uncertainties, as follows. The resulting expected kinematic distributions have integer event rates and are referred to as ‘pseudo-experiments’.
 - (a) To account for uncertainties in the nuisance parameters during the generation of each pseudo-experiment, these parameters are randomly sampled according to the same prior PDFs used in the marginalisation method. The exception to this is for the ‘atmospheric’ parameters, $\sin^2\theta_{23}$ and Δm_{3j}^2 , where the observed T2K constraint on these parameters is incorporated into the constraint on δ_{CP} as prior knowledge. This is done by randomly drawing the atmospheric parameters from the marginal likelihood distribution resulting from a simultaneous fit to a simulated data set with the following

true values (see Table 5.8): $\sin^2 \theta_{12}$ and Δm_{12}^2 taken from global fits, and $\sin^2 \theta_{23}$, Δm_{3j}^2 , $\sin^2 \theta_{13}$ and δ_{CP} equal to the best fit points from the fit to T2K data. This treatment of the atmospheric parameters is used instead of taking the marginal likelihood distribution directly from the T2K data fit, as such a method would cause the critical values close to the best fit value of δ_{CP} to become smaller due to the generated pseudo-experiments artificially corresponding more closely to the observed data, shrinking the confidence region.

- (b) The randomly selected nuisance parameter values are taken together with the parameter of interest values and are used to generate kinematic distributions according to the method of Section 5.1.1.1.
 - (c) To account for statistical uncertainties during the generation of each pseudo-experiment, the event rates in each kinematic bin are randomly fluctuated according to a Poisson distribution with mean equal to the un-fluctuated event rate.
2. For each pseudo-experiment, a test statistic value is calculated as follows:

- (a) The likelihood is marginalised at each grid point used for the data fit to calculate $\lambda_{\text{marg}}(E | \vec{o}_I)$, where E denotes a pseudo-experiment.
- (b) The marginal likelihood at the \vec{o}_I corresponding to the true grid point, $\lambda_{\text{marg}}(E | \vec{o}_{I,\text{true}})$, is extracted.
- (c) The marginal likelihood maximised across all \vec{o}_I (i.e. across both δ_{CP} and mass orderings), $\lambda_{\text{marg}}^{\max}(E | \vec{o}_{I,\text{bf}})$, is extracted.
- (d) The test statistic, $\Delta\chi_{\text{FC}}^2$ is calculated according to Eq. (5.7). This is analogous to the test statistic used for the constant $\Delta\chi^2$ method (see Eq. (5.5)), but here a pseudo-experiment takes the place of the observed data, and due to $\vec{o}_{I,\text{true}}$ being known for pseudo-experiments, $\Delta\chi_{\text{FC}}^2$ is a fixed value rather than having explicit \vec{o}_I dependence.

$$\Delta\chi_{\text{FC}}^2 = -2 \ln \left[\frac{\lambda_{\text{marg}}(E | \vec{o}_{I,\text{true}})}{\lambda_{\text{marg}}^{\max}(E | \vec{o}_{I,\text{bf}})} \right] \quad (5.7)$$

3. A probability density distribution of $\Delta\chi_{\text{FC}}^2$, $f(\Delta\chi_{\text{FC}}^2)$, is formed from all pseudo-experiments at this grid point.
4. Critical values at the $X\%$ confidence level, $\Delta\chi_{\text{crit},\text{FC}}^2 \equiv \Delta\chi_{\text{crit},\text{FC}}^2(\vec{o}_{I,\text{true}}, X)$, are then defined as

$$\Delta\chi_{\text{crit},\text{FC}}^2 : \int_0^{\Delta\chi_{\text{crit},\text{FC}}^2} f(\Delta\chi_{\text{FC}}^2) d(\Delta\chi_{\text{FC}}^2) = X\% \quad (5.8)$$

5.1.3 Validation of the Analysis

The analyses presented in this thesis have undergone extensive validation procedures, with the treatment of the nominal Super-K MC, the application and effects of systematic parameters, predicted kinematic distributions, expected sensitivities, FC critical values, and results compared in detail with two other T2K oscillation analysis fitters. This acts as a cross-check and ensures that the results produced are not overly sensitive to the implementation details of each fitter. These fitters are described in detail in Refs. [3, 204, 205], and briefly summarised in the following paragraphs (with the fitter used in this thesis referred as ‘Analysis A’).

One such fitter (referred to as ‘Analysis B’) is primarily different in the kinematic variables used to bin the MC and data events, using the reconstructed momentum and angle of the primary outgoing lepton, (p, θ) , for the e -like samples, while the analysis presented in this thesis uses (E_{rec}, θ) binning for these samples.

The other fitter (referred to as ‘Analysis C’) is different in a number of ways. Instead of applying oscillation probabilities and systematic parameters on a bin-by-bin basis, as in this thesis, they are applied on an event-by-event basis. Instead of propagating the results of the near detector fit to the far detector using a covariance matrix, they fit both near and far detector data simultaneously. Additionally, instead of calculating a marginal likelihood on a grid in the space of the parameters of interest, they use a Markov chain MC method to sample the space of all systematic and oscillation parameters, and from this produce a Bayesian joint posterior probability density of the parameters of interest, instead of a log-likelihood ratio function. From this, they produce constraints on the oscillation parameters as credible intervals, rather than confidence intervals. Credible intervals are a Bayesian analogue of frequentist confidence intervals: whereas the X% confidence interval contains the (fixed) true parameter value in X% of repeated experiments, the X% credible interval has an X% probability of containing the (uncertain) true parameter value.

Despite the differences in kinematic binning and statistical methods between the three fitters, all comparisons between them for all analyses are in good agreement [202, 206–209]. An example of the level of agreement is shown in Fig. 5.1 for a δ_{CP} sensitivity study. The minor differences between fitters in the $\Delta\chi^2$ functions shown in this figure have a negligible effect on any the conclusions drawn from it, e.g. the confidence intervals, and the source of such differences have been extensively studied and found to be caused by implementation choices such as binning and the use of separate or simultaneous near detector fits [202, 209, 210].

Additionally, there are many valid competing interaction models, predicting different cross-sections for the same processes and are weakly constrained by both external and T2K data. The oscillation parameter constraints produced by T2K aim to be independent of such choices of valid models, and the procedures used to test this assumption and to correct for any model-dependence are discussed in more detail in Section 5.5.

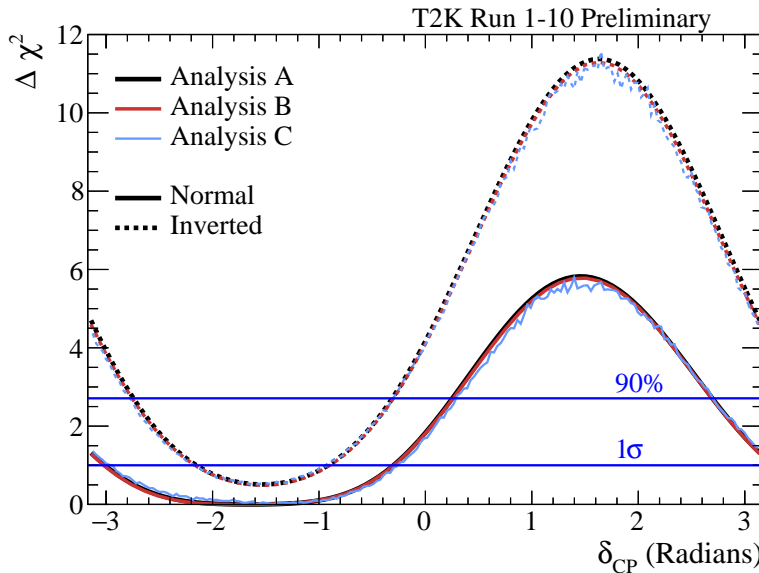


Figure 5.1: Predicted sensitivities to δ_{CP} generated by three different fitters, referred to as Analyses A, B, and C. Predictions are generated under the assumption of the true oscillation parameters labelled ‘Asimov A’ in Table 5.8 and without the constraint on $\sin^2 2\theta_{13}$ from reactor experiments. Critical values are calculated using the constant $\Delta\chi^2$ method.

5.2 Summary of Analysis Inputs and Implementation Choices

5.2.1 Beam Exposure

This analysis is performed using Super-K data from the full T2K Run 1-10 data collection period (see Section 3.1), corresponding to beam exposures of 1.97×10^{21} POT and 1.63×10^{21} POT in ν and $\bar{\nu}$ modes, respectively. Systematic parameters are constrained using the fit to near detector data described in Section 4.3, using T2K Run 2-9 data, corresponding to exposures of 1.50×10^{21} POT and 0.83×10^{21} POT in ν and $\bar{\nu}$ modes, respectively. These data sets are used at the near detectors because the barrel ECAL had not yet been installed during T2K Run 1 and the Run 10 data has not yet been analysed at the near detectors.

5.2.2 Reaction Modes

The neutrino-nucleus interaction model is as described in Section 4.2. In brief, interactions are simulated by a NEUT MC simulation using the following base models: the nuclear ground state model for CCQE interactions uses the Benhar Spectral Function model [122]; 2p2h interactions are modelled according to Nieves et al. [192]; pion production is modelled according to the Rein-Sehgal [145] model, with a NEUT Cascade model describing pion SI and FSI; DIS interactions are modelled using the GRV98 [162] parton distribution functions, with modifications to the low- Q^2 region according to Bodek and Yang [163]. All of which have been tuned to external data [119, 120].

68 true reaction modes (neutrino-nucleus interaction type + initial and final neut-

rino flavours) are used in the analysis to categorise Super-K MC events. The majority of the energy range spanned by the T2K flux is below the threshold for τ or $\bar{\tau}$ production, so charged current (CC) reaction modes involving ν_τ or $\bar{\nu}_\tau$ are neglected. Additionally, for the neutral current (NC) reaction modes, $\bar{\nu}_\alpha$ is taken as being a mixture of $\bar{\nu}_\mu + \bar{\nu}_e + \bar{\nu}_\tau$ as a result of oscillations, so to avoid double-counting, no corresponding oscillated reaction modes are used. Also, no NCQE or NC2p2h reaction modes are considered, as these are effectively elastic neutrino-nucleus scatters and would not be visible in Super-K. The reaction modes considered in this analysis are as follows:

- 6 CC quasi-elastic interactions (CCQE);

$$\nu_\mu, \bar{\nu}_\mu, \nu_e, \bar{\nu}_e, \nu_\mu \rightarrow \nu_e, \bar{\nu}_\mu \rightarrow \bar{\nu}_e$$
- 6 CC two particle two hole interactions (CC2p2h);

$$\nu_\mu, \bar{\nu}_\mu, \nu_e, \bar{\nu}_e, \nu_\mu \rightarrow \nu_e, \bar{\nu}_\mu \rightarrow \bar{\nu}_e$$
- 6 CC single neutral pion resonant production (CC1 π^0);

$$\nu_\mu, \bar{\nu}_\mu, \nu_e, \bar{\nu}_e, \nu_\mu \rightarrow \nu_e, \bar{\nu}_\mu \rightarrow \bar{\nu}_e$$
- 6 CC single charged pion resonant production (CC1 π^\pm);

$$\nu_\mu, \bar{\nu}_\mu, \nu_e, \bar{\nu}_e, \nu_\mu \rightarrow \nu_e, \bar{\nu}_\mu \rightarrow \bar{\nu}_e$$
- 6 CC coherent pion production (CCcoh);

$$\nu_\mu, \bar{\nu}_\mu, \nu_e, \bar{\nu}_e, \nu_\mu \rightarrow \nu_e, \bar{\nu}_\mu \rightarrow \bar{\nu}_e$$
- 6 CC multiple pion production (CCmulti- π);

$$\nu_\mu, \bar{\nu}_\mu, \nu_e, \bar{\nu}_e, \nu_\mu \rightarrow \nu_e, \bar{\nu}_\mu \rightarrow \bar{\nu}_e$$
- 6 CC deep inelastic scattering (CCDIS);

$$\nu_\mu, \bar{\nu}_\mu, \nu_e, \bar{\nu}_e, \nu_\mu \rightarrow \nu_e, \bar{\nu}_\mu \rightarrow \bar{\nu}_e$$
- 6 Groups of miscellaneous CC processes (CCmisc);

$$\nu_\mu, \bar{\nu}_\mu, \nu_e, \bar{\nu}_e, \nu_\mu \rightarrow \nu_e, \bar{\nu}_\mu \rightarrow \bar{\nu}_e$$
- 4 NC single neutral pion production (NC1 π^0); $\nu_\mu, \bar{\nu}_\mu, \nu_e, \bar{\nu}_e$
- 4 NC single charged pion production (NC1 π^\pm); $\nu_\mu, \bar{\nu}_\mu, \nu_e, \bar{\nu}_e$
- 4 NC coherent interactions (NCcoh); $\nu_\mu, \bar{\nu}_\mu, \nu_e, \bar{\nu}_e$
- 4 NC single gamma production (NC1 γ); $\nu_\mu, \bar{\nu}_\mu, \nu_e, \bar{\nu}_e$
- 4 Groups of miscellaneous NC processes (NCmisc); $\nu_\mu, \bar{\nu}_\mu, \nu_e, \bar{\nu}_e$

In the above list of reaction modes, the following CC processes form the ‘miscellaneous’ category: CC1K, CC1 η , CC diffractive pion production, and CC1 γ . The NC miscellaneous category is formed of the equivalent NC processes, in addition to NC multiple pion production and NC DIS, and without NC1 γ , which is tracked separately. Processes that are neither listed here nor in the above list are not tracked in the NEUT MC simulation.

5.2.3 Kinematic Binning

The expected and observed kinematic distributions share the same binning schemes. They are binned in E_{rec} , for the μ -like samples, and (E_{rec}, θ) for the e -like samples, as specified in Tables 5.1 to 5.3. As mentioned in Section 5.1.1.1, the Super-K MC events are placed into MC templates binned in $(E_{\text{true}}, E_{\text{rec}}, \theta)$ before being summed over E_{true} bins. This E_{true} binning is the same for all samples and is specified in Table 5.4.

The μ -like samples are binned in E_{rec} up to 30 GeV, after which the neutrino flux is negligible. The e -like samples are only binned up to 1.25 GeV, as beyond this energy, the flux is primarily composed of NC and the intrinsic unoscillated ν_e and $\bar{\nu}_e$ components of the beam [105].

The binning schemes have been optimised (as described in Appendix I of Ref. [187]) to balance sensitivity to the oscillation parameters against computational requirements while ensuring a non-negligible number of events in each bin of the kinematic distributions.

The e -like samples include multiple θ bins for the following reasons. As discussed in Section 2.2.4.1, measurements of both neutrinos and antineutrinos are required to effectively measure δ_{CP} , so it is important to separate $\nu_\mu \rightarrow \nu_e$ and $\bar{\nu}_\mu \rightarrow \bar{\nu}_e$ flavour components. As shown in Figs. 5.2 and 5.4, while the ν -mode and $\bar{\nu}$ -mode $\bar{\nu}_e$ CCQE-like samples appear similar in E_{rec} their shape is clearly different in θ .

Range	Single Bin Width	Number of Bins
0 – 3 GeV	0.05 GeV	60
3 – 4 GeV	0.25 GeV	4
4 – 6 GeV	0.5 GeV	4
6 – 10 GeV	1 GeV	4
10 – 30 GeV	20 GeV	1
0 – 180°	180°	1

Table 5.1: (E_{rec}, θ) binning scheme used for both expected and observed kinematic distributions in the ν -mode and $\bar{\nu}$ -mode $\bar{\nu}_\mu$ CCQE-like samples. There are a total of 73 E_{rec} and 1 θ bins.

Range	Single Bin Width	Number of Bins
0 – 1.25 GeV	0.05 GeV	25
0 – 140°	10°	14
140 – 180°	40°	1

Table 5.2: (E_{rec}, θ) binning scheme used for both expected and observed kinematic distributions in the ν -mode and $\bar{\nu}$ -mode $\bar{\nu}_e$ CCQE-like samples. There are a total of 25 E_{rec} and 15 θ bins.

Range	Single Bin Width	Number of Bins
0 – 0.4 GeV	0.4 GeV	1
0.4 – 0.55 GeV	0.15 GeV	1
0.55 – 1.25 GeV	0.1 GeV	7
0 – 180°	60°	3

Table 5.3: (E_{rec}, θ) binning scheme used for both expected and observed kinematic distributions in the ν -mode $\bar{\nu}_e \text{CC}1\pi^+$ -like sample. There are a total of 9 E_{rec} and 3 θ bins.

Range (GeV)	Single Bin Width (GeV)	Number of Bins
0.0 – 0.3	0.05	6
0.3 – 1	0.025	28
1 – 3	0.05	40
3 – 3.5	0.1	5
3.5 – 4	0.5	1
4 – 5	1	1
5 – 7	2	1
7 – 10	3	1
10 – 30	20	1

Table 5.4: E_{true} binning scheme used in all samples to bin Super-K MC events. There are a total of 84 E_{true} bins.

5.2.4 Treatment of Systematic and Oscillation Parameters

A total of 137 systematic parameters are incorporated into the analysis to account for the effects of systematic uncertainties in the flux, detector and interaction models. These are detailed in Appendix A. All systematic parameters are randomised (accounting for correlations) when computing the marginal likelihood of Eq. (5.4), using a multivariate Gaussian prior PDF as defined by two covariance matrices, with the only exceptions being the 2p2h energy dependence parameters ($f_{\text{Shape}_{2p2hLowE\nu}}^{\text{ND}}$, $f_{\text{Shape}_{2p2hHighE\nu}}^{\text{ND}}$, $f_{\text{Shape}_{2p2hLowE\nu}}^{\text{ND}}$, $f_{\text{Shape}_{2p2hHighE\nu}}^{\text{ND}}$), which use uniform prior PDFs due to a lack of constraint from both the near detectors and external data (see Section 4.2.3). These covariance matrices are the near detector matrix (see Section 4.3), characterising flux and cross-section systematic parameters, and the Super-K matrix (see Section 4.5), characterising detector effects in Super-K as well as secondary interactions (SI) and the photonuclear effect (PN). These matrices are shown in Figs. 4.36, A.1 and A.2.

Oscillation parameters are randomised according to the prior PDFs defined in Table 5.5. As discussed in Section 2.2.4.1, T2K has little sensitivity to θ_{12} and Δm_{21}^2 , so these parameters are constrained with Gaussian prior PDFs from the PDG2019 global

Parameter(s)	Prior PDF	Range
$\sin^2 \theta_{23}$	Uniform	[0.3, 0.7]
$\sin^2 \theta_{13}$ T2K-only	Uniform	[0, 0.4]
$\sin^2 2\theta_{13}$ reactors	Gaussian	0.0853 ± 0.0027
$\sin^2 2\theta_{12}$	Gaussian	0.851 ± 0.020
$ \Delta m_{3j}^2 $	Uniform	$[2.3, 2.7] \times 10^{-3} \text{ eV}^2/\text{c}^4$
Δm_{21}^2	Gaussian	$(7.53 \pm 0.18) \times 10^{-5} \text{ eV}^2/\text{c}^4$
δ_{CP}	Uniform	$[-\pi, +\pi]$
Mass Ordering	Fixed	NO or IO

Table 5.5: Oscillation parameters prior PDFs used in the T2K Run 1-10 oscillation analysis. All Gaussian priors are from [35].

fit average ($\sin^2 2\theta_{12} = 0.851 \pm 0.020$ and $\Delta m_{21}^2 = [7.53 \pm 0.18] \times 10^{-5} \text{ eV}^2/\text{c}^4$) [35]. As T2K is sensitive to $\sin^2 \theta_{23}$, $|\Delta m_{3j}^2|$, and δ_{CP} , uniform prior PDFs spanning the entire range of these parameters would be applicable, although in practice their parameter space is sampled in reduced ranges (as listed in Table 5.5). This is done in order to maintain efficiency (adequately sampling the full ranges requires a computationally-intractable number of samples), while ensuring that reducing these ranges does not alter the results.

T2K is sensitive to and produces constraints on θ_{13} ; however, the world’s most accurate measurements of this parameter are from reactor antineutrino experiments (see Section 2.3). So, to better constrain this parameter and obtain increased sensitivity to other parameters, the PDG2019 global fit [35] reactor average of 0.0853 ± 0.0027 is used as a prior PDF on $\sin^2 2\theta_{13}$ for most measurements presented in this chapter. This prior PDF will subsequently be referred to as the ‘reactor constraint’ and constraints produced with it will be denoted ‘T2K+reactor’, as opposed to those produced with the use of a uniform prior PDF on $\sin^2 2\theta_{13}$, denoted ‘T2K-only’.

As discussed in Section 5.1.1.2, the nuisance parameter space is randomly sampled to calculate the marginal likelihood and that the number of samples depends on the dimensionality of this space and how tightly constraining its prior PDFs are. Therefore the number of random samples varies with the number of parameters of interest and whether the reactor constraint is or isn’t applied, as shown in Table 5.6. The marginal likelihood is evaluated at a number of grid points in the space of the parameter(s) of interest, as specified in Table 5.7.

Number of Parameters of Interest	With Reactor	Without Reactor
	Constraint	Constraint
1	4×10^4	8×10^4
2	1×10^4	2×10^4

Table 5.6: The number of randomly drawn samples of the nuisance parameter space used to compute the marginal likelihood, varying with the number of parameters of interest and whether the constraint on $\sin^2 2\theta_{13}$ from reactor experiments is used.

Parameter(s) of interest	Number of Points	Range
$\sin^2 \theta_{23}$	101	[0.3, 0.7]
$\sin^2 \theta_{13}$ T2K-only	101	[0.007, 0.053]
$ \Delta m_{3j}^2 $	101	$[2.2, 2.8] \times 10^{-3} \text{ eV}^2/\text{c}^4$
δ_{CP}	101	$[-\pi, \pi]$
$\sin^2 \theta_{23}, \Delta m_{3j}^2 $	81×51	[0.3, 0.7], $[2.2, 2.8] \times 10^{-3} \text{ eV}^2/\text{c}^4$
$\sin^2 \theta_{13}, \delta_{CP}$ T2K-only	81×51	[0.007, 0.053], $[-\pi, \pi]$
$\sin^2 \theta_{13}, \delta_{CP}$ T2K+reactor	81×51	[0.015, 0.036], $[-\pi, \pi]$

Table 5.7: The grid points used to evaluate the marginal likelihood as a function of the parameter(s) of interest. The grid points are evenly spaced within the specified ranges.

For the purpose of determining predicted event rates, kinematic distributions, and sensitivities, a number of simulated pseudo-data sets are used, each referred to as an ‘Asimov’ data set. These are generated using an assumed set of fixed oscillation and systematic parameter values and without statistical fluctuations. The Asimov data sets are used as representative data in order to determine the median sensitivity to the oscillation parameters without requiring the generation of large numbers of pseudo-data sets. The Asimov data sets are denoted ‘Asimov A’, ‘Asimov B’, ‘Asimov BF NO’, and ‘Asimov BF IO’ and have oscillation parameter values chosen as follows and summarised in Table 5.8. In all cases, the systematic parameters are set to their nominal values.

- **Asimov A** - The central values of the PDG2019 global fit averages are used for $\sin^2 2\theta_{12}$, Δm_{21}^2 , and $\sin^2 2\theta_{13}$, while for the other oscillation parameters the most probable values from the T2K Run 1-4 ν -mode Bayesian analysis [191] are used (which remain close to the recent T2K best fit values [5]). Specifically, the Asimov A data set corresponds to near-maximal CP-violation and a $\sin^2 \theta_{23}$ value in the upper octant. The purpose of this data set is to evaluate the expected results close to the most likely parameter values (as indicated by previous T2K results), before un-blinding the observed data.
- **Asimov B** - This data set is generated with the same values of the oscillation parameters as for Asimov A, except for δ_{CP} , which is set to the CP-conserving

value of 0, and for $\sin^2 \theta_{23}$, which is set to a value in the lower octant. The purpose of this data set is to evaluate the expected results (before un-blinding the observed data) at values of δ_{CP} and $\sin^2 \theta_{23}$ far from the most likely values (as indicated by previous T2K results) while still being consistent with values allowed by neutrino global fit results (see Section 2.3).

- **Asimov BF NO/IO** - These data sets contain the observed T2K Run 1-10 best-fit values (for NO and IO, respectively), calculated with the reactor constraint (see Table 5.13). The parameters $\sin^2 \theta_{12}$ and Δm_{12}^2 are not measured by T2K, so the PDG2019 [35] global best-fit values are used. The purpose of these data sets are to assess the compatibility of predictions produced at the observed best-fit points with the observed T2K data and to assess the extremity of the observations, as will be discussed in Section 5.6.4.

Parameter(s)	Asimov A	Asimov B	Asimov BF NO	Asimov BF IO
$\sin^2 \theta_{23}$	0.528	0.45	0.552	0.556
$\sin^2 \theta_{13}$ reactors	0.0218	0.0218	0.0218	0.0221
$\sin^2 \theta_{12}$	0.307	0.307	0.307	0.307
$ \Delta m_{3j}^2 $ $(10^{-3} \text{ eV}^2/\text{c}^4)$	2.51	2.51	2.49	2.46
Δm_{21}^2 $(10^{-5} \text{ eV}^2/\text{c}^4)$	7.53	7.53	7.53	7.53
δ_{CP}	-1.60	0	-2.01	-1.38
Mass Ordering	Normal	Normal	Normal	Inverted

Table 5.8: Four sets of Asimov oscillation parameters values used to compute expected event rates and kinematic distributions. The Asimov A and B parameter sets are used to evaluate the sensitivity of T2K to the oscillation parameters before un-blinding the data. The Asimov BF NO/IO sets use the best-fit points from fits to the T2K Run 1-10 data for all oscillation parameters except for $\sin^2 \theta_{12}$ and Δm_{12}^2 , for which the PDG2019 [35] global best-fit values are used. The Asimov BF NO/IO sets are used to calculate Feldman-Cousins critical values (see Section 5.1.1.2).

5.2.5 Updates Since the Previous Analysis

In this thesis, results are presented from T2K analyses using data collected over two run periods, T2K Runs 1-9 and 1-10. While the analysis presented in this chapter uses Run 1-10 data, it is worth briefly highlighting the main improvements compared to the Run 1-9 analysis, reported in [3, 5]. As a result of the the following improvements, the overall uncertainties on the predicted event rates decreased by a factor of 1.1 - 1.8, depending on the sample.

- During T2K Run 10 the beam was set purely to ν -mode corresponding to an increase of 31.6% more ν -mode data for Super-K.

- 98.8% and 117% more data in the ν and $\bar{\nu}$ modes, respectively, used for the near-detector fit.
- Improved constraints on the flux: Results from the NA61/SHINE experiment have been used for a number of analysis iterations to better understand the charged hadron yields resulting from a proton beam impacting a graphite target, as is used to produce the neutrino beam that serves T2K. Previous analysis iterations used data collected using a 2 cm long graphite target, whereas now a 90 cm long replica of the target for T2K is used. The result is a reduction of flux uncertainties, most notably for the unoscillated right-sign neutrino flux, where the uncertainty has reduced from $\sim 10\%$ to $\sim 5\%$ [84].
- Improvements to the interaction model, all detailed in Ref. [119]:
 - The nuclear ground state model for CCQE interactions has changed from the relativistic Fermi gas (RFG) to the Benhar spectral function (SF) model. Instead of characterising the nucleus as a constant-density ‘box’ with fixed maximum nucleon momentum, as in RFG, SF is a shell model description of the nucleon momentum and removal energy, based on both theoretical calculations and electron scattering data. The SF model is strongly preferred over RFG by both electron scattering data [123] and exclusive neutrino cross-section measurements [124, 125].
 - Additional systematic parameters have been added to suppress the predicted CCQE cross-section at low Q^2 in order to increase compatibility with both MINERvA [211] and ND280 [135] measurements. These replace the random phase approximation corrections used in the RFG model.
 - As the SF is more compatible with electron scattering data, more detailed comparisons to such data can be made, resulting in both a more sophisticated treatment of and reduced uncertainties in the nucleon removal energy. This now reflects the nuclear shell structure rather than being a single value, and is implemented in terms of modifying outgoing lepton kinematics rather than the previous ad hoc implementation.
 - An uncertainty in the energy-dependence of 2p2h interactions has been quantified, and results from differences between three valid interaction models: Nieves [192], Martini [142] and SuSAv2 [144].
 - The near detector analysis shows a discrepancy between the predicted and observed low momentum pion spectrum at ND280 [119]. This is believed to originate from the non-resonant isospin-1/2 pion production channels of the Rein-Sehgal model, which is tuned to ν -mode data sets only, with a lack of $\bar{\nu}$ -mode samples that can be tuned to. To account for this, an ad hoc uncertainty was added to anti-neutrino interactions producing low momentum

charged pions, introducing $\nu/\bar{\nu}$ freedom for true pion-producing events that have a high likelihood of entering the CCQE-like selections at Super-K.

- Improved constraints and tuning of pion FSI from external DUET data (amongst others) [168, 169] gives both a smaller uncertainty on such processes and a correlated treatment between carbon and oxygen (as ND280 performs measurements on both hydrocarbon and water targets). Therefore, unlike in previous analyses, FSI parameters can be fit at the near detectors.
 - The treatment of pion secondary interactions (SI) in NEUT is improved with the implementation of a cascade model [169], replacing the previously used GEANT4 prediction, which showed significant discrepancies compared to external data [212]. The result is a reduction of pion SI uncertainties.
 - The modelling and parametrization of the uncertainties of both multi-pion production and DIS has been substantially improved. Many small updates were made to the DIS interaction model, as well as using updated Bodek-Yang corrections to the low- Q^2 region. Additionally, in previous analysis iterations, a single uncertainty was applied to cover all of CCDIS, CCmulti- π and CCmisc (i.e. CC1K, CC1 η , CC diffractive pion production, and CC1 γ); however, due to their importance in future T2K/SK atmospheric and T2K/NO ν A joint fits, a separate and more sophisticated treatment of CCDIS and CCmulti- π uncertainties were required.
 - Modifications to the outgoing lepton momentum in CC interactions are now applied in order to account for the electrostatic Coulomb potential of the nucleus. This potential has been fit to electron scattering data [129].
- Improvements to the near detector fit, all detailed in Ref. [90]:
 - The near detector fit now incorporates the updated neutrino flux and interaction models and constraints, as detailed above.
 - A new selection framework is implemented, that introduces new $\bar{\nu}$ -mode ν_μ and $\bar{\nu}_\mu$ multi- π selections, matching the existing ν -mode selections, instead of selecting based on track multiplicity, as in previous analyses.
 - A new parameterisation to include the effect of limited Monte-Carlo statistics on the likelihood, using the Barlow-Beeston method [184].
 - All existing Super-K data from all runs were reprocessed with an updated PMT gain correction [105]. The result is a minor change in the number of observed neutrino events from Runs 1-9 that pass selection cuts, as shown in Table 5.9.

Sample	Number of Candidate Events	
	Before	After
ν -mode	$\bar{\nu}_\mu$ CCQE-like	243
	$\bar{\nu}_e$ CCQE-like	75
	$\bar{\nu}_e$ CC1 π^+ -like	15
$\bar{\nu}$ -mode	$\bar{\nu}_\mu$ CCQE-like	140
	$\bar{\nu}_e$ CCQE-like	15

Table 5.9: Change in the number of observed candidate neutrino events that pass Super-K selection cuts in the T2K Run 1-9 dataset as a result of corrections to the PMT gain. Modified from Ref [105].

5.3 Predicted Kinematic Distributions and Event Rates

In this section, expected kinematic distributions and event rates are presented. Unless otherwise noted, all predictions are generated using the Asimov A parameters shown in Table 5.8 (as the Asimov A values are closer to previous T2K best-fit values than Asimov B) and with the full T2K Run 1-10 beam exposure. Additionally, the effects of systematic uncertainties on such predictions will be discussed. Although the observed data are displayed in a number of figures and tables in this section, all sensitivity studies were performed blind with respect to the T2K Run 10 data.

Figures 5.3 and 5.4 shows the unoscillated and Asimov A predicted kinematic distributions, respectively. The comparison of these distributions clearly shows the oscillation ‘dip’ close to the flux peak in the μ -like samples, corresponding to $\bar{\nu}_\mu$ disappearance, and the e -like samples show the corresponding increase in events from $\bar{\nu}_e$ appearance. Additionally, a clear $\nu/\bar{\nu}$ separation is observed in the $\bar{\nu}_e$ CCQE-like samples in the θ dimension, as shown by Fig. 5.2. While the μ -like samples extend up to $E_{\text{rec}} = 30$ GeV, these plots only display up to 3 GeV to highlight the regions of greatest oscillation probability, but the full range is used in the likelihood calculations.

Integrating the kinematic distributions over E_{rec} and θ yields the total event rate for each sample. These are displayed, for four predicted oscillation pseudo-data sets and the observed T2K Run 1-10 data in Table 5.10. Additionally, this is shown broken down by contributions from individual reaction modes for the Asimov A prediction in Tables B.1 to B.5. As Table 5.10 shows, T2K can clearly distinguish between the no oscillation and Asimov A/B/BF pseudo-data sets and, as shown in Section 2.3, neutrinos have conclusively been shown to oscillate, so the no oscillation case will not be considered further in this thesis.

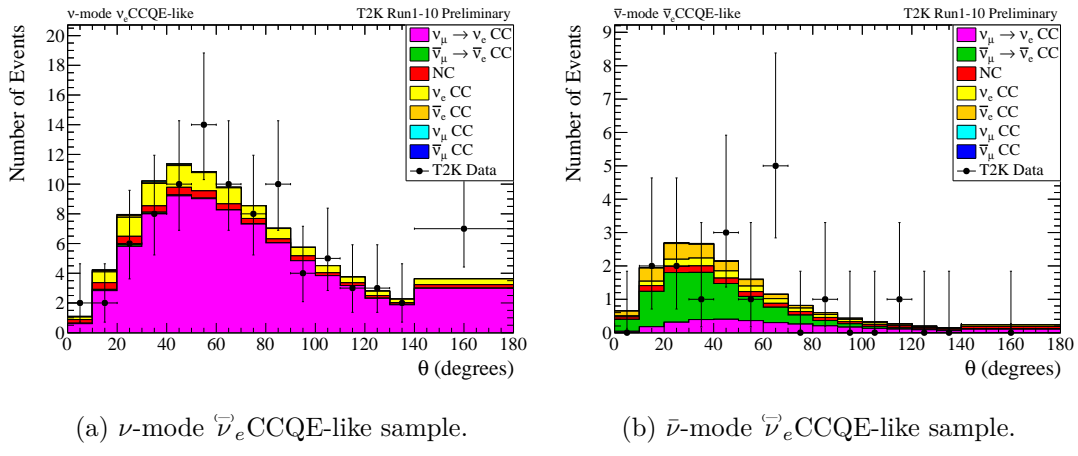


Figure 5.2: θ projections of the Asimov A predicted kinematic distributions (coloured histograms) shown in Figs. 5.4c and 5.4d, compared to observed kinematic distributions (black or white/blue points). Predictions are generated with the Asimov A oscillation parameter values in Table 5.8, nominal values of the systematic parameters, and are normalised to the T2K Run 1-10 beam exposure. The uncertainty shown around the data points on the 1D plots accounts for statistical uncertainty only. The uncertainty range is chosen to include all points for which the measured number of data events is inside the 68% confidence interval of a Poisson distribution centred at that point.

Sample	Predicted Asimov Hypothesis					Observed
	No osc.	A	B	BF	NO	
ν -mode	$\langle\bar{\nu}_\mu\rangle$ CCQE-like	1571.4	345.5	361.8	354.0	318
	$\langle\bar{\nu}_e\rangle$ CCQE-like	19.6	93.8	69.8	95.2	94
	$\langle\bar{\nu}_e\rangle$ CC1 π^+ -like	2.9	8.8	6.8	8.9	14
$\bar{\nu}$ -mode	$\langle\nu_\mu\rangle$ CCQE-like	444.5	135.1	138.8	137.9	137
	$\langle\nu_e\rangle$ CCQE-like	6.3	15.9	16.4	16.9	16
Best-fit $-2 \ln \lambda$		-	8.4	8.6	8.2	476.2

Table 5.10: Predicted and observed event rates in each sample, using the full T2K Run 1-10 beam exposure and data. Four different hypotheses have been used to generate the predictions: no neutrino oscillations, the Asimov A and B oscillation parameter sets defined in Table 5.8, and an Asimov parameter set with true values equal to the T2K Run 1-10 best fit values (Asimov BF NO) from Table 5.13. Also shown are the best-fit $-2 \ln \lambda$ values for the predicted and observed data, with a detailed discussion of the agreement between data and prediction following in Section 5.6.4.

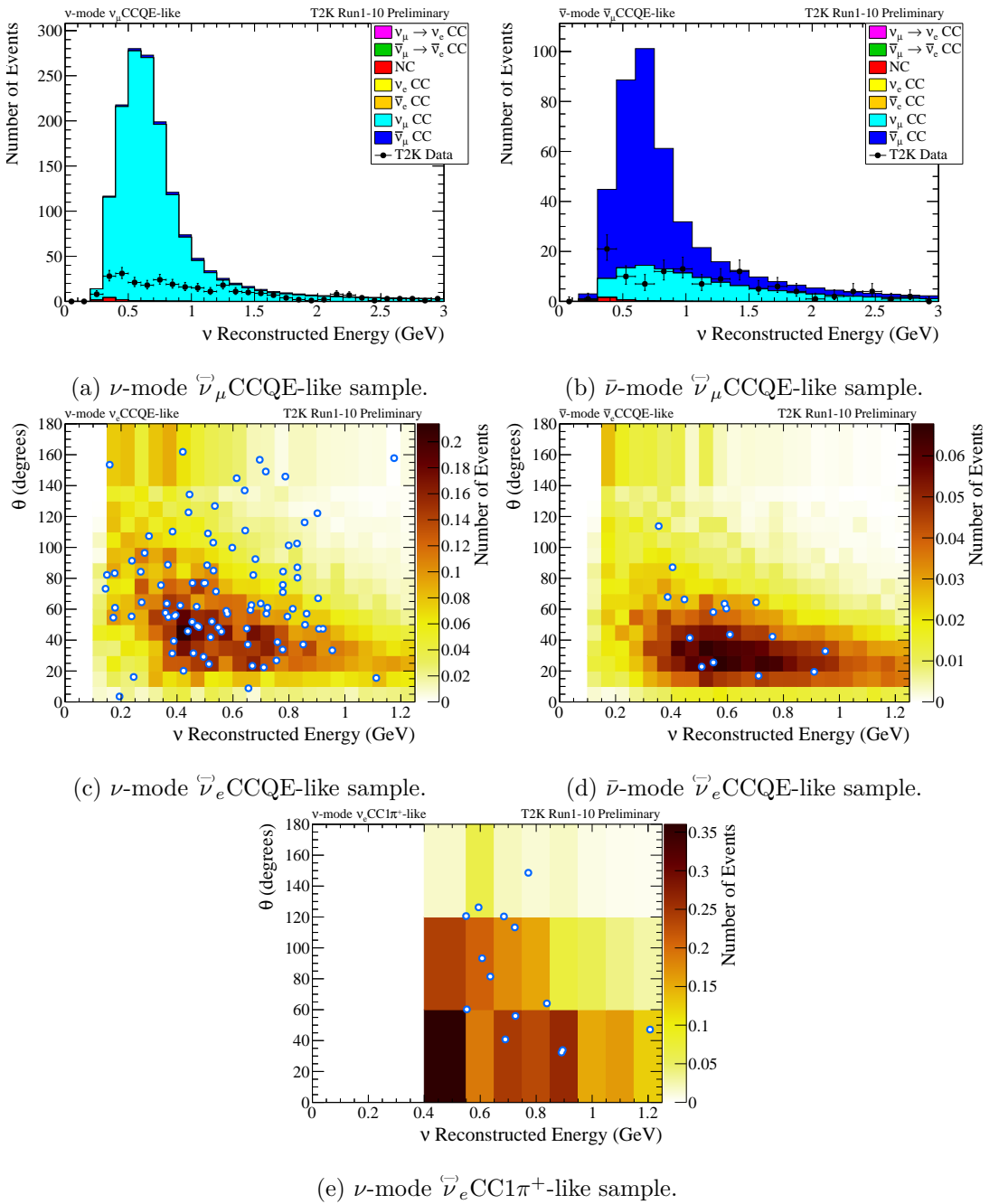


Figure 5.3: Unoscillated predicted kinematic distributions (coloured histograms) compared to the T2K Run 1-10 observed kinematic distributions (black or white/blue points). Predictions are generated under the assumption of no neutrino oscillations, with nominal values of the systematic parameters, and are normalised to the T2K Run 1-10 beam exposure. The uncertainty shown around the data points on the 1D plots accounts for statistical uncertainty only. The uncertainty range is chosen to include all points for which the measured number of data events is inside the 68% confidence interval of a Poisson distribution centred at that point.

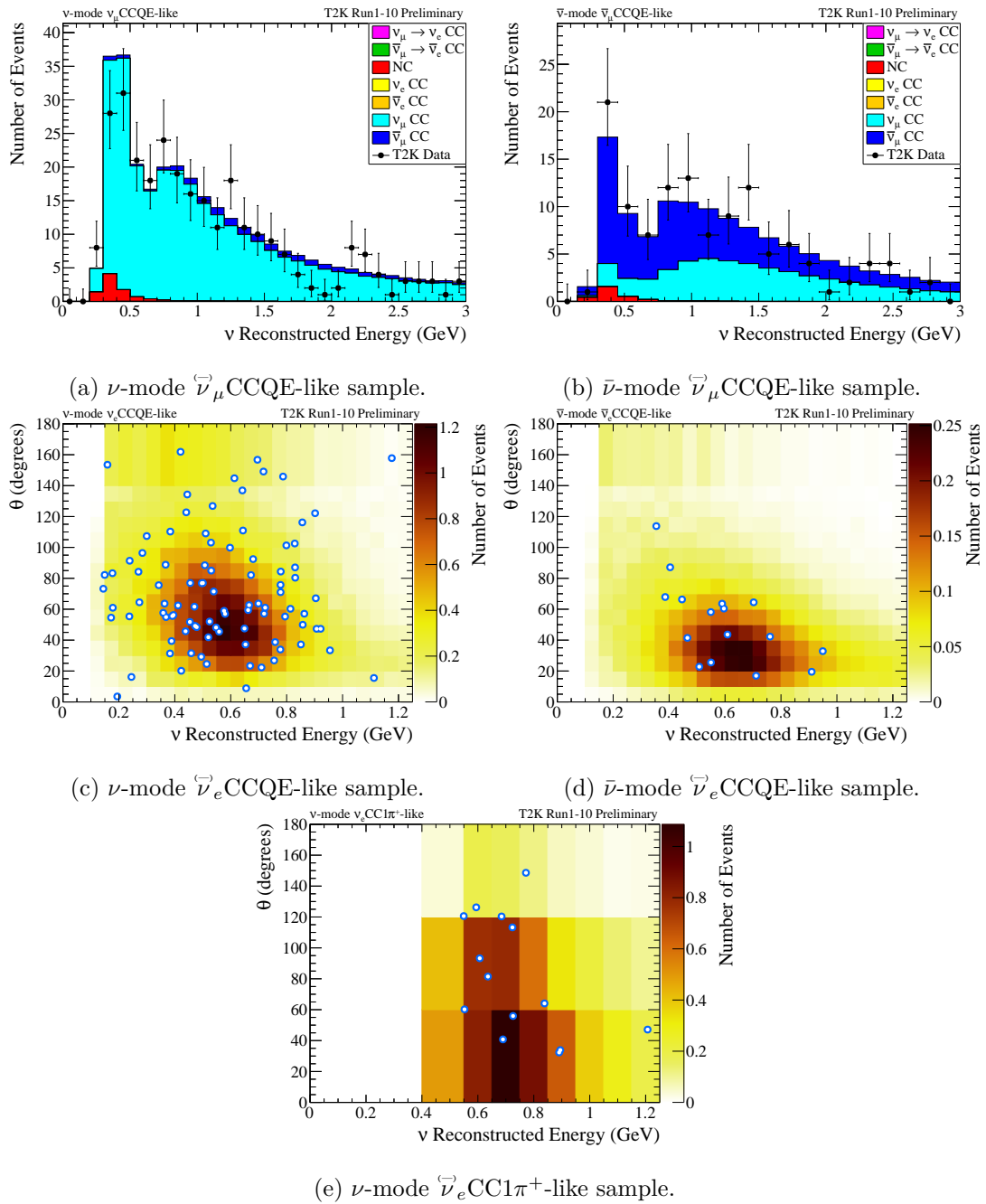


Figure 5.4: Asimov A predicted kinematic distributions (coloured histograms) compared to observed kinematic distributions (black or white/blue points). Predictions are generated with the Asimov A oscillation parameter values in Table 5.8, nominal values of the systematic parameters, and are normalised to the T2K Run 1-10 beam exposure. The uncertainty shown around the data points on the 1D plots accounts for statistical uncertainty only. The uncertainty range is chosen to include all points for which the measured number of data events is inside the 68% confidence interval of a Poisson distribution centred at that point.

5.3.1 Effect of Systematic Uncertainties on the Predicted Kinematic Distributions

This analysis includes 137 systematic parameters to account for the effects of flux, cross-section, and Super-K detector + SI + PN uncertainties. Of these parameters, almost all of the flux and cross-section parameters are constrained in the near detector fit (see Appendix A). It is important to understand the effect of systematic uncertainties on the predicted kinematic distributions, particularly on the ratio of ν and $\bar{\nu}$ event rates, for the following reasons:

- In general, underestimating the size of systematic uncertainties causes a corresponding underestimation of the uncertainty in the predicted kinematic distributions, resulting in less of the parameter space being compatible with observations and therefore artificially tightening the observed oscillation parameter constraints. Conversely, overestimating the size of systematic uncertainties results in artificially weakening the observed oscillation parameter constraints.
- If correlations between systematic parameters exist but are not taken into account (or are improperly accounted for), the oscillation parameter constraints could be biased. This is demonstrated for δ_{CP} as follows: As discussed in Section 2.2.4.1, the effect of δ_{CP} is to introduce a difference between $P(\nu_\mu \rightarrow \nu_e)$ and $P(\bar{\nu}_\mu \rightarrow \bar{\nu}_e)$, which results in the ν -mode ($\bar{\nu}$ -mode) e -like event rate reaching a minimum (maximum) at $+\frac{\pi}{2}$ and a maximum (minimum) at $-\frac{\pi}{2}$, as illustrated by Fig. 5.22a. From this, measurements of the e -like event rates in both ν and $\bar{\nu}$ modes are crucial to determining δ_{CP} . Therefore, if there exists an anti-correlation in the ν and $\bar{\nu}$ event rates caused by systematic effects, the predicted ν -mode and $\bar{\nu}$ -mode e -like event rates for each value of δ_{CP} could shift to mimic the event rates that would be produced by different values of δ_{CP} in the absence of such an anti-correlation, resulting in a biased (i.e. shifted) constraint on δ_{CP} .

Correlated parameters of particular importance in this regard are those representing the uncertainties on the ν_e/ν_μ and $\bar{\nu}_e/\bar{\nu}_\mu$ CC cross-section ratios, σ_{ν_e} and $\sigma_{\bar{\nu}_e}$, which are applied respectively to ν_e and $\bar{\nu}_e$ events. Their fractional error from the near detector fit is $\sim 2.8\%$ and they are partially anti-correlated, with non-diagonal elements in the covariance matrix of -0.0004 [210]. As shown in Table 5.11, these parameters are major contributors to systematic uncertainties in the e -like event rates and give the largest contribution to the uncertainty in the ratio of ν to $\bar{\nu}$ e -like event rates.

For the reasons listed above, it is important to correctly model systematic uncertainties and their correlations. As detailed in Chapter 4, the list of considered systematic uncertainties is comprehensive and (due to fits to near detector, Super-K atmospheric, and external data) results in predictions that are generally in excellent agreement with data. In the near detector and Super-K atmospheric fits, correlations between systematic parameters are automatically accounted for and constrained. For some interaction

processes, most notably 2p2h (see Section 4.2.3), there exist a number of valid, competing interaction models, potentially having different systematic uncertainties. The effects of these alternate models, their uncertainties, and any biases they may cause, are considered in Section 5.5.

The effects of each category of systematic parameter on the expected event rates are shown in Table 5.11, with the effects of the unconstrained cross-section parameters also shown individually. This shows that the ν -mode $\overset{\leftrightarrow}{\nu}_e \text{CC}1\pi^+$ -like sample has by far the largest systematic uncertainty out of all samples, driven primarily by Super-K detector, SI, and PN uncertainties. Figure 5.5 shows a comparison between the pre ND fit and post ND fit E_{rec} projections of the nominal Asimov A kinematic distributions and associated 1σ systematic uncertainties. The postfit distributions show a large reduction in systematic uncertainties compared to the prefit distributions, clearly demonstrating the value of the near detector constraint.

Error source	$\overset{\leftrightarrow}{\nu}_\mu \text{CCQE-like}$		$\overset{\leftrightarrow}{\nu}_e \text{CC}1\pi^+$ -like		$\overset{\leftrightarrow}{\nu}_e \text{CCQE-like}$	
	ν -mode	$\bar{\nu}$ -mode	ν -mode	$\bar{\nu}$ -mode	$\nu/\bar{\nu}$	
SK detector + SI + PN	2.2	1.9	13.2	3.0	4.0	1.3
Flux+xsec (constr.)	2.0	2.3	4.0	2.0	2.3	1.7
2p2h energy dependence	0.4	0.4	0.0	0.2	0.2	0.2
Isospin $\frac{1}{2}$ non-res. (low p_π)	0.5	2.6	0.1	0.2	2.3	2.1
$\sigma_{\nu_e}, \sigma_{\bar{\nu}_e}$	0.4	0.4	2.7	2.6	1.5	3.0
NC 1γ	0.4	0.4	0.0	1.4	2.4	1.0
NC misc.	0.5	0.5	0.8	0.3	0.4	0.3
Flux+xsec (un-constr.)	0.6	2.6	2.7	2.9	3.6	3.8
All syst.	3.1	4.1	14.1	4.8	6.0	4.4

Table 5.11: Fractional uncertainties (%) on the event rates by error source and sample, calculated with expected events rates generated according to the Asimov A oscillation parameter values from Table 5.8 and by randomly drawing 10^4 sets of the indicated systematic parameters. The final column is the fractional uncertainty (%) on the ratio of ν -mode to $\bar{\nu}$ -mode events in the $\overset{\leftrightarrow}{\nu}_e \text{CCQE-like}$ sample. The central block of rows show the contributions to the uncertainties from the cross-section (xsec) parameters that are un-constrained in the near detector fit. The final row, ‘All syst.’, does not include the effects of any oscillation parameters. For all uncertainties except for those in the final row, not all correlations are taken into account, so the sum in quadrature of the individual uncertainties is not expected to equal the total error.

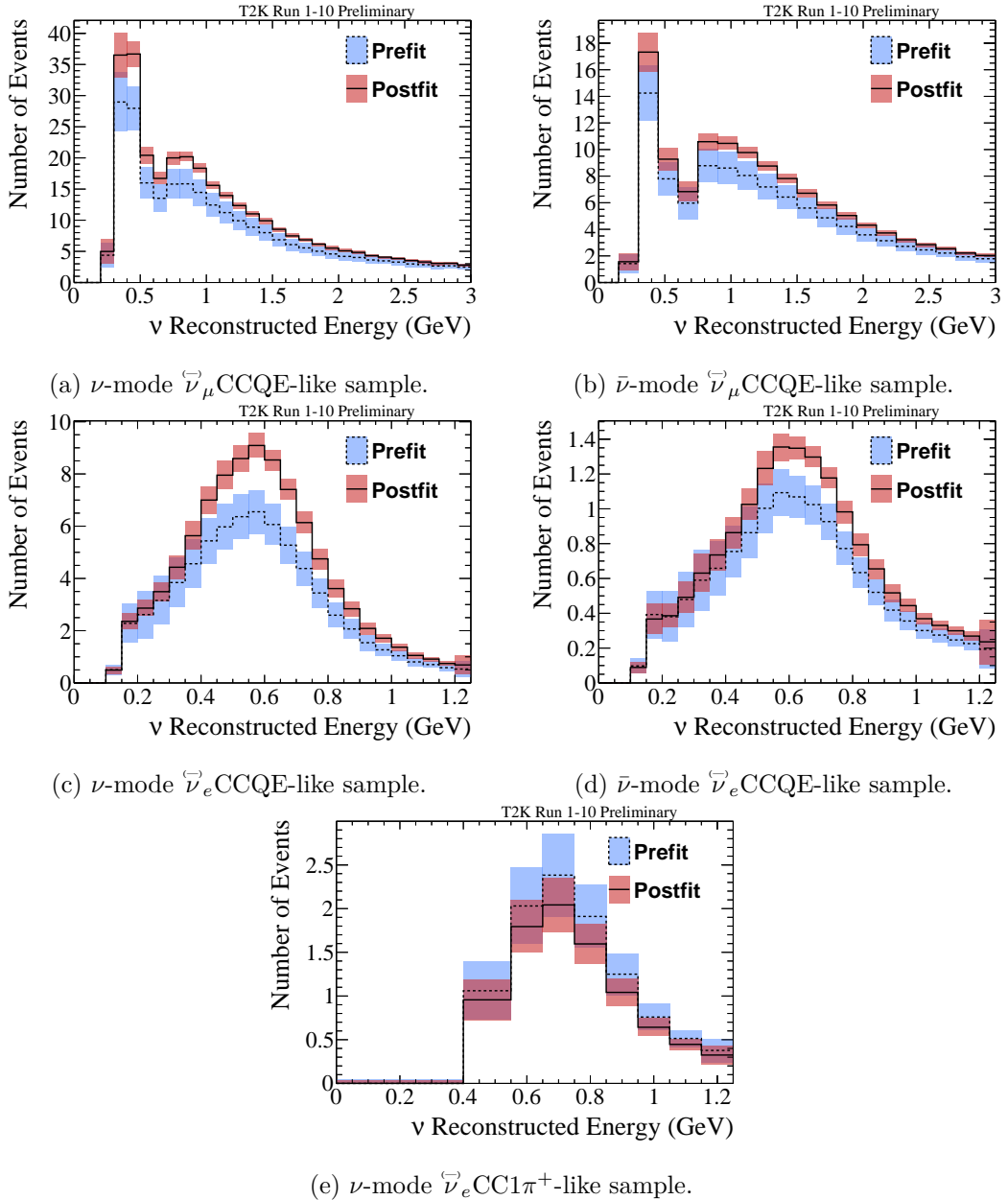


Figure 5.5: Predicted nominal E_{rec} distributions (black lines) with $\pm 1\sigma$ systematic errors (shaded regions), both pre and post near detector fit. Generated with the Asimov A oscillation parameter values in Table 5.8 and by randomly sampling 10000 sets of systematic parameters.

5.4 Predicted Sensitivity to the Oscillation Parameters

Sensitivity studies have been performed to gauge the ability of T2K to measure various oscillation parameters of interest under the assumption of various oscillation hypotheses, in particular, those with the Asimov A and B oscillation parameter values listed in Table 5.8. The sensitivity has been evaluated (according to the method described in Section 5.1) in both mass orderings and with and without the constraint on $\sin^2 \theta_{13}$ from reactor experiments. The predicted $\Delta\chi^2$ functions and the corresponding 1D confidence regions are shown in Figs. 5.6 to 5.9 for δ_{CP} , $\sin^2 \theta_{13}$, $\sin^2 \theta_{23}$, and $|\Delta m_{3j}^2|$,

respectively. Additionally, to show correlations between the oscillation parameters, 2D confidence regions are shown in Fig. 5.10 for δ_{CP} vs. $\sin^2 \theta_{13}$ and in Fig. 5.11 for $|\Delta m_{3j}^2|$ vs. $\sin^2 \theta_{23}$. All confidence regions are defined with respect to the maximum marginal likelihood across both mass orderings, as in Eq. (5.5).

Due to computational requirements, these sensitivity studies are performed with the constant $\Delta\chi^2$ method for constructing confidence regions, rather than the more accurate Feldman-Cousins method described in Section 5.1.2. As a result, the coverage of the expected δ_{CP} confidence regions are not expected to be perfectly accurate.

As Fig. 5.6 shows, the Asimov A pseudo-data set (true $\delta_{CP} = -1.601$) gives a far stronger constraint on δ_{CP} than that of Asimov B (true $\delta_{CP} = 0$): while in the Asimov A NO with reactor constraint case, CP-conservation ($\delta_{CP} = 0, \pm\pi$) is expected to be excluded at the 90% confidence level (CL), only a small region around $(+)\frac{\pi}{2}$ is excluded in the Asimov B NO (IO) with reactor constraint case.

Additionally, Asimov A with the reactor constraint disfavours the IO, excluding it entirely at the 1σ CL and excluding all but a small region close to $\delta_{CP} = -\frac{\pi}{2}$ at the 90% CL. By contrast, Asimov B has little sensitivity to the MO, barely preferring a best fit point near $\delta_{CP} = -\pi$ in the IO instead of near the true value of $\delta_{CP} = 0$ in the NO. This results from the NO δ_{CP} and IO $\pi - \delta_{CP}$ degeneracy discussed in Section 2.2.4.1, combined with the small value of the $\sin \delta_{CP}$ interference term of the $P(\bar{\nu}_\mu \rightarrow \bar{\nu}_e)$ oscillation probability (see Eq. (2.30)) close to the CP-conserving values of δ_{CP} .

The use of the reactor constraint on $\sin^2 2\theta_{13}$ is clearly advantageous to measurements of δ_{CP} : For both Asimov A and B, it allows significantly larger region of δ_{CP} to be excluded, and for Asimov A, a larger separation between mass orderings is produced.

As Figs. 5.7 and 5.10 show, both with and without the use of the reactor constraint, $\sin^2 \theta_{13}$ is expected to be consistent with the PDG 2019 global best fit value at the 1σ CL. Correlations between δ_{CP} and $\sin^2 \theta_{13}$ are expected, and result in the widening of the δ_{CP} confidence regions compared to the above 1D δ_{CP} case.

As Fig. 5.11 shows, even with the reactor constraint applied, for NO, both Asimov A (true upper octant) or Asimov B (true lower octant) cases are expected to be consistent with both octants of $\sin^2 \theta_{23}$ at the 1σ CL.

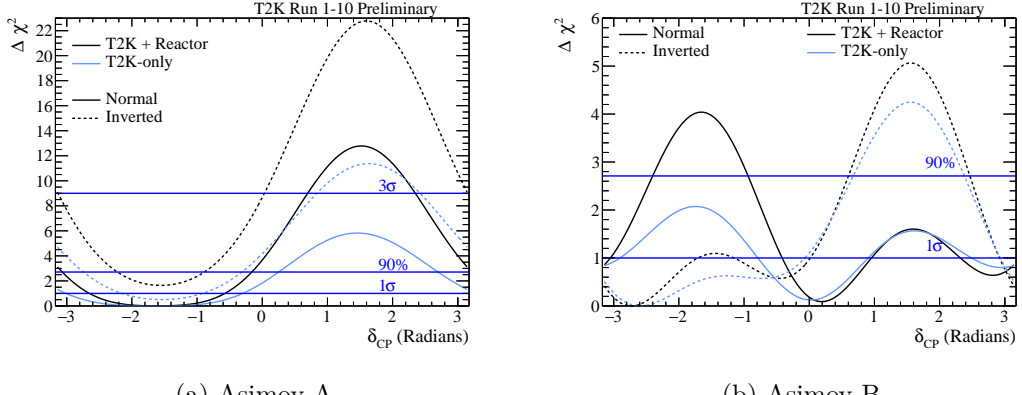


Figure 5.6: Predicted $\Delta\chi^2$ functions as a function of δ_{CP} , shown with and without the reactor constraint on $\sin^2 2\theta_{13}$, for both mass orderings, and with both Asimov A and B pseudo-data sets. Critical values are calculated using the constant $\Delta\chi^2$ method.

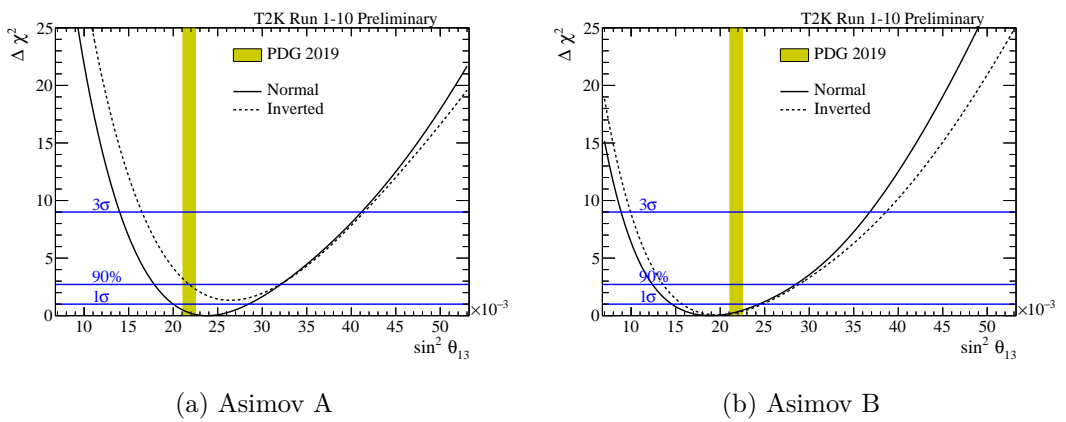


Figure 5.7: Predicted $\Delta\chi^2$ functions as a function of $\sin^2 \theta_{13}$, shown without the reactor constraint on $\sin^2 2\theta_{13}$ and shown for both mass orderings and with both Asimov A and B pseudo-data sets. Critical values are calculated using the constant $\Delta\chi^2$ method.

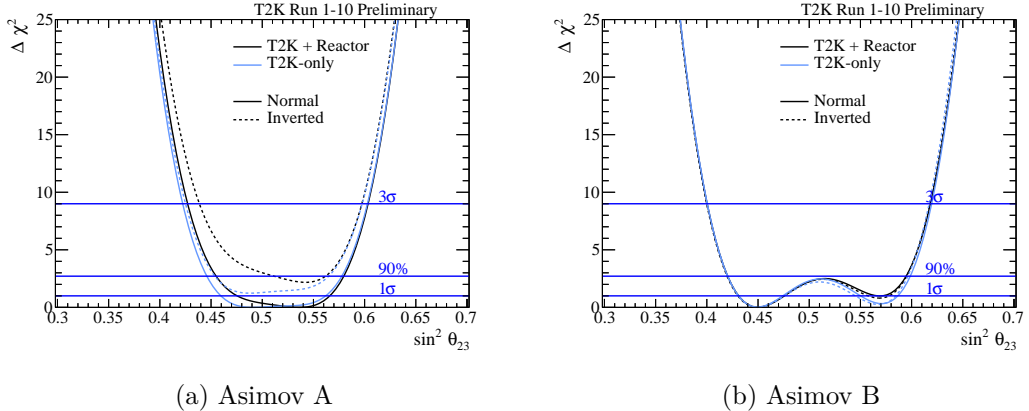


Figure 5.8: Predicted $\Delta\chi^2$ functions as a function of $\sin^2 \theta_{23}$, shown with and without the reactor constraint on $\sin^2 2\theta_{13}$, for both mass orderings, and with both Asimov A and B pseudo-data sets. Critical values are calculated using the constant $\Delta\chi^2$ method.

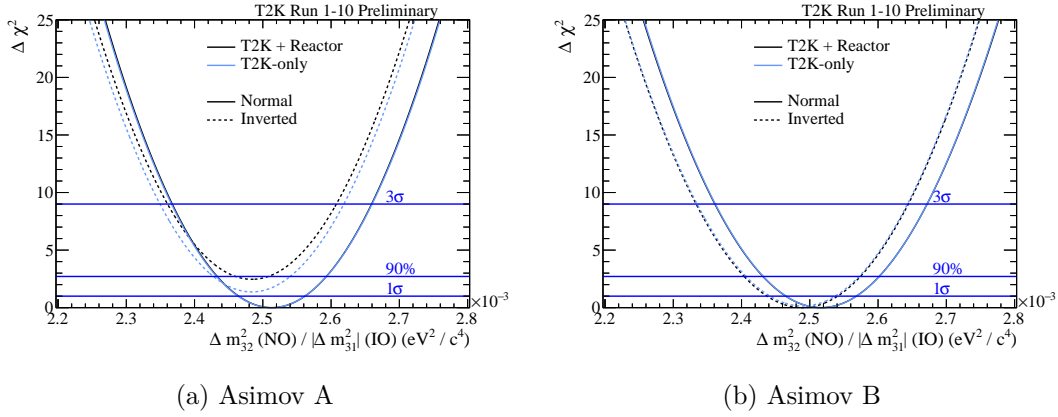


Figure 5.9: Predicted $\Delta\chi^2$ functions as a function of Δm_{32}^2 (NO) or $|\Delta m_{31}^2|$ (IO), shown with and without the reactor constraint on $\sin^2 2\theta_{13}$, for both mass orderings, and with both Asimov A and B pseudo-data sets. Critical values are calculated using the constant $\Delta\chi^2$ method.

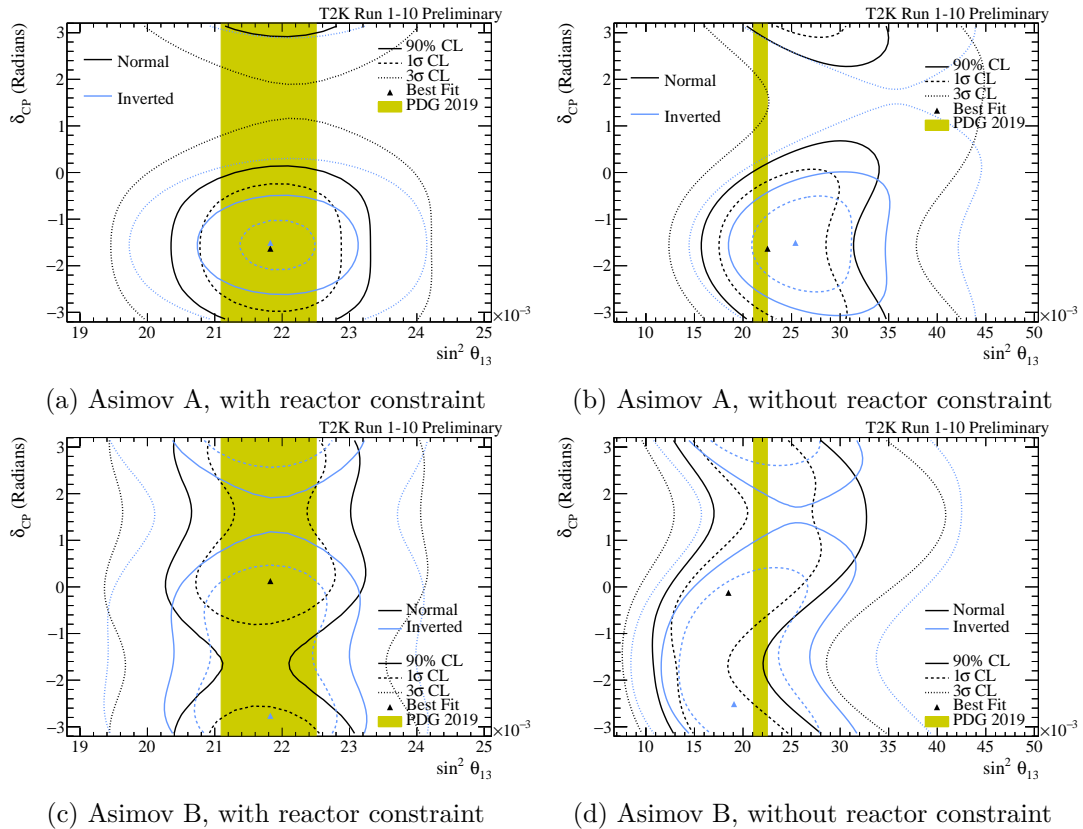


Figure 5.10: Predicted constraints on δ_{CP} vs. $\sin^2 \theta_{13}$, shown with and without the reactor constraint on $\sin^2 2\theta_{13}$, for both mass orderings, and with both Asimov A and B pseudo-data sets. The best fit value and $\pm 1\sigma$ error on $\sin^2 \theta_{13}$ from the 2019 PDG global fit [35] is shown as a vertical coloured band. Critical values are calculated using the constant $\Delta\chi^2$ method.

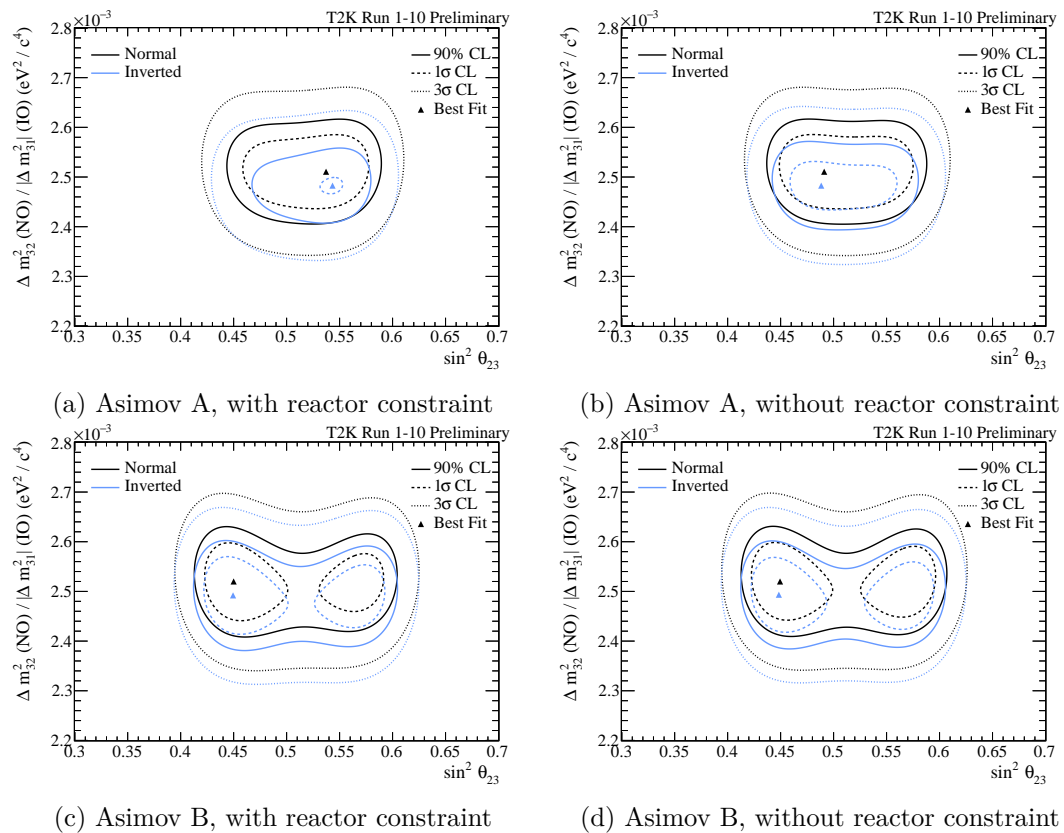


Figure 5.11: Predicted constraints on $|\Delta m_{32}^2|$ vs. $\sin^2 \theta_{23}$, shown with and without the reactor constraint on $\sin^2 2\theta_{13}$, for both mass orderings, and with both Asimov A and B pseudo-data sets. Critical values are calculated using the constant $\Delta\chi^2$ method.

5.5 Robustness of the Analysis to Alternate Cross-Section Models

Note: this section does not represent my own work and is summarised from Ref. [213], but is important for interpreting the results shown in later sections.

In the near detector fit, both flux and cross-section parameters are fit simultaneously, under the assumption of a particular cross-section model (see Section 4.2). Potential deficiencies [213] in the cross-section model that would result in an under or over-prediction of the event rates in the near or far detectors can be compensated by a corresponding change in the flux model to give the correct event rate prediction. Similarly, a deficiency in the flux model may be compensated for by an equivalent change in the cross-section model, making the analysis somewhat robust against differences between the models and near detector data. However, while such an approach ensures good agreement in the event rates, it can create biases in the shape of the predicted kinematic distributions at Super-K and therefore a shift in the oscillation parameter best-fit points and confidence regions.

To determine whether the conclusions of the oscillation analysis are robust against such biases, a number of studies have been performed, each corresponding to an alternative cross-section model. For each study, the ND280 and Super-K MC events are re-weighted according to the alternate models, then the near detector fit is regenerated and used along with the re-weighted Super-K MC as inputs to Asimov A and B oscillation parameter sensitivity studies. Any shifts in the oscillation parameter confidence regions are recorded and accounted for in the analysis as will be described below.

Although seven alternative cross-section models were studied, here only the alternate models that contribute to the largest shifts in the confidence regions will be discussed, which are as follows:

- **Non-QE CC0 π** - To account for the 10% MC/data discrepancy in the CC0 π selections at ND280 [119, 135], the T2K Run 1-10 oscillation analysis incorporates seven Q^2 normalisation parameters, applied to CCQE interactions, which allows the model a large amount of freedom to correct this difference. It is possible that such freedom is masking deficiencies in the non-QE contributions to the CC0 π sample, i.e. from 2p2h and pion absorption, and this is supported by MINERvA measurements [119, 211]. This alternative cross-section model is constructed by assigning the variation from the Q^2 normalisation parameters that is nominally assigned to CCQE to the CC0 π non-QE contributions to the CC0 π selection.
- **3-component CCQE** - In the nominal interaction model, a dipole form factor is assumed for the CCQE cross-section (see Section 4.2.2); however, this assumption is not theoretically well motivated and causes an underestimation of the uncertainties at high Q^2 , where external data are sparse [120, 213]. This alternative model instead uses a more sophisticated 3-component form factor, extending the two-component model of Ref. [214] with a quickly-decaying exponential term to

provide additional freedom [120].

- **Martini 2p2h** - A number of valid models exist that describe the poorly-constrained 2p2h process, and they differ by up to a factor of two on the total 2p2h cross-section, as well as giving different ν and $\bar{\nu}$ predictions. Rather than using the nominal Nieves 2p2h model, this alternative model is that of Martini [142], which principally increases the 2p2h cross-section for neutrinos by about a factor of two compared to the Nieves model.

Non-negligible shifts in the confidence regions and/or best-fit points were only observed for Δm_{3j}^2 and δ_{CP} . For Δm_{3j}^2 , this resulted from the Martini 2p2h alternative model described above. As the $\Delta\chi^2$ functions for Δm_{3j}^2 are approximately parabolic (see Fig. 5.9) and therefore the marginal likelihood function is approximately Gaussian, the shift is incorporated as an additional uncertainty of 1.428×10^{-5} by directly smearing the marginal likelihood function according to a Gaussian function, allowing the marginal likelihood to ‘migrate’ between grid points, widening the confidence regions. All Δm_{3j}^2 expected and observed constraints presented in this thesis have this additional uncertainty applied.

For δ_{CP} , all three of the previously described alternative models give non-negligible shifts to at least one confidence region, the largest of which are shown in Table 5.12. The $\Delta\chi^2$ functions for δ_{CP} cannot be reasonably approximated as parabolas (see Fig. 5.6), so the above smearing method used for Δm_{3j}^2 cannot be used. Instead, these shifts are to be quoted alongside the observed confidence intervals to ensure that the conclusions of the analysis are robust against alternative interaction model choices.

CL	Lower Edge		Upper Edge	
	Shift	Source	Shift	Source
1σ	-0.07	Martini 2p2h	0.06	Non-QE CC0 π
90%	-0.07	Martini 2p2h	0.08	Non-QE CC0 π
2σ	-0.07	3-comp. CCQE	0.09	Non-QE CC0 π
3σ	-0.11	Non-QE CC0 π	0.14	Non-QE CC0 π

Table 5.12: The largest shifts (in radians) of the upper and lower boundaries of the δ_{CP} confidence region as a result of the use of alternative valid cross-section models. Reproduced from Ref [213].

5.6 Results

In this section, the observed T2K Run 1-10 data set is used to produce constraints on the three-flavour PMNS oscillation parameters.

5.6.1 Comparison of Predicted and Observed Kinematic Distributions

The observed event rates in each sample for the T2K Run 1-10 data set are displayed in Table 5.10, and are compared to the expected event rates from the no oscillation, Asimov A, and Asimov B pseudo-data sets. Additionally, this table shows the expected event rates according to an Asimov data set, Asimov BF NO, generated at the observed T2K Run 1-10 best-fit values of Table 5.13, obtained with use of the reactor constraint on $\sin^2 2\theta_{13}$. The kinematic distributions of the observed events are compared to those obtained from the no oscillation, Asimov A and Asimov BF NO pseudo-data sets in Figs. 5.3, 5.4, 5.12 and 5.13.

By comparing the observed and expected total event rates in each sample, along with statistical and systematic uncertainties added in quadrature, it is clear that the Asimov A pseudo-data set more closely reproduces the observed event rates than Asimov B. This is particularly evident in the ν -mode $\bar{\nu}_e$ CCQE-like and $\bar{\nu}_e$ CC1 π^+ -like samples, which, for Asimov B, show 2.7σ and 2.6σ differences with respect to the data, as opposed to respective differences of 0.0σ and 1.6σ for the Asimov A pseudo-data set. For the Asimov BF NO pseudo-data set, slight tensions exist between prediction and data, with a 1.7σ deficit in the ν -mode $\bar{\nu}_\mu$ CCQE-like sample and a 1.6σ excess in the ν -mode $\bar{\nu}_e$ CC1 π^+ -like sample, although both the normalisation and shape of the kinematic distributions for all samples (see Figs. 5.12 and 5.13) show generally good agreement within the uncertainties. Additionally, excellent agreement is seen in the ν -mode $\bar{\nu}_e$ CCQE-like and $\bar{\nu}$ -mode $\bar{\nu}_\mu$ CCQE-like and $\bar{\nu}_e$ CCQE-like samples.

5.6.2 Observed Constraints on the Oscillation Parameters

The observed $\Delta\chi^2$ functions and the corresponding 1D confidence regions are shown in Fig. 5.14 for δ_{CP} , $\sin^2 \theta_{13}$, $\sin^2 \theta_{23}$, and $|\Delta m_{3j}^2|$, respectively. Additionally, to show correlations between the oscillation parameters, 2D confidence regions are shown in Fig. 5.15 for δ_{CP} vs. $\sin^2 \theta_{13}$ and in Fig. 5.16 for $|\Delta m_{3j}^2|$ vs. $\sin^2 \theta_{23}$. Best-fit points and confidence interval resulting from the 1D fits are displayed in Table 5.13. All such confidence regions are constructed using the constant $\Delta\chi^2$ method (see Section 5.1.2), rather than the more accurate Feldman-Cousins method, used only for δ_{CP} with the reactor constraint and discussed later in this section.

For all fits, the best-fit point was found to be in the normal mass ordering. For $\sin^2 \theta_{13}$, the observed 1σ confidence region is compatible with that of the PDG 2019 [35] global fit to reactor data, but as expected from previous measurements (see Section 2.3), T2K obtains a weaker constraint on $\sin^2 \theta_{13}$ than compared to the constraint from reactor experiments. For $\sin^2 \theta_{23}$, the fit with the reactor constraint finds a best-fit point in the upper octant, but is compatible with maximal mixing ($\sin^2 \theta_{23} \sim 0.51$, see Section 2.2.4.1) at the 1σ confidence level. Without the use of the reactor constraint, the best-fit point for $\sin^2 \theta_{23}$ is in the lower octant, but is compatible with a broad range of $\sin^2 \theta_{23}$ values including both maximal mixing and the T2K+reactor best-fit

point in the upper octant. For $|\Delta m_{3j}^2|$, the fits with and without the reactor constraint find the same best-fit value and normal mass ordering confidence intervals. At the 1σ confidence level, no allowed regions were found in the inverted mass ordering for the 1D fits to $\sin^2 \theta_{13}$, $\sin^2 \theta_{23}$, or $|\Delta m_{3j}^2|$. The observed constraints on δ_{CP} will be discussed in the following section.

Parameter	Reactor Constraint?	Best-Fit	1σ Interval	90% Interval
$\sin^2 \theta_{13} (10^{-2})$	No	2.54	[2.16, 3.03]	[1.93, 3.34]
$\sin^2 \theta_{23}$	No	0.480	[0.453, 0.570]	[0.441, 0.585]
	Yes	0.552	[0.504, 0.576]	[0.459, 0.588]
$ \Delta m_{32}^2 (10^{-3} \text{eV}^2/\text{c}^4)$	No	2.49	[2.44, 2.54]	[2.40, 2.57]
	Yes	2.49	[2.44, 2.54]	[2.40, 2.57]
δ_{CP}	No	-2.32	[-3.08, -1.12]	[2.73, -0.24]
	Yes	-2.01	N.A.	N.A.

(a) Normal Mass Ordering

Parameter	Reactor Constraint?	Best-Fit	1σ Interval	90% Interval
$\sin^2 \theta_{13} (10^{-2})$	No	2.82	-	[2.32, 3.46]
$\sin^2 \theta_{23}$	No	0.476	-	[0.446, 0.574]
	Yes	0.556	-	[0.545, 0.563]
$ \Delta m_{31}^2 (10^{-3} \text{eV}^2/\text{c}^4)$	No	2.46	-	[2.40, 2.52]
	Yes	2.46	-	-
δ_{CP}	No	-1.27	[-3.08, -1.12]	[-2.45, -0.25]
	Yes	-1.38	N.A.	N.A.

(b) Inverted Mass Ordering

Table 5.13: The measured oscillation parameter best-fit, 1σ , and 90% confidence intervals, shown both with and without the constraint on $\sin^2 2\theta_{13}$ from reactor experiments. All intervals are obtained from 1D fits to the parameter of interest. Intervals are shown for both normal and inverted mass orderings, and are calculated with respect to the best-fit across both orderings, which in all cases is the normal mass ordering. The intervals are calculated using the constant $\Delta\chi^2$ method described in Section 5.1.2. As this method does not provide the correct coverage for δ_{CP} , its confidence intervals calculated with the reactor constraint are not shown here and are discussed separately.

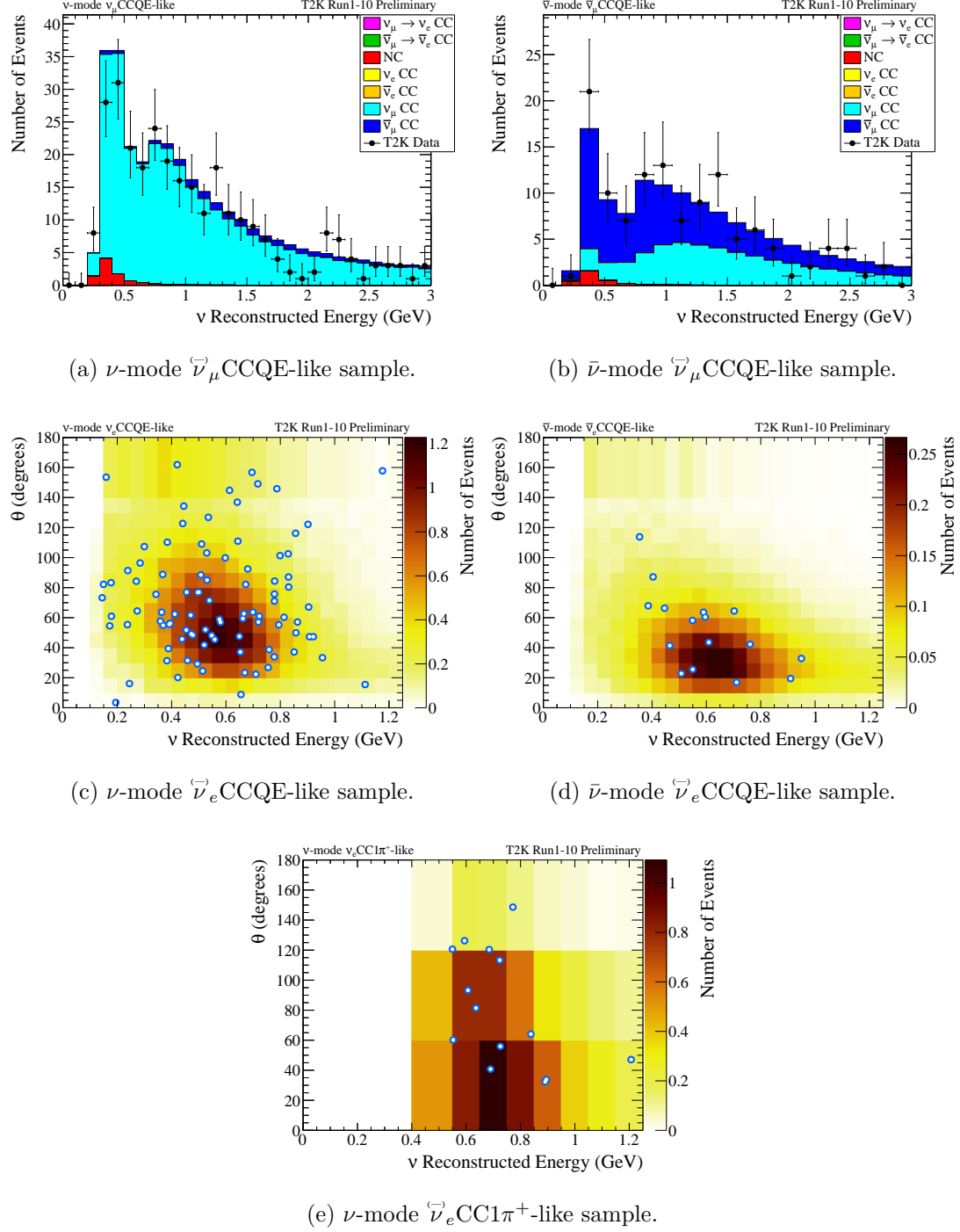


Figure 5.12: Best-fit predicted kinematic distributions (coloured histograms) compared to observed kinematic distributions (black or white/blue points). Predictions are generated with the observed T2K Run 1-10 best-fit oscillation parameter values in Table 5.13, along with the global best-fit values of $\sin^2 \theta_{12}$ and Δm_{12}^2 [35], nominal values of the systematic parameters, and are normalised to the T2K Run 1-10 beam exposure. The uncertainty shown around the data points on the 1D plots accounts for statistical uncertainty only. The uncertainty range is chosen to include all points for which the measured number of data events is inside the 68% confidence interval of a Poisson distribution centred at that point.

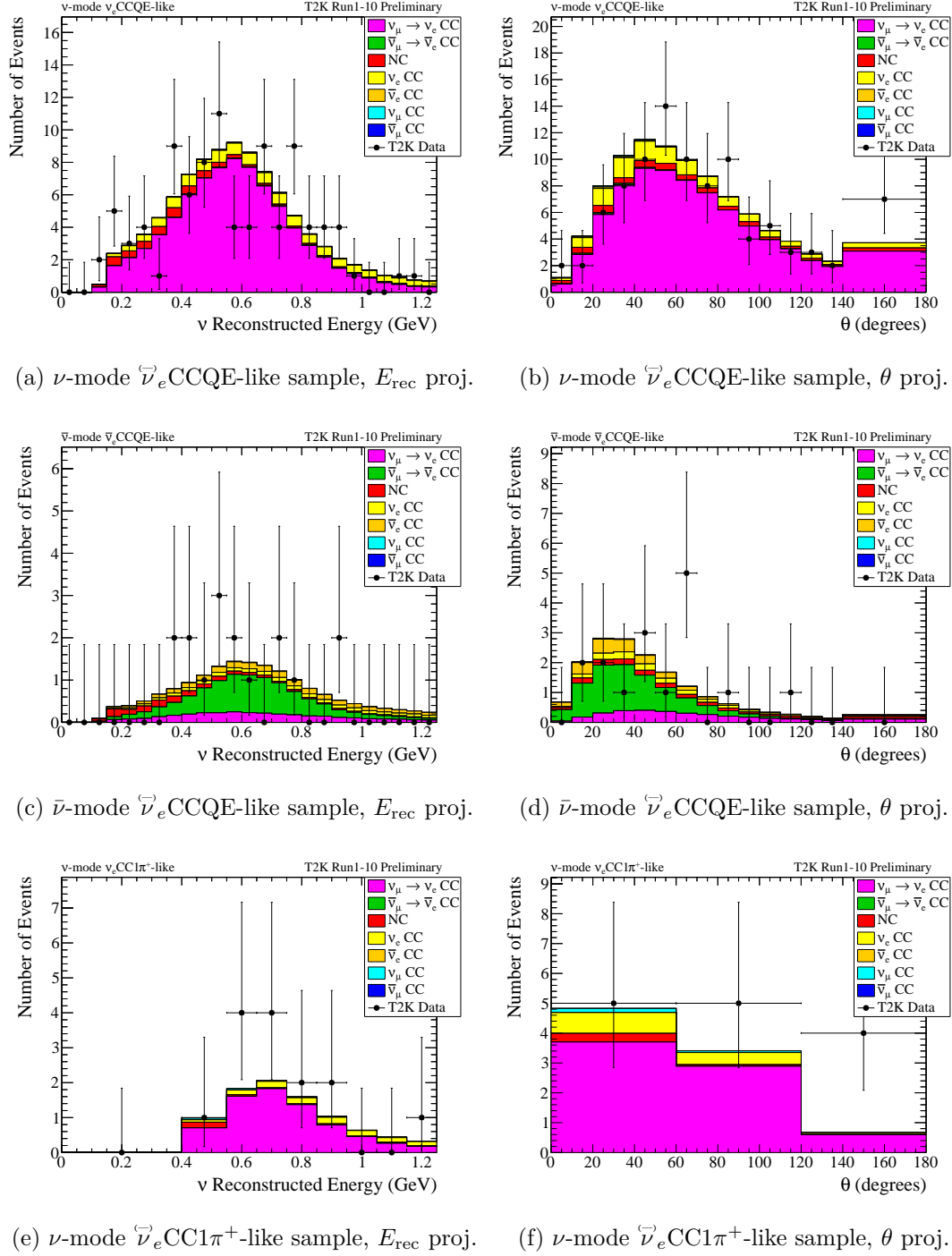


Figure 5.13: E_{rec} and θ projections of the best-fit predicted kinematic distributions (coloured histograms) for the e -like samples, compared to observed kinematic distributions (black or white/blue points). Predictions are generated with the observed T2K Run 1-10 best-fit oscillation parameter values in Table 5.13, along with the global best-fit values of $\sin^2 \theta_{12}$ and Δm_{12}^2 [35], nominal values of the systematic parameters, and are normalised to the T2K Run 1-10 beam exposure. The uncertainty shown around the data points on the 1D plots accounts for statistical uncertainty only. The uncertainty range is chosen to include all points for which the measured number of data events is inside the 68% confidence interval of a Poisson distribution centred at that point.

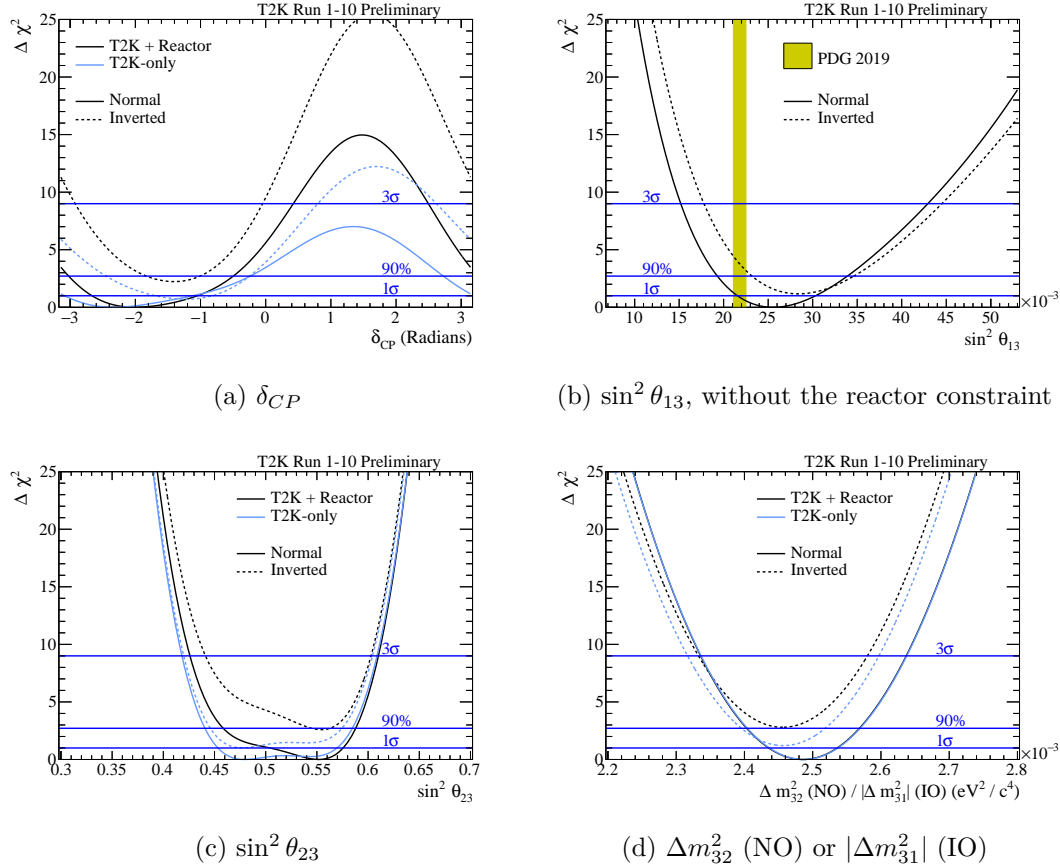


Figure 5.14: Observed $\Delta\chi^2$ functions resulting from 1D fits to oscillation parameters of interest, shown with and without the reactor constraint on $\sin^2 2\theta_{13}$ and for both mass orderings. Critical values are calculated using the constant $\Delta\chi^2$ method.

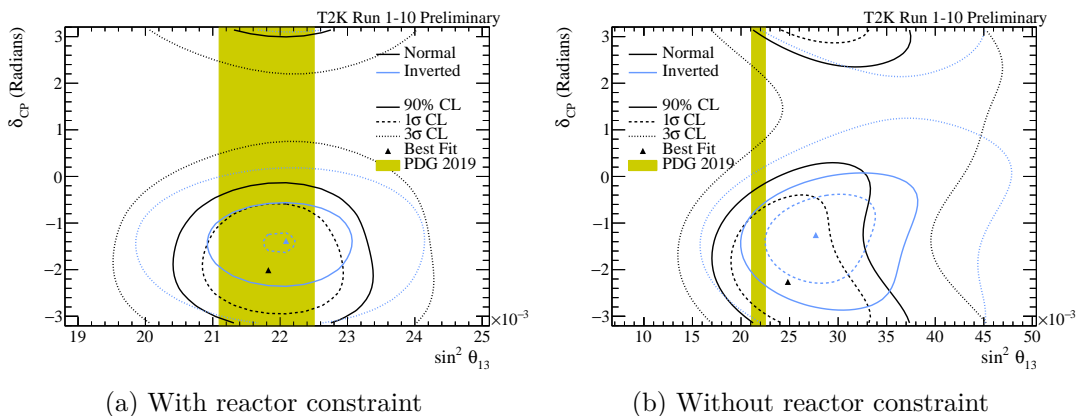


Figure 5.15: Observed constraints on δ_{CP} vs. $\sin^2 \theta_{13}$, shown with and without the reactor constraint on $\sin^2 2\theta_{13}$, for both mass orderings. The best fit value and $\pm 1\sigma$ error on $\sin^2 \theta_{13}$ from the 2019 PDG global fit [35] is shown as a vertical coloured band. Critical values are calculated using the constant $\Delta\chi^2$ method.

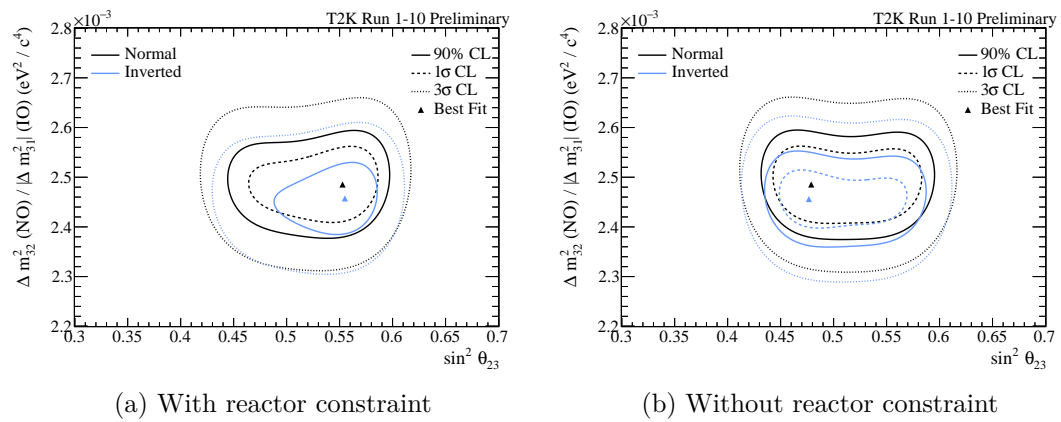


Figure 5.16: Observed constraints on Δm_{32}^2 (NO) or $|\Delta m_{31}^2|$ (IO) vs. $\sin^2 \theta_{23}$, shown with and without the reactor constraint on $\sin^2 2\theta_{13}$, for both mass orderings. Critical values are calculated using the constant $\Delta\chi^2$ method.

5.6.3 Feldman-Cousins Confidence Intervals for δ_{CP}

As discussed in Section 5.1.2, the cyclic nature and physical boundaries of δ_{CP} may result in the constant $\Delta\chi^2$ method producing confidence intervals with incorrect coverage, but the Feldman-Cousins method can be used to numerically calculate confidence intervals with exact coverage. Following the procedure of Section 5.1.2, at each true value of δ_{CP} , an ensemble of 4×10^4 pseudo-experiments have been generated using the joint marginal likelihood distribution of $|\Delta m_{3j}^2|$ vs. $\sin^2 \theta_{23}$ as a prior PDF on these parameters, shown in Fig. 5.17, and resulting from fits to the Asimov BF NO/IO parameter sets defined in Table 5.8. Due to the computationally expensive nature of this procedure, the Feldman-Cousins method is only used along with the constraint on $\sin^2 2\theta_{13}$ from reactor experiments.

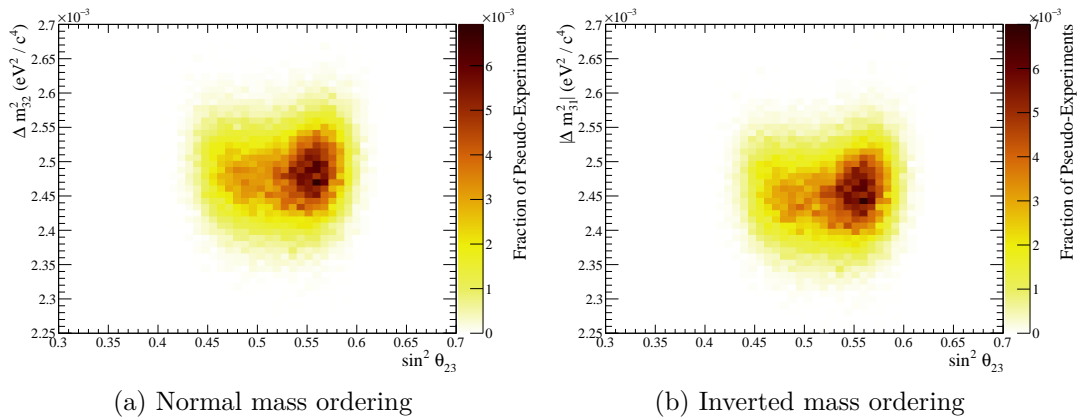


Figure 5.17: The joint marginal likelihood distribution of $|\Delta m_{3j}^2|$ vs. $\sin^2 \theta_{23}$ for both mass orderings. Generated from a fit to the Asimov BF NO/IO parameter sets (see Table 5.8).

The Feldman-Cousins critical values, shown in Fig. 5.18, are calculated according to the method of Section 5.1.2 at 11 true values of δ_{CP} , $[-1, -0.75, -0.5, -0.25, 0.0, 0.125, 0.25, 0.5, 0.75, 0.825, 1]\pi$, and are linearly interpolated between them. At all confidence levels, significant deviations from the critical values of the constant $\Delta\chi^2$ method are observed, which are $\Delta\chi_{\text{crit}}^2 = n^2$ for the $n\sigma$ confidence level and $\Delta\chi_{\text{crit}}^2 = 2.7$ for the 90% confidence level. As discussed in Ref. [3], such deviations are primarily due to the boundaries in the event rates at $\delta_{CP} = \pm\frac{\pi}{2}$ lowering the critical values in these regions, an effect which increases at higher confidence levels due to such critical values being determined by pseudo-experiments resulting from the more extreme statistical fluctuations. Additionally, the inclusion of the mass ordering as a parameter of interest increases the critical values, as it acts as an extra pseudo-degree-of-freedom, but without sufficient freedom to fully behave as a second degree-of-freedom.

To reduce uncertainties related to interpolation, the density of δ_{CP} points used for the calculation of critical values is greatest close to the boundaries of the 3σ confidence intervals. The number of generated pseudo-experiments was chosen to reduce the MC statistical uncertainty to a negligible size for the 2σ confidence level; however, the

number required to do this for the 3σ confidence level would be computationally intractable. To account for this uncertainty and to obtain conservative confidence intervals, they are widened by their $+1\sigma$ MC statistics binomial error. Additionally, as discussed in Section 5.5, the robustness of the confidence intervals to alternative cross-section models will also be considered, using the shifts in confidence interval boundaries listed in Table 5.12.

The normal mass ordering Feldman-Cousins confidence intervals, shown in Table 5.14 and Fig. 5.19, exclude CP-conservation ($\delta_{CP} = 0, \pm\pi$) at the 1σ and 90% confidence levels; however, the 90% exclusion is not robust against the use of the Martini 2p2h alternative cross-section model, which would cause $\delta_{CP} = \pm\pi$ to be barely included at this confidence level. So instead, it is sufficient to state that T2K excludes CP-conservation at close to the 90% confidence level. At the 2σ confidence level, $\delta_{CP} = 0$ is excluded. At the 3σ confidence level, neither CP-conserving values of δ_{CP} are excluded, but the region around $\delta_{CP} = \frac{\pi}{2}$ is excluded. For the inverted mass ordering, CP-conservation is excluded at up to the 3σ confidence level, but the 3σ exclusion of $\delta_{CP} = 0$ is not robust against the use of the Non-QE CC0 π alternative cross-section model.

Confidence Level	Confidence Interval	
	Normal Ordering	Inverted Ordering
1σ	$[-2.77, -1.08]$	-
90%	$[-3.09, -0.51]$	$[-1.97, -0.86]$
2σ	$[-\pi, -0.24] \cup [3.03, \pi]$	$[-2.28, -0.62]$
3σ	$[-\pi, 0.34] \cup [2.53, \pi]$	$[-2.86, -0.10]$

Table 5.14: Feldman-Cousins confidence intervals for δ_{CP} , all calculated with the use of the constraint on $\sin^2 2\theta_{13}$ from reactor experiments. Intervals are shown for both normal and inverted mass orderings, and are calculated with respect to the best-fit across both orderings, which in all cases is the normal mass ordering.

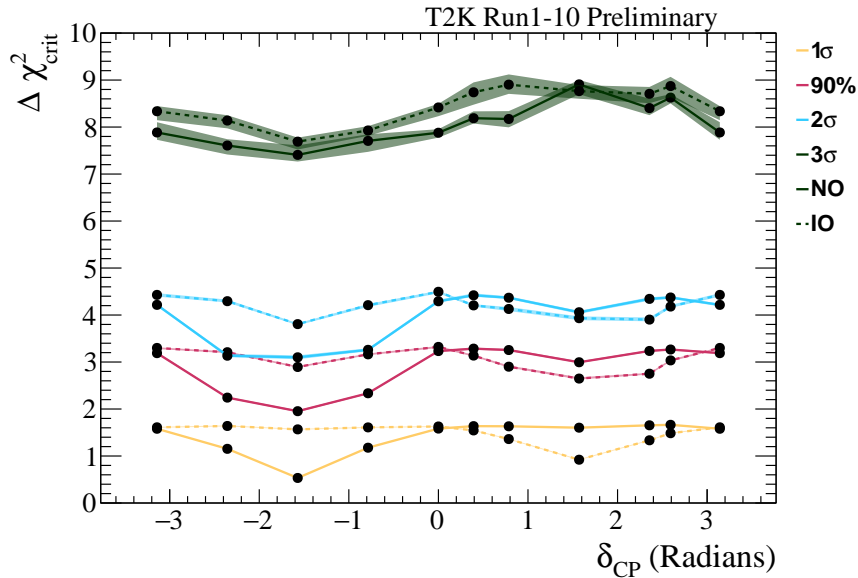


Figure 5.18: Feldman-Cousins critical values as a function of δ_{CP} and mass ordering at the 1σ , 90%, 2 σ , and 3 σ confidence levels. The critical values are generated at 11 points of δ_{CP} in the range $[-\pi, \pi]$ and are linearly interpolated between points. $\pm 1\sigma$ uncertainties due to limited MC statistics are shown as coloured bands.

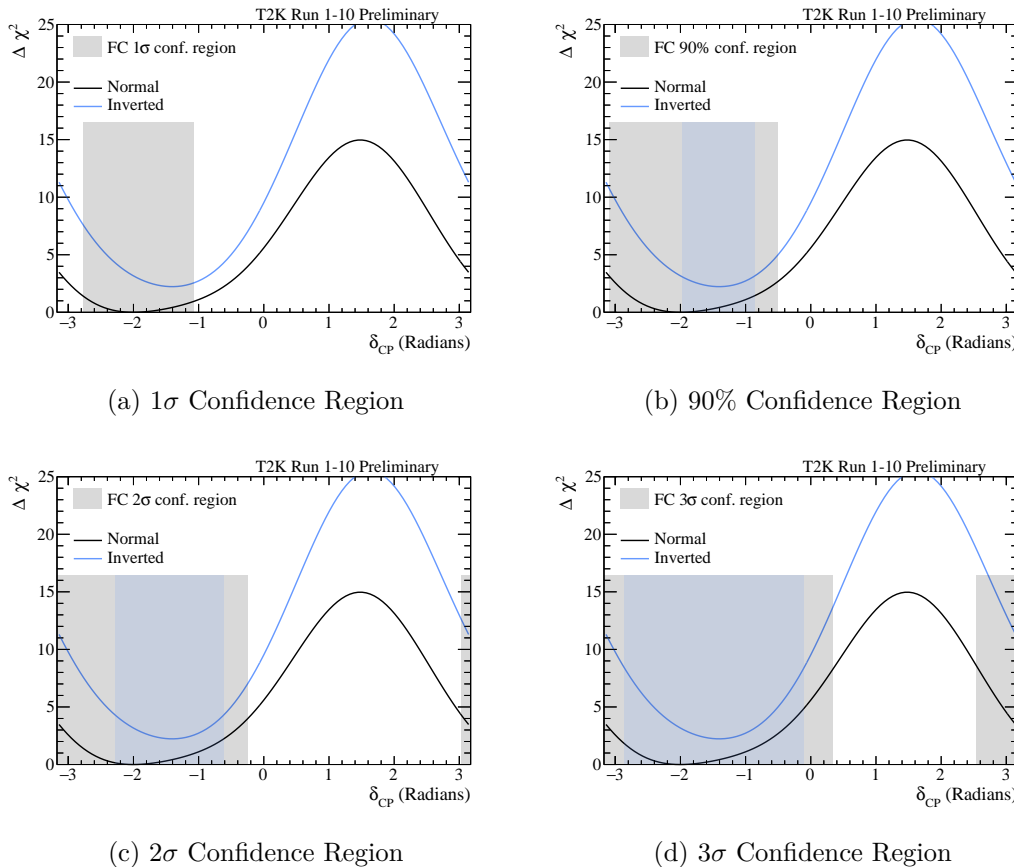


Figure 5.19: Observed $\Delta \chi^2$ functions resulting from 1D fits to δ_{CP} , shown with the reactor constraint on $\sin^2 2\theta_{13}$ and for both mass orderings. Feldman-Cousins confidence intervals for δ_{CP} are shown as shaded regions, and are calculated with respect to the best-fit across both orderings, which in all cases is the normal mass ordering.

5.6.4 Comparison of Predicted and Observed Constraints

By comparing Fig. 5.14a against Figs. 5.6a and 5.6b, it is clear that the observed constraint on δ_{CP} is somewhat stronger than expected from the sensitivity study generated with the Asimov A parameter set, and far stronger than that of Asimov B. However, these constraints cannot be directly compared in detail as they all correspond to different true or best-fit values of the oscillation parameters. So to obtain a direct comparison of the observed and expected constraints, one must compare to the sensitivity of an Asimov pseudo-data set generated at the observed best-fit points, i.e. the Asimov BF NO parameter set defined in Table 5.8. This direct comparison is shown in Fig. 5.20, and again the observed constraint is stronger than expected. Two effects are evident from this: First, there is a generally improved constraint for all values of δ_{CP} , and is particularly noticeable within the range $\sim [-\frac{\pi}{2}, \pi]$. Second, the best-fit point of the expectation shifts away from the true value of δ_{CP} and towards $-\frac{\pi}{2}$, indicating either that there exists a bias in the oscillation parameter measurements (both the alternative model studies and the studies below show no evidence for such biases) or that the model has insufficient freedom to perfectly reproduce the observation.

To understand why the observed constraint is stronger than expected, it is useful to see the individual effect of each sample on the observed constraint. In Fig. 5.21, hybrid pseudo-data sets are formed by replacing the observations for each sample in turn by the corresponding expectation, then the constraint on δ_{CP} is re-evaluated. The strongest effect, most evident in the range $\sim [0, \pi]$, comes from the ν -mode $\bar{\nu}_e CC1\pi^+$ -like sample, but there are also non-negligible contributions from the ν and $\bar{\nu}$ modes $\bar{\nu}_e CCQE$ -like samples in the range $\sim [-\frac{\pi}{2}, 0]$.

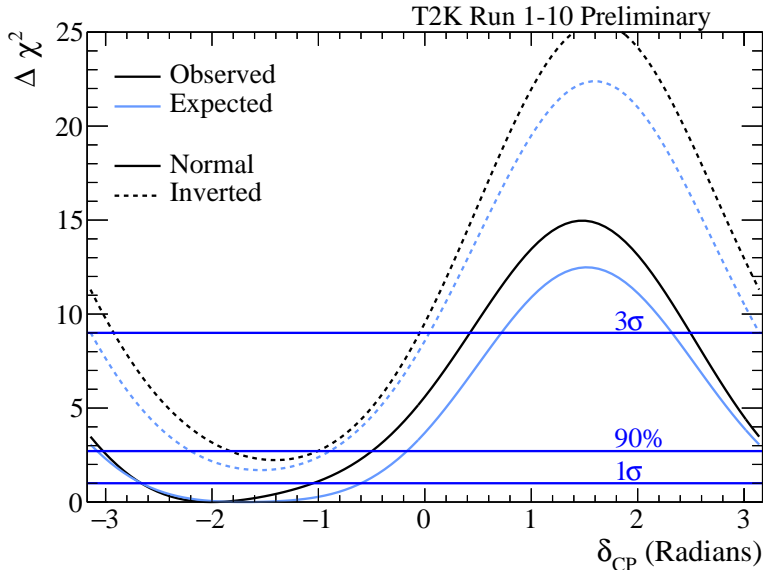


Figure 5.20: Comparison of observed and expected $\Delta\chi^2$ functions resulting from 1D fits to δ_{CP} , shown with the reactor constraint on $\sin^2 2\theta_{13}$ and for both mass orderings. The expected constraint is generated according to the Asimov BF NO oscillation parameter set from Table 5.8. Critical values are calculated using the constant $\Delta\chi^2$ method.

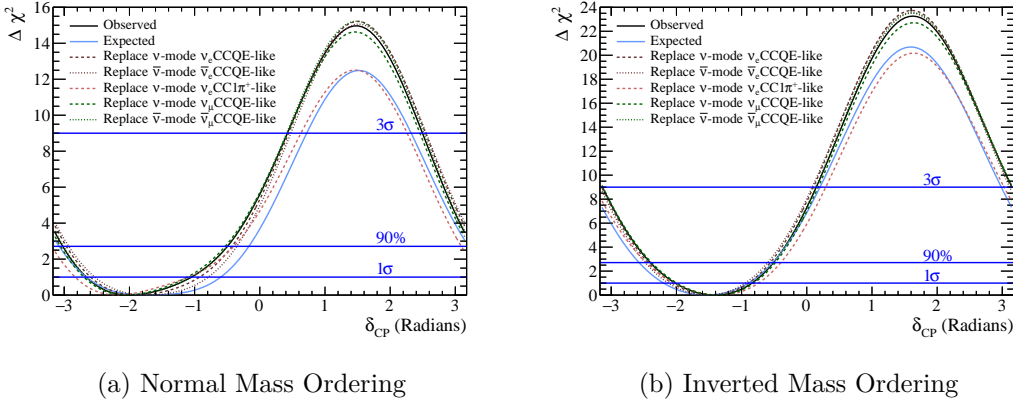


Figure 5.21: Changes to the observed constraint on δ_{CP} when the observations for each sample are replaced with the corresponding expectation. Shown with the reactor constraint on $\sin^2 2\theta_{13}$. The expected constraints are generated according to the Asimov BF NO oscillation parameter set from Table 5.8. Here the $\Delta\chi^2$ values are calculated relative to the maximum marginal likelihood in the true mass ordering, rather than relative to the maximum across both mass orderings, as usual. Critical values are calculated using the constant $\Delta\chi^2$ method.

To explain why the observed data in the e -like samples cause a stronger constraint than expected, Fig. 5.22a is a useful aid. It shows how the predicted e -like event rates in ν and $\bar{\nu}$ modes (combining the event rates from the $\bar{\nu}_e$ CCQE-like and $\bar{\nu}_e$ CC1 π^+ -like samples) vary with δ_{CP} , θ_{23} , and mass ordering, and also shows a comparison to the prediction at the T2K Run 1-10 best-fit point and to the observed data. The predictions form ellipses in δ_{CP} , with maxima (minima) in the ν -mode e -like event rate at $\delta_{CP} = -\frac{\pi}{2}$ ($+\frac{\pi}{2}$). As the observed data contains more ν -mode e -like events than the model can produce (at the best-fit values of θ_{23} , θ_{13} and the systematic parameters), the value of δ_{CP} that gives the maximum number of ν -mode e -like events is favoured (i.e. $\delta_{CP} = -\frac{\pi}{2}$) and values of δ_{CP} away from this maximum are excluded more strongly than would be expected at the best-fit point.

From the simplistic comparison of only the rate of e -like events, as discussed above and shown in Fig. 5.22a, one may expect the best-fit value of δ_{CP} to have been $-\frac{\pi}{2}$; however, this is not the case, as the best-fit point is $\delta_{CP,bf} = -2.01$ radians (i.e. $\sim -0.64\pi$) and the observed $\Delta\chi^2$ function is asymmetric about the best-fit point, with the region $\delta_{CP,bf} < \delta_{CP} < 0$ excluded more strongly than the region $-\pi < \delta_{CP} < \delta_{CP,bf}$. To explain this, one must consider the *shape* of the kinematic distributions in the e -like samples as well as their event rates. A simple rate and shape comparison is shown in Fig. 5.22b, that counts the sum of e -like events across all event samples (as a function of δ_{CP} , θ_{23} , and mass ordering) with E_{rec} less than the oscillation maximum vs. greater than the oscillation maximum. From this, it is clear that the observed slight excess in events in this former group and the slight deficit in events in the latter group compared to the best-fit prediction produces a preference for the region $-\pi \lesssim \delta_{CP} \lesssim -\frac{\pi}{2}$ over $-\frac{\pi}{2} \lesssim \delta_{CP} \lesssim 0$.

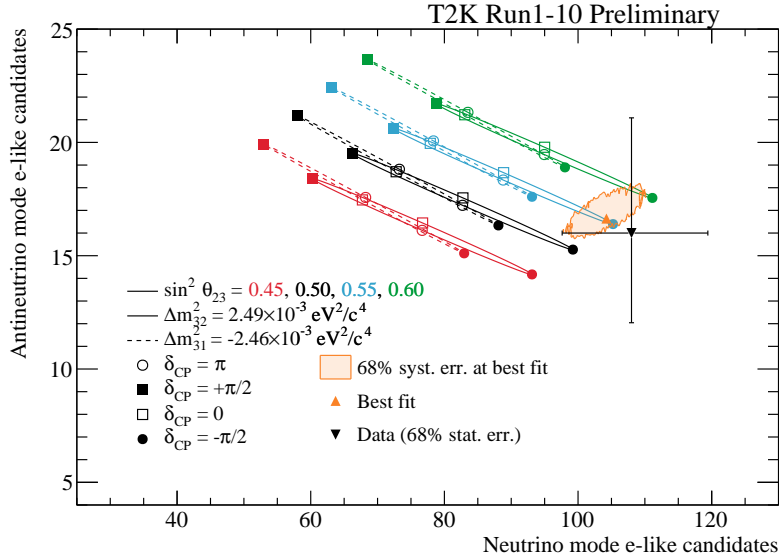
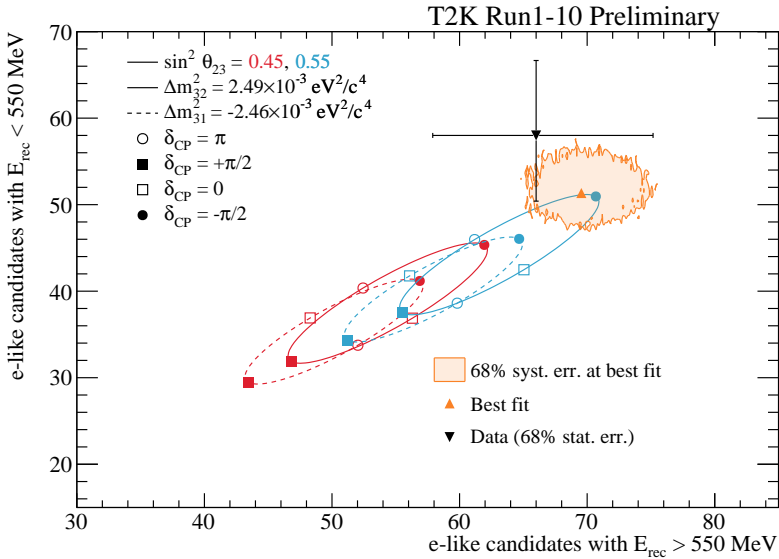
(a) $\bar{\nu}$ -mode $\bar{\nu}_e$ vs. ν -mode $\bar{\nu}_e$ candidate events.(b) ν and $\bar{\nu}$ modes $\bar{\nu}_e$ candidate events with $E_{\text{rec}} < 550 \text{ MeV}$ vs. $E_{\text{rec}} \geq 550 \text{ MeV}$.

Figure 5.22: Bi-event plots showing candidate events in the e -like samples (combining the event rates from the $\bar{\nu}_e$ CCQE-like and $\bar{\nu}_e$ CC1 π^+ -like samples). Predictions are generated for multiple δ_{CP} and $\sin^2 \theta_{23}$ values in normal (solid lines) and inverted (dashed lines) mass orderings, and using the T2K Run 1-10 best-fit value of $|\Delta m_{3j}^2|$, global best-fit values of $\sin^2 \theta_{13}$, $\sin^2 \theta_{12}$ and Δm_{12}^2 [35] (see Table 5.8), and nominal systematic parameter values. Also shown are the observed T2K Run 1-10 data with 1σ statistical uncertainties and a prediction generated with the observed T2K Run 1-10 best-fit oscillation parameter values from Table 5.13 with 1σ systematic uncertainties.

In this section, a number of excesses and deficits have been shown to exist in the observed event rates compared to the best-fit prediction, leading to a stronger constraint on δ_{CP} than expected. Additionally, the best-fit $-2 \ln \lambda$ value resulting from the fit to observed T2K data, 476.2, is much larger than expected (corresponding to a worse fit), as shown in Table 5.10. This raises the question of whether the three-flavour oscillation model is capable of reproducing the observed data at all, i.e. whether the data and the observed constraint are consistent with the best-fit prediction to within statistical and systematic uncertainties. While the bi-event plots of Fig. 5.22 clearly show that the 1σ statistical uncertainty on the the considered data overlaps with the 1σ systematic uncertainty region around the best-fit point, these plots are simple explanatory aids and do not take into account all of the available information, so a more sophisticated treatment is required to fully answer this question. This is done by generating a large ensemble of pseudo-experiments so that the observed $\Delta\chi^2$ vs. δ_{CP} function can be compared to the expected distribution of $\Delta\chi^2$ values at each grid point of δ_{CP} and mass ordering, using the following method:

1. An ensemble of 4×10^4 pseudo-experiments are generated assuming true δ_{CP} and mass ordering equal to the T2K Run 1-10 best fit values (i.e. -2.01 radians and normal ordering, respectively). The method used to generate these pseudo-experiments is as described in step 1 of the method used to calculate Feldman-Cousins critical values (see Section 5.1.2).
2. For each pseudo-experiment, the marginal likelihood is calculated at all 101 grid points of δ_{CP} and in each mass ordering, and from this the test statistic, $\Delta\chi^2$, is calculated according to Eq. (5.5).
3. At each grid point of δ_{CP} and mass ordering, a distribution of $\Delta\chi^2$ is formed from the ensemble of pseudo-experiments. These distributions are integrated from the minimum $\Delta\chi^2$ value to obtain the range of $\Delta\chi^2$ values (as a function of δ_{CP} and mass ordering) below which 68.27% and 95.45% of pseudo-experiments are included.
4. The observed constraint can be directly compared to the ranges calculated above to evaluate how extreme the constraint is across all values of δ_{CP} and both mass orderings.

Using the above method, in Fig. 5.23 the observed constraint on δ_{CP} in each mass ordering is compared to the 68.27% and 95.45% ranges of expected constraints from pseudo-experiments, while accounting for both statistical and systematic uncertainties. It can be seen that the observed constraint in each mass ordering is partially contained within the expected 68.27% range and fully contained within the 95.45% range, so is therefore compatible with the three-flavour oscillation model, with any deviations from its predictions being compatible with modest statistical fluctuations.

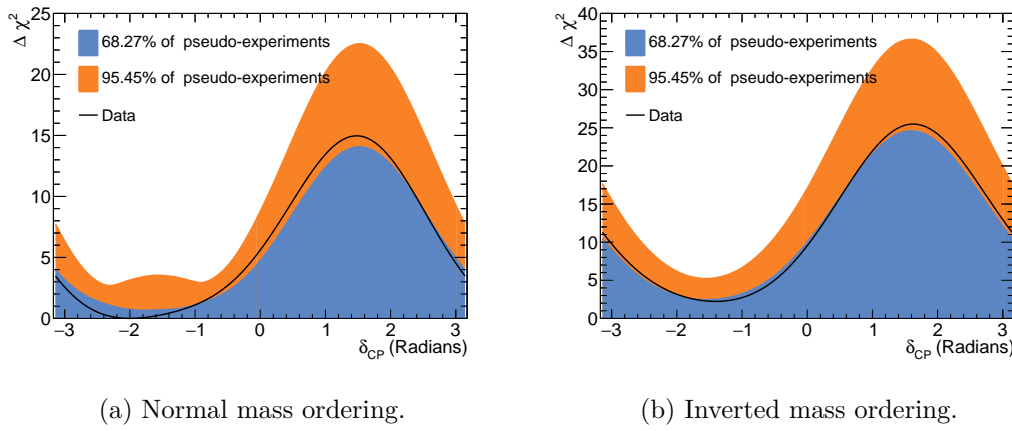


Figure 5.23: One-sided distributions of $\Delta\chi^2$ vs. δ_{CP} , generated from 4×10^4 pseudo-experiments with true normal mass ordering and true $\delta_{CP} = -2.01$ (i.e. the T2K Run 1-10 normal ordering best-fit point, see Table 5.13a). The pseudo-experiments are fit against 101 δ_{CP} values in the range $[-\pi, \pi]$ and in normal (left) and inverted (right) mass orderings, then the ranges of $\Delta\chi^2$ values encompassing 68.27% and 95.45% of pseudo-experiments are displayed.

5.6.5 Comparison to the Previous T2K Results

Note: this section does not represent my own work and is summarised from Ref. [202], but is included here to put the results into context.

Despite the observed constraints on δ_{CP} being stronger than expected, the constraint has weakened in comparison to the previous iteration of the analysis (using T2K Run 1-9 data and reported in Refs. [3, 5]). There have been a number of changes to the analysis since the previous iteration, all detailed in Section 5.2.5, and all contributing to the change in constraint by varying amounts. The effects of these changes are shown in Fig. 5.24, and the incremental contributions are summarised below, along with explanations for each difference in the constraint, using the same labelling as in the Figure. Each successive contribution includes the effects of all previous contributions. The effects of contributions B, C, and D all weaken the constraint by modest, and approximately equal amounts, while the largest effect is the weakening of the constraint from the inclusion of the T2K Run 10 data.

- **A = OA2018 (run1-9d)** - This is the observed constraint on δ_{CP} from the previous iteration of the analysis, without modification.
 - **B = A + 2020xsec+BANFF** - The constraint is updated using the improved flux and cross-section (xsec) models, as well as incorporating the improvements to the near detector fit (referred to as ‘BANFF’). The change is likely driven by the change of the nuclear ground state model for CCQE interactions from RFG to SF, in line with previous studies of this change on the expected δ_{CP} constraint [174].
 - **C = B + PDG2019 RC** - The constraint on δ_{CP} is updated using the constraint on $\sin^2 2\theta_{13}$ from reactor experiments from the PDG 2019 global fit, whereas the

previous analysis used the 2018 version. This constraint is implemented in the analysis as a Gaussian prior PDF with central and $\pm 1\sigma$ values of $(8.30 \pm 0.31) \times 10^{-2}$ for the 2018 constraint and $(8.53 \pm 0.27) \times 10^{-2}$ for 2019. As shown by Fig. 5.10, the correlations between $\sin^2 \theta_{13}$ and δ_{CP} mean that such an increase in the central value of the reactor constraint causes the δ_{CP} constraint to weaken.

- **D = C + SK reprocessing** - The constraint is updated using T2K Run 1-9 data after the effects of the Super-K PMT gain corrections. As shown in Fig. 5.22a, the ν -mode ($\bar{\nu}$ -mode) e -like sample event rate reaches a maximum (minimum) at $\delta_{CP} = -\frac{\pi}{2}$ in the normal (inverted) mass ordering, so observing a greater (lesser) event rate than expected results in a stronger exclusion of δ_{CP} values away from $-\frac{\pi}{2}$. In the T2K run 1-9 data set, the Asimov BF NO pseudo-data set predicted 6.9 and 17.2 events in the ν -mode $\bar{\nu}_e CC1\pi^+$ -like and $\bar{\nu}$ -mode $\bar{\nu}_e CCQE$ -like samples, respectively, while 15 events were observed in both samples, thus giving a greater constraint on δ_{CP} than expected. After the T2K run 1-9 data set was reprocessed following the Super-K PMT gain corrections, the ν -mode $\bar{\nu}_e CC1\pi^+$ -like sample lost an event while the $\bar{\nu}$ -mode $\bar{\nu}_e CCQE$ -like sample gained an event (see Table 5.9), bringing the observed data closer to the expectation and weakening the constraint.
- **E = D + run10 = OA2020** - Finally, the constraint is updated with the addition of the T2K Run 10 data. The change in constraint is primarily caused by the non-observation of new events in the ν -mode $\bar{\nu}_e CC1\pi^+$ -like sample in the T2K Run 10 dataset. As discussed above, for the T2K Run 1-9 data set, 15 events were observed in this sample, while only 6.9 events were predicted. The addition of the T2K Run 10 beam exposure has increased this prediction to 8.9 events (see Table 5.10), bringing the prediction closer to the observation and therefore weakening the constraint on δ_{CP} .

5.7 Putting the Results into Context - the Current Status of Neutrino Oscillation Parameter Measurements

Note: this section does not represent my own work and is summarised from Ref. [56], but is included here to put the results into context.

In Section 2.3, the status of the three-flavour PMNS oscillation parameter measurements in 2018 were discussed using global fits to multiple experiments including T2K. The T2K data used in those global fits corresponded to T2K Runs 1-8 (see Section 3.1), whereas the data sets analysed in this thesis include T2K Runs 9 and 10, corresponding to increases of 34% and 114% in ν -mode and $\bar{\nu}$ -mode mode beam exposures, respectively.

In this section, the results of updated global fits will be shown. These are from NuFIT 2020 [56] and includes the T2K Run 1-10 data analysed in this chapter. The

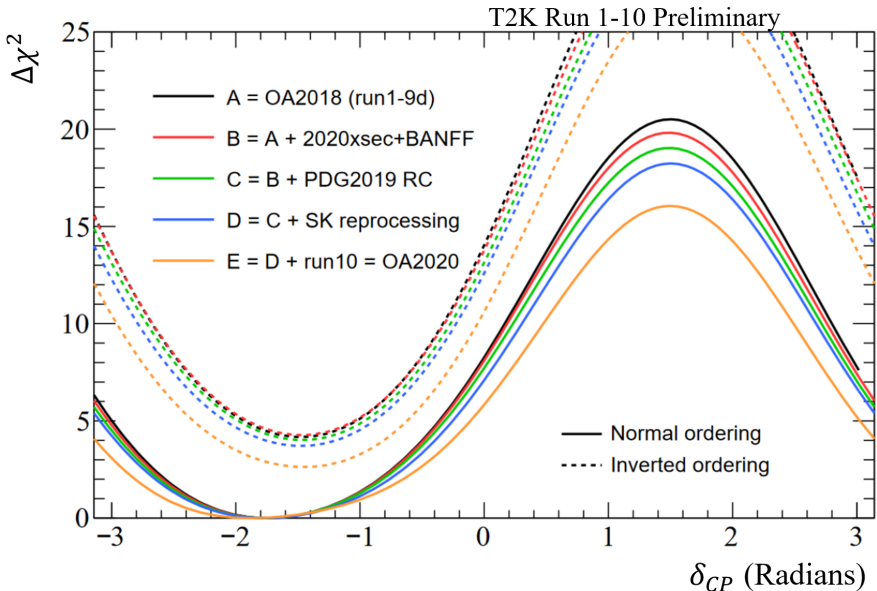


Figure 5.24: Incremental contributions to the change in the constraint on δ_{CP} between the current (Run 1-10) and previous (Run 1-9d) T2K analyses. Shown with the reactor constraint on $\sin^2 2\theta_{13}$ and for both mass orderings. Adapted from Ref. [202] and produced by the T2K oscillation analysis fitter that uses (p, θ) kinematic binning for the e -like samples, as outlined in Section 5.1.3.

results shown in Section 5.6 will be put into context with comparisons to other neutrino oscillation experiments and to the NuFIT 2018 [57] global fits. The solar parameters, θ_{12} and Δm_{21}^2 , are not constrained by T2K data due to limited sensitivity, so will not be discussed in this chapter; however, the current status of these parameters was already discussed in Section 2.3.1.

The T2K constraints shown in the figures in this section are produced by the NuFIT global fitter group using the same T2K data analysed in this chapter. While their fit methodology and treatment of systematic uncertainties is not as sophisticated as those of this thesis, their results are in good agreement with those shown in this thesis and therefore their comparisons of T2K results to those from other experiments also applies to the results of this thesis.

5.7.1 θ_{23} , $|\Delta m_{3j}^2|$ and the Mass Ordering

The T2K observed constraints on Δm_{3j}^2 vs. $\sin^2 \theta_{23}$ are shown in Fig. 5.25 compared to those of other accelerator-based long-baseline neutrino oscillation experiments, to reactor antineutrino experiments, and to their combination.

For $\sin^2 \theta_{23}$ in both mass orderings, it is clear that the strongest constraint comes from the T2K experiment, which therefore drives the global fit. Competitive constraints are also produced by the NOvA experiment, which shows good compatibility with the T2K constraint. Both T2K and NOvA find a best-fit point in the upper octant, but are also consistent with both maximal mixing and the lower octant at the 2σ confidence level. Compared to the 2018 T2K and NOvA results (see Fig. 2.13), the allowed region

has shifted to lower values of $\sin^2 \theta_{23}$, increasing compatibility with the lower octant and maximal mixing.

For Δm_{3j}^2 , the T2K, NOvA and Daya Bay experiments all provide constraints of approximately similar strength, all of which are compatible with each other at the 1σ confidence level [56], despite minor differences in the best-fit points. Compared to the 2018 results, there has been a general tightening of the constraint and no significant change in the best-fit point.

For each experiment and therefore the global fit, the best-fit point was found to be in the normal mass ordering and the inverted mass ordering is disfavoured with $\Delta\chi^2_{\text{IO-NO}} = 7.1$ ($\sim 2.7\sigma$). Compared to the 2018 global fit result, the amount by which the IO is excluded has weakened by 2.2 units of $\Delta\chi^2_{\text{IO-NO}}$, in part due to the weakening of the T2K constraints discussed in Section 5.6.5.

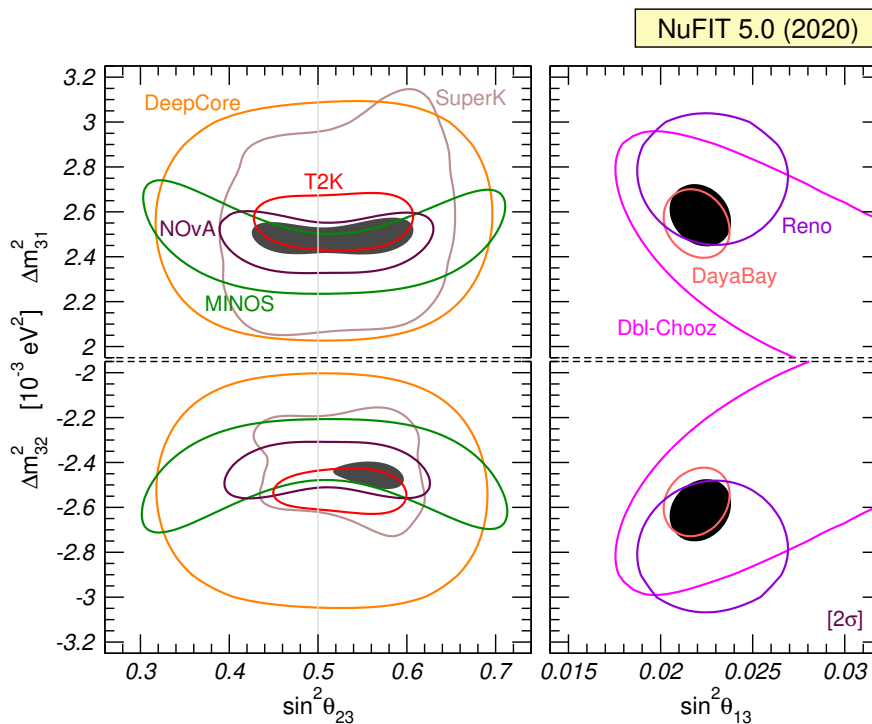


Figure 5.25: 2σ confidence regions for Δm_{3j}^2 vs. $\sin^2 \theta_{23}$ (left) and Δm_{3j}^2 vs. $\sin^2 \theta_{13}$ (right). Upper panels correspond to the normal mass ordering (i.e. $j = 1$, $\Delta m_{31}^2 = \Delta m_{32}^2 + \Delta m_{21}^2 > 0$), while lower panels correspond to the inverted mass ordering (i.e. $j = 2$, $\Delta m_{32}^2 = \Delta m_{31}^2 - \Delta m_{21}^2 < 0$). Confidence regions are shown for various atmospheric, reactor and accelerator-based LBL experiments (coloured hollow regions), as well as a combined fit (black solid regions). The regions are defined with respect to the best-fit across both mass orderings, so the IO confidence regions are smaller than those of the NO, in which the best-fit point is found. Adapted from Ref. [56].

5.7.2 θ_{13} and δ_{CP}

The $\sin^2 \theta_{13}$ constraints shown in Fig. 5.25 do not include those of accelerator-based long-baseline experiments such as T2K; however, by comparing to Fig. 5.14b, it is clear that observed T2K constraint is compatible with those of the reactor antineutrino

experiments at the 1σ confidence level.

The T2K observed constraints on δ_{CP} are shown in Fig. 5.26 compared to those of NOvA, MINOS, and their combination. T2K observes by far the strongest constraints on δ_{CP} in both mass orderings and finds a best-fit point in the normal mass ordering of -0.64π (245° in the angle convention used by NuFIT), close to the maximally CP-violating value of -0.5π . NOvA observed weaker constraints in both mass orderings than those of T2K, and finds a best-fit point in the normal mass ordering of 0.82π (148° in the angle convention used by NuFIT) and a large allowed region, with all δ_{CP} values allowed at the 2σ level. Despite the different best-fit values, the T2K and NOvA constraints in the normal mass ordering agree at close to the 1σ confidence level, and overall across all fitted parameters, the T2K/NOvA data sets agree at the $1.4 - 1.7\sigma$ confidence level [56]. In the inverted mass ordering, the observed T2K and NOvA best-fit points are in good agreement.

While the global fit is mainly driven by T2K, its best-fit point of -0.91π is a compromise between the T2K and NOvA best-fit points in order to maintain compatibility with both the observed ν -mode $\bar{\nu}_e$ CCQE-like and $\bar{\nu}_e$ CC1 π^+ -like candidate events in T2K and the observed ν_e candidate events in NOvA [56]. The weakening of the T2K constraint compared to that in 2018 [57] has caused a corresponding weakening of the global constraint. This is demonstrated by the allowed 3σ region, which in 2018 was $[-\pi, 0.56] \cup [2.09, \pi]$ and in 2020 has widened to $[-\pi, 0.75] \cup [1.85, \pi]$.

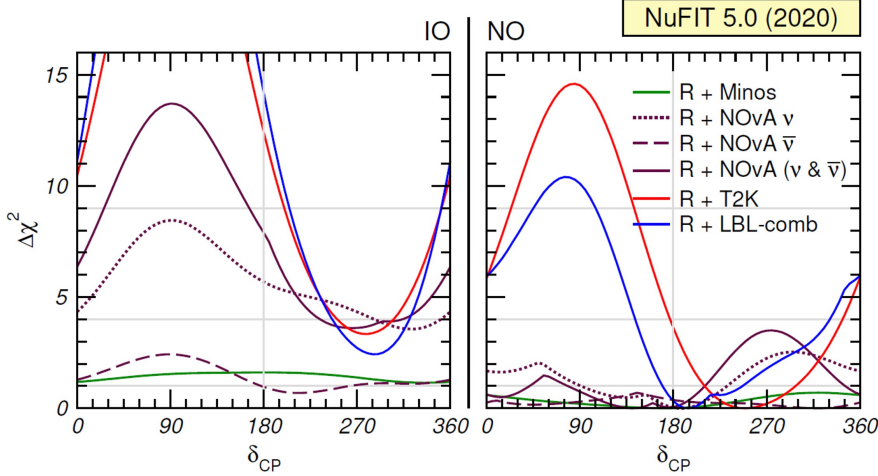


Figure 5.26: $\Delta\chi^2$ as a function of δ_{CP} for various accelerator-based LBL experiments as well as their combination. Left (right) panels are for IO (NO), and $\Delta\chi^2$ is defined with respect to the minimum across both mass orderings. The $\Delta\chi^2$ functions are produced using the full information from both accelerator and reactor experiments on θ_{13} , θ_{23} and Δm_{3j}^2 . Δm_{21}^2 and $\sin^2 \theta_{12}$ are fixed to the global best-fit values. Adapted from Ref. [56].

5.8 Summary

Data from the T2K experiment has been used to search for leptonic CP-violation and to produce constraints on the three-flavour neutrino oscillation parameters $\sin^2 \theta_{23}$, $\sin^2 \theta_{13}$, $|\Delta m_{3j}^2|$, and δ_{CP} . The data set used in this analysis is the T2K Run 1-10 data, corresponding to integrated beam exposures of 1.97×10^{21} and 1.63×10^{21} POT in ν and $\bar{\nu}$ modes, respectively.

This analysis predicted (observed) the following event rates in each Super-K sample: 354.0 ± 11.0 (318) for ν -mode $\bar{\nu}_\mu$ CCQE-like, 95.2 ± 4.6 (94) for ν -mode $\bar{\nu}_e$ CCQE-like, 8.9 ± 1.3 (14) for ν -mode $\bar{\nu}_e$ CC1 π^+ -like, 137.9 ± 5.7 (137) for $\bar{\nu}$ -mode $\bar{\nu}_\mu$ CCQE-like, and 16.9 ± 1.0 (16) for $\bar{\nu}$ -mode $\bar{\nu}_e$ CCQE-like, where the displayed uncertainties correspond to that of systematic uncertainties.

The analysis was performed by simultaneously fitting both ν and $\bar{\nu}$ mode Super-K data, under the assumption of three-flavour neutrino oscillations in constant density matter, and with systematic uncertainties accounted for via constraints on the flux and cross-section models from a fit to near-detector data.

Best-fit points and confidence intervals for the measured oscillation parameters are shown in Tables 5.13 and 5.14. In all fits, the best-fit point is in the normal mass ordering. For $\sin^2 \theta_{13}$, the observed constraint is compatible with those of reactor antineutrino experiments [35]. For $\sin^2 \theta_{23}$, the best-fit point is in the upper octant, but is compatible with maximal mixing at the 1σ confidence level. For δ_{CP} , the best-fit point is -2.01, close to the maximally CP-violating value of $-\frac{\pi}{2}$, and CP-conservation is excluded at close to the 90% confidence level. Although the observed constraint on δ_{CP} is stronger than expected from sensitivity studies, the results are still compatible with the three-flavour oscillation model. The stronger constraint is primarily due to the observed excess of events in the ν -mode $\bar{\nu}_e$ CC1 π^+ -like sample, which has reduced compared to previous T2K analyses, therefore also weakening the observed constraint.

The T2K constraints on Δm_{32}^2 and $\sin^2 \theta_{13}$ are competitive with recent measurements from other experiments, and are world-leading for $\sin^2 \theta_{23}$ and δ_{CP} . For δ_{CP} in particular, the T2K results strongly drive the global constraint and are compatible with those of the NOvA experiment at approximately the 1σ confidence level.

Chapter 6

Search for $\bar{\nu}_\mu \rightarrow \bar{\nu}_e$ Oscillations

In this chapter, data from the T2K experiment will be used to perform two tests of the $\bar{\nu}_\mu \rightarrow \bar{\nu}_e$ oscillation channel (referred to as ‘ $\bar{\nu}_e$ appearance’). In particular, whether T2K can distinguish the appearance of $\bar{\nu}_e$ events from the expected backgrounds and whether the observed event rates and kinematic distributions are compatible with the predictions of the three-flavour PMNS neutrino oscillation framework described in Section 2.2.

First, Section 6.1 introduces the tested hypotheses and the test statistics used to evaluate them. Then, Section 6.2 describes the method used to evaluate the compatibility of the T2K data with each hypothesis. Finally, the expected and observed results will be discussed in Section 6.5.

This analysis, reported in Refs. [3, 4], has been performed using the VALOR neutrino fitting software. A number of differences in the analysed datasets and other analysis inputs exist between this analysis and the analysis described in Chapter 5, all of which will be described in Section 6.3.

6.1 Aims and the Tested Hypotheses

In order to evaluate the significance of $\bar{\nu}_e$ appearance, the usual three-flavour PMNS oscillation probability is multiplied by a dimensionless parameter, β :

$$P(\bar{\nu}_\mu \rightarrow \bar{\nu}_e) = \beta \times P_{\text{PMNS}}(\bar{\nu}_\mu \rightarrow \bar{\nu}_e) \quad (6.1)$$

The parameter β is fixed to either 0 or 1 to select between the two independent null hypotheses: No $\bar{\nu}_e$ appearance ($\beta = 0$), to determine whether the observed $\bar{\nu}_e$ appearance data can be distinguished from background processes, and three-flavour PMNS $\bar{\nu}_e$ appearance ($\beta = 1$), to determine whether the observed $\bar{\nu}_e$ appearance data is compatible with the current best knowledge of the PMNS oscillation parameters. The significance to exclude each hypothesis are given by p -values produced from two analyses: a rate-only analysis, using the number of events in the $\bar{\nu}$ -mode $\bar{\nu}_e$ CCQE-like sample as the test statistic, and a rate+shape analysis, using the marginal negative log-likelihood ratio between the $\beta = 0$ and $\beta = 1$ cases as the test statistic, as will be described in more detail in Section 6.2.

To date, the world's most accurate measurement of this process is reported by the NOvA experiment, which reports a $\bar{\nu}_e$ appearance signal of 4.4σ above the estimated backgrounds [215]. T2K has previously searched for this process, and reported a 1.8σ deficiency of $\bar{\nu}_e$ events compared to the three-flavour PMNS prediction and reported consistency with the estimated backgrounds [42]. The analysis reported in this chapter improves on the previous T2K analysis with 113% and 118% increases to the ν and $\bar{\nu}$ modes datasets, respectively, as well as benefiting from the addition of constraints from the recently added ν -mode $\bar{\nu}_e CC1\pi^+$ -like sample, an updated Super-K event reconstruction algorithm, and an updated cross-section model (with the latter two both detailed in Ref. [3]).

6.2 Hypothesis Test Methodology

To test each hypotheses while accounting for systematic uncertainties, an ensemble of pseudo-experiments is produced, resulting in a distribution of the test statistic for each analysis, which are then integrated to obtain p -values. In this section, the method used to produce such p -values is described.

While this analysis has been performed using the same VALOR neutrino fitting software used in the main analysis (see Chapter 5), there are three key differences between the analyses: First, in the way the likelihood is calculated; Second, the $\bar{\nu}_e$ appearance analysis is one of hypothesis testing rather than producing confidence intervals on parameters of interest; Finally, the parameter used to select the null hypothesis, β , is the sole parameter of interest, meaning that all oscillation parameters (except β), including the mass ordering are treated as systematic/nuisance parameters, denoted \vec{f} , and are therefore marginalised. These differences will be discussed in detail in the following sections.

6.2.1 Construction of the Marginal Likelihood

To evaluate the likelihood of a given set of β and systematic parameter values given a pseudo-experiment, pseudo-data, or observed data, expected kinematic distributions are produced according to Eq. (5.1) but with one modification: The oscillation probability is modified according to Eq. (6.1) to account for β and to only apply it to events corresponding to true $\bar{\nu}_\mu \rightarrow \bar{\nu}_e$ oscillations.

These expected kinematic distributions are then used to calculate the likelihood in each sample according to Eq. (5.2), as in the main analysis; however, here the combination of the likelihoods for each sample to form a total likelihood differs from the main analysis: The $\bar{\nu}$ -mode $\bar{\nu}_e CCQE$ -like sample is of primary interest and its likelihood, $\lambda_{\bar{\nu}_e}$, is calculated given a pseudo-experiment, E, while for the other four samples, the data (observed data or Asimov pseudo-data), D, is used instead of a pseudo-experiment in order to constrain the oscillation and systematic parameters according to the observations in these samples. These four samples are referred to as ‘control samples’, with

likelihood λ_c calculated according to Eq. (6.2), and with a total five sample likelihood, λ , calculated according to Eq. (6.3). The use of the control samples in this way is equivalent to using the control sample data as a prior constraint when randomising nuisance parameters. When calculating the test statistics of the observed T2K data, the data is used in place of the pseudo-experiment in Eq. (6.3).

$$\lambda_c(D | \beta, \vec{f}) = \prod_{s \neq \bar{\nu}_e} \lambda_s(D | \beta, \vec{f}) \quad (6.2)$$

$$\lambda(E(\beta), D | \beta, \vec{f}) = \lambda_{\bar{\nu}_e}(E(\beta) | \beta, \vec{f}) \cdot \lambda_c(D | \beta, \vec{f}) \quad (6.3)$$

Using this new total likelihood, the marginal likelihood is calculated according to Eq. (5.4) using 2×10^5 sets of systematic parameters, randomly drawn from the prior PDFs in Table 6.1. A factor of five times more random samples are used in this analysis compared to the main analysis, as the inclusion of δ_{CP} and the mass ordering as systematic parameters broadens the nuisance parameter space to be integrated over. Additionally, the nuisance parameter space must be accurately sampled as these parameters have a large impact on the $\nu_\mu \rightarrow \nu_e$ reaction modes, which are significant backgrounds in the search for $\bar{\nu}_e$ appearance due to the inability of Super-K to distinguish ν_e from $\bar{\nu}_e$.

6.2.2 Construction of the Hypothesis Test

In order to produce p -values for each null hypothesis, distributions of the test statistics must be formed under the assumption of each hypothesis. These are generated from an ensemble of pseudo-experiments for each true value of β , as follows:

1. A pool containing a large number ($> 10^6$) of pseudo-experiments are produced randomly drawing parameters from the distributions in Table 6.1 and with Poisson statistical fluctuations applied.
2. The control sample likelihood, λ_c , is calculated for each pseudo-experiment using Eq. (6.2). Then the maximum control sample likelihood across all pseudo-experiments, λ_{\max} , is stored.
3. A single proposed pseudo-experiment is drawn from the pool produced in step 1.
4. A random number R is drawn uniformly from the range $[0, 1]$.
5. If λ_c/λ_{\max} is greater than R , the proposed pseudo-experiment is entered into the ensemble of accepted pseudo-experiments.
6. The procedure is repeated from step 3 until 2×10^4 pseudo-experiments have been accepted. So by using this method, the systematic parameter space is randomly sampled (while maintaining correlations between all systematic parameters) to select an ensemble of only the most likely pseudo-experiments according to the control sample data.

7. The rate-only and rate+shape test statistics are calculated for each accepted pseudo-experiment as follows:
 - (a) The test statistic for the rate-only analysis is simply the number of events in the $\bar{\nu}$ -mode $\bar{\nu}_e$ CCQE-like sample, denoted N_{events} .
 - (b) The test statistic for the rate+shape analysis is denoted $\Delta\chi_\beta^2$, and is defined in Eq. (6.4). Unlike the $\Delta\chi^2$ or $\Delta\chi_{\text{FC}}^2$ values used in the main analysis, $\Delta\chi_\beta^2$ is not calculated relative to a best-fit marginal likelihood, as the sole parameter of interest, β , is not a fitted parameter. From Eq. (6.4), it is clear that negative (positive) values of $\Delta\chi_\beta^2$ correspond to pseudo-experiments that are more consistent with the $\beta = 0$ ($\beta = 1$) hypothesis.
8. The calculated test statistics are used to populate the distributions $f_\beta(N_{\text{events}})$ and $f_\beta(\Delta\chi_\beta^2)$, of which there is one of each distribution for each true value of β .

$$\Delta\chi_\beta^2 = -2 \ln \left[\frac{\lambda_{\text{marg}}(E(\beta), D | \beta = 0)}{\lambda_{\text{marg}}(E(\beta), D | \beta = 1)} \right] \quad (6.4)$$

Now that test statistic distributions of the pseudo-experiments have been generated for each null hypothesis, p -values are produced by integrating these distributions from the test statistic of the pseudo or observed data, $N_{\text{events}}^{\text{obs}}$ and $\Delta\chi_\beta^2{}^{\text{obs}}$. As the test statistics of the pseudo and observed data (see Fig. 6.3) lie to the right (left) of the peak of the distributions for true $\beta = 0$ ($\beta = 1$), a right(left)-tailed p -value is used and calculated according to Eq. (6.5) (Eq. (6.6)), where t denotes either the rate-only or rate+shape test statistic, as appropriate.

$$p\text{-value}(\beta = 0, \text{right-tailed}) = \frac{\int_{t_{\text{obs}}}^{+\infty} f_0(t) dt}{\int_{-\infty}^{+\infty} f_0(t) dt} \quad (6.5)$$

$$p\text{-value}(\beta = 1, \text{left-tailed}) = \frac{\int_{-\infty}^{t_{\text{obs}}} f_1(t) dt}{\int_{-\infty}^{+\infty} f_1(t) dt} \quad (6.6)$$

The test statistic distributions used to calculate the p -values are filled with a finite number of pseudo-experiments, N_{PE} . This introduces a binomial MC statistical error, Δp , on the p -value, p , calculated as follows:

$$\Delta p = \sqrt{\frac{p(1-p)}{N_{\text{PE}}}} \quad (6.7)$$

To aid in the interpretation of the p -values, they may be expressed in terms of the standard deviation of the normal distribution, σ . The conversion is as follows, where erf^{-1} is the inverse of the error function.

$$\sigma = \sqrt{2} \text{ erf}^{-1}(1 - p) \quad (6.8)$$

6.2.3 Validation of the Analysis

The results of the $\bar{\nu}_e$ appearance analysis are validated against those of another T2K oscillation analysis fitter, as described in Section 5.1.3. This other fitter uses (p, θ) kinematic binning instead of (E_{rec}, θ) , and enters each pseudo-experiment into the test statistic distribution with a weight equal to its control sample likelihood rather than sampling the parameter space and accepting/rejecting pseudo-experiments based on this likelihood. Good agreement was found between the two fitters across all tests, with minor differences found to be caused primarily from the use of different kinematic variables.

Additionally, the robustness of the analysis to the use alternative valid cross-section models is considered, as in Section 5.5. For both the expected and observed results, the alternative models caused no change larger than 0.2σ and the conclusions of the analysis remained unchanged [208].

6.3 Summary of Analysis Inputs and Implementation Choices

This analysis has been performed using the VALOR neutrino fitting software, described in Chapter 5, and was undertaken prior to the collection of the T2K Run 10 dataset used in the main analysis, instead making use of the T2K Run 1-9 dataset (the Run 10 dataset corresponds purely to ν -mode data, so is not directly relevant for this analysis). There have been a number of changes to the analysis inputs between T2K Runs 9 and 10, including differences in the flux and cross-section models, all of which are described in Section 5.2.5. As there are many common elements between the inputs used for these analyses, this section will discuss only those that are different.

6.3.1 Beam Exposure

This analysis is performed using Super-K data from the T2K Run 1-9 data collection period (see Section 3.1), corresponding to beam exposures of 1.49×10^{21} and 1.63×10^{21} POT in ν and $\bar{\nu}$ modes, respectively. Systematic parameters are constrained using the fit to near detector data described in Section 4.3, using T2K Run 2-6 data corresponding to exposures of 0.58×10^{21} and 0.28×10^{21} POT in ν and $\bar{\nu}$ modes, respectively.

6.3.2 Reaction Modes

The neutrino-nucleus interaction model is as described in Section 5.2.5 and in Refs. [3, 120]. 50 true reaction modes are used in the analysis to categorise Super-K MC events as listed in Section 5.2.2, but with the CCDIS and CCmulti- π modes grouped into CCmisc, and with CC1 π^0 and CC1 π^\pm grouped together as CC1 π .

6.3.3 Kinematic Binning

The kinematic binning is the same as that used for the main analysis (see Section 5.2.3) with one exception: For the ν -mode $\bar{\nu}_e$ CC1 π^+ -like sample, the same (E_{rec}, θ) binning

Parameter(s)	Prior PDF	Range
$\sin^2 \theta_{23}$	Uniform	[0.3, 0.7]
$\sin^2 2\theta_{13}$ reactors	Gaussian	0.0830 ± 0.0031
$\sin^2 2\theta_{12}$	Gaussian	0.846 ± 0.021
$ \Delta m_{3j}^2 $	Uniform	$[2.3, 2.7] \times 10^{-3} \text{ eV}^2/\text{c}^4$
Δm_{21}^2	Gaussian	$(7.53 \pm 0.18) \times 10^{-5} \text{ eV}^2/\text{c}^4$
δ_{CP}	Uniform	$[-\pi, +\pi]$
Mass Ordering	Two-point	0.5 NO, 0.5 IO

Table 6.1: Treatment of the oscillation parameters in the T2K Run 1-9 $\bar{\nu}_e$ appearance analysis. All Gaussian priors are from [35], with that of $\sin^2 2\theta_{13}$ being from the global fit to reactor experiments.

scheme is used as for the $\bar{\nu}_e$ CCQE-like samples in Table 5.2, which is significantly more granular than the binning scheme used in the T2K Run 1-10 analysis.

6.3.4 Treatment of Systematic and Oscillation Parameters

A total of 119 systematic parameters are incorporated into the analysis to account for the effects of systematic uncertainties in the flux, detector and interaction models. These are detailed, along with the best-fit and pre/post ND fit uncertainties in the appendix of Ref. [3]. All systematic parameters are randomised (accounting for correlations) when computing the marginal likelihood of Eq. (5.4), using a multivariate Gaussian prior PDF as defined by the near detector (characterising flux and cross-section model uncertainties) and Super-K covariance matrices (characterising the Super-K detector, FSI, SI, and PN model uncertainties).

Oscillation parameters are randomised according to the prior PDFs defined in Table 6.1. All $\bar{\nu}_e$ appearance analysis results have been produced using the constraint on $\sin^2 2\theta_{13}$ from reactor experiments. As T2K is sensitive to $\sin^2 \theta_{23}$, $|\Delta m_{3j}^2|$, and δ_{CP} , uniform prior PDFs spanning the entire range of these parameters would be applicable, although in practice their parameter space is sampled in reduced ranges (as listed in Table 6.1). This is done in order to maintain efficiency (adequately sampling the full ranges requires a computationally-intractable number of samples), while ensuring that reducing these ranges does not alter the results.

As in the main analysis, an Asimov data set is used as representative data in order to determine the median sensitivity without requiring the generation of large numbers of pseudo-data sets. The oscillation parameters used to generate this Asimov data set is shown in Table 6.2. The central values of the PDG2018 global fit averages are used for $\sin^2 2\theta_{12}$, Δm_{21}^2 , and $\sin^2 2\theta_{13}$, while for the other oscillation parameters, the most probable values from the T2K Run 1-4 ν -mode Bayesian analysis [191] are used. Finally, β is fixed to 1, i.e. to $\bar{\nu}_e$ appearance according to the current best knowledge of the three-flavour PMNS mixing parameters.

Parameter(s)	Asimov A Value
$\sin^2 \theta_{23}$	0.528
$\sin^2 \theta_{13}$ reactors	0.0212
$\sin^2 \theta_{12}$	0.304
$ \Delta m_{3j}^2 $	$2.51 \times 10^{-3} \text{ eV}^2/\text{c}^4$
Δm_{21}^2	$7.53 \times 10^{-5} \text{ eV}^2/\text{c}^4$
δ_{CP}	-1.60
Mass Ordering	Normal
β	1

Table 6.2: Asimov oscillation parameters values used to compute expected event rates, kinematic distributions, and test statistic distributions in the T2K Run 1-9 $\bar{\nu}_e$ appearance analysis.

6.4 Predicted Kinematic Distributions and Event Rates

In this section, expected kinematic distributions and event rates are presented. Unless otherwise noted, all predictions are generated using the Asimov A parameters shown in Table 6.2 and with the T2K Run 1-9 beam exposure. Although the observed data is displayed in a number of figures and tables in this section, all sensitivity studies were performed blind with respect to the T2K Run 9 data. The effects of systematic uncertainties on the total event rates are discussed in detail in Ref. [3], and is 7.1% in the $\bar{\nu}$ -mode $\bar{\nu}_e$ CCQE-like sample, with the largest contribution (3.7%) coming from uncertainties in the nucleon removal energy.

Figure 6.2 shows the Asimov A predicted kinematic distributions, with E_{rec} and θ projections shown in Fig. 6.1 for the $\bar{\nu}$ -mode $\bar{\nu}_e$ CCQE-like sample under the assumption of each hypotheses, showing a clear difference in the kinematic distributions between hypotheses. While the μ -like samples extend up to $E_{\text{rec}} = 30$ GeV, these plots only display up to 3 GeV to highlight the regions of greatest oscillation probability, but the full range is used in the likelihood calculations.

Integrating the kinematic distributions over E_{rec} and θ yields the total event rate for each sample. These are displayed, for the Asimov A pseudo-data set under the assumption of both $\beta = 0$ and $\beta = 1$, without neutrino oscillations (of any flavours), and for the observed T2K Run 1-9 data in Table 6.3.

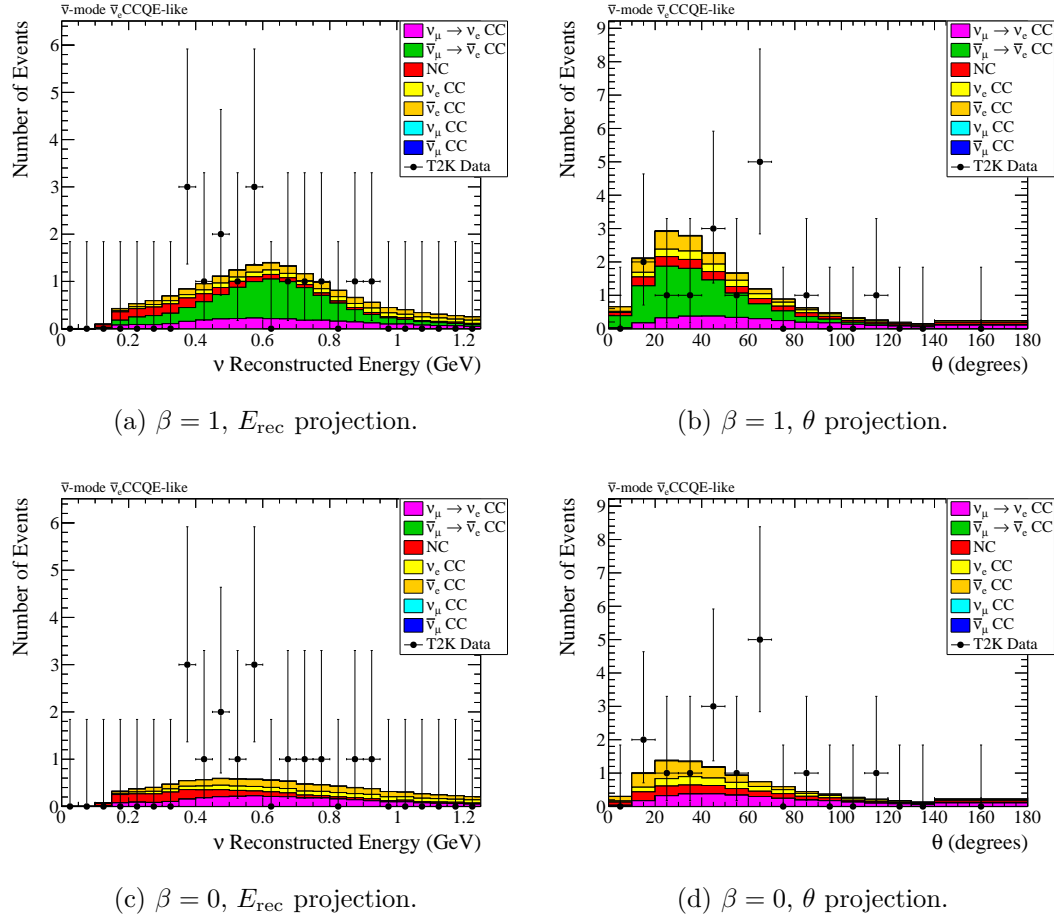


Figure 6.1: E_{rec} and θ projections of the Asimov A predicted kinematic distributions (coloured histograms) for the $\bar{\nu}$ -mode $\bar{\nu}_e$ CCQE-like sample, compared to observed kinematic distributions (black points). Predictions are generated with the Asimov A oscillation parameter values in Table 6.2, with β fixed to 0 and 1, with nominal values of the systematic parameters, and are normalised to the T2K Run 1-9 beam exposure. The uncertainty shown around the data points on the 1D plots accounts for statistical uncertainty only. The uncertainty range is chosen to include all points for which the measured number of data events is inside the 68% confidence interval of a Poisson distribution centred at that point.

Sample	Predicted Asimov Hypothesis			Observed	
	No osc.	A ($\beta = 0$)	A ($\beta = 1$)		
ν -mode	$\bar{\nu}_\mu$ CCQE-like	1226.6	272.4	272.4	243
	$\bar{\nu}_e$ CCQE-like	15.6	72.4	72.8	75
	$\bar{\nu}_e$ CC1 π^+ -like	2.6	6.9	6.9	15
$\bar{\nu}$ -mode	$\bar{\nu}_\mu$ CCQE-like	459.1	139.5	139.5	140
	$\bar{\nu}_e$ CCQE-like	7.0	9.3	16.8	15

Table 6.3: Predicted and observed event rates in each sample, using the T2K Run 1-9 beam exposure and data. Three different hypotheses have been used to generate the predictions: no neutrino oscillations and the Asimov A oscillation parameter set defined in Table 6.2, with β set to 0 and 1.

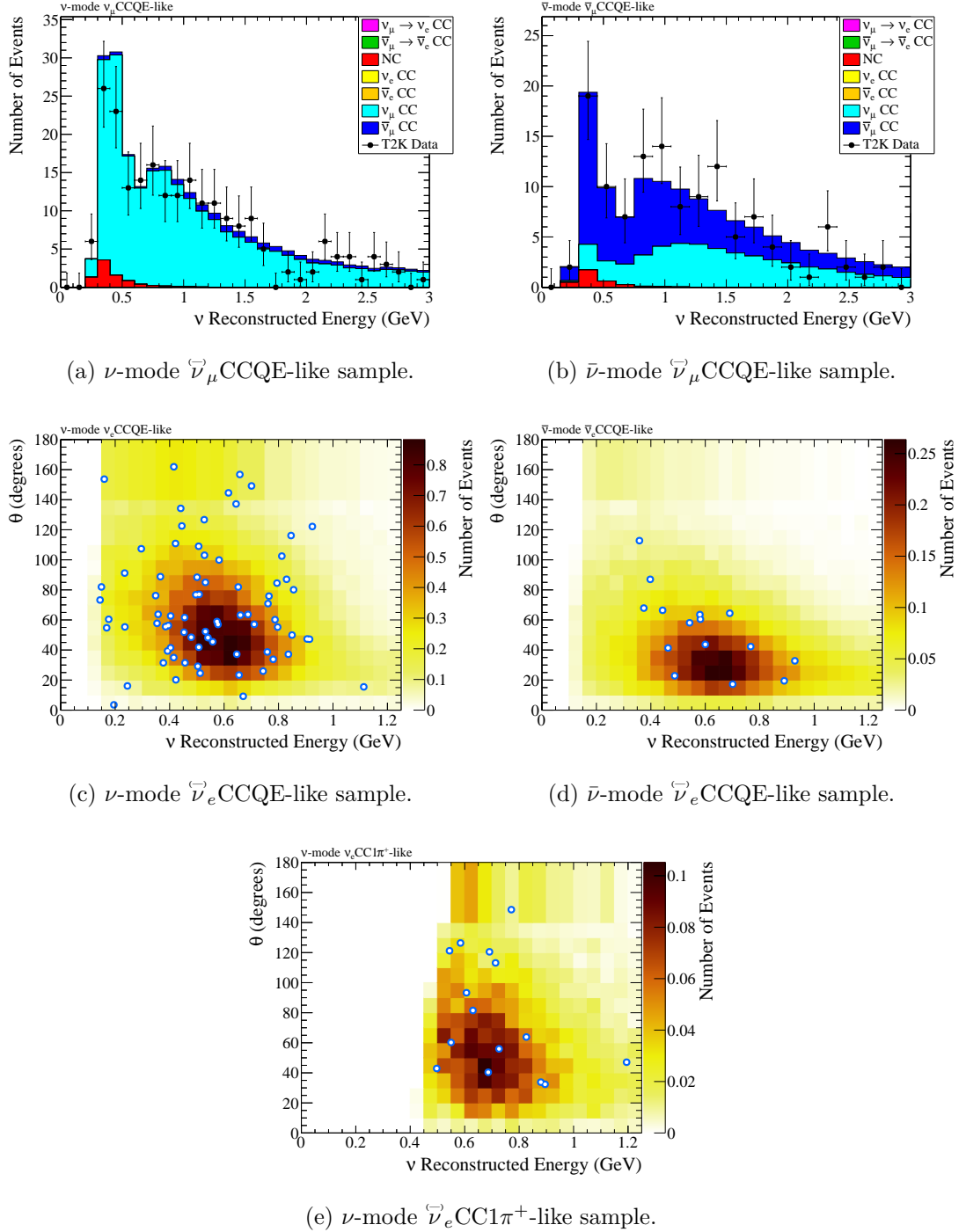


Figure 6.2: Asimov A predicted kinematic distributions (coloured histograms) compared to observed kinematic distributions (black or white/blue points). Predictions are generated with the Asimov A oscillation parameter values in Table 6.2, nominal values of the systematic parameters, and are normalised to the T2K Run 1-9 beam exposure. The uncertainty shown around the data points on the 1D plots accounts for statistical uncertainty only. The uncertainty range is chosen to include all points for which the measured number of data events is inside the 68% confidence interval of a Poisson distribution centred at that point.

6.5 Expected and Observed Results

A sensitivity study has been performed to gauge the ability of T2K to exclude each null hypothesis and differentiate between them. The study is performed under the assumption of the Asimov A (with $\beta = 1$) pseudo-data set, generated with the oscillation parameter values listed in Table 6.2. The expected and observed data test statistic values for each analysis are listed in Table 6.4, the test statistic distributions resulting from the generated ensemble of pseudo-experiments are shown compared to the data test statistics in Fig. 6.3, and the resulting expected and observed p -values to exclude each hypothesis for each analysis are shown in Table 6.5.

Analysis	Data Test Statistic	
	Expected	Observed
rate-only ($N_{\text{events}}^{\text{obs}}$)	16.8	15
rate+shape ($\Delta\chi_\beta^2{}^{\text{obs}}$)	6.27	3.81

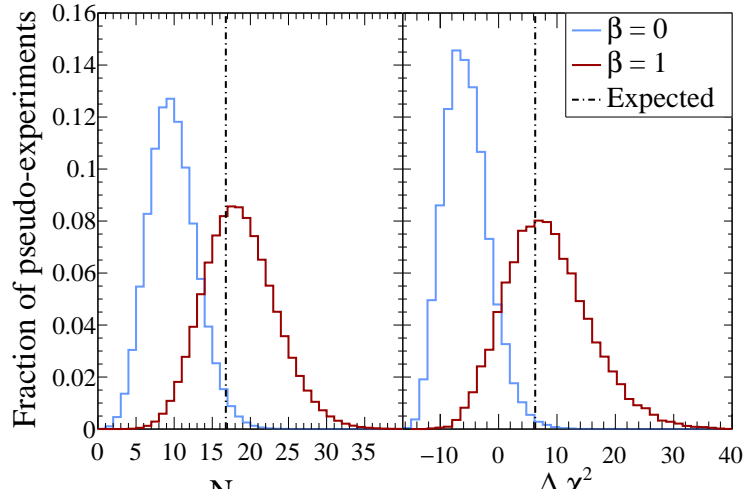
Table 6.4: Expected and observed rate-only and rate+shape test statistic values. The expected values are generated with the Asimov A oscillation parameter values in Table 6.2 and nominal values of the systematic parameters.

β	Analysis	p -value		Significance (σ)	
		Expected	Observed	Expected	Observed
0	rate-only	0.019	0.059	2.4	1.9
	rate+shape	0.006	0.016	2.8	2.4
1	rate-only	0.379	0.321	0.9	1.0
	rate+shape	0.409	0.300	0.8	1.0

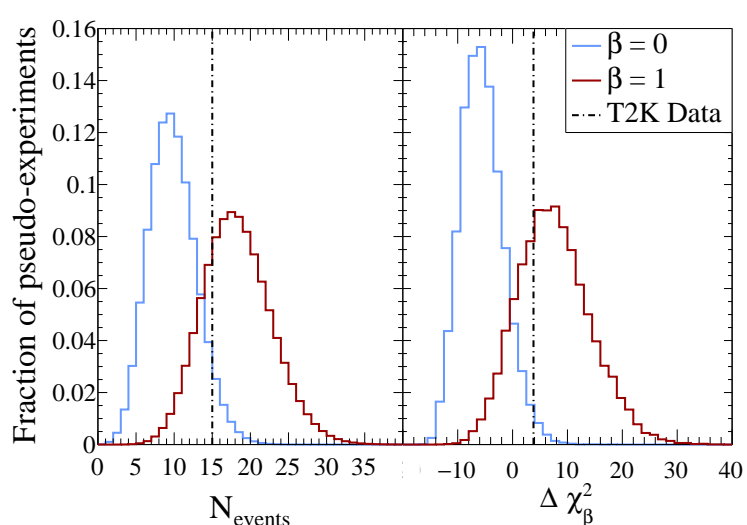
Table 6.5: Expected and observed p -values and significance to exclude the $\beta = 0$ and $\beta = 1$ hypotheses using both the rate-only and rate+shape analyses. The expected values are generated with the Asimov A oscillation parameter values in Table 6.2 and nominal values of the systematic parameters. The effects of limited MC statistics were considered and the effects on the quoted figures are negligible.

For the Asimov A sensitivity study (i.e. with true $\beta = 1$), the expected data test statistics lie at or close to the peak of the $\beta = 1$ test statistic distributions, showing consistency with the assumed true hypothesis (due to exclusions of $\sim 1\sigma$ being insignificant) as one would expect for an Asimov data set. Both rate-only and rate+shape analyses produce largely consistent results. The expected data test statistic for the rate+shape analysis is $\Delta\chi_\beta^2{}^{\text{obs}} = 6.27$, giving an expected 2.8σ exclusion of the $\beta = 0$ hypothesis.

Compared to the expectation of 16.8 events in the $\bar{\nu}$ -mode $\bar{\nu}_e$ CCQE-like sample, only 15 were observed, weakening both the observed rate-only and rate+shape exclusions of the $\beta = 0$ hypothesis. Additionally, the shape of the observed kinematic



(a) Expected



(b) Observed

Figure 6.3: Expected and observed test statistics compared to test statistic distributions generated under the assumption of the $\beta = 0$ and $\beta = 1$ hypotheses and for both rate-only (left) and rate+shape (right) analyses.

distribution in this sample is more background-like than expected, corresponding to $\Delta\chi^2_{\beta} \text{ obs} = 3.81$ and further weakening the observed rate+shape exclusion of the $\beta = 0$ hypothesis, which the observed T2K Run 1-9 data excludes at the $1.9 - 2.4\sigma$ level. Finally, the observed T2K Run 1-9 data is consistent with the $\beta = 1$ hypothesis, with an insignificant exclusion of 1.0σ .

While the analyses reported in this thesis fix β to either 0 or 1, a complementary analysis of the same T2K Run 1-9 data allows β to freely vary. The analysis is reported in Ref. [4] and was performed by the Bayesian Markov chain MC based oscillation analysis fitter discussed in Section 5.1.3. The results of this analysis were compatible with the $\beta = 1$ three-flavour model at the 1σ level.

The previous iteration of the $\bar{\nu}_e$ appearance analysis was reported in Ref. [42] using T2K Run 1-7 data. 4 events were observed in the $\bar{\nu}$ -mode $\bar{\nu}_e$ CCQE-like sample compared to an expectation of 6.28 events, and the relatively background-like kinematic distribution of the observed events in this gave $\Delta\chi^2_\beta^{\text{obs}} = -2.51$. These corresponded to consistency with the $\beta = 0$ hypothesis and a 1.8σ exclusion of the $\beta = 1$ hypothesis. With the addition of the T2K Runs 8 and 9 data, the $\bar{\nu}$ -mode beam exposure increased by a factor of 2.2, while the number of observed events in this sample increased by a factor of 3.75. This, and the more signal-like kinematic distribution accounts for the why the analysis reported in this chapter is now instead consistent with the $\beta = 1$ three-flavour model.

6.5.1 Comparison to the NOvA Experiment

While the analyses presented in this chapter observes a $\bar{\nu}_e$ appearance signal at a significance of 2.4σ above the expected backgrounds, the NOvA experiment observes this at the $>4\sigma$ level [216]. There are two reasons for the weaker significance at T2K: While NOvA expected a total of 33.2 events (including a background of 14.0 events) and observed 33 events, T2K expected a total of 16.8 events (including a background of 9.3 events) and observed 15 events. So T2K observes a slight deficit compared to the expectation while NOvA does not. Also, the number of observed events relative to the size of the background is much larger in NOvA compared to T2K, resulting in a signal that is clearly less background-like.

6.6 Summary

Data from the T2K experiment has been used to perform two tests of the $\bar{\nu}_\mu \rightarrow \bar{\nu}_e$ oscillation channel: Whether the observed data is consistent with the predictions from the current best knowledge of the three-flavour neutrino oscillation framework, and whether $\bar{\nu}_\mu \rightarrow \bar{\nu}_e$ candidate events can be distinguished from the expected backgrounds.

The dataset used in this analysis is the T2K Run 1-9 data, corresponding to integrated beam exposures of 1.49×10^{21} and 1.63×10^{21} POT in ν and $\bar{\nu}$ modes, respectively. The analysis was produced by comparing the observed kinematic distribution of the $\bar{\nu}$ -mode $\bar{\nu}_e$ CCQE-like sample to those from a large ensemble of randomly-generated pseudo-experiments, to account for uncertainties in all oscillation and systematic parameters. The robustness of the analysis was tested against valid changes to both the statistical methodology and cross-section models, and in all cases the conclusions of the analysis were found to be robust.

This analysis predicted 16.8 ± 1.2 events (including an expected background of 9.3 ± 0.7 events) and observed 15 events in the $\bar{\nu}$ -mode $\bar{\nu}_e$ CCQE-like sample. Using information from both the rate and shape of the observed kinematic distributions, the observed data were found to be consistent with the three-flavour PMNS neutrino oscillation framework at the 1.0σ level. Additionally, the observed $\bar{\nu}_\mu \rightarrow \bar{\nu}_e$ events could

not be fully distinguished from the expected backgrounds, with the background-only hypothesis disfavoured at a significance of 2.4σ .

Chapter 7

Conclusions and Outlook

In this thesis two analyses were presented, using neutrino and antineutrino beam data collected by the T2K experiment. Both analyses involved comparing the predictions of the three-flavour oscillation model (binned in reconstructed neutrino energy and lepton angle) to observations in five high-purity Super-K event samples, corresponding to both ν_μ and ν_e CCQE-like events in ν and $\bar{\nu}$ beam modes, with an additional ν -mode ν_e CC1 π^+ -like sample. In this chapter, the main results of these analyses will be shown before giving a brief overview of the expected future of T2K and measurements of the CP-violating phase, δ_{CP} .

7.1 Summary of the T2K Oscillation Parameter Constraints

Data from T2K Runs 1-10 were used to produce constraints on a number of three-flavour neutrino oscillation parameters by constructing Frequentist confidence regions from Poisson log-likelihood ratios with all nuisance parameters marginalised. The resulting normal ordering best-fit points and 1σ confidence intervals are as shown in Eq. (7.1), with the best-fit being in the normal mass ordering in all cases. All results except those for $\sin^2 \theta_{13}$ are produced using a constraint applied on $\sin^2 2\theta_{13}$ from reactor experiments. The results obtained with and without the use of this constraint were found to be in excellent agreement.

$$\begin{aligned}\delta_{CP} &= -2.01^{+0.93}_{-0.76} \\ \sin^2 \theta_{23} &= 0.552^{+0.024}_{-0.048} \\ \Delta m_{32}^2 &= 2.49 \pm 0.05 \times 10^{-3} \text{ eV}^2 \text{c}^{-4} \\ \sin^2 \theta_{13} &= 2.54^{+0.49}_{-0.38} \times 10^{-2}\end{aligned}\tag{7.1}$$

For δ_{CP} , the best-fit point is close to the maximally CP-violating value of $-\frac{\pi}{2}$, and CP-conservation is excluded at close to the 90% confidence level. The observed constraint on δ_{CP} is stronger than expected from sensitivity studies, but was found to be compatible with the three-flavour oscillation model. For $\sin^2 \theta_{23}$, the best-fit point was found to be in the upper-octant, but is compatible with maximal mixing at the 1σ confidence level. The T2K constraints on Δm_{32}^2 and $\sin^2 \theta_{13}$ are competitive with

recent measurements from other experiments, and are world-leading for $\sin^2 \theta_{23}$ and δ_{CP} .

7.2 Summary of the Search for $\bar{\nu}_\mu \rightarrow \bar{\nu}_e$ Oscillations

The other analysis used data from T2K Runs 1-9 to perform two tests of the $\bar{\nu}_\mu \rightarrow \bar{\nu}_e$ oscillation channel: Whether the observed data is consistent with the predictions from the current best knowledge of the three-flavour neutrino oscillation model, and whether $\bar{\nu}_\mu \rightarrow \bar{\nu}_e$ candidate events can be distinguished from the expected backgrounds. The analysis predicted 16.8 ± 1.2 events (including an expected background of 9.3 ± 0.7 events) and observed 15 events in the $\bar{\nu}$ -mode $\bar{\nu}_e$ CCQE-like sample. Using information from both the rate and shape of the observed kinematic distributions, the observed data were found to be consistent with the three-flavour neutrino oscillation model at the 1.0σ level. Additionally, the observed $\bar{\nu}_\mu \rightarrow \bar{\nu}_e$ events could not be fully distinguished from the expected backgrounds, with the background-only hypothesis disfavoured at a significance of 2.4σ . By contrast, the NOvA experiment observes the appearance of $\bar{\nu}_\mu \rightarrow \bar{\nu}_e$ over the expected backgrounds at the $> 4\sigma$ level [216].

7.3 The Future of T2K and CP-violation Measurements

The T2K experiment has continued to take data beyond what has been presented in this thesis, with an additional exposure of 0.179×10^{21} POT delivered in ν -mode (constituting T2K Run 11), which at the time of writing, is beginning to be processed and soon analysed. After the collection of the Run 11 data, the J-PARC beamline entered into a shut-down period to allow preparations for the next phase of operations, T2K-II. This new phase, the proposal for which has been approved and is detailed in Ref. [217], will collect data up to a total exposure of 20×10^{21} POT (an increase of ~ 5.6 times the T2K Runs 1-10 exposure) by the time the next generation of accelerator-based long-baseline neutrino oscillation experiments, DUNE and Hyper-K, are expected to begin operation in 2026.

T2K-II aims to improve upon the current measurements of δ_{CP} , not just by increasing the quantity of data collected, but also by greatly reducing systematic uncertainties. In order to achieve these goals, the following upgrades [217] will be put into effect by the start of T2K-II operations (expected in late 2022):

- **Beam power upgrade** - Upgrades to the J-PARC main ring accelerator power supply, beamline cooling capacity, and the magnetic focussing horns will increase the beam power from its current design intensity of 750 kW to a maximum of 1.3 MW, allowing for an exposure of up to 20×10^{21} POT to be accumulated.
- **Near detector upgrades** - Upgrades to the FGDs and TPCs will provide a more granular detector with the ability to reconstruct high-angle leptons and improved reconstruction of the hadronic part of neutrino interactions with the

ability to track stopping protons and pions in addition to distinguishing between electrons from ν_e events and converted photons. Together with interaction model improvements, these upgrades will aid in the goal of reducing the overall systematic uncertainties to the $\sim 4\%$ level [218].

- **Super-K gadolinium doping** - The water in Super-K is currently doped with a 0.02% concentration of $\text{Gd}_2(\text{SO}_4)_3$, which will be increased to 0.2% to give a neutron capture efficiency of $\sim 90\%$ [107]. This will allow for neutrino and antineutrino events to be distinguished by detecting the neutron in the reaction $\bar{\nu}_l + p \rightarrow l^+ + n$ and will reduce backgrounds in the $\bar{\nu}_\mu \rightarrow \bar{\nu}_e$ searches.
- **Improved Super-K event selection** - Increasing the number of $\bar{\nu}_\mu$ CC events used in the oscillation analyses increases the T2K sensitivity to θ_{23} and Δm_{32}^2 and indirectly to δ_{CP} . To achieve this, a sample for $\bar{\nu}_\mu$ CC1 π^+ -like events is under development, potentially increasing the number of $\bar{\nu}_\mu$ CC events by up to 40% [217, 219]. Similarly, to directly enhance the sensitivity to δ_{CP} , an additional $\bar{\nu}_e$ CC1 π^+ -like sample with the resonance pion above Cherenkov threshold is under development, as well as an updated $\bar{\nu}_e$ CCQE-like sample to increase the selection efficiency and purity [219].
- **Improved interaction model** - CCQE interactions will continue to be the dominant contribution during T2K-II, so improving the current shortcomings of the CCQE model is necessary for reducing uncertainties and potential biases. For example, the current dipole form factor and ad hoc CCQE Q^2 normalisation uncertainties are being replaced by a more theoretically-motivated approach and the effects of shell occupancy in the spectral function are being accounted for in more detail. With the addition of more pion-like event samples at Super-K, the accurate modelling of pion interactions becomes increasingly important, so a more detailed treatment of uncertainties in pion kinematics is being implemented along with improved modelling of pion FSI and simulating the effect of nucleon removal energy in resonance pion production interactions. Finally, the new information available from the upgraded ND280 detectors (such as proton tagging and transverse kinematics) will greatly aid in constraining the interaction model and reducing systematic uncertainties [220–222].

With the above T2K-II improvements bringing the total systematic uncertainties to the $\sim 4\%$ level and with an accumulated beam exposure of 20×10^{21} POT, the expected T2K-II sensitivity to exclude CP-conservation is shown in Fig. 7.1. A number of experiments (such as JUNO [223], NOvA [224], and ORCA [225]) are expected to determine the mass ordering either before or during the T2K-II run period, so sensitivities are shown both with known and unknown mass orderings.

T2K is not the only neutrino oscillation experiment attempting to measure δ_{CP} and joint fits can take advantage of synergies with between experiments, increasing

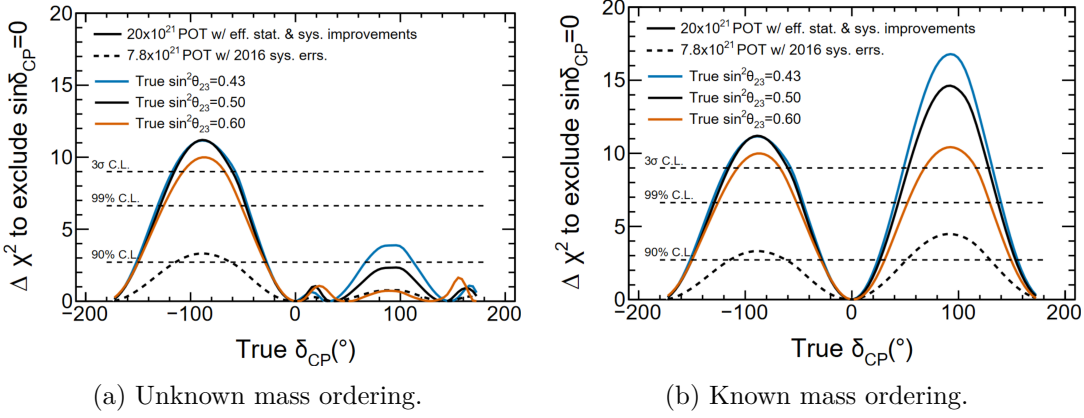


Figure 7.1: The expected T2K-II sensitivity to exclude CP-conservation as a function of true δ_{CP} for various θ_{23} values. The true mass ordering is assumed to be normal. Reproduced from Ref. [218].

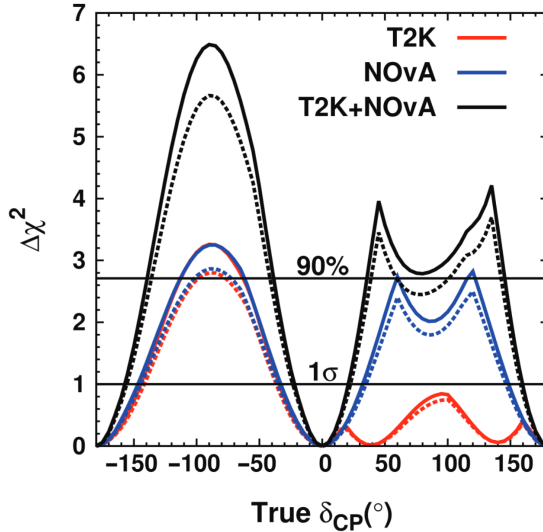


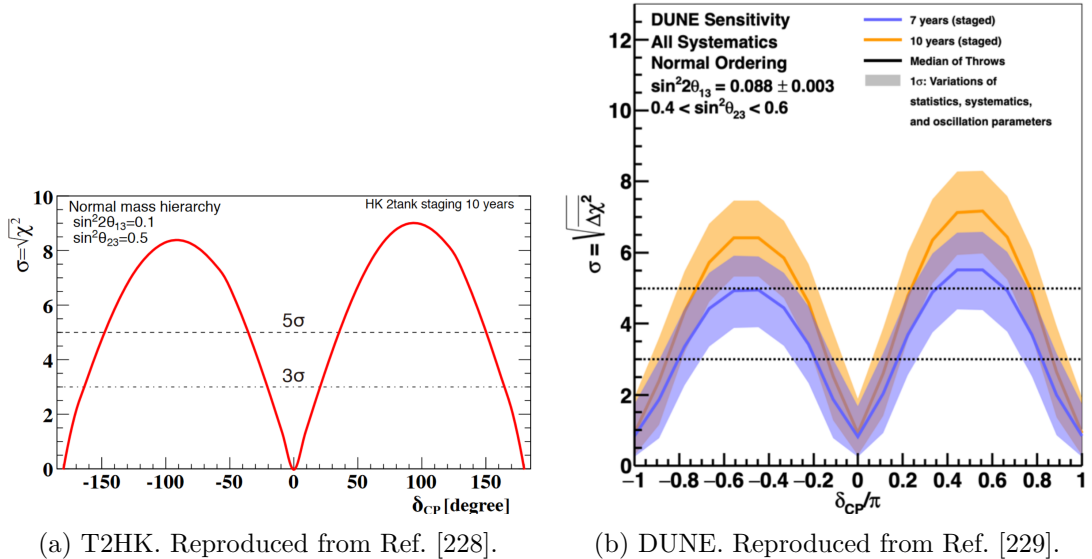
Figure 7.2: The expected T2K, NOvA, and joint sensitivities to exclude CP-conservation as a function of true δ_{CP} . Solid lines correspond to an analysis with no normalisation uncertainties, while they are included in the analysis used to produce the dotted lines. Predictions are generated with equal beam exposures in ν and $\bar{\nu}$ modes for both experiments. The true value of $\sin^2 \theta_{23}$ is set to 0.5 and the mass ordering is assumed to be unknown and the true ordering is normal. Reproduced from Ref. [226].

sensitivity to δ_{CP} while using a common analysis methodology, a common interaction model, and accounting for correlated uncertainties between experiments. An example of such a joint fit is between the T2K and NOvA experiments, expected in 2022 [222], with an example of the expected joint sensitivity to exclude CP-conservation shown in Fig. 7.2. In addition, work is ongoing towards a joint fit of T2K and Super-K atmospheric neutrino data, also expected in 2022.

After the completion of T2K-II (expected 2026) it will be succeeded by the T2HK (Tokai to Hyper-Kamiokande) experiment [227], using the upgraded J-PARC neutrino beam together with the two (currently under construction) Hyper-Kamiokande water Cherenkov far detectors. Each detector will be a 190 kton fiducial mass water tank

(each an increase in fiducial mass by a factor of ~ 8.4 compared to Super-K), with either both detectors located underground 8 km south of the current Super-K detector. The T2HK ν_μ or $\bar{\nu}_\mu$ beam will be sharply peaked at ~ 0.6 GeV (the same as for T2K) before passing through the upgraded near detector suite and an intermediate water Cherenkov detector before travelling to the far detectors. The expected T2HK sensitivity to exclude CP-conservation is shown in Fig. 7.3a.

Alongside T2HK will operate another next-generation accelerator-based long-baseline neutrino oscillation experiment, DUNE (Deep Underground Neutrino Experiment). A broad ν_μ or $\bar{\nu}_\mu$ beam peaked at ~ 2.5 GeV will be produced at Fermilab in the USA before passing through a near detector and travelling 1285 km to the underground 40 kton liquid argon far detector in South Dakota, USA. The expected DUNE sensitivity to exclude CP-conservation is shown in Fig. 7.3b.



(a) T2HK. Reproduced from Ref. [228].

(b) DUNE. Reproduced from Ref. [229].

Figure 7.3: The expected T2HK and DUNE sensitivities to exclude CP-conservation as a function of true δ_{CP} . In both cases, the true mass ordering is assumed to be normal and is assumed to be known. The T2HK sensitivity is generated with fixed true values for θ_{13} and θ_{23} and is shown for after ten years of operation. The DUNE sensitivity is shown, for seven and ten years of operation, as an ensemble of predictions with statistical, systematic, and oscillation parameter varied as indicated.

Over the next 15 years, there is much potential for resolving the question of whether CP-symmetry is violated in the lepton sector, with T2K-II able to provide 3σ hints of CP-violation for a narrow range of true δ_{CP} values around the current T2K best-fit point, and with DUNE and T2HK able to discover CP-violation to $> 5\sigma$ across a wide range of true δ_{CP} values.

Appendix A

Flux, Interaction Model, and Detector Systematic Parameters used in the T2K Run 1-10 Analysis

A total of 50 flux, 42 interaction/cross-section, and 45 Super-K detector + SI + PN systematic parameters have been used in the T2K Run 1-10 analysis in order to account for the effects of systematic uncertainties. These parameters are summarised, along with their nominal and pre/post-fit uncertainties, in Tables A.1 to A.6 [90]. A number of the cross-section parameters are intentionally not constrained during the near detector fit due to a lack of sensitivity to these parameters at the near detectors; however, they are included in the analyses presented in this thesis as Super-K is sensitive to them. These are $f_{ShapeBgRESlowPpi}^{\text{ND}}$, $f_{Norm_{NC1\gamma}}^{\text{ND}}$, $f_{Shape_{2p2hlowEnu}}^{\text{ND}}$, $f_{Shape_{2p2hhhighEnu}}^{\text{ND}}$, $f_{Shape_{2p2hlowEnubar}}^{\text{ND}}$, $f_{Shape_{2p2hhhighEnubar}}^{\text{ND}}$, $f_{Norm_{\bar{\nu}_e \rightarrow \bar{\nu}_\mu}}^{\text{ND}}$, $f_{Norm_{\nu_e \rightarrow \nu_\mu}}^{\text{ND}}$, and $f_{Norm_{NCOthfar}}^{\text{ND}}$, and in the following tables such parameters have equal prefit and postfit fractional errors. The systematic parameters 1σ fractional errors and correlations between them are shown in Figs. 4.36, A.1 and A.2.

Two types of systematic parameters are listed in the tables below: normalisation and shape parameters. Normalisation parameters (any parameter not labelled as ‘Shape’) simply act to scale the event rates in all applicable ($E_{\text{true}}, E_{\text{rec}}, \theta$) kinematic bins and for all relevant interaction modes, as indicated, and the scaling factor is equal to the parameter value. Shape parameters also act to scale the event rates in all applicable kinematic bins and interaction modes, but the scaling factor can be different for each bin and interaction mode and are determined by response functions of arbitrary shape. These response functions are pre-calculated by the XsecResponse [1] software package.

All parameter values and their uncertainties are listed as a fraction of the corresponding parameter value (if non-zero) used to generate the NEUT v5.4.0 MC and SKDETSIM simulations, so do not necessarily directly correspond to the value of a physical quantity. For all parameters related to Super-K flux, detector, SI, and PN uncertainties, these generated values are 1. For the interaction model parameters, the

generated values are listed in Ref. [119]. For example, the generated M_A^{QE} value in NEUT v5.4.0 is 1.03 GeV [119], while the post ND fit nominal value of the corresponding systematic parameter in VALOR, $f_{Shape_{M_A^{QE}}}^{\text{ND}}$, is 0.969, corresponding to a postfit M_A^{QE} value of 0.998 GeV.

Index	Parameter	Description	Best fit	1σ pre/postfit fractional error
0	$f_{0;t,r}^{\text{ND}}$	ν -mode ν_μ flux norm., $E_{\text{true}} = 0.0 - 0.4$ GeV	1.110	0.067 / 0.048
1	$f_{1;t,r}^{\text{ND}}$	ν -mode ν_μ flux norm., $E_{\text{true}} = 0.4 - 0.5$ GeV	1.095	0.057 / 0.039
2	$f_{2;t,r}^{\text{ND}}$	ν -mode ν_μ flux norm., $E_{\text{true}} = 0.5 - 0.6$ GeV	1.082	0.053 / 0.034
3	$f_{3;t,r}^{\text{ND}}$	ν -mode ν_μ flux norm., $E_{\text{true}} = 0.6 - 0.7$ GeV	1.075	0.047 / 0.032
4	$f_{4;t,r}^{\text{ND}}$	ν -mode ν_μ flux norm., $E_{\text{true}} = 0.7 - 1.0$ GeV	1.063	0.074 / 0.039
5	$f_{5;t,r}^{\text{ND}}$	ν -mode ν_μ flux norm., $E_{\text{true}} = 1.0 - 1.5$ GeV	1.031	0.070 / 0.037
6	$f_{6;t,r}^{\text{ND}}$	ν -mode ν_μ flux norm., $E_{\text{true}} = 1.5 - 2.5$ GeV	1.032	0.062 / 0.035
7	$f_{7;t,r}^{\text{ND}}$	ν -mode ν_μ flux norm., $E_{\text{true}} = 2.5 - 3.5$ GeV	1.008	0.074 / 0.041
8	$f_{8;t,r}^{\text{ND}}$	ν -mode ν_μ flux norm., $E_{\text{true}} = 3.5 - 5.0$ GeV	0.975	0.089 / 0.036
9	$f_{9;t,r}^{\text{ND}}$	ν -mode ν_μ flux norm., $E_{\text{true}} = 5.0 - 7.0$ GeV	0.924	0.102 / 0.037
10	$f_{10;t,r}^{\text{ND}}$	ν -mode ν_μ flux norm., $E_{\text{true}} = 7.0 - 30.0$ GeV	0.907	0.117 / 0.045
11	$f_{11;t,r}^{\text{ND}}$	ν -mode $\bar{\nu}_\mu$ flux norm., $E_{\text{true}} = 0.0 - 0.7$ GeV	1.056	0.093 / 0.084
12	$f_{12;t,r}^{\text{ND}}$	ν -mode $\bar{\nu}_\mu$ flux norm., $E_{\text{true}} = 0.7 - 1.0$ GeV	1.045	0.062 / 0.052
13	$f_{13;t,r}^{\text{ND}}$	ν -mode $\bar{\nu}_\mu$ flux norm., $E_{\text{true}} = 1.0 - 1.5$ GeV	1.039	0.074 / 0.061
14	$f_{14;t,r}^{\text{ND}}$	ν -mode $\bar{\nu}_\mu$ flux norm., $E_{\text{true}} = 1.5 - 2.5$ GeV	1.049	0.080 / 0.069
15	$f_{15;t,r}^{\text{ND}}$	ν -mode $\bar{\nu}_\mu$ flux norm., $E_{\text{true}} = 2.5 - 30.0$ GeV	1.037	0.079 / 0.063
16	$f_{16;t,r}^{\text{ND}}$	ν -mode ν_e flux norm., $E_{\text{true}} = 0.0 - 0.5$ GeV	1.087	0.057 / 0.040
17	$f_{17;t,r}^{\text{ND}}$	ν -mode ν_e flux norm., $E_{\text{true}} = 0.5 - 0.7$ GeV	1.075	0.054 / 0.036
18	$f_{18;t,r}^{\text{ND}}$	ν -mode ν_e flux norm., $E_{\text{true}} = 0.7 - 0.8$ GeV	1.063	0.052 / 0.035
19	$f_{19;t,r}^{\text{ND}}$	ν -mode ν_e flux norm., $E_{\text{true}} = 0.8 - 1.5$ GeV	1.042	0.059 / 0.038
20	$f_{20;t,r}^{\text{ND}}$	ν -mode ν_e flux norm., $E_{\text{true}} = 1.5 - 2.5$ GeV	0.998	0.082 / 0.041
21	$f_{21;t,r}^{\text{ND}}$	ν -mode ν_e flux norm., $E_{\text{true}} = 2.5 - 4.0$ GeV	0.981	0.086 / 0.039
22	$f_{22;t,r}^{\text{ND}}$	ν -mode ν_e flux norm., $E_{\text{true}} = 4.0 - 30.0$ GeV	0.983	0.095 / 0.055
23	$f_{23;t,r}^{\text{ND}}$	ν -mode $\bar{\nu}_e$ flux norm., $E_{\text{true}} = 0.0 - 2.5$ GeV	1.023	0.098 / 0.086
24	$f_{24;t,r}^{\text{ND}}$	ν -mode $\bar{\nu}_e$ flux norm., $E_{\text{true}} = 2.5 - 30.0$ GeV	1.095	0.132 / 0.114

Table A.1: Summary of ν -mode flux systematic normalisation parameters.

Index	Parameter	Description	Best fit	1σ pre/postfit fractional error
25	$f_{0;t,r}^{\text{ND}}$ $\bar{\nu}$ -mode	$\bar{\nu}$ -mode ν_μ flux norm., $E_{\text{true}} = 0.0 - 0.7 \text{ GeV}$	1.107	0.086 / 0.061
26	$f_{1;t,r}^{\text{ND}}$ $\bar{\nu}$ -mode	$\bar{\nu}$ -mode ν_μ flux norm., $E_{\text{true}} = 0.7 - 1.0 \text{ GeV}$	1.067	0.065 / 0.046
27	$f_{2;t,r}^{\text{ND}}$ $\bar{\nu}$ -mode	$\bar{\nu}$ -mode ν_μ flux norm., $E_{\text{true}} = 1.0 - 1.5 \text{ GeV}$	1.072	0.061 / 0.038
28	$f_{3;t,r}^{\text{ND}}$ $\bar{\nu}$ -mode	$\bar{\nu}$ -mode ν_μ flux norm., $E_{\text{true}} = 1.5 - 2.5 \text{ GeV}$	1.072	0.068 / 0.041
29	$f_{4;t,r}^{\text{ND}}$ $\bar{\nu}$ -mode	$\bar{\nu}$ -mode ν_μ flux norm., $E_{\text{true}} = 2.5 - 30.0 \text{ GeV}$	1.024	0.069 / 0.041
30	$f_{5;t,r}^{\text{ND}}$ $\bar{\nu}$ -mode	$\bar{\nu}$ -mode $\bar{\nu}_\mu$ flux norm., $E_{\text{true}} = 0.0 - 0.4 \text{ GeV}$	1.093	0.068 / 0.052
31	$f_{6;t,r}^{\text{ND}}$ $\bar{\nu}$ -mode	$\bar{\nu}$ -mode $\bar{\nu}_\mu$ flux norm., $E_{\text{true}} = 0.4 - 0.5 \text{ GeV}$	1.087	0.059 / 0.041
32	$f_{7;t,r}^{\text{ND}}$ $\bar{\nu}$ -mode	$\bar{\nu}$ -mode $\bar{\nu}_\mu$ flux norm., $E_{\text{true}} = 0.5 - 0.6 \text{ GeV}$	1.067	0.057 / 0.038
33	$f_{8;t,r}^{\text{ND}}$ $\bar{\nu}$ -mode	$\bar{\nu}$ -mode $\bar{\nu}_\mu$ flux norm., $E_{\text{true}} = 0.6 - 0.7 \text{ GeV}$	1.063	0.047 / 0.032
34	$f_{9;t,r}^{\text{ND}}$ $\bar{\nu}$ -mode	$\bar{\nu}$ -mode $\bar{\nu}_\mu$ flux norm., $E_{\text{true}} = 0.7 - 1.0 \text{ GeV}$	1.092	0.079 / 0.042
35	$f_{10;t,r}^{\text{ND}}$ $\bar{\nu}$ -mode	$\bar{\nu}$ -mode $\bar{\nu}_\mu$ flux norm., $E_{\text{true}} = 1.0 - 1.5 \text{ GeV}$	1.055	0.079 / 0.041
36	$f_{11;t,r}^{\text{ND}}$ $\bar{\nu}$ -mode	$\bar{\nu}$ -mode $\bar{\nu}_\mu$ flux norm., $E_{\text{true}} = 1.5 - 2.5 \text{ GeV}$	1.010	0.063 / 0.042
37	$f_{12;t,r}^{\text{ND}}$ $\bar{\nu}$ -mode	$\bar{\nu}$ -mode $\bar{\nu}_\mu$ flux norm., $E_{\text{true}} = 2.5 - 3.5 \text{ GeV}$	1.007	0.066 / 0.048
38	$f_{13;t,r}^{\text{ND}}$ $\bar{\nu}$ -mode	$\bar{\nu}$ -mode $\bar{\nu}_\mu$ flux norm., $E_{\text{true}} = 3.5 - 5.0 \text{ GeV}$	0.955	0.090 / 0.061
39	$f_{14;t,r}^{\text{ND}}$ $\bar{\nu}$ -mode	$\bar{\nu}$ -mode $\bar{\nu}_\mu$ flux norm., $E_{\text{true}} = 5.0 - 7.0 \text{ GeV}$	0.959	0.086 / 0.057
40	$f_{15;t,r}^{\text{ND}}$ $\bar{\nu}$ -mode	$\bar{\nu}$ -mode $\bar{\nu}_\mu$ flux norm., $E_{\text{true}} = 7.0 - 30.0 \text{ GeV}$	0.930	0.119 / 0.093
41	$f_{16;t,r}^{\text{ND}}$ $\bar{\nu}$ -mode	$\bar{\nu}$ -mode $\bar{\nu}_e$ flux norm., $E_{\text{true}} = 0.0 - 2.5 \text{ GeV}$	1.031	0.091 / 0.071
42	$f_{17;t,r}^{\text{ND}}$ $\bar{\nu}$ -mode	$\bar{\nu}$ -mode $\bar{\nu}_e$ flux norm., $E_{\text{true}} = 2.5 - 30.0 \text{ GeV}$	1.029	0.085 / 0.066
43	$f_{18;t,r}^{\text{ND}}$ $\bar{\nu}$ -mode	$\bar{\nu}$ -mode $\bar{\nu}_e$ flux norm., $E_{\text{true}} = 0.0 - 0.5 \text{ GeV}$	1.082	0.058 / 0.042
44	$f_{19;t,r}^{\text{ND}}$ $\bar{\nu}$ -mode	$\bar{\nu}$ -mode $\bar{\nu}_e$ flux norm., $E_{\text{true}} = 0.5 - 0.7 \text{ GeV}$	1.071	0.054 / 0.037
45	$f_{20;t,r}^{\text{ND}}$ $\bar{\nu}$ -mode	$\bar{\nu}$ -mode $\bar{\nu}_e$ flux norm., $E_{\text{true}} = 0.7 - 0.8 \text{ GeV}$	1.058	0.056 / 0.042
46	$f_{21;t,r}^{\text{ND}}$ $\bar{\nu}$ -mode	$\bar{\nu}$ -mode $\bar{\nu}_e$ flux norm., $E_{\text{true}} = 0.8 - 1.5 \text{ GeV}$	1.037	0.057 / 0.041
47	$f_{22;t,r}^{\text{ND}}$ $\bar{\nu}$ -mode	$\bar{\nu}$ -mode $\bar{\nu}_e$ flux norm., $E_{\text{true}} = 1.5 - 2.5 \text{ GeV}$	1.007	0.080 / 0.061
48	$f_{23;t,r}^{\text{ND}}$ $\bar{\nu}$ -mode	$\bar{\nu}$ -mode $\bar{\nu}_e$ flux norm., $E_{\text{true}} = 2.5 - 4.0 \text{ GeV}$	1.008	0.090 / 0.069
49	$f_{24;t,r}^{\text{ND}}$ $\bar{\nu}$ -mode	$\bar{\nu}$ -mode $\bar{\nu}_e$ flux norm., $E_{\text{true}} = 4.0 - 30.0 \text{ GeV}$	1.089	0.152 / 0.127

Table A.2: Summary of $\bar{\nu}$ -mode flux systematic normalisation parameters.

Index	Parameter	Description	Best fit	1σ pre/postfit fractional error
50	$f_{Norm_{2p2h\nu}}^{ND}$	2p2h norm. for ^{16}O	1.058	1.000 / 0.153
51	$f_{Shape_{C_5^A}}^{ND}$	C_5^A nucleon to Δ transition axial form factor	0.974	0.149 / 0.058
52	$f_{Shape_{BgRES}}^{ND}$	Scale of isospin $\frac{1}{2}$ nonres. background	0.665	0.308 / 0.180
53	$f_{Shape_{BgRESlowPpi}}^{ND}$	Scale of isospin $\frac{1}{2}$ nonres. background ($\bar{\nu}, p_\pi < 0.2$ GeV)	0.738	1.000 / 1.000
54	$f_{Shape_{M_A^{QE}}}^{ND}$	CCQE axial-mass scaling factor	0.969	0.050 / 0.034
55	$f_{Shape_{M_A^{RES}}}^{ND}$	Resonance-production axial-mass scaling factor	0.831	0.158 / 0.052
56	$f_{Norm_{NCcoh}}^{ND}$	NC coherent norm.	1.018	0.300 / 0.299
57	$f_{Norm_{\nu_e \rightarrow \nu_\mu}}^{ND}$	CC ν_e norm.	1.000	0.028 / 0.028
58	$f_{Norm_{NC1\gamma}}^{ND}$	NC 1γ norm.	1.000	1.000 / 1.000
59	$f_{Norm_{\bar{\nu}_e \rightarrow \bar{\nu}_\mu}}^{ND}$	CC $\bar{\nu}_e$ norm.	1.000	0.028 / 0.028
60	$f_{Norm_{2p2h\bar{\nu}}}^{ND}$	$\bar{\nu}$ 2p2h norm. for ^{16}O	0.722	1.000 / 0.162
61	$f_{Shape_{2p2h\nu}}^{ND}$	ν 2p2h ^{16}O shape	-0.003	3.000 / 0.174
62	$f_{Norm_{2p2hCtoO}}^{ND}$	2p2h ^{12}C to ^{16}O norm.	1.046	0.200 / 0.147
63	$f_{Shape_{2p2hLowE\nu}}^{ND}$	2p2h energy dependence ($\nu < 0.6$ GeV)	1.000	1.000 / 1.000
64	$f_{Shape_{2p2hHighE\nu}}^{ND}$	2p2h energy dependence ($\nu > 0.6$ GeV)	1.000	1.000 / 1.000
65	$f_{Shape_{2p2hLowE\bar{\nu}}}^{ND}$	2p2h energy dependence ($\bar{\nu} < 0.6$ GeV)	1.000	1.000 / 1.000
66	$f_{Shape_{2p2hHighE\bar{\nu}}}^{ND}$	2p2h energy dependence ($\bar{\nu} > 0.6$ GeV)	1.000	1.000 / 1.000
67	$f_{Shape_{Q2_0}}^{ND}$	CCQE Q^2 norm. ($0.00 - 0.05$ GeV 2)	-0.216	0.165 / 0.047
68	$f_{Shape_{Q2_1}}^{ND}$	CCQE Q^2 norm. ($0.05 - 0.10$ GeV 2)	-0.113	0.145 / 0.040
69	$f_{Shape_{Q2_2}}^{ND}$	CCQE Q^2 norm. ($0.10 - 0.15$ GeV 2)	0.023	0.130 / 0.052
70	$f_{Shape_{Q2_3}}^{ND}$	CCQE Q^2 norm. ($0.15 - 0.20$ GeV 2)	0.027	0.150 / 0.077

Table A.3: Summary of cross section systematic parameters.

Index	Parameter	Description	Best fit	1σ pre/postfit fractional error
71	$f_{Shape_{Q^{24}}}^{\text{ND}}$	CCQE Q^2 norm. ($0.20 - 0.25 \text{ GeV}^2$)	0.087	0.160 / 0.099
72	$f_{Shape_{Q^{25}}}^{\text{ND}}$	CCQE Q^2 norm. ($0.25 - 0.50 \text{ GeV}^2$)	0.257	0.110 / 0.058
73	$f_{Shape_{Q^{26}}}^{\text{ND}}$	CCQE Q^2 norm. ($0.50 - 1.005 \text{ GeV}^2$)	0.136	0.180 / 0.081
74	$f_{Shape_{Q^{27}}}^{\text{ND}}$	CCQE Q^2 norm. ($> 1.00 \text{ GeV}^2$)	0.259	0.400 / 0.141
75	$f_{Shape_{\Delta EbO\nu}}^{\text{ND}}$	^{16}O nucleon removal energy shift for ν (MeV)	2.546	6.000 / 3.076
76	$f_{Shape_{\Delta EbO\bar{\nu}}}^{\text{ND}}$	^{16}O nucleon removal energy shift for $\bar{\nu}$ (MeV)	-1.262	6.000 / 3.189
77	$f_{Norm_{CC\nu}}^{\text{ND}}$	Coulomb shift scale factor for ν	0.999	0.020 / 0.020
78	$f_{Norm_{CC\bar{\nu}}}^{\text{ND}}$	Coulomb shift scale factor for $\bar{\nu}$	1.001	0.010 / 0.010
79	$f_{Shape_{CCBYDIS}}^{\text{ND}}$	Bodek-Yang corrections for CC DIS	1.042	1.000 / 0.191
80	$f_{Shape_{CCBYMPi}}^{\text{ND}}$	Bodek-Yang corrections for CC multi- π	-0.032	1.000 / 0.184
81	$f_{Shape_{CCAGKYMPi}}^{\text{ND}}$	Reweighting of multi- π multiplicity model	0.139	1.000 / 0.713
82	$f_{Norm_{CCMisc}}^{\text{ND}}$	CC1 γ , CC1K and CC1 η norm.	2.278	1.000 / 0.432
83	$f_{Norm_{CCCDISMPi\nu}}^{\text{ND}}$	ν CC DIS and multi- π norm.	1.062	0.035 / 0.030
84	$f_{Norm_{CCCDISMPi\bar{\nu}}}^{\text{ND}}$	$\bar{\nu}$ CC DIS and multi- π norm.	0.935	0.065 / 0.060
85	$f_{Norm_{CCCoherO}}^{\text{ND}}$	^{16}O CC coherent norm.	0.609	0.300 / 0.216
86	$f_{Norm_{NCOtherfar}}^{\text{ND}}$	NC miscellaneous norm.	1.000	0.300 / 0.300
87	$f_{Shape_{FSIQElowP}}^{\text{ND}}$	π FSI (QE scattering $p_\pi < 0.5 \text{ GeV}$)	0.826	0.293 / 0.095
88	$f_{Shape_{FSIQEhighP}}^{\text{ND}}$	π FSI (QE scattering $p_\pi > 0.4 \text{ GeV}$)	0.748	0.471 / 0.157
89	$f_{Shape_{FSIInelastic}}^{\text{ND}}$	π FSI (hadron production $p_\pi > 0.4 \text{ GeV}$)	1.715	1.099 / 0.308
90	$f_{Shape_{FSIAbsorption}}^{\text{ND}}$	π FSI (absorption $p_\pi < 0.5 \text{ GeV}$)	1.190	0.308 / 0.124
91	$f_{Shape_{FSIchargeexchange}}^{\text{ND}}$	π FSI (charge exchange $p_\pi > 0.4 \text{ GeV}$)	0.777	0.438 / 0.345

Table A.4: Summary of cross section systematic parameters (continued).

Index	Parameter	Description	1σ fractional error
92	$f_{0;t,r}^{SK}$	$E_{\text{rec}} = 0.00 - 0.40 \text{ GeV}; \nu_\mu/\bar{\nu}_\mu$ CCQE; ν -mode $\langle\bar{\nu}_\mu\rangle$ CCQE-like	0.008
93	$f_{1;t,r}^{SK}$	$E_{\text{rec}} = 0.40 - 1.10 \text{ GeV}; \nu_\mu/\bar{\nu}_\mu$ CCQE; ν -mode $\langle\bar{\nu}_\mu\rangle$ CCQE-like	0.010
94	$f_{2;t,r}^{SK}$	$E_{\text{rec}} = 1.10 - 30.00 \text{ GeV}; \nu_\mu/\bar{\nu}_\mu$ CCQE; ν -mode $\langle\bar{\nu}_\mu\rangle$ CCQE-like	0.012
95	$f_{3;t,r}^{SK}$	$E_{\text{rec}} = 0.00 - 30.00 \text{ GeV}; \nu_\mu/\bar{\nu}_\mu$ CCnQE; ν -mode $\langle\bar{\nu}_\mu\rangle$ CCQE-like	0.048
96	$f_{4;t,r}^{SK}$	$E_{\text{rec}} = 0.00 - 30.00 \text{ GeV}; \nu_e/\bar{\nu}_e/\text{sig}\nu_e$ CC; ν -mode $\langle\bar{\nu}_\mu\rangle$ CCQE-like	1.007
97	$f_{5;t,r}^{SK}$	$E_{\text{rec}} = 0.00 - 30.00 \text{ GeV}; \text{all NC}; \nu$ -mode $\langle\bar{\nu}_\mu\rangle$ CCQE-like	0.649
98	$f_{6;t,r}^{SK}$	$E_{\text{rec}} = 0.00 - 0.35 \text{ GeV}; \text{Osc. } \nu_e$ CC; ν -mode $\langle\bar{\nu}_e\rangle$ CCQE-like	0.029
99	$f_{7;t,r}^{SK}$	$E_{\text{rec}} = 0.35 - 0.80 \text{ GeV}; \text{Osc. } \nu_e$ CC; ν -mode $\langle\bar{\nu}_e\rangle$ CCQE-like	0.028
100	$f_{8;t,r}^{SK}$	$E_{\text{rec}} = 0.80 - 1.25 \text{ GeV}; \text{Osc. } \nu_e$ CC; ν -mode $\langle\bar{\nu}_e\rangle$ CCQE-like	0.042
101	$f_{9;t,r}^{SK}$	$E_{\text{rec}} = 0.00 - 0.35 \text{ GeV}; \nu_\mu/\bar{\nu}_\mu$ CC; ν -mode $\langle\bar{\nu}_e\rangle$ CCQE-like	0.296
102	$f_{10;t,r}^{SK}$	$E_{\text{rec}} = 0.35 - 0.80 \text{ GeV}; \nu_\mu/\bar{\nu}_\mu$ CC; ν -mode $\langle\bar{\nu}_e\rangle$ CCQE-like	0.304
103	$f_{11;t,r}^{SK}$	$E_{\text{rec}} = 0.80 - 1.25 \text{ GeV}; \nu_\mu/\bar{\nu}_\mu$ CC; ν -mode $\langle\bar{\nu}_e\rangle$ CCQE-like	0.444
104	$f_{12;t,r}^{SK}$	$E_{\text{rec}} = 0.00 - 0.35 \text{ GeV}; \nu_e/\bar{\nu}_e$ CC; ν -mode $\langle\bar{\nu}_e\rangle$ CCQE-like	0.025
105	$f_{13;t,r}^{SK}$	$E_{\text{rec}} = 0.35 - 0.80 \text{ GeV}; \nu_e/\bar{\nu}_e$ CC; ν -mode $\langle\bar{\nu}_e\rangle$ CCQE-like	0.030
106	$f_{14;t,r}^{SK}$	$E_{\text{rec}} = 0.80 - 1.25 \text{ GeV}; \nu_e/\bar{\nu}_e$ CC; ν -mode $\langle\bar{\nu}_e\rangle$ CCQE-like	0.055
107	$f_{15;t,r}^{SK}$	$E_{\text{rec}} = 0.00 - 0.35 \text{ GeV}; \text{all NC}; \nu$ -mode $\langle\bar{\nu}_e\rangle$ CCQE-like	0.410
108	$f_{16;t,r}^{SK}$	$E_{\text{rec}} = 0.35 - 0.80 \text{ GeV}; \text{all NC}; \nu$ -mode $\langle\bar{\nu}_e\rangle$ CCQE-like	0.192
109	$f_{17;t,r}^{SK}$	$E_{\text{rec}} = 0.80 - 1.25 \text{ GeV}; \text{all NC}; \nu$ -mode $\langle\bar{\nu}_e\rangle$ CCQE-like	0.496

Table A.5: Summary of SK detector + SI + PN systematic normalisation parameters.

Index	Parameter	Description	1σ fractional error
110	$f_{0;t,r}^{SK}$ $\bar{\nu}$ -mode	$E_{\text{rec}} = 0.00 - 0.40 \text{ GeV}$; $\nu_\mu/\bar{\nu}_\mu$ CCQE; $\bar{\nu}$ -mode $\langle \bar{\nu}_\mu \rangle$ CCQE-like	0.008
111	$f_{1;t,r}^{SK}$ $\bar{\nu}$ -mode	$E_{\text{rec}} = 0.40 - 1.10 \text{ GeV}$; $\nu_\mu/\bar{\nu}_\mu$ CCQE; $\bar{\nu}$ -mode $\langle \bar{\nu}_\mu \rangle$ CCQE-like	0.008
112	$f_{2;t,r}^{SK}$ $\bar{\nu}$ -mode	$E_{\text{rec}} = 1.10 - 30.00 \text{ GeV}$; $\nu_\mu/\bar{\nu}_\mu$ CCQE; $\bar{\nu}$ -mode $\langle \bar{\nu}_\mu \rangle$ CCQE-like	0.009
113	$f_{3;t,r}^{SK}$ $\bar{\nu}$ -mode	$E_{\text{rec}} = 0.00 - 30.00 \text{ GeV}$; $\nu_\mu/\bar{\nu}_\mu$ CCnQE; $\bar{\nu}$ -mode $\langle \bar{\nu}_\mu \rangle$ CCQE-like	0.048
114	$f_{4;t,r}^{SK}$ $\bar{\nu}$ -mode	$E_{\text{rec}} = 0.00 - 30.00 \text{ GeV}$; $\nu_e/\bar{\nu}_e/\text{sig}\nu_e$ CC; $\bar{\nu}$ -mode $\langle \bar{\nu}_\mu \rangle$ CCQE-like	1.007
115	$f_{5;t,r}^{SK}$ $\bar{\nu}$ -mode	$E_{\text{rec}} = 0.00 - 30.00 \text{ GeV}$; all NC; $\bar{\nu}$ -mode $\langle \bar{\nu}_\mu \rangle$ CCQE-like	0.651
116	$f_{6;t,r}^{SK}$ $\bar{\nu}$ -mode	$E_{\text{rec}} = 0.00 - 0.35 \text{ GeV}$; Osc. ν_e CC; $\bar{\nu}$ -mode $\langle \bar{\nu}_e \rangle$ CCQE-like	0.036
117	$f_{7;t,r}^{SK}$ $\bar{\nu}$ -mode	$E_{\text{rec}} = 0.35 - 0.80 \text{ GeV}$; Osc. ν_e CC; $\bar{\nu}$ -mode $\langle \bar{\nu}_e \rangle$ CCQE-like	0.030
118	$f_{8;t,r}^{SK}$ $\bar{\nu}$ -mode	$E_{\text{rec}} = 0.80 - 1.25 \text{ GeV}$; Osc. ν_e CC; $\bar{\nu}$ -mode $\langle \bar{\nu}_e \rangle$ CCQE-like	0.054
119	$f_{9;t,r}^{SK}$ $\bar{\nu}$ -mode	$E_{\text{rec}} = 0.00 - 0.35 \text{ GeV}$; $\nu_\mu/\bar{\nu}_\mu$ CC; $\bar{\nu}$ -mode $\langle \bar{\nu}_e \rangle$ CCQE-like	0.374
120	$f_{10;t,r}^{SK}$ $\bar{\nu}$ -mode	$E_{\text{rec}} = 0.35 - 0.80 \text{ GeV}$; $\nu_\mu/\bar{\nu}_\mu$ CC; $\bar{\nu}$ -mode $\langle \bar{\nu}_e \rangle$ CCQE-like	0.339
121	$f_{11;t,r}^{SK}$ $\bar{\nu}$ -mode	$E_{\text{rec}} = 0.80 - 1.25 \text{ GeV}$; $\nu_\mu/\bar{\nu}_\mu$ CC; $\bar{\nu}$ -mode $\langle \bar{\nu}_e \rangle$ CCQE-like	0.336
122	$f_{12;t,r}^{SK}$ $\bar{\nu}$ -mode	$E_{\text{rec}} = 0.00 - 0.35 \text{ GeV}$; $\nu_e/\bar{\nu}_e$ CC; $\bar{\nu}$ -mode $\langle \bar{\nu}_e \rangle$ CCQE-like	0.026
123	$f_{13;t,r}^{SK}$ $\bar{\nu}$ -mode	$E_{\text{rec}} = 0.35 - 0.80 \text{ GeV}$; $\nu_e/\bar{\nu}_e$ CC; $\bar{\nu}$ -mode $\langle \bar{\nu}_e \rangle$ CCQE-like	0.032
124	$f_{14;t,r}^{SK}$ $\bar{\nu}$ -mode	$E_{\text{rec}} = 0.80 - 1.25 \text{ GeV}$; $\nu_e/\bar{\nu}_e$ CC; $\bar{\nu}$ -mode $\langle \bar{\nu}_e \rangle$ CCQE-like	0.060
125	$f_{15;t,r}^{SK}$ $\bar{\nu}$ -mode	$E_{\text{rec}} = 0.00 - 0.35 \text{ GeV}$; all NC; $\bar{\nu}$ -mode $\langle \bar{\nu}_e \rangle$ CCQE-like	0.410
126	$f_{16;t,r}^{SK}$ $\bar{\nu}$ -mode	$E_{\text{rec}} = 0.35 - 0.80 \text{ GeV}$; all NC; $\bar{\nu}$ -mode $\langle \bar{\nu}_e \rangle$ CCQE-like	0.197
127	$f_{17;t,r}^{SK}$ $\bar{\nu}$ -mode	$E_{\text{rec}} = 0.80 - 1.25 \text{ GeV}$; all NC; $\bar{\nu}$ -mode $\langle \bar{\nu}_e \rangle$ CCQE-like	0.468
128	$f_{0;t,r}^{SK} \langle \bar{\nu}_e \rangle$ CC1 π^+ -like	$E_{\text{rec}} = 0.30 - 0.80 \text{ GeV}$; Osc. ν_e CC; ν -mode $\langle \bar{\nu}_e \rangle$ CC1 π^+ -like	0.146
129	$f_{1;t,r}^{SK} \langle \bar{\nu}_e \rangle$ CC1 π^+ -like	$E_{\text{rec}} = 0.80 - 1.25 \text{ GeV}$; Osc. ν_e CC; ν -mode $\langle \bar{\nu}_e \rangle$ CC1 π^+ -like	0.120
130	$f_{2;t,r}^{SK} \langle \bar{\nu}_e \rangle$ CC1 π^+ -like	$E_{\text{rec}} = 0.30 - 0.80 \text{ GeV}$; $\nu_\mu/\bar{\nu}_\mu$ CC; ν -mode $\langle \bar{\nu}_e \rangle$ CC1 π^+ -like	0.418
131	$f_{3;t,r}^{SK} \langle \bar{\nu}_e \rangle$ CC1 π^+ -like	$E_{\text{rec}} = 0.80 - 1.25 \text{ GeV}$; $\nu_\mu/\bar{\nu}_\mu$ CC; ν -mode $\langle \bar{\nu}_e \rangle$ CC1 π^+ -like	0.302
132	$f_{4;t,r}^{SK} \langle \bar{\nu}_e \rangle$ CC1 π^+ -like	$E_{\text{rec}} = 0.30 - 0.80 \text{ GeV}$; $\nu_e/\bar{\nu}_e$ CC; ν -mode $\langle \bar{\nu}_e \rangle$ CC1 π^+ -like	0.144
133	$f_{5;t,r}^{SK} \langle \bar{\nu}_e \rangle$ CC1 π^+ -like	$E_{\text{rec}} = 0.80 - 1.25 \text{ GeV}$; $\nu_e/\bar{\nu}_e$ CC; ν -mode $\langle \bar{\nu}_e \rangle$ CC1 π^+ -like	0.146
134	$f_{6;t,r}^{SK} \langle \bar{\nu}_e \rangle$ CC1 π^+ -like	$E_{\text{rec}} = 0.30 - 0.80 \text{ GeV}$; all NC; ν -mode $\langle \bar{\nu}_e \rangle$ CC1 π^+ -like	0.998
135	$f_{7;t,r}^{SK} \langle \bar{\nu}_e \rangle$ CC1 π^+ -like	$E_{\text{rec}} = 0.80 - 1.25 \text{ GeV}$; all NC; ν -mode $\langle \bar{\nu}_e \rangle$ CC1 π^+ -like	0.546
136	$f_{E;r}^{SK}$	Super-K E_{rec} scale	0.021

Table A.6: Summary of SK detector + SI + PN systematic normalisation parameters (continued).

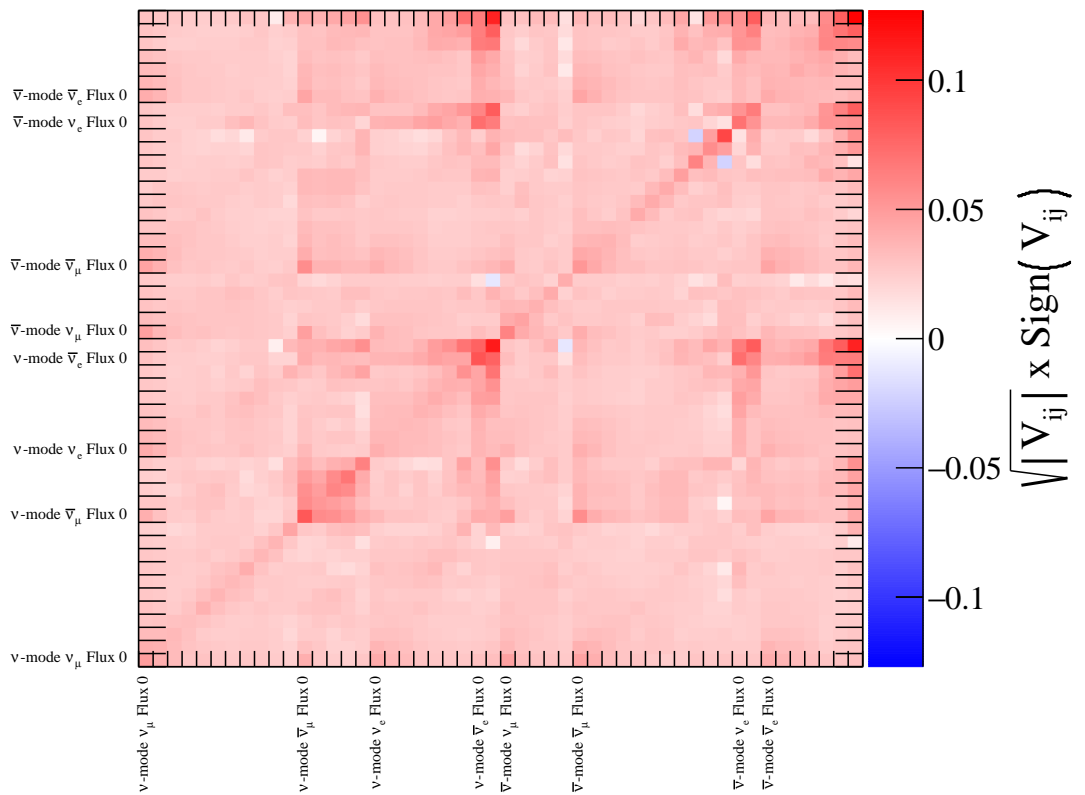


Figure A.1: The flux covariance matrix resulting from the near detector fit. The parameters are presented in the same order as in Tables A.1 and A.2.

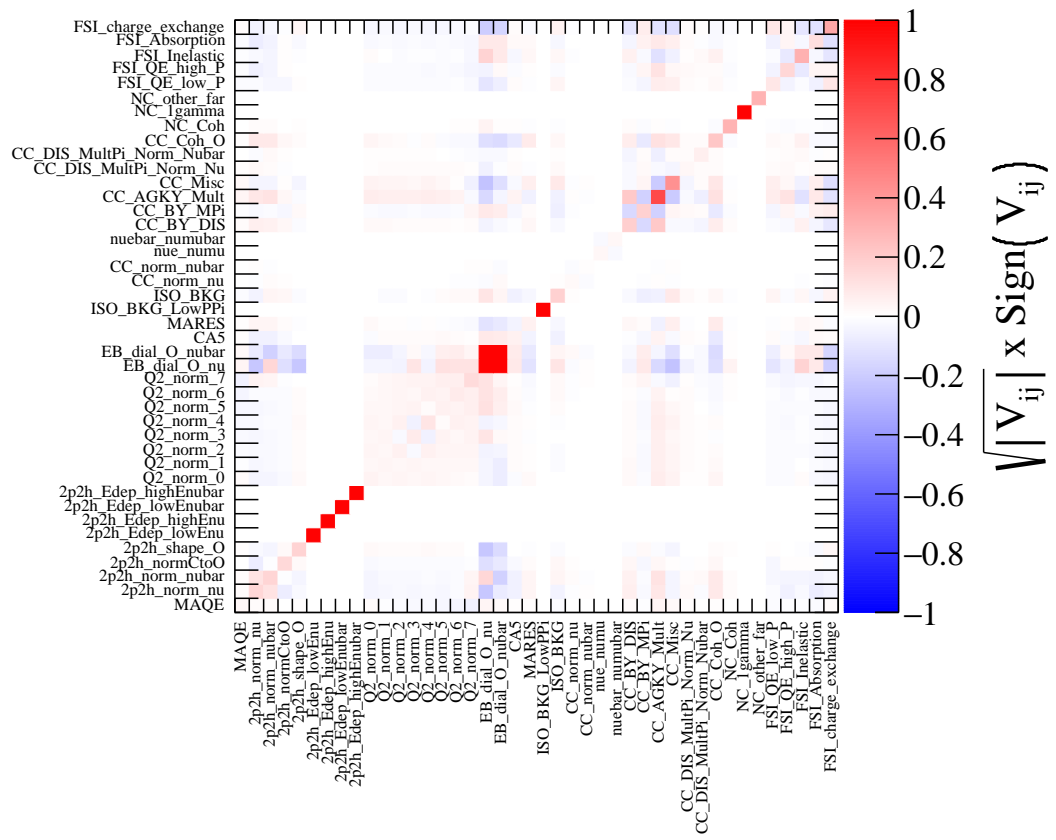


Figure A.2: The cross-section covariance matrix resulting from the near detector fit.

Appendix B

Predicted Event Rates for the T2K Run 1-10 Analysis

Tables B.1 to B.5 show the predicted event rates generated with the full T2K Run 1-10 beam exposure (see Section 3.1) and with the Asimov A oscillation parameters listed in Table 5.8. Shown are both the total predicted event rates and the contributions from all true reaction modes.

	$\nu_\mu \rightarrow \nu_\mu$	$\bar{\nu}_\mu \rightarrow \bar{\nu}_\mu$	$\nu_e \rightarrow \nu_e$	$\nu_\mu \rightarrow \nu_e$	$\bar{\nu}_e \rightarrow \bar{\nu}_e$	$\bar{\nu}_\mu \rightarrow \bar{\nu}_e$	Total
CCQE	224.6762	13.9450	0.0053	0.0428	0.0004	0.0002	238.6700
CC1 π^\pm	35.9936	3.2272	0.0035	0.0391	0.0001	0.0000	39.2635
CC1 π^0	6.5506	0.4460	0.0000	0.0066	0.0000	0.0000	7.0033
CCcoh	0.3084	0.0707	0.0000	0.0000	0.0000	0.0000	0.3791
CC2p2h	39.0220	2.0948	0.0018	0.0130	0.0000	0.0000	41.1317
CCDIS	0.8147	0.0442	0.0000	0.0000	0.0000	0.0000	0.8589
CCmulti- π	7.6338	0.4421	0.0010	0.0022	0.0000	0.0000	8.0791
CCmisc	1.2084	0.0741	0.0000	0.0000	0.0000	0.0000	1.2825
NC1 π^\pm	5.3290	0.1973	0.1155	N/A	0.0110	N/A	5.6528
NC1 π^0	0.5151	0.0191	0.0160	N/A	0.0015	N/A	0.5517
NCcoh	0.0000	0.0000	0.0005	N/A	0.0000	N/A	0.0005
NCmisc	2.4032	0.1343	0.0993	N/A	0.0101	N/A	2.6469
NC1 γ	0.0092	0.0000	0.0000	N/A	0.0000	N/A	0.0092
Total	324.4644	20.6947	0.2429	0.1037	0.0233	0.0003	345.5293

Table B.1: Event rates for the ν -mode $\bar{\nu}_\mu$ CCQE-like sample, generated with the Asimov A oscillation parameter values in Table 5.8 and nominal values of the systematic parameters.

	$\nu_\mu \rightarrow \nu_\mu$	$\bar{\nu}_\mu \rightarrow \bar{\nu}_\mu$	$\nu_e \rightarrow \nu_e$	$\nu_\mu \rightarrow \nu_e$	$\bar{\nu}_e \rightarrow \bar{\nu}_e$	$\bar{\nu}_\mu \rightarrow \bar{\nu}_e$	Total
CCQE	34.0427	59.3696	0.0015	0.0006	0.0019	0.0030	93.4194
CC1 π^\pm	8.4598	8.7887	0.0004	0.0007	0.0003	0.0002	17.2500
CC1 π^0	1.5285	1.2326	0.0001	0.0001	0.0000	0.0000	2.7613
CCcoh	0.0629	0.2156	0.0000	0.0000	0.0000	0.0002	0.2787
CC2p2h	7.7405	7.0818	0.0004	0.0007	0.0003	0.0003	14.8239
CCDIS	0.1382	0.1123	0.0000	0.0000	0.0000	0.0000	0.2505
CCmulti- π	1.9899	1.0450	0.0001	0.0001	0.0001	0.0002	3.0353
CCmisc	0.3567	0.1718	0.0000	0.0000	0.0001	0.0000	0.5286
NC1 π^\pm	0.6827	0.9456	0.0263	N/A	0.0222	N/A	1.6767
NC1 π^0	0.0773	0.0756	0.0034	N/A	0.0015	N/A	0.1578
NCcoh	0.0006	0.0000	0.0000	N/A	0.0000	N/A	0.0006
NCmisc	0.6242	0.3481	0.0255	N/A	0.0139	N/A	1.0117
NC1 γ	0.0000	0.0000	0.0000	N/A	0.0000	N/A	0.0000
Total	55.7039	79.3867	0.0577	0.0022	0.0403	0.0039	135.1946

Table B.2: Event rates for the $\bar{\nu}$ -mode $\bar{\nu}_\mu$ CCQE-like sample, generated with the Asimov A oscillation parameter values in Table 5.8 and nominal values of the systematic parameters.

	$\nu_\mu \rightarrow \nu_\mu$	$\bar{\nu}_\mu \rightarrow \bar{\nu}_\mu$	$\nu_e \rightarrow \nu_e$	$\nu_\mu \rightarrow \nu_e$	$\bar{\nu}_e \rightarrow \bar{\nu}_e$	$\bar{\nu}_\mu \rightarrow \bar{\nu}_e$	Total
CCQE	0.2691	0.0103	8.0402	59.5872	0.2998	0.3473	68.5539
CC1 π^\pm	0.0393	0.0032	1.2321	6.0308	0.0778	0.0624	7.4457
CC1 π^0	0.0126	0.0007	0.2662	1.2368	0.0100	0.0077	1.5339
CCcoh	0.0000	0.0001	0.0097	0.0418	0.0028	0.0028	0.0572
CC2p2h	0.0532	0.0019	1.5280	9.0715	0.0542	0.0510	10.7597
CCDIS	0.0000	0.0000	0.0106	0.0009	0.0019	0.0000	0.0135
CCmulti- π	0.0195	0.0003	0.1833	0.1261	0.0084	0.0031	0.3406
CCmisc	0.0006	0.0002	0.0279	0.0288	0.0016	0.0005	0.0596
NC1 π^\pm	0.2956	0.0129	0.0090	N/A	0.0008	N/A	0.3183
NC1 π^0	1.9777	0.0795	0.0392	N/A	0.0047	N/A	2.1011
NCcoh	0.3158	0.0314	0.0062	N/A	0.0019	N/A	0.3553
NCmisc	0.5671	0.0238	0.0187	N/A	0.0025	N/A	0.6121
NC1 γ	1.4978	0.0653	0.0337	N/A	0.0031	N/A	1.5999
Total	5.0481	0.2298	11.4048	76.1239	0.4696	0.4747	93.7509

Table B.3: Event rates for the ν -mode $\bar{\nu}_e$ CCQE-like sample, generated with the Asimov A oscillation parameter values in Table 5.8 and nominal values of the systematic parameters.

	$\nu_\mu \rightarrow \nu_\mu$	$\bar{\nu}_\mu \rightarrow \bar{\nu}_\mu$	$\nu_e \rightarrow \nu_e$	$\nu_\mu \rightarrow \nu_e$	$\bar{\nu}_e \rightarrow \bar{\nu}_e$	$\bar{\nu}_\mu \rightarrow \bar{\nu}_e$	Total
CCQE	0.0348	0.0529	1.0389	2.2586	1.6464	5.7498	10.7815
CC1 π^\pm	0.0097	0.0143	0.2060	0.3188	0.2753	0.6692	1.4933
CC1 π^0	0.0026	0.0032	0.0428	0.0690	0.0344	0.0759	0.2279
CCcoh	0.0000	0.0005	0.0012	0.0018	0.0132	0.0422	0.0589
CC2p2h	0.0104	0.0077	0.2473	0.4147	0.2386	0.7025	1.6211
CCDIS	0.0000	0.0000	0.0005	0.0003	0.0010	0.0000	0.0019
CCmulti- π	0.0030	0.0023	0.0432	0.0227	0.0185	0.0129	0.1025
CCmisc	0.0010	0.0000	0.0082	0.0037	0.0044	0.0013	0.0187
NC1 π^\pm	0.0520	0.0427	0.0019	N/A	0.0011	N/A	0.0977
NC1 π^0	0.2484	0.3414	0.0103	N/A	0.0084	N/A	0.6084
NCcoh	0.0449	0.1509	0.0016	N/A	0.0029	N/A	0.2003
NCmisc	0.1348	0.0632	0.0069	N/A	0.0029	N/A	0.2078
NC1 γ	0.1746	0.2868	0.0069	N/A	0.0053	N/A	0.4736
Total	0.7163	0.9657	1.6155	3.0896	2.2525	7.2538	15.8936

Table B.4: Event rates for the $\bar{\nu}$ -mode $\bar{\nu}_e$ CCQE-like sample, generated with the Asimov A oscillation parameter values in Table 5.8 and nominal values of the systematic parameters.

	$\nu_\mu \rightarrow \nu_\mu$	$\bar{\nu}_\mu \rightarrow \bar{\nu}_\mu$	$\nu_e \rightarrow \nu_e$	$\nu_\mu \rightarrow \nu_e$	$\bar{\nu}_e \rightarrow \bar{\nu}_e$	$\bar{\nu}_\mu \rightarrow \bar{\nu}_e$	Total
CCQE	0.0514	0.0011	0.0413	0.4154	0.0024	0.0035	0.5152
CC1 π^\pm	0.0396	0.0017	0.8920	6.1824	0.0026	0.0022	7.1206
CC1 π^0	0.0254	0.0007	0.0296	0.1560	0.0007	0.0009	0.2133
CCcoh	0.0004	0.0000	0.0164	0.0931	0.0002	0.0001	0.1100
CC2p2h	0.0113	0.0004	0.0283	0.1408	0.0012	0.0012	0.1832
CCDIS	0.0000	0.0002	0.0034	0.0003	0.0000	0.0000	0.0039
CCmulti- π	0.0401	0.0005	0.1427	0.1467	0.0027	0.0012	0.3339
CCmisc	0.0113	0.0001	0.0097	0.0045	0.0002	0.0001	0.0260
NC1 π^\pm	0.0701	0.0029	0.0034	N/A	0.0005	N/A	0.0768
NC1 π^0	0.0279	0.0010	0.0008	N/A	0.0000	N/A	0.0297
NCcoh	0.0000	0.0000	0.0000	N/A	0.0000	N/A	0.0000
NCmisc	0.1967	0.0202	0.0107	N/A	0.0020	N/A	0.2297
NC1 γ	0.0000	0.0003	0.0000	N/A	0.0002	N/A	0.0005
Total	0.4742	0.0291	1.1783	7.1393	0.0126	0.0092	8.8428

Table B.5: Event rates for the ν -mode $\bar{\nu}_e$ CC1 π^+ -like sample, generated with the Asimov A oscillation parameter values in Table 5.8 and nominal values of the systematic parameters.

Bibliography

- [1] P. Dunne *et al.* (2021). “XsecResponse software repository,” [Online]. Available: <https://github.com/t2k-software/XsecResponse/>.
- [2] C. Andreopoulos *et al.* (2021). “VALOR neutrino fitter public website,” [Online]. Available: <https://valor.pp.rl.ac.uk/>.
- [3] K. Abe *et al.*, “Improved constraints on neutrino mixing from the T2K experiment with 3.13×10^{21} protons on target,” Jan. 2021. arXiv: 2101.03779 [hep-ex].
- [4] K. Abe *et al.*, “Search for electron antineutrino appearance in a long-baseline muon antineutrino beam,” *Physical Review Letters*, vol. 124, no. 16, Apr. 2020, ISSN: 1079-7114. DOI: 10.1103/physrevlett.124.161802. [Online]. Available: <http://dx.doi.org/10.1103/PhysRevLett.124.161802>.
- [5] K. Abe *et al.*, “Constraint on the matter–antimatter symmetry-violating phase in neutrino oscillations,” *Nature*, vol. 580, no. 7803, pp. 339–344, 2020, [Erratum: Nature 583, E16 (2020)]. DOI: 10.1038/s41586-020-2177-0. arXiv: 1910.03887 [hep-ex].
- [6] J. Chadwick, “The intensity distribution in the magnetic spectrum of beta particles from radium (B + C),” *Verh. Phys. Gesell.*, vol. 16, pp. 383–391, 1914.
- [7] C. D. Ellis *et al.*, “The average energy of disintegration of radium e,” 1927, pp. 109–123. DOI: 10.1098/rspa.1927.0168.
- [8] W. Pauli, “On the earlier and more recent history of the neutrino,” in *Writings on Physics and Philosophy*, C. P. Enz and K. von Meyenn, Eds. Springer Berlin Heidelberg, 1994, pp. 193–218. DOI: 10.1007/978-3-662-02994-7_22.
- [9] C. L. Cowan *et al.*, “Detection of the free neutrino: A Confirmation,” *Science*, vol. 124, pp. 103–104, 1956. DOI: 10.1126/science.124.3212.103.
- [10] G. Danby *et al.*, “Observation of High-Energy Neutrino Reactions and the Existence of Two Kinds of Neutrinos,” *Phys. Rev. Lett.*, vol. 9, pp. 36–44, 1962. DOI: 10.1103/PhysRevLett.9.36.
- [11] M. L. Perl *et al.*, “Evidence for Anomalous Lepton Production in e+ - e- Annihilation,” *Phys. Rev. Lett.*, vol. 35, pp. 1489–1492, 1975. DOI: 10.1103/PhysRevLett.35.1489.
- [12] K. Kodama *et al.*, “Observation of tau neutrino interactions,” *Phys. Lett.*, vol. B504, pp. 218–224, 2001. DOI: 10.1016/S0370-2693(01)00307-0. arXiv: hep-ex/0012035.
- [13] S. Schael *et al.*, “Precision electroweak measurements on the Z resonance,” *Phys. Rept.*, vol. 427, pp. 257–454, 2006. DOI: 10.1016/j.physrep.2005.12.006. arXiv: hep-ex/0509008 [hep-ex].

- [14] A. Aguilar *et al.*, “Evidence for neutrino oscillations from the observation of $\bar{\nu}_e$ appearance in a $\bar{\nu}_\mu$ beam,” *Phys. Rev. D*, vol. 64, p. 112 007, 11 Nov. 2001. DOI: 10.1103/PhysRevD.64.112007.
- [15] A. Aguilar-Arevalo *et al.*, “Significant Excess of ElectronLike Events in the Mini-BooNE Short-Baseline Neutrino Experiment,” *Phys. Rev. Lett.*, vol. 121, no. 22, p. 221 801, 2018. DOI: 10.1103/PhysRevLett.121.221801. arXiv: 1805.12028 [hep-ex].
- [16] C. Giunti *et al.*, “KATRIN bound on 3+1 active-sterile neutrino mixing and the reactor antineutrino anomaly,” *JHEP*, vol. 05, p. 061, 2020. DOI: 10.1007/JHEP05(2020)061. arXiv: 1912.12956 [hep-ph].
- [17] B. T. Cleveland *et al.*, “Measurement of the solar electron neutrino flux with the Homestake chlorine detector,” *Astrophys. J.*, vol. 496, pp. 505–526, 1998. DOI: 10.1086/305343.
- [18] M. Bonifacie, “Chlorine isotopes,” in *Encyclopedia of Geochemistry: A Comprehensive Reference Source on the Chemistry of the Earth*, W. M. White, Ed. Cham: Springer International Publishing, 2018, pp. 244–248, ISBN: 978-3-319-39312-4. DOI: 10.1007/978-3-319-39312-4_90.
- [19] K. S. Hirata *et al.*, “Observation of B-8 Solar Neutrinos in the Kamiokande-II Detector,” *Phys. Rev. Lett.*, vol. 63, p. 16, 1989. DOI: 10.1103/PhysRevLett.63.16.
- [20] Y. Fukuda *et al.*, “Solar neutrino data covering solar cycle 22,” *Phys. Rev. Lett.*, vol. 77, pp. 1683–1686, 1996. DOI: 10.1103/PhysRevLett.77.1683.
- [21] J. N. Abdurashitov *et al.*, “Measurement of the solar neutrino capture rate with gallium metal,” *Phys. Rev.*, vol. C60, p. 055 801, 1999. DOI: 10.1103/PhysRevC.60.055801. arXiv: astro-ph/9907113.
- [22] W. Hampel *et al.*, “Gallex solar neutrino observations: Results for gallex iv,” *Physics Letters B*, vol. 447, no. 1, pp. 127–133, 1999, ISSN: 0370-2693. DOI: [https://doi.org/10.1016/S0370-2693\(98\)01579-2](https://doi.org/10.1016/S0370-2693(98)01579-2).
- [23] J. N. Bahcall and C. Peña-Garay, “Solar models and solar neutrino oscillations,” *New Journal of Physics*, vol. 6, pp. 63–63, Jun. 2004. DOI: 10.1088/1367-2630/6/1/063.
- [24] Y. Fukuda, T. Hayakawa *et al.*, “Evidence for oscillation of atmospheric neutrinos,” *Phys. Rev. Lett.*, vol. 81, pp. 1562–1567, 1998. DOI: 10.1103/PhysRevLett.81.1562. arXiv: hep-ex/9807003.
- [25] S. Hatakeyama *et al.*, “Measurement of the flux and zenith-angle distribution of upward through-going muons in kamiokande ii + iii,” *Phys. Rev. Lett.*, vol. 81, pp. 2016–2019, 10 Sep. 1998. DOI: 10.1103/PhysRevLett.81.2016.
- [26] Y. Fukuda *et al.*, “Study of the atmospheric neutrino flux in the multi-GeV energy range,” *Phys. Lett.*, vol. B436, pp. 33–41, 1998. DOI: 10.1016/S0370-2693(98)00876-4. arXiv: hep-ex/9805006.
- [27] R. Becker-Szendy *et al.*, “The Electron-neutrino and muon-neutrino content of the atmospheric flux,” *Phys. Rev. D*, vol. 46, pp. 3720–3724, 1992. DOI: 10.1103/PhysRevD.46.3720.
- [28] W. Allison *et al.*, “The Atmospheric neutrino flavor ratio from a 3.9 fiducial kiloton year exposure of Soudan-2,” *Phys. Lett. B*, vol. 449, pp. 137–144, 1999. DOI: 10.1016/S0370-2693(99)00056-8. arXiv: hep-ex/9901024.

- [29] T. Kajita, “Atmospheric neutrinos,” *New Journal of Physics*, vol. 6, pp. 194–194, Dec. 2004. DOI: 10.1088/1367-2630/6/1/194. [Online]. Available: <https://doi.org/10.1088%2F1367-2630%2F6%2F1%2F194>.
- [30] Q. R. Ahmad *et al.*, “Direct evidence for neutrino flavor transformation from neutral current interactions in the Sudbury Neutrino Observatory,” *Phys. Rev. Lett.*, vol. 89, p. 011301, 2002. DOI: 10.1103/PhysRevLett.89.011301. arXiv: nucl-ex/0204008.
- [31] K. Eguchi *et al.*, “First results from KamLAND: Evidence for reactor anti-neutrino disappearance,” *Phys. Rev. Lett.*, vol. 90, p. 021802, 2003. DOI: 10.1103/PhysRevLett.90.021802. arXiv: hep-ex/0212021.
- [32] Y. Fukuda *et al.*, “Study of the atmospheric neutrino flux in the multi-GeV energy range,” *Phys. Lett. B*, vol. 436, pp. 33–41, 1998. DOI: 10.1016/S0370-2693(98)00876-4. arXiv: hep-ex/9805006.
- [33] A. Himmel and S.-K. Collaboration, “Recent results from super-kamiokande,” *AIP Conference Proceedings*, vol. 1604, no. 1, pp. 345–352, 2014. DOI: 10.1063/1.4883450.
- [34] B. Kayser, “Neutrino physics,” *eConf*, vol. C040802, J. Hewett *et al.*, Eds., p. L004, 2004. arXiv: hep-ph/0506165.
- [35] M. Tanabashi *et al.*, “Review of particle physics 2018 with 2019 update,” *Phys. Rev. D*, vol. 98, p. 030001, 3 Aug. 2018. DOI: 10.1103/PhysRevD.98.030001.
- [36] R. N. Cahn *et al.*, “White Paper: Measuring the Neutrino Mass Hierarchy,” in *Proceedings, 2013 Community Summer Study on the Future of U.S. Particle Physics: Snowmass on the Mississippi (CSS2013): Minneapolis, MN, USA, July 29-August 6, 2013*, 2013. arXiv: 1307.5487.
- [37] B. Kayser, *Neutrino physics*, 2005. arXiv: hep-ph/0506165 [hep-ph].
- [38] L. Wolfenstein, “Neutrino Oscillations in Matter,” *Phys. Rev. D*, vol. 17, pp. 2369–2374, 1978. DOI: 10.1103/PhysRevD.17.2369.
- [39] K. Hagiwara *et al.*, “The earth matter effects in neutrino oscillation experiments from tokai to kamioka and korea,” *Journal of High Energy Physics*, vol. 2011, no. 9, Sep. 2011, ISSN: 1029-8479. DOI: 10.1007/jhep09(2011)082.
- [40] J. Arafune *et al.*, “Cp violation and matter effect in long baseline neutrino oscillation experiments,” *Phys. Rev. D*, vol. 56, pp. 3093–3099, 5 Sep. 1997. DOI: 10.1103/PhysRevD.56.3093, Erratum “Erratum: Cp violation and matter effect in long baseline neutrino oscillation experiments [phys. rev. d 56, 3093 (1997)],” *Phys. Rev. D*, vol. 60, p. 119905, 11 Oct. 1999. DOI: 10.1103/PhysRevD.60.119905.
- [41] H. Nunokawa *et al.*, “Cp violation and neutrino oscillations,” *Progress in Particle and Nuclear Physics*, vol. 60, no. 2, pp. 338–402, 2008, ISSN: 0146-6410. DOI: <https://doi.org/10.1016/j.ppnp.2007.10.001>.
- [42] K. Abe *et al.*, “Measurement of neutrino and antineutrino oscillations by the T2K experiment including a new additional sample of ν_e interactions at the far detector,” *Phys. Rev. D*, vol. 96, p. 092006, 9 Nov. 2017. DOI: 10.1103/PhysRevD.96.092006.
- [43] C. Giunti and C. W. Kim, *Fundamentals of Neutrino Physics and Astrophysics*. Apr. 2007, ISBN: 978-0-19-850871-7.
- [44] M. Goldhaber *et al.*, “Helicity of Neutrinos,” *Phys. Rev.*, vol. 109, pp. 1015–1017, 1958. DOI: 10.1103/PhysRev.109.1015.

- [45] I. Baldes, “Early universe cosmology and the matter-antimatter asymmetry,” Ph.D. dissertation, Melbourne U., 2015.
- [46] H.-Y. Chiu, “Symmetry between particle and anti-particle populations in the universe,” *Phys. Rev. Lett.*, vol. 17, p. 712, 1966. DOI: 10.1103/PhysRevLett.17.712.
- [47] M. Thomson, *Modern Particle Physics*. Cambridge University Press, 2013. DOI: 10.1017/CBO9781139525367.
- [48] L. Canetti *et al.*, “Matter and antimatter in the universe,” *New Journal of Physics*, vol. 14, no. 9, p. 095012, Sep. 2012. DOI: 10.1088/1367-2630/14/9/095012. [Online]. Available: <https://doi.org/10.1088%2F1367-2630%2F14%2F9%2F095012>.
- [49] A. D. Sakharov, “Violation of CP Invariance, c Asymmetry, and Baryon Asymmetry of the Universe,” *Pisma Zh. Eksp. Teor. Fiz.*, vol. 5, pp. 32–35, 1967. DOI: 10.1070/PU1991v034n05ABEH002497.
- [50] V. A. Rubakov, “Baryon asymmetry of the universe,” in *Techniques and Concepts of High-Energy Physics*, H. B. Prosper and M. Danilov, Eds. Dordrecht: Springer Netherlands, 2001, pp. 97–141, ISBN: 978-94-010-0522-7. DOI: 10.1007/978-94-010-0522-7_3. [Online]. Available: https://doi.org/10.1007/978-94-010-0522-7_3.
- [51] J. H. Christenson *et al.*, “Evidence for the 2π Decay of the K_2^0 Meson,” *Phys. Rev. Lett.*, vol. 13, pp. 138–140, 4 Jul. 1964. DOI: 10.1103/PhysRevLett.13.138. [Online]. Available: <https://link.aps.org/doi/10.1103/PhysRevLett.13.138>.
- [52] C. Jarlskog, “Commutator of the Quark Mass Matrices in the Standard Electroweak Model and a Measure of Maximal CP Nonconservation,” *Phys. Rev. Lett.*, vol. 55, pp. 1039–1042, 10 Sep. 1985. DOI: 10.1103/PhysRevLett.55.1039. [Online]. Available: <https://link.aps.org/doi/10.1103/PhysRevLett.55.1039>.
- [53] N. Okada and Q. Shafi, *Leptonic CP Violation and Leptogenesis in Minimal Supersymmetric $SU(4)_c \times SU(2)_L \times SU(2)_R$* , 2018. arXiv: 1109.4963 [hep-ph].
- [54] J. Christenson *et al.*, “Evidence for the 2π Decay of the K_2^0 Meson,” *Phys. Rev. Lett.*, vol. 13, pp. 138–140, 1964. DOI: 10.1103/PhysRevLett.13.138.
- [55] P. Zyla *et al.*, “Review of Particle Physics,” *Progress of Theoretical and Experimental Physics*, vol. 2020, no. 8, Aug. 2020, 083C01, ISSN: 2050-3911. DOI: 10.1093/ptep/ptaa104. [Online]. Available: <https://doi.org/10.1093/ptep/ptaa104>.
- [56] I. Esteban *et al.*, “The fate of hints: Updated global analysis of three-flavor neutrino oscillations,” *Journal of High Energy Physics*, vol. 2020, no. 9, Sep. 2020, ISSN: 1029-8479. DOI: 10.1007/jhep09(2020)178. [Online]. Available: [http://dx.doi.org/10.1007/JHEP09\(2020\)178](http://dx.doi.org/10.1007/JHEP09(2020)178).
- [57] I. Esteban *et al.*, “Global analysis of three-flavour neutrino oscillations: synergies and tensions in the determination of θ_{23} , δ_{CP} , and the mass ordering,” *Journal of High Energy Physics*, vol. 2019, no. 1, Jan. 2019, ISSN: 1029-8479. DOI: 10.1007/jhep01(2019)106. [Online]. Available: [http://dx.doi.org/10.1007/JHEP01\(2019\)106](http://dx.doi.org/10.1007/JHEP01(2019)106).

- [58] M. H. Ahn *et al.*, “Measurement of neutrino oscillation by the k2k experiment,” *Physical Review D*, vol. 74, no. 7, Oct. 2006, ISSN: 1550-2368. DOI: 10.1103/physrevd.74.072003. [Online]. Available: <http://dx.doi.org/10.1103/PhysRevD.74.072003>.
- [59] P. Adamson *et al.*, “Combined Analysis of ν_μ Disappearance and $\nu_\mu \rightarrow \nu_e$ Appearance in MINOS Using Accelerator and Atmospheric Neutrinos,” *Physical Review Letters*, vol. 112, no. 19, May 2014, ISSN: 1079-7114. DOI: 10.1103/physrevlett.112.191801. [Online]. Available: <http://dx.doi.org/10.1103/PhysRevLett.112.191801>.
- [60] N. Gupta, “Galactic PeV Neutrinos,” *Astropart. Phys.*, vol. 48, pp. 75–77, 2013. DOI: 10.1016/j.astropartphys.2013.07.003. arXiv: 1305.4123 [astro-ph.HE].
- [61] C. V. Achar *et al.*, “Detection of muons produced by cosmic ray neutrinos deep underground,” *Phys. Lett.*, vol. 18, pp. 196–199, 1965. DOI: 10.1016/0031-9163(65)90712-2.
- [62] F. Reines *et al.*, “Evidence for high-energy cosmic ray neutrino interactions,” *Phys. Rev. Lett.*, vol. 15, pp. 429–433, 1965. DOI: 10.1103/PhysRevLett.15.429.
- [63] K. Hirata *et al.*, “Experimental Study of the Atmospheric Neutrino Flux,” J. Tran Thanh Van, Ed., pp. 235–246, Mar. 1988. DOI: 10.1016/0370-2693(88)91690-5.
- [64] M. G. Aartsen *et al.*, “Measurement of atmospheric tau neutrino appearance with icecube deepcore,” *Physical Review D*, vol. 99, no. 3, Feb. 2019, ISSN: 2470-0029. DOI: 10.1103/physrevd.99.032007. [Online]. Available: <http://dx.doi.org/10.1103/PhysRevD.99.032007>.
- [65] N. Agafonova *et al.*, “Final Results of the OPERA Experiment on ν_τ Appearance in the CNGS Neutrino Beam,” *Phys. Rev. Lett.*, vol. 120, p. 211801, 21 May 2018. DOI: 10.1103/PhysRevLett.120.211801. [Online]. Available: <https://link.aps.org/doi/10.1103/PhysRevLett.120.211801>.
- [66] M. Apollonio *et al.*, “Search for neutrino oscillations on a long base-line at the chooz nuclear power station,” *The European Physical Journal C*, vol. 27, no. 3, pp. 331–374, Apr. 2003, ISSN: 1434-6052. DOI: 10.1140/epjc/s2002-01127-9. [Online]. Available: <http://dx.doi.org/10.1140/epjc/s2002-01127-9>.
- [67] F. Boehm *et al.*, “Final results from the Palo Verde neutrino oscillation experiment,” *Physical Review D*, vol. 64, no. 11, Nov. 2001, ISSN: 1089-4918. DOI: 10.1103/physrevd.64.112001. [Online]. Available: <http://dx.doi.org/10.1103/PhysRevD.64.112001>.
- [68] K. Abe *et al.*, “Indication of Electron Neutrino Appearance from an Accelerator-produced Off-axis Muon Neutrino Beam,” *Phys. Rev. Lett.*, vol. 107, p. 041801, 2011. DOI: 10.1103/PhysRevLett.107.041801. arXiv: 1106.2822.
- [69] F. P. An *et al.*, “Observation of electron-antineutrino disappearance at daya bay,” *Phys. Rev. Lett.*, vol. 108, p. 171803, 17 Apr. 2012. DOI: 10.1103/PhysRevLett.108.171803. [Online]. Available: <https://link.aps.org/doi/10.1103/PhysRevLett.108.171803>.
- [70] K. Abe *et al.*, “The t2k experiment,” *Nuclear Instruments and Methods in Physics Research Section A: Accelerators, Spectrometers, Detectors and Associated Equipment*, vol. 659, no. 1, pp. 106–135, 2011, ISSN: 0168-9002. DOI: <https://doi.org/10.1016/j.nima.2011.06.067>.

- [71] K. Nishikawa, “Letter of Intent Neutrino Oscillation Experiment at JHF,” 2003. [Online]. Available: <https://neutrino.kek.jp/jhfnu/loi/loi.v2.030528.pdf>.
- [72] ——, “Tokai-to-Kamioka (T2K) Long Baseline Neutrino Oscillation Experiment Proposal,” 2006. [Online]. Available: http://j-parc.jp/researcher/Hadron/en/pac_0606/pdf/p11-Nishikawa.pdf.
- [73] K. Abe *et al.*, “Indication of electron neutrino appearance from an accelerator-produced off-axis muon neutrino beam,” *Physical Review Letters*, vol. 107, no. 4, Jul. 2011. DOI: [10.1103/physrevlett.107.041801](https://doi.org/10.1103/physrevlett.107.041801).
- [74] K. Abe *et al.*, “Observation of electron neutrino appearance in a muon neutrino beam,” *Phys. Rev. Lett.*, vol. 112, p. 061802, 6 Feb. 2014. DOI: [10.1103/PhysRevLett.112.061802](https://doi.org/10.1103/PhysRevLett.112.061802). [Online]. Available: <https://link.aps.org/doi/10.1103/PhysRevLett.112.061802>.
- [75] ——, “Precise Measurement of the Neutrino Mixing Parameter θ_{23} from Muon Neutrino Disappearance in an Off-Axis Beam,” *Phys. Rev. Lett.*, vol. 112, p. 181801, 18 May 2014. DOI: [10.1103/PhysRevLett.112.181801](https://doi.org/10.1103/PhysRevLett.112.181801). [Online]. Available: <https://link.aps.org/doi/10.1103/PhysRevLett.112.181801>.
- [76] K. Abe *et al.*, “First measurement of the charged current $\bar{\nu}_\mu$ double differential cross section on a water target without pions in the final state,” *Phys. Rev. D*, vol. 102, no. 1, p. 012007, 2020. DOI: [10.1103/PhysRevD.102.012007](https://doi.org/10.1103/PhysRevD.102.012007). arXiv: [1908.10249 \[hep-ex\]](https://arxiv.org/abs/1908.10249).
- [77] K. Abe *et al.*, “Measurement of the charged-current electron (anti-)neutrino inclusive cross-sections at the t2k off-axis near detector nd280,” *Journal of High Energy Physics*, vol. 2020, no. 10, Oct. 2020, ISSN: 1029-8479. DOI: [10.1007/jhep10\(2020\)114](https://doi.org/10.1007/jhep10(2020)114). [Online]. Available: [http://dx.doi.org/10.1007/JHEP10\(2020\)114](http://dx.doi.org/10.1007/JHEP10(2020)114).
- [78] K. Abe *et al.*, “Search for light sterile neutrinos with the t2k far detector super-kamiokande at a baseline of 295 km,” *Physical Review D*, vol. 99, no. 7, Apr. 2019, ISSN: 2470-0029. DOI: [10.1103/physrevd.99.071103](https://doi.org/10.1103/physrevd.99.071103). [Online]. Available: <http://dx.doi.org/10.1103/PhysRevD.99.071103>.
- [79] K. Abe *et al.*, “Search for lorentz and cpt violation using sidereal time dependence of neutrino flavor transitions over a short baseline,” *Physical Review D*, vol. 95, no. 11, Jun. 2017, ISSN: 2470-0029. DOI: [10.1103/physrevd.95.111101](https://doi.org/10.1103/physrevd.95.111101). [Online]. Available: <http://dx.doi.org/10.1103/PhysRevD.95.111101>.
- [80] H. Hotchi *et al.*, “Achievement of a low-loss 1-MW beam operation in the 3-GeV rapid cycling synchrotron of the Japan Proton Accelerator Research Complex,” *Phys. Rev. Accel. Beams*, vol. 20, no. 6, p. 060402, 2017. DOI: [10.1103/PhysRevAccelBeams.20.060402](https://doi.org/10.1103/PhysRevAccelBeams.20.060402).
- [81] M. Yoshii *et al.*, “Present Status and Future Upgrades of the J-PARC Ring RF Systems,” in *9th International Particle Accelerator Conference*, 2018, TUPAK011. DOI: [10.18429/JACoW-IPAC2018-TUPAK011](https://doi.org/10.18429/JACoW-IPAC2018-TUPAK011).
- [82] *Developing power converter control software for the j-parc particle accelerator*, <https://uk.mathworks.com/company/newsletters/articles/developing-power-converter-control-software-for-the-jparc-particle-accelerator.html>.
- [83] M. Friend, “J-PARC accelerator and neutrino beamline upgrade programme,” *Journal of Physics: Conference Series*, vol. 888, p. 012042, Sep. 2017. DOI: [10.1088/1742-6596/888/1/012042](https://doi.org/10.1088/1742-6596/888/1/012042).

- [84] T. Vladisavljevic *et al.*, “Flux Prediction and Uncertainty with NA61/SHINE 2009 Replica-Target Data v3.3,” T2K Collaboration, Tech. Rep. T2K-TN354, 2020.
- [85] K. Matsuoka *et al.*, “Design and performance of the muon monitor for the t2k neutrino oscillation experiment,” *Nuclear Instruments and Methods in Physics Research Section A: Accelerators, Spectrometers, Detectors and Associated Equipment*, vol. 624, no. 3, pp. 591–600, 2010, ISSN: 0168-9002. DOI: <https://doi.org/10.1016/j.nima.2010.09.074>.
- [86] K. Abe *et al.*, “Measurement of the muon neutrino inclusive charged-current cross section in the energy range of 1–3 gev with the t2k ingrid detector,” *Physical Review D*, vol. 93, no. 7, Apr. 2016, ISSN: 2470-0029. DOI: [10.1103/physrevd.93.072002](https://doi.org/10.1103/physrevd.93.072002).
- [87] K. Abe *et al.*, “Measurements of the t2k neutrino beam properties using the ingrid on-axis near detector,” *Nuclear Instruments and Methods in Physics Research Section A: Accelerators, Spectrometers, Detectors and Associated Equipment*, vol. 694, pp. 211–223, Dec. 2012, ISSN: 0168-9002. DOI: [10.1016/j.nima.2012.03.023](https://doi.org/10.1016/j.nima.2012.03.023).
- [88] K. Abe *et al.*, *T2K ND280 – Technical Design Report*, 2006. [Online]. Available: <http://www.nd280.org/convenors/ND280%20Review%20document%202006/tdr.pdf/download>.
- [89] P.-A. Amaudruz *et al.*, “The t2k fine-grained detectors,” *Nuclear Instruments and Methods in Physics Research Section A: Accelerators, Spectrometers, Detectors and Associated Equipment*, vol. 696, pp. 1–31, 2012, ISSN: 0168-9002. DOI: <https://doi.org/10.1016/j.nima.2012.08.020>.
- [90] M. Munteanu *et al.*, “Constraining the Flux and Cross Section Models with Data from ND280 using FGD1 and FGD2 for the 2020 Oscillation Analysis,” T2K Collaboration, Tech. Rep. T2K-TN395, 2020.
- [91] N. Abgrall *et al.*, “Time projection chambers for the t2k near detectors,” *Nuclear Instruments and Methods in Physics Research Section A: Accelerators, Spectrometers, Detectors and Associated Equipment*, vol. 637, no. 1, pp. 25–46, 2011, ISSN: 0168-9002. DOI: <https://doi.org/10.1016/j.nima.2011.02.036>.
- [92] Y. Giomataris *et al.*, “Micromegas: A high-granularity position-sensitive gaseous detector for high particle-flux environments,” *Nuclear Instruments and Methods in Physics Research Section A: Accelerators, Spectrometers, Detectors and Associated Equipment*, vol. 376, no. 1, pp. 29–35, 1996, ISSN: 0168-9002. DOI: [https://doi.org/10.1016/0168-9002\(96\)00175-1](https://doi.org/10.1016/0168-9002(96)00175-1).
- [93] S. Assylbekov *et al.*, “The t2k nd280 off-axis pi-zero detector,” *Nuclear Instruments and Methods in Physics Research Section A: Accelerators, Spectrometers, Detectors and Associated Equipment*, vol. 686, pp. 48–63, 2012, ISSN: 0168-9002. DOI: <https://doi.org/10.1016/j.nima.2012.05.028>.
- [94] D. Allan *et al.*, “The electromagnetic calorimeter for the t2k near detector ND280,” *Journal of Instrumentation*, vol. 8, no. 10, P10019–P10019, Oct. 2013. DOI: [10.1088/1748-0221/8/10/p10019](https://doi.org/10.1088/1748-0221/8/10/p10019).
- [95] S. Aoki *et al.*, “The t2k side muon range detector (smrd),” *Nuclear Instruments and Methods in Physics Research Section A: Accelerators, Spectrometers, Detectors and Associated Equipment*, vol. 698, pp. 135–146, 2013, ISSN: 0168-9002. DOI: <https://doi.org/10.1016/j.nima.2012.10.001>.

- [96] S. Fukuda *et al.*, “The super-kamiokande detector,” *Nuclear Instruments and Methods in Physics Research Section A: Accelerators, Spectrometers, Detectors and Associated Equipment*, vol. 501, no. 2, pp. 418–462, 2003, ISSN: 0168-9002. DOI: [https://doi.org/10.1016/S0168-9002\(03\)00425-X](https://doi.org/10.1016/S0168-9002(03)00425-X).
- [97] Y. Fukuda *et al.*, “Measurements of the solar neutrino flux from super-kamiokande’s first 300 days,” *Phys. Rev. Lett.*, vol. 81, pp. 1158–1162, 6 Aug. 1998. DOI: 10.1103/PhysRevLett.81.1158.
- [98] ———, “Measurement of the solar neutrino energy spectrum using neutrino-electron scattering,” *Phys. Rev. Lett.*, vol. 82, pp. 2430–2434, 12 Mar. 1999. DOI: 10.1103/PhysRevLett.82.2430.
- [99] M. Shiozawa *et al.*, “Search for Proton Decay via $p \rightarrow e^+ \pi^0$ in a Large Water Cherenkov Detector,” *Phys. Rev. Lett.*, vol. 81, pp. 3319–3323, 16 Oct. 1998. DOI: 10.1103/PhysRevLett.81.3319.
- [100] Y. Hayato *et al.*, “Search for Proton Decay through $p \rightarrow \bar{\nu} K^+$ in a Large Water Cherenkov Detector,” *Phys. Rev. Lett.*, vol. 83, pp. 1529–1533, 8 Aug. 1999. DOI: 10.1103/PhysRevLett.83.1529.
- [101] S. Ahn *et al.*, “Detection of accelerator-produced neutrinos at a distance of 250 km,” *Physics Letters B*, vol. 511, no. 2, pp. 178–184, 2001, ISSN: 0370-2693. DOI: [https://doi.org/10.1016/S0370-2693\(01\)00647-5](https://doi.org/10.1016/S0370-2693(01)00647-5).
- [102] S. Li and J. Beacom, “First calculation of cosmic-ray muon spallation backgrounds for mev astrophysical neutrino signals in super-kamiokande,” *Physical Review C*, vol. 89, no. 4, Apr. 2014, ISSN: 1089-490X. DOI: 10.1103/physrevc.89.045801.
- [103] P. A. Cherenkov, “Visible luminescence of pure liquids under the influence of γ -radiation,” *Dokl. Akad. Nauk SSSR*, vol. 2, no. 8, pp. 451–454, 1934. DOI: 10.3367/UFNr.0093.196710n.0385.
- [104] K. Abe *et al.*, “Measurements of neutrino oscillation in appearance and disappearance channels by the T2K experiment with 6.6×10^{20} protons on target,” *Phys. Rev. D*, vol. 91, p. 072010, 7 Apr. 2015. DOI: 10.1103/PhysRevD.91.072010. [Online]. Available: <https://link.aps.org/doi/10.1103/PhysRevD.91.072010>.
- [105] D. Barrow *et al.*, “Super-Kamiokande Data Quality, MC, and Systematics in Run 10,” T2K Collaboration, Tech. Rep. T2K-TN399, 2020.
- [106] J. F. Beacom and M. R. Vagins, “Antineutrino spectroscopy with large water čerenkov detectors,” *Phys. Rev. Lett.*, vol. 93, p. 171101, 17 Oct. 2004. DOI: 10.1103/PhysRevLett.93.171101.
- [107] H. Sekiya, “The Super-Kamiokande Gadolinium Project,” *PoS*, vol. ICHEP2016, p. 982, 2016. DOI: 10.22323/1.282.0982.
- [108] J. Hignight *et al.*, “Super-Kamiokande event displays for T2K Run1-4 analysis candidates,” T2K Collaboration, Tech. Rep. T2K-TN148, 2013.
- [109] T. T. Böhlen *et al.*, “The FLUKA Code: Developments and Challenges for High Energy and Medical Applications,” *Nucl. Data Sheets*, vol. 120, pp. 211–214, 2014. DOI: 10.1016/j.nds.2014.07.049.
- [110] R. Brun *et al.*, “GEANT3,” Sep. 1987.
- [111] K. Abe *et al.*, “T2k neutrino flux prediction,” *Phys. Rev. D*, vol. 87, p. 012001, 1 Jan. 2013. DOI: 10.1103/PhysRevD.87.012001.

- [112] C. Zeitnitz and T. A. Gabriel, “The GEANT - CALOR interface and benchmark calculations of ZEUS test calorimeters,” *Nucl. Instrum. Meth. A*, vol. 349, pp. 106–111, 1994. DOI: 10.1016/0168-9002(94)90613-0.
- [113] N. Abgrall *et al.*, “Na61/shine facility at the cern sps: Beams and detector system,” *Journal of Instrumentation*, vol. 9, no. 06, P06005–P06005, Jun. 2014, ISSN: 1748-0221. DOI: 10.1088/1748-0221/9/06/p06005.
- [114] N. Abgrall *et al.*, “Measurements of π^\pm differential yields from the surface of the T2K replica target for incoming 31 GeV/c protons with the NA61/SHINE spectrometer at the CERN SPS,” *The European Physical Journal C*, vol. 76, no. 11, Nov. 2016, ISSN: 1434-6052. DOI: 10.1140/epjc/s10052-016-4440-y.
- [115] N. Abgrall *et al.*, “Measurement of production properties of positively charged kaons in proton-carbon interactions at 31 gev/c,” *Physical Review C*, vol. 85, no. 3, Mar. 2012, ISSN: 1089-490X. DOI: 10.1103/physrevc.85.035210.
- [116] A. Fiorentini *et al.*, “Flux Prediction and Uncertainty Updates with NA61 2009 Thin Target Data and Negative Focussing Mode Predictions,” T2K Collaboration, Tech. Rep. T2K-TN217, 2018.
- [117] Y. Hayato, “A neutrino interaction simulation program library NEUT,” *Acta Phys. Polon. B*, vol. 40, pp. 2477–2489, 2009.
- [118] Y. Hyato *et al.*, “The NEUT Neutrino Monte Carlo Generator: Physics and User Manual,” T2K Collaboration, Tech. Rep. T2K-TN351, 2018.
- [119] S. Bolognesi *et al.*, “Niwg model and uncertainties for 2019-2020 oscillation analysis,” T2K Collaboration, Tech. Rep. T2K-TN344, 2019.
- [120] ——, “Niwg model and uncertainties for 2017 oscillation analysis,” T2K Collaboration, Tech. Rep. T2K-TN315, 2017.
- [121] K. Abe *et al.*, “Search for CP Violation in Neutrino and Antineutrino Oscillations by the T2K Experiment with 2.2×10^{21} Protons on Target,” *Phys. Rev. Lett.*, vol. 121, p. 171802, 17 Oct. 2018. DOI: 10.1103/PhysRevLett.121.171802. [Online]. Available: <https://link.aps.org/doi/10.1103/PhysRevLett.121.171802>.
- [122] O. Benhar *et al.*, “Spectral function of finite nuclei and scattering of GeV electrons,” *Nucl. Phys. A*, vol. 579, pp. 493–517, 1994. DOI: 10.1016/0375-9474(94)90920-2.
- [123] A. M. Ankowski *et al.*, “Improving the accuracy of neutrino energy reconstruction in charged-current quasielastic scattering off nuclear targets,” *Phys. Rev. D*, vol. 91, p. 033005, 3 Feb. 2015. DOI: 10.1103/PhysRevD.91.033005.
- [124] K. Abe *et al.*, “Characterization of nuclear effects in muon-neutrino scattering on hydrocarbon with a measurement of final-state kinematics and correlations in charged-current pionless interactions at t2k,” *Phys. Rev. D*, vol. 98, p. 032003, 3 Aug. 2018. DOI: 10.1103/PhysRevD.98.032003. [Online]. Available: <https://link.aps.org/doi/10.1103/PhysRevD.98.032003>.
- [125] X.-G. Lu *et al.*, “Measurement of Final-State Correlations in Neutrino Muon-Proton Mesonless Production on Hydrocarbon at $\langle E_\nu \rangle = 3$ GeV,” *Phys. Rev. Lett.*, vol. 121, p. 022504, 2 Jul. 2018. DOI: 10.1103/PhysRevLett.121.022504. [Online]. Available: <https://link.aps.org/doi/10.1103/PhysRevLett.121.022504>.
- [126] S. Dolan, “Exploring Nuclear Effects in Neutrino-Nucleus Interactions Using Measurements of Transverse Kinematic Imbalance from T2K and MINERvA,” Oct. 2018. arXiv: 1810.06043 [hep-ex].

- [127] D. Dutta *et al.*, “A Study of the quasielastic (e,e' -prime p) reaction on C-12, Fe-56 and Au-97,” *Phys. Rev. C*, vol. 68, p. 064603, 2003. DOI: 10.1103/PhysRevC.68.064603. arXiv: nucl-ex/0303011.
- [128] M. Leuschner *et al.*, “Quasielastic proton knockout from O-16,” *Phys. Rev. C*, vol. 49, pp. 955–967, 1994. DOI: 10.1103/PhysRevC.49.955.
- [129] P. Guèye *et al.*, “Coulomb distortion measurements by comparing electron and positron quasielastic scattering off ^{12}C and ^{208}Pb ,” *Phys. Rev. C*, vol. 60, p. 044308, 4 Sep. 1999. DOI: 10.1103/PhysRevC.60.044308. [Online]. Available: <https://link.aps.org/doi/10.1103/PhysRevC.60.044308>.
- [130] C. Llewellyn Smith, “Neutrino reactions at accelerator energies,” *Physics Reports*, vol. 3, no. 5, pp. 261–379, 1972, ISSN: 0370-1573. DOI: [https://doi.org/10.1016/0370-1573\(72\)90010-5](https://doi.org/10.1016/0370-1573(72)90010-5).
- [131] K. Kuzmin *et al.*, “Quasielastic axial-vector mass from experiments on neutrino-nucleus scattering,” *The European Physical Journal C*, vol. 54, no. 4, pp. 517–538, Apr. 2008, ISSN: 1434-6052. DOI: 10.1140/epjc/s10052-008-0582-x.
- [132] V. Bernard *et al.*, “Axial structure of the nucleon,” *Journal of Physics G: Nuclear and Particle Physics*, vol. 28, no. 1, R1–R35, Nov. 2001, ISSN: 1361-6471. DOI: 10.1088/0954-3899/28/1/201.
- [133] A. Chappell, “CP violation and neutrino mass ordering at the T2K experiment,” Ph.D. dissertation, University of Warwick, Apr. 2019. [Online]. Available: <http://wrap.warwick.ac.uk/134815/>.
- [134] P. A. Rodrigues *et al.*, “Identification of nuclear effects in neutrino-carbon interactions at low three-momentum transfer,” *Physical Review Letters*, vol. 116, no. 7, Feb. 2016, ISSN: 1079-7114. DOI: 10.1103/physrevlett.116.071802.
- [135] K. Abe *et al.*, “Simultaneous measurement of the muon neutrino charged-current cross section on oxygen and carbon without pions in the final state at t2k,” *Physical Review D*, vol. 101, no. 11, Jul. 2020, ISSN: 2470-0029. DOI: 10.1103/physrevd.101.112004. [Online]. Available: <http://dx.doi.org/10.1103/PhysRevD.101.112004>.
- [136] T. Katori and M. Martini, “Neutrino–nucleus cross sections for oscillation experiments,” *Journal of Physics G: Nuclear and Particle Physics*, vol. 45, no. 1, p. 013001, Dec. 2017. DOI: 10.1088/1361-6471/aa8bf7.
- [137] J. E. Amaro and E. Ruiz Arriola, “Axial-vector dominance predictions in quasielastic neutrino-nucleus scattering,” *Physical Review D*, vol. 93, no. 5, Mar. 2016, ISSN: 2470-0029. DOI: 10.1103/physrevd.93.053002.
- [138] A. S. Meyer *et al.*, “Deuterium target data for precision neutrino-nucleus cross sections,” *Physical Review D*, vol. 93, no. 11, Jun. 2016, ISSN: 2470-0029. DOI: 10.1103/physrevd.93.113015.
- [139] B. Bhattacharya *et al.*, “Model-independent determination of the axial mass parameter in quasielastic neutrino-nucleon scattering,” *Physical Review D*, vol. 84, no. 7, Oct. 2011, ISSN: 1550-2368. DOI: 10.1103/physrevd.84.073006.
- [140] B. Bhattacharya *et al.*, “Model-independent determination of the axial mass parameter in quasielastic antineutrino-nucleon scattering,” *Physical Review D*, vol. 92, no. 11, Dec. 2015, ISSN: 1550-2368. DOI: 10.1103/physrevd.92.113011.
- [141] J. Nieves *et al.*, “Inclusive charged-current neutrino-nucleus reactions,” *Physical Review C*, vol. 83, no. 4, Apr. 2011, ISSN: 1089-490X. DOI: 10.1103/physrevc.83.045501.

- [142] M. Martini *et al.*, “Unified approach for nucleon knock-out and coherent and incoherent pion production in neutrino interactions with nuclei,” *Physical Review C*, vol. 80, no. 6, Dec. 2009, ISSN: 1089-490X. DOI: 10.1103/physrevc.80.065501. [Online]. Available: <http://dx.doi.org/10.1103/PhysRevC.80.065501>.
- [143] R. González-Jiménez *et al.*, “Extensions of superscaling from relativistic mean field theory: The susav2 model,” *Physical Review C*, vol. 90, no. 3, Sep. 2014, ISSN: 1089-490X. DOI: 10.1103/physrevc.90.035501.
- [144] I. R. Simo *et al.*, “Relativistic model of 2p-2h meson exchange currents in (anti)neutrino scattering,” *Journal of Physics G: Nuclear and Particle Physics*, vol. 44, no. 6, p. 065 105, Apr. 2017, ISSN: 1361-6471. DOI: 10.1088/1361-6471/aa6a06. [Online]. Available: <http://dx.doi.org/10.1088/1361-6471/aa6a06>.
- [145] D. Rein and L. M. Sehgal, “Neutrino Excitation of Baryon Resonances and Single Pion Production,” *Annals Phys.*, vol. 133, pp. 79–153, 1981. DOI: 10.1016/0003-4916(81)90242-6.
- [146] C. Berger and L. M. Sehgal, “Lepton mass effects in single pion production by neutrinos,” *Physical Review D*, vol. 76, no. 11, Dec. 2007, ISSN: 1550-2368. DOI: 10.1103/physrevd.76.113004.
- [147] K. S. Kuzmin *et al.*, “Extended rein–sehgal model for tau lepton production,” *Nuclear Physics B - Proceedings Supplements*, vol. 139, pp. 158–161, Feb. 2005, ISSN: 0920-5632. DOI: 10.1016/j.nuclphysbps.2004.11.213.
- [148] K. M. Graczyk and J. T. Sobczyk, “Lepton mass effects in weak charged current single pion production,” *Physical Review D*, vol. 77, no. 5, Mar. 2008, ISSN: 1550-2368. DOI: 10.1103/physrevd.77.053003.
- [149] O. Lalakulich *et al.*, “Resonance production by neutrinos: The second resonance region,” *Phys. Rev. D*, vol. 74, p. 014 009, 1 Jul. 2006. DOI: 10.1103/PhysRevD.74.014009.
- [150] K. M. Graczyk and J. T. Sobczyk, “Form factors in the quark resonance model,” *Phys. Rev. D*, vol. 77, p. 053 001, 5 Mar. 2008. DOI: 10.1103/PhysRevD.77.053001.
- [151] K. Iwamoto *et al.*, “Inelastic Single Pion Signal Study in ν_e Appearance using Modified Decay Electron Cut,” T2K Collaboration, Tech. Rep. T2K-TN233, 2016.
- [152] S. Ahmad *et al.*, “Neutrino induced charged current 1 pi+ production at intermediate energies,” *Phys. Rev. D*, vol. 74, p. 073 008, 2006. DOI: 10.1103/PhysRevD.74.073008. arXiv: nucl-th/0607069.
- [153] G. M. Radecky *et al.*, “Study of Single Pion Production by Weak Charged Currents in Low-energy Neutrino d Interactions,” *Phys. Rev. D*, vol. 25, pp. 1161–1173, 1982, [Erratum: Phys.Rev.D 26, 3297 (1982)]. DOI: 10.1103/PhysRevD.25.1161.
- [154] T. Kitagaki *et al.*, “Charged Current Exclusive Pion Production in Neutrino Deuterium Interactions,” *Phys. Rev. D*, vol. 34, pp. 2554–2565, 1986. DOI: 10.1103/PhysRevD.34.2554.
- [155] C. Wilkinson *et al.*, “Reanalysis of bubble chamber measurements of muon-neutrino induced single pion production,” *Phys. Rev. D*, vol. 90, no. 11, p. 112 017, 2014. DOI: 10.1103/PhysRevD.90.112017. arXiv: 1411.4482 [hep-ex].

- [156] A. A. Aguilar-Arevalo *et al.*, “Measurement of neutrino-induced charged-current charged pion production cross sections on mineral oil at $E_{\nu} = 1$ GeV,” *Physical Review D*, vol. 83, no. 5, Mar. 2011, ISSN: 1550-2368. DOI: [10.1103/physrevd.83.052007](https://doi.org/10.1103/physrevd.83.052007).
- [157] M. Kabirnezhad, “Single pion production in electron-nucleon interactions,” *Phys. Rev. D*, vol. 102, no. 5, p. 053009, 2020. DOI: [10.1103/PhysRevD.102.053009](https://doi.org/10.1103/PhysRevD.102.053009). arXiv: [2006.13765 \[hep-ph\]](https://arxiv.org/abs/2006.13765).
- [158] D. Rein and L. M. Sehgal, “Coherent π^0 production in neutrino reactions,” *Nuclear Physics B*, vol. 223, no. 1, pp. 29–44, 1983, ISSN: 0550-3213. DOI: [https://doi.org/10.1016/0550-3213\(83\)90090-1](https://doi.org/10.1016/0550-3213(83)90090-1).
- [159] A. Higuera *et al.*, “Measurement of Coherent Production of π^{\pm} in Neutrino and Antineutrino Beams on Carbon from E_{ν} of 1.5 to 20 GeV,” *Phys. Rev. Lett.*, vol. 113, p. 261802, 26 Dec. 2014. DOI: [10.1103/PhysRevLett.113.261802](https://doi.org/10.1103/PhysRevLett.113.261802).
- [160] C. Berger and L. M. Sehgal, “Partially conserved axial vector current and coherent pion production by low energy neutrinos,” *Physical Review D*, vol. 79, no. 5, Mar. 2009, ISSN: 1550-2368. DOI: [10.1103/physrevd.79.053003](https://doi.org/10.1103/physrevd.79.053003).
- [161] D. Rein, “Diffractive Pion Production in Neutrino Reactions,” *Nucl. Phys. B*, vol. 278, pp. 61–77, 1986. DOI: [10.1016/0550-3213\(86\)90106-9](https://doi.org/10.1016/0550-3213(86)90106-9).
- [162] M. Glück *et al.*, “Dynamical parton distributions revisited,” *Eur. Phys. J. C*, vol. 5, pp. 461–470, 1998. DOI: [10.1007/s100520050289](https://doi.org/10.1007/s100520050289). arXiv: [hep-ph/9806404](https://arxiv.org/abs/hep-ph/9806404).
- [163] A. Bodek and U.-k. Yang, “A Unified model for inelastic e - N and nu - N cross-sections at all Q^{**2} ,” *AIP Conf. Proc.*, vol. 792, no. 1, W. H. Smith and S. R. Dasu, Eds., pp. 257–260, 2005. DOI: [10.1063/1.2122031](https://doi.org/10.1063/1.2122031). arXiv: [hep-ph/0508007](https://arxiv.org/abs/hep-ph/0508007).
- [164] M. Derrick *et al.*, “Properties of the hadronic system resulting from $\bar{\nu}_{\mu}p$ interactions,” *Phys. Rev. D*, vol. 17, pp. 1–15, 1 Jan. 1978. DOI: [10.1103/PhysRevD.17.1](https://doi.org/10.1103/PhysRevD.17.1).
- [165] T. Yang *et al.*, “A hadronization model for few-gev neutrino interactions,” *The European Physical Journal C*, vol. 63, no. 1, pp. 1–10, Aug. 2009, ISSN: 1434-6052. DOI: [10.1140/epjc/s10052-009-1094-z](https://doi.org/10.1140/epjc/s10052-009-1094-z).
- [166] T. Sjostrand, “High-energy physics event generation with PYTHIA 5.7 and JETSET 7.4,” *Comput. Phys. Commun.*, vol. 82, pp. 74–90, 1994. DOI: [10.1016/0010-4655\(94\)90132-5](https://doi.org/10.1016/0010-4655(94)90132-5).
- [167] R. D. Woods and D. S. Saxon, “Diffuse surface optical model for nucleon-nuclei scattering,” *Phys. Rev.*, vol. 95, pp. 577–578, 2 Jul. 1954. DOI: [10.1103/PhysRev.95.577](https://doi.org/10.1103/PhysRev.95.577).
- [168] E. S. Pinzon Guerra *et al.*, “Measurement of σ_{ABS} and σ_{CX} of π^+ on carbon by the Dual Use Experiment at TRIUMF (DUET),” *Phys. Rev. C*, vol. 95, p. 045203, 4 Apr. 2017. DOI: [10.1103/PhysRevC.95.045203](https://doi.org/10.1103/PhysRevC.95.045203).
- [169] T. Feusels *et al.*, “Tuning of the NEUT Cascade Model using π^{\pm} -A Scattering External Data to Improve Final State Interaction and Secondary Interaction Systematic Uncertainties,” T2K Collaboration, Tech. Rep. T2K-TN325, 2017.
- [170] C. J. *et al.*, “Simulations from a new neutrino event generator,” *Nuclear Physics B - Proceedings Supplements*, vol. 159, pp. 211–216, 2006, Proceedings of the 4th International Workshop on Neutrino-Nucleus Interactions in the Few-GeV Region, ISSN: 0920-5632. DOI: <https://doi.org/10.1016/j.nuclphysbps.2006.08.069>.

- [171] P. Perio *et al.*, “Pion Hadronic Secondary Interactions in Super-Kamiokande,” T2K Collaboration, Tech. Rep. T2K-TN105, 2012.
- [172] A. Bodek and T. Cai, “Removal energies and final state interaction in lepton nucleus scattering,” *The European Physical Journal C*, vol. 79, no. 4, Apr. 2019, ISSN: 1434-6052. DOI: 10.1140/epjc/s10052-019-6750-3.
- [173] S. Dolan *et al.*, “Implementation of the susav2-meson exchange current 1p1h and 2p2h models in genie and analysis of nuclear effects in t2k measurements,” *Physical Review D*, vol. 101, no. 3, Feb. 2020, ISSN: 2470-0029. DOI: 10.1103/physrevd.101.033003.
- [174] S. Bienstock *et al.*, “TN-331 Update for Neutrino2018: Assessing the effect of cross-section model uncertainties on the T2K oscillation analyses with simulated data studies using the BANFF and P-Theta fit frameworks,” T2K Collaboration, Tech. Rep. T2K-TN331, 2018.
- [175] J. A. Caballero, “General study of superscaling in quasielastic (e, e') and (ν, μ) reactions using the relativistic impulse approximation,” *Phys. Rev. C*, vol. 74, p. 015502, 1 Jul. 2006. DOI: 10.1103/PhysRevC.74.015502.
- [176] J. Tena-Vidal *et al.*, *Neutrino-nucleon cross-section model tuning in genie v3*, 2021. arXiv: 2104.09179 [hep-ph].
- [177] C. L. McGivern *et al.*, “Cross sections for ν_μ and $\bar{\nu}_\mu$ induced pion production on hydrocarbon in the few-GeV region using MINERvA,” *Phys. Rev. D*, vol. 94, p. 052005, 5 Sep. 2016. DOI: 10.1103/PhysRevD.94.052005.
- [178] M. Day and K. S. McFarland, “Differences in quasielastic cross sections of muon and electron neutrinos,” *Physical Review D*, vol. 86, no. 5, Sep. 2012, ISSN: 1550-2368. DOI: 10.1103/physrevd.86.053003.
- [179] E. Wang *et al.*, “Photon emission in neutral current interactions at the t2k experiment,” *Physical Review D*, vol. 92, no. 5, Sep. 2015, ISSN: 1550-2368. DOI: 10.1103/physrevd.92.053005.
- [180] E. Wang *et al.*, “Photon emission in neutral-current interactions at intermediate energies,” *Physical Review C*, vol. 89, no. 1, Jan. 2014, ISSN: 1089-490X. DOI: 10.1103/physrevc.89.015503.
- [181] M. Dunkman *et al.*, “Updated Recommendation of the 2014-5 Oscillation Parameters,” T2K Collaboration, Tech. Rep. T2K-TN256, 2015.
- [182] P. Bartet *et al.*, “ ν_μ CC event selections in the ND280 tracker using Run 2++3+4 data,” T2K Collaboration, Tech. Rep. T2K-TN212, 2015.
- [183] M. Hartz *et al.*, “Constraining the Flux and Cross Section Models with Data from the ND280 Detector for the 2014/15 Oscillation Analysis,” T2K Collaboration, Tech. Rep. T2K-TN220, 2015.
- [184] R. Barlow and C. Beeston, “Fitting using finite monte carlo samples,” *Computer Physics Communications*, vol. 77, no. 2, pp. 219–228, 1993, ISSN: 0010-4655. DOI: [https://doi.org/10.1016/0010-4655\(93\)90005-W](https://doi.org/10.1016/0010-4655(93)90005-W). [Online]. Available: <http://www.sciencedirect.com/science/article/pii/001046559390005W>.
- [185] J. Conway, “Incorporating Nuisance Parameters in Likelihoods for Multisource Spectra,” 115–120. 6 p, Mar. 2011, Comments: Presented at PHYSTAT 2011, CERN, Geneva, Switzerland, January 2011, to be published in a CERN Yellow Report. DOI: 10.5170/CERN-2011-006.115. arXiv: 1103.0354.
- [186] C. Bojechko *et al.*, “CC-multiple-pion ν_μ event selections in the ND280 tracker using Run 1+2+3+4 data,” T2K Collaboration, Tech. Rep. T2K-TN152, 2013.

- [187] C. Andreopoulos *et al.*, “T2K 3.010×10^{20} -POT 3-Flavour Muon-Neutrino Disappearance Analysis,” T2K Collaboration, Tech. Rep. T2K-TN141, 2013.
- [188] L. Xiaoyue *et al.*, “FiTQun Event Selection Optimization,” T2K Collaboration, Tech. Rep. T2K-TN319, 2017.
- [189] J. Imber *et al.*, “T2K-SK Systematic Error Summary for the 2017 Oscillation Analysis,” T2K Collaboration, Tech. Rep. T2K-TN326, 2017.
- [190] R. Akutsu *et al.*, “Super-Kamiokande data quality for T2K Run 9,” T2K Collaboration, Tech. Rep. T2K-TN355, 2019.
- [191] K. Abe *et al.*, “Measurements of neutrino oscillation in appearance and disappearance channels by the T2K experiment with 6×10^{20} protons on target,” *Phys. Rev. D*, vol. 91, p. 072010, 7 Apr. 2015. DOI: 10.1103/PhysRevD.91.072010.
- [192] J. Nieves *et al.*, “The nucleon axial mass and the miniboone quasielastic neutrino–nucleus scattering problem,” *Physics Letters B*, vol. 707, no. 1, pp. 72–75, Jan. 2012, ISSN: 0370-2693. DOI: 10.1016/j.physletb.2011.11.061. [Online]. Available: <http://dx.doi.org/10.1016/j.physletb.2011.11.061>.
- [193] K. Abe *et al.*, “First muon-neutrino disappearance study with an off-axis beam,” *Phys. Rev. D*, vol. 85, p. 031103, 3 Feb. 2012. DOI: 10.1103/PhysRevD.85.031103. [Online]. Available: <https://link.aps.org/doi/10.1103/PhysRevD.85.031103>.
- [194] K. Abe *et al.*, “Measurement of neutrino oscillation parameters from muon neutrino disappearance with an off-axis beam,” *Phys. Rev. Lett.*, vol. 111, p. 211803, 21 Nov. 2013. DOI: 10.1103/PhysRevLett.111.211803. [Online]. Available: <https://link.aps.org/doi/10.1103/PhysRevLett.111.211803>.
- [195] K. Abe *et al.*, “Measurement of muon antineutrino oscillations with an accelerator-produced off-axis beam,” *Phys. Rev. Lett.*, vol. 116, p. 181801, 18 May 2016. DOI: 10.1103/PhysRevLett.116.181801.
- [196] K. Abe *et al.*, “Updated T2K measurements of muon neutrino and antineutrino disappearance using 1.5×10^{21} protons on target,” *Phys. Rev. D*, vol. 96, p. 011102, 1 Jul. 2017. DOI: 10.1103/PhysRevD.96.011102. [Online]. Available: <https://link.aps.org/doi/10.1103/PhysRevD.96.011102>.
- [197] ——, “Combined analysis of neutrino and antineutrino oscillations at t2k,” *Phys. Rev. Lett.*, vol. 118, p. 151801, 15 Apr. 2017. DOI: 10.1103/PhysRevLett.118.151801. [Online]. Available: <https://link.aps.org/doi/10.1103/PhysRevLett.118.151801>.
- [198] ——, “Measurement of neutrino and antineutrino oscillations by the T2K experiment including a new additional sample of ν_e interactions at the far detector,” *Phys. Rev. D*, vol. 96, p. 092006, 9 Nov. 2017. DOI: 10.1103/PhysRevD.96.092006. [Online]. Available: <https://link.aps.org/doi/10.1103/PhysRevD.96.092006>.
- [199] J. KOPP, “Efficient numerical diagonalization of hermitian 3×3 matrices,” *International Journal of Modern Physics C*, vol. 19, no. 03, pp. 523–548, 2008. DOI: 10.1142/S0129183108012303. eprint: <https://doi.org/10.1142/S0129183108012303>. [Online]. Available: <https://doi.org/10.1142/S0129183108012303>.
- [200] W. H. Press, S. A. Teukolsky *et al.*, *Numerical Recipes in C: The Art of Scientific Computing, Third Edition*. Cambridge University Press, 2007, ISBN: 9780521880688.

- [201] S. S. Wilks, “The large-sample distribution of the likelihood ratio for testing composite hypotheses,” *Ann. Math. Statist.*, vol. 9, no. 1, pp. 60–62, Mar. 1938. DOI: 10.1214/aoms/1177732360. [Online]. Available: <https://doi.org/10.1214/aoms/1177732360>.
- [202] L. Berns *et al.*, “Five Sample Joint Oscillation Analysis with T2K Run1–10 Data,” T2K Collaboration, Tech. Rep. T2K-TN397, 2020.
- [203] G. J. Feldman and R. D. Cousins, “A Unified approach to the classical statistical analysis of small signals,” *Phys. Rev.*, vol. D57, pp. 3873–3889, 1998. DOI: 10.1103/PhysRevD.57.3873. arXiv: physics/9711021.
- [204] T. Vladislavljevic, “Predicting the T2K Neutrino Flux and Measuring Oscillation Parameters,” Ph.D. dissertation, Oxford U., 2020. DOI: 10.1007/978-3-030-51174-6.
- [205] K. Nakamura, “Measurement of Neutrino Oscillation with a High Intensity Neutrino Beam,” Ph.D. dissertation, Kyoto U., 2018. DOI: 10.14989/doctor.k21441.
- [206] A. Atkin *et al.*, “Measuring PMNS parameters in a joint ND280-SK analysis using MCMC,” T2K Collaboration, Tech. Rep. T2K-TN393, 2020.
- [207] C. Andreopoulos *et al.*, “T2K Neutrino and Anti-Neutrino 3-Flavour Joint Analysis of Run 1-10 (1.97×10^{21} -POT ν 1.63×10^{21} -POT $\bar{\nu}$) data sets,” T2K Collaboration, Tech. Rep. T2K-TN394, 2020.
- [208] T. Koga *et al.*, “Updated p-theta $\bar{\nu}_e$ appearance search using the T2K full RUN1-9 data set,” T2K Collaboration, Tech. Rep. T2K-TN353, 2019.
- [209] C. Andreopoulos *et al.*, “ $\bar{\nu}_e$ Appearance Analysis with the 3-Flavour Joint Fit Framework for T2K Run 1-9c (1.4938×10^{21} -POT Neutrino and 1.1236×10^{21} -POT Anti-Neutrino) and Run 1-9d (1.4938×10^{21} -POT Neutrino and 1.6346×10^{21} -POT Anti-Neutrino) Data Sets”, T2K Collaboration, Tech. Rep. T2K-TN356, 2019.
- [210] ———, “T2K Neutrino and Anti-Neutrino 3-Flavour Joint Analysis of Run 1-9 (1.49×10^{21} -POT ν 1.63×10^{21} -POT $\bar{\nu}$) data sets,” T2K Collaboration, Tech. Rep. T2K-TN360, 2019.
- [211] P. A. Rodrigues *et al.*, “Identification of nuclear effects in neutrino-carbon interactions at low three-momentum transfer,” *Phys. Rev. Lett.*, vol. 116, p. 071802, 7 Feb. 2016. DOI: 10.1103/PhysRevLett.116.071802. [Online]. Available: <https://link.aps.org/doi/10.1103/PhysRevLett.116.071802>.
- [212] P. de Perio *et al.*, “NEUT Nuclear Effects (FSI),” T2K Collaboration, Tech. Rep. T2K-TN033, 2012.
- [213] S. Bolognesi *et al.*, “Assessing the effect of cross-section model uncertainties on the T2K oscillation analyses with simulated data studies using the BANFF and P-Theta fit frameworks,” T2K Collaboration, Tech. Rep. T2K-TN396, 2020.
- [214] C. Adamuščín *et al.*, “Two-component model for the axial form factor of the nucleon,” *Physical Review C*, vol. 78, no. 3, Sep. 2008, ISSN: 1089-490X. DOI: 10.1103/physrevc.78.035201.
- [215] M. A. Acero *et al.*, “First Measurement of Neutrino Oscillation Parameters using Neutrinos and Antineutrinos by NOvA,” *Phys. Rev. Lett.*, vol. 123, no. 15, p. 151803, 2019. DOI: 10.1103/PhysRevLett.123.151803. arXiv: 1906.04907 [hep-ex].
- [216] A. Himmel, “New Oscillation Results from the NOvA Experiment. Presented at the Neutrino 2020 (neutrino2020) conference,” 2020. DOI: 10.5281/zenodo.4142045.

- [217] K. Abe *et al.*, *Sensitivity of the T2K accelerator-based neutrino experiment with an Extended run to 20×10^{21} POT*, 2016. arXiv: 1607.08004 [hep-ex].
- [218] K. Abe *et al.*, *T2K ND280 Upgrade – Technical Design Report*, 2020. arXiv: 1901.03750 [physics.ins-det].
- [219] L. S. Mohan, *Status of Multi Ring Samples in the Far Detector*, Internal report, 2021. [Online]. Available: <https://t2k.org/meet/collab/t2k-collaboration-meeting-19th-26th-May-2021/talks/mon24may2021/MR%20status%20update>.
- [220] L. Pickering *et al.*, *NIWG Conveners' Report*, Internal report, 2021. [Online]. Available: <https://t2k.org/meet/collab/t2k-collaboration-meeting-19th-26th-May-2021/talks/mon24may2021/niwgconvrept>.
- [221] J. Chakrani *et al.*, *Updates to the CCQE model: To OA2021... and Beyond!* Internal report, 2021. [Online]. Available: <https://t2k.org/meet/collab/t2k-collaboration-meeting-19th-26th-May-2021/talks/mon24may2021/CCQEUpdates>.
- [222] C. Bronner *et al.*, *Global analysis plan in coming years*, Internal report, 2021. [Online]. Available: <https://t2k.org/meet/collab/t2k-collaboration-meeting-19th-26th-May-2021/talks/wed19may2021/global-analysis-plan-in-coming-years>.
- [223] F. An *et al.*, “Neutrino physics with JUNO,” *Journal of Physics G: Nuclear and Particle Physics*, vol. 43, no. 3, p. 030 401, Feb. 2016, ISSN: 1361-6471. DOI: 10.1088/0954-3899/43/3/030401.
- [224] R. Patterson, “The NOvA experiment: status and outlook,” *Nuclear Physics B - Proceedings Supplements*, vol. 235-236, pp. 151–157, Feb. 2013, ISSN: 0920-5632. DOI: 10.1016/j.nuclphysbps.2013.04.005.
- [225] U. F. Katz, *The ORCA Option for KM3NeT*, 2014. arXiv: 1402.1022 [astro-ph.IM].
- [226] K. Abe *et al.*, “Neutrino oscillation physics potential of the T2K experiment,” *Progress of Theoretical and Experimental Physics*, vol. 2015, no. 4, Apr. 2015, 043C01, ISSN: 2050-3911. DOI: 10.1093/ptep/ptv031.
- [227] K. Abe *et al.*, *Hyper-kamiokande design report*, 2018. arXiv: 1805.04163 [physics.ins-det].
- [228] C. Bronner, “Physics potential of Hyper-Kamiokande for neutrino oscillation measurements,” *PoS*, vol. NuFact2017, p. 053, 2018. DOI: 10.22323/1.295.0053.
- [229] B. Abi *et al.*, *Long-baseline neutrino oscillation physics potential of the dune experiment*, 2020. arXiv: 2006.16043 [hep-ex].

Acronyms

CC Charged Current.

CL Confidence Level.

CP Charge-Parity Symmetry.

CPT Charge-Parity-Time reversal Symmetry.

CR Confidence Region.

DAQ Data AQuisition.

DIS Deep Inelastic Scattering.

DUNE Deep Underground Neutrino Experiment.

ECAL Electromagnetic CALorimeter.

ES Elastic Scattering.

FC Feldman-Cousins method.

FD Far Detector.

FGD Fine-Grained Detector.

FSI Final State Interactions.

HK Hyper-Kamiokande.

ID Super-Kamiokande Inner Detector.

INGRID Interactive Neutrino GRID.

IO Inverted mass Ordering.

LBL Long BaseLine.

LINAC LINear ACcelerator.

MC Monte Carlo simulation.

MH Mass Hierarchy.

MO Mass Ordering.

MR Main Ring synchrotron.

NC Neutral Current.

ND Near Detector.

ND280 Near Detector at 280m.

NO Normal mass Ordering.

OD Super-Kamiokande Outer Detector.

P0D π^0 Detector.

PDF Probability Density Function.

PDF Parton Distribution Function.

PID Particle IDentification.

PMT PhotoMultiplier Tube.

PN PhotoNuclear effect.

POT Protons On Target.

RCS Rapid Cycling Synchrotron.

RFG Relativistic Fermi Gas.

SF Spectral Function.

SI Secondary Interactions.

SK Super-Kamiokande.

SSM Standard Solar Model.

T2HK Tokai to Hyper-Kamiokande.

T2K Tokai to Kamioka.

TPC Time Projection Chamber.

List of Figures

2.1	Beta decay spectrum of ^{210}Bi	4
2.2	Example of a ν_τ event observed by the DONUT experiment.	5
2.3	Solar neutrino flux spectra broken down by source.	7
2.4	Double ratio of atmospheric neutrino fluxes, as measured by several experiments.	7
2.5	Observed total ^8B solar flux compared to predictions of the standard solar model.	8
2.6	Dependence of the atmospheric flux double ratio on the zenith angle.	9
2.7	Dependence of the observed and predicted neutrino event rate on the zenith angle in the Super-K Experiment.	10
2.8	Ratio of observed and predicted $\bar{\nu}_e$ fluxes in the KamLAND experiment.	11
2.9	Illustration of the normal and inverted neutrino mass orderings.	14
2.10	Variation of oscillation probabilities at T2K with the oscillation parameters and L/E	19
2.11	The baryon asymmetry as a function of δ_{CP} for various assumed values of the Majorana phases.	23
2.12	Predicted and observed constraints on Δm_{21}^2 and θ_{12} from various solar models and KamLAND data, respectively.	25
2.13	The 2018 observed constraints on Δm_{3j}^2 vs. $\sin^2 \theta_{23}$ and Δm_{3j}^2 vs. $\sin^2 \theta_{13}$ from various experiments and their combination.	26
2.14	The 2018 observed constraints on δ_{CP} from the MINOS, NOvA, and T2K experiments and their combination.	29
3.1	A diagram of the path taken by the T2K neutrino beam from its creation in the J-PARC facility, through the near detectors, and towards the far detector, Super-Kamiokande.	32
3.2	Accelerator layout at J-PARC.	32
3.3	Diagram of the neutrino beamlines at J-PARC.	33
3.4	Accumulation of POT over time, divided into run periods. The power of the J-PARC proton beam is also shown.	33
3.5	Predicted unoscillated neutrino fluxes at Super-K, broken down by neutrino flavour.	34
3.6	Variation of neutrino energy with pion energy and off-axis angle.	36

3.7	The effect of the off-axis angle on the predicted unoscillated flux at Super-K.	36
3.8	The near detector complex containing the two main detectors, ND280 (off-axis) and INGRID (on-axis).	37
3.9	The INGRID on-axis detector.	38
3.10	Observed event rates and direction of the J-PARC neutrino beam over the history of the T2K experiment, as measured by INGRID and MUMON.	38
3.11	Exploded view of the ND280 off-axis detector and its sub-detectors.	39
3.12	The total energy deposited by charged particle tracks in FGD1 as a function of track range.	40
3.13	Distribution of the energy loss in the TPCs as a function of momentum.	41
3.14	The particle identification statistic for the barrel ECAL, showing the ability to distinguish between track-like and shower-like particle events in both MC and data.	42
3.15	Predicted and observed energy resolution of the Downstream ECal for electromagnetic showers.	43
3.16	Track finding efficiency of SMRD-only reconstruction for events with at least two muon hits in the detector as a function of true muon momentum.	43
3.17	Cutaway view of the Super-Kamiokande detector.	45
3.18	Examples of single-lepton events at Super-K and their resulting Cherenkov rings.	46
4.1	High-level overview of the oscillation analysis, showing the flux, cross-section, detector, and oscillation model inputs to the near and far detector fits and how the fits relate to each other.	48
4.2	The predicted phase space of hadrons that decay to produce neutrinos, compared to the phase space covered by the NA61/SHINE experiment.	50
4.3	Ratio of the tuned to nominal unoscillated predicted neutrino fluxes at Super-K.	51
4.4	The total fractional uncertainty, and contributing uncertainties on the unoscillated flux predictions.	52
4.5	Predicted neutrino CC cross-sections per nucleon as a function of neutrino energy overlaid with the predicted fluxes at ND280 FDG1 and at Super-K.	53
4.6	The relativistic Fermi gas model and the Benhar spectral function describing the nuclear ground state for ^{16}O as a function of initial nucleon momentum and removal energy.	54
4.7	Feynman diagrams for CCQE interactions.	56
4.8	Comparison of spectral function model predictions to observations from the MINERvA experiment as a function of four-momentum transfer.	57

4.9	Cross-sections for 3 GeV neutrinos incident on ^{12}C as a function of energy and three-momentum transfer.	58
4.10	Feynman diagram examples for various processes that result in a single-pion being detected in the final state.	59
4.11	Predicted and observed coherent pion production differential cross-sections.	60
4.12	Illustration of the dominant types of π^+ FSI with the remnant nucleus.	62
4.13	Variations in the differential cross-section for QE interactions as the nucleon removal energy is changed.	64
4.14	Variations in predicted reconstructed neutrino energy distributions at Super-K when the nucleon removal energies are changed.	68
4.15	The flux and cross-section covariance matrix resulting from the near detector fit.	74
4.16	Flux parameter values before and after the near detector fit.	75
4.17	Interaction model parameter values before and after the near detector fit. .	76
4.18	Comaprison of the observed p_μ distributions at FGD1 in ND280 to predictions generated after the near detector fit.	76
4.19	Distribution of the simulated and observed number of reconstructed Cherenkov rings in the ν_μ CCQE-like sample, with Super-K selection criteria superimposed.	79
4.20	Distribution of the simulated and observed ν_μ/ν_e discrimination PID parameter in the ν_μ CCQE-like sample, with Super-K selection criteria superimposed.	80
4.21	Distribution of the simulated and observed number of reconstructed decay electrons in the ν_μ CCQE-like sample, with Super-K selection criteria superimposed.	80
4.22	Distribution of the simulated and observed ν_μ/π^+ discrimination PID parameter in the ν_μ CCQE-like sample, with Super-K selection criteria superimposed.	81
4.23	Distribution of the simulated and observed reconstructed neutrino energy in the ν_μ CCQE-like sample, after all Super-K selection criteria have been applied.	81
4.24	Distribution of the simulated and observed number of reconstructed Cherenkov rings in the ν_e CCQE-like sample, with Super-K selection criteria superimposed.	84
4.25	Distribution of the simulated and observed ν_e/ν_μ discrimination PID parameter in the ν_e CCQE-like sample, with Super-K selection criteria superimposed.	84
4.26	Distribution of the simulated and observed visible energy in the ν_e CCQE-like sample, with Super-K selection criteria superimposed.	85

4.27 Distribution of the simulated and observed number of reconstructed decay electrons in the $\bar{\nu}_e$ CCQE-like sample, with Super-K selection criteria superimposed.	85
4.28 Distribution of the simulated and observed reconstructed neutrino energy in the $\bar{\nu}_e$ CCQE-like sample, with Super-K selection criteria superimposed.	86
4.29 Distribution of the simulated and observed $\bar{\nu}_e/\pi^0$ discrimination PID parameter in the $\bar{\nu}_e$ CCQE-like sample, with Super-K selection criteria superimposed.	86
4.30 Distribution of the simulated and observed reconstructed neutrino energy in the $\bar{\nu}_e$ CCQE-like sample, after all Super-K selection criteria have been applied.	87
4.31 Distribution of the simulated and observed number of reconstructed Cherenkov rings and $\bar{\nu}_e/\bar{\nu}_\mu$ discrimination PID parameter in the ν -mode $\bar{\nu}_e$ CC1 π^+ -like sample, with Super-K selection criteria superimposed.	89
4.32 Distribution of the simulated and observed visible energy and the number of reconstructed decay electrons in the ν -mode $\bar{\nu}_e$ CC1 π^+ -like sample, with Super-K selection criteria superimposed.	90
4.33 Distribution of the simulated and observed reconstructed neutrino energy and $\bar{\nu}_e/\pi^0$ discrimination PID parameter in the ν -mode $\bar{\nu}_e$ CC1 π^+ -like sample, with Super-K selection criteria superimposed.	90
4.34 Distribution of the simulated and observed reconstructed neutrino energy in the ν -mode $\bar{\nu}_e$ CC1 π^+ -like sample, after all Super-K selection criteria have been applied.	91
4.35 Posterior predictive PID and ring-counting distributions of the Super-K atmospheric MCMC fit to determine detector systematic uncertainties.	95
4.36 The Super-K detector + SI + PN covariance matrix.	97
 5.1 Comaprison of the predicted sensitivities to δ_{CP} generated by three different oscillation analysis fitter groups in T2K.	106
5.2 θ projections of the predicted Asimov A kinematic distributions compared to T2K Runs 1-10 observations.	116
5.3 Predicted unoscillated kinematic distributions compared to T2K Runs 1-10 observations.	117
5.4 Predicted Asimov A kinematic distributions compared to T2K Runs 1-10 observations.	118
5.5 Predicted nominal E_{rec} distributions with $\pm 1\sigma$ systematic errors, both pre and post near detector fit.	121
5.6 Asimov A and B predicted constraints on δ_{CP}	123
5.7 Asimov A and B predicted constraints on $\sin^2 \theta_{13}$	123
5.8 Asimov A and B predicted constraints on $\sin^2 \theta_{23}$	123
5.9 Asimov A and B predicted constraints on Δm_{32}^2 (NO) or $ \Delta m_{31}^2 $ (IO).	124

5.10 Asimov A and B predicted constraints on δ_{CP} vs. $\sin^2 \theta_{13}$	124
5.11 Asimov A and B predicted constraints on $ \Delta m_{3j}^2 $ vs. $\sin^2 \theta_{23}$	125
5.12 Predicted kinematic distributions generated at the T2K Runs 1-10 best-fit values compared to T2K Runs 1-10 observations.	130
5.13 E_{rec} and θ projections of predicted kinematic distributions generated at the T2K Runs 1-10 best-fit values compared to T2K Runs 1-10 observations.	131
5.14 Observed constraints on δ_{CP} , $\sin^2 \theta_{13}$, $\sin^2 \theta_{23}$, and Δm_{3j}^2	132
5.15 Observed constraints on δ_{CP} vs. $\sin^2 \theta_{13}$	132
5.16 Observed constraints on Δm_{3j}^2 vs. $\sin^2 \theta_{23}$	133
5.17 The joint marginal likelihood distribution of $ \Delta m_{3j}^2 $ vs. $\sin^2 \theta_{23}$ used as a prior PDF when generating pseudo-experiments for calculating Feldman-Cousins critical values.	134
5.18 Feldman-Cousins critical values as a function of δ_{CP} and mass ordering. .	136
5.19 Observed constraints on δ_{CP} with Feldman-Cousins confidence intervals superimposed.	136
5.20 Comparison of observed and expected constraints on δ_{CP}	137
5.21 Changes to the observed constraint on δ_{CP} when the observations for each sample are replaced with the corresponding expectation.	138
5.22 Bi-event plots showing variations in the e -like sample event rates as δ_{CP} , $\sin^2 \theta_{23}$, and $ \Delta m_{3j}^2 $ are varied.	139
5.23 Comparison of the observed constraint on δ_{CP} to an ensemble of pseudo-experiments in order to assess the extremity of the observations.	141
5.24 Incremental contributions to the change in the constraint on δ_{CP} between the current (Run 1-10) and previous (Run 1-9d) T2K analyses.	143
5.25 The 2020 observed constraints on Δm_{3j}^2 vs. $\sin^2 \theta_{23}$ and Δm_{3j}^2 vs. $\sin^2 \theta_{13}$ from various experiments and their combination.	144
5.26 The 2020 observed constraints on δ_{CP} from the MINOS, NOvA, and T2K experiments and their combination.	145
6.1 E_{rec} and θ projections of the predicted Asimov A kinematic distributions compared to T2K Runs 1-9 observations. Shown with the $\bar{\nu}_\mu \rightarrow \bar{\nu}_e$ oscillation probability switched on and off.	154
6.2 Predicted Asimov A kinematic distributions compared to T2K Runs 1-9 observations.	155
6.3 Expected and observed test statistics in the $\bar{\nu}_e$ appearance analysis.	157
7.1 The expected T2K-II sensitivity to exclude CP-conservation as a function of true δ_{CP}	164
7.2 The expected T2K, NOvA, and joint sensitivities to exclude CP-conservation as a function of true δ_{CP}	164

LIST OF FIGURES

7.3	The expected T2HK and DUNE sensitivities to exclude CP-conservation as a function of true δ_{CP} .	165
A.1	The flux covariance matrix resulting from the near detector fit.	173
A.2	The cross-section covariance matrix resulting from the near detector fit.	174

List of Tables

4.1	The expected and observed number of ν -mode $\bar{\nu}_\mu$ CCQE-like candidate events passing each Super-K selection stage.	79
4.2	The expected and observed number of $\bar{\nu}$ -mode $\bar{\nu}_\mu$ CCQE-like candidate events passing each Super-K selection stage.	82
4.3	The expected and observed number of ν -mode $\bar{\nu}_e$ CCQE-like candidate events passing each Super-K selection stage.	87
4.4	The expected and observed number of $\bar{\nu}$ -mode $\bar{\nu}_e$ CCQE-like candidate events passing each Super-K selection stage.	88
4.5	The expected and observed number of ν -mode $\bar{\nu}_e$ CC1 π^+ -like candidate events passing each Super-K selection stage.	91
4.6	Contributions to the Super-K detector uncertainties.	93
5.1	The (E_{rec}, θ) binning scheme used for the ν -mode and $\bar{\nu}$ -mode $\bar{\nu}_\mu$ CCQE-like samples.	108
5.2	The (E_{rec}, θ) binning scheme used for the ν -mode and $\bar{\nu}$ -mode $\bar{\nu}_e$ CCQE-like samples.	108
5.3	The (E_{rec}, θ) binning scheme used for the ν -mode $\bar{\nu}_e$ CC1 π^+ -like samples.	109
5.4	The E_{true} binning scheme used for all samples.	109
5.5	Oscillation parameters prior PDFs used in the T2K Run 1-10 oscillation analysis.	110
5.6	The number of randomly drawn samples of the nuisance parameter space used to compute the marginal likelihood.	111
5.7	The grid points used to evaluate the marginal likelihood as a function of the parameter(s) of interest.	111
5.8	Definitions of four sets of Asimov oscillation parameters values used to compute expected event rates and kinematic distributions.	112
5.9	Change in the number of observed candidate neutrino events that pass Super-K selection cuts in the T2K Run 1-9 dataset as a result of corrections to the PMT gain.	115
5.10	Predicted and observed event rates in each sample, using the full T2K Run 1-10 beam exposure and data.	116
5.11	Fractional uncertainty on the event rates by error source and sample.	120

5.12	Shifts in the upper and lower boundaries of the δ_{CP} confidence region as a result of the use of alternative valid cross-section models.	127
5.13	Measured oscillation parameter best-fit, 1σ , and 90% confidence intervals.	129
5.14	Feldman-Cousins confidence intervals for δ_{CP}	135
6.1	Oscillation parameters prior PDFs used in the T2K Run 1-9 $\bar{\nu}_e$ appearance analysis.	152
6.2	Definition of the Asimov oscillation parameters values used to compute expected event rates and kinematic distributions in the T2K Run 1-9 $\bar{\nu}_e$ appearance analysis.	153
6.3	Predicted and observed event rates in each sample, using the T2K Run 1-9 beam exposure and data.	154
6.4	Expected and observed rate-only and rate+shape test statistic values for the $\bar{\nu}_e$ appearance analysis.	156
6.5	Expected and observed p -values and significance to exclude each considered hypothesis in the $\bar{\nu}_e$ appearance analysis.	156
A.1	Summary of ν -mode flux systematic normalisation parameters.	168
A.2	Summary of $\bar{\nu}$ -mode flux systematic normalisation parameters.	169
A.3	Summary of cross section systematic parameters.	170
A.4	Summary of cross section systematic parameters (continued).	171
A.5	Summary of SK detector + SI + PN systematic normalisation parameters.	171
A.6	Summary of SK detector + SI + PN systematic normalisation parameters (continued).	172
B.1	Breakdown of the expected event rates for the ν -mode $\bar{\nu}_\mu$ CCQE-like sample.	175
B.2	Breakdown of the expected event rates for the $\bar{\nu}$ -mode $\bar{\nu}_\mu$ CCQE-like sample.	176
B.3	Breakdown of the expected event rates for the ν -mode $\bar{\nu}_e$ CCQE-like sample.	176
B.4	Breakdown of the expected event rates for the $\bar{\nu}$ -mode $\bar{\nu}_e$ CCQE-like sample.	177
B.5	Breakdown of the expected event rates for the ν -mode $\bar{\nu}_e$ CC1 π^+ -like sample.	177